

REPUBLIC OF TURKEY
YILDIZ TECHNICAL UNIVERSITY
GRADUATE SCHOOL OF NATURAL AND APPLIED SCIENCES

INVESTIGATION AND EXPERIMENTAL VERIFICATION
OF UNTETHERED MICROROBOT MOTION BEHAVIOR
SUBJECT TO LAMINAR FLOW

Ali Anil DEMIRCALI

DOCTOR OF PHILOSOPHY THESIS
Department of Mechatronics Engineering
Program of Mechatronics Engineering

Advisor
Asst. Prof. Huseyin UVET

February, 2021

REPUBLIC OF TURKEY
YILDIZ TECHNICAL UNIVERSITY
GRADUATE SCHOOL OF NATURAL AND APPLIED SCIENCES

**INVESTIGATION AND EXPERIMENTAL VERIFICATION OF
UNTETHERED MICROROBOT MOTION BEHAVIOR SUBJECT TO
LAMINAR FLOW**

A thesis submitted by Ali Anil DEMIRCALI in partial fulfillment of the requirements for the degree of **DOCTOR OF PHILOSOPHY** is approved by the committee on 15.02.2021 in Department of Mechatronics Engineering, Program of Mechatronics Engineering.

Asst. Prof. Huseyin UVET
Yildiz Technical University
Advisor

Approved By the Examining Committee

Asst. Prof. Huseyin UVET , Advisor
Yildiz Technical University

Assoc. Prof. Kadir ERKAN, Member
Yildiz Technical University

Asst. Prof. Muhammed Enes ORUC, Member
Gebze Technical University

Assoc. Prof. Cenk ULU, Member
Yildiz Technical University

Assoc. Prof. Gokhan Bora ESMER, Member
Marmara University

I hereby declare that I have obtained the required legal permissions during data collection and exploitation procedures, that I have made the in-text citations and cited the references properly, that I haven't falsified and/or fabricated research data and results of the study and that I have abided by the principles of the scientific research and ethics during my Thesis Study under the title of Investigation and Experimental Verification of Untethered Microrobot Motion Behavior Subject to Laminar Flow supervised by my supervisor, Asst. Prof. Huseyin UVET . In the case of a discovery of false statement, I am to acknowledge any legal consequence.

Ali Anil DEMIRCALI

Signature

This study was supported by the Scientific and Technological Research Council of Turkey (TUBITAK) Grant No: 116E743.

Dedicated to my family

ACKNOWLEDGEMENTS

I wish to acknowledge the following people for their role in the completion of this thesis: My parents, Kadriye and Arif Engin DEMIRCALI for always supporting my choices in life; my brother, Kaan DEMIRCALI for helping me not to give up; my grandfathers Selami ACIKGOZ, Ali DEMIRCALI and my uncle Abdullah AKKIZAL for their place in my heart forever; My supervisor, Asst. Prof. Dr. Hüseyin UVET for his guidance and wise suggestions to the my career steps; Assoc. Prof. Dr. Kadir ERKAN for improving thesis with new methodology and constructive proofreading.

Thank you for helping me to write a Ph.D. thesis I can be proud of.

Ali Anil DEMIRCALI

TABLE OF CONTENTS

LIST OF SYMBOLS	ix
LIST OF ABBREVIATIONS	xi
LIST OF FIGURES	xii
LIST OF TABLES	xxv
ABSTRACT	xxvi
ÖZET	xxviii
1 INTRODUCTION	1
1.1 Literature Review	1
1.1.1 Microrobot Precise Motion Capability	2
1.1.2 Challenge in Miniaturization of Magnetic Microrobots	3
1.1.3 Drag Force Effect in Liquid Media	4
1.1.4 Microrobot Control in Liquid Media	4
1.1.5 Microrobot Motion Behaviour Subject to Laminar FLOW	6
1.2 Objective of the Thesis	7
1.3 Hypothesis	8
2 MAGNETICALLY LEVITATED UNTETHERED MICROROBOT DESIGN	10
2.1 Background Information	10
2.2 Mathematical Models	11
2.2.1 Schematic of microrobot	11
2.2.2 Theoretical Background	15
2.3 FEM Analysis	19
2.3.1 Mesh Structure	20
2.3.2 Drag Coefficient Calculation	23
2.3.3 Determination of Levitation Characteristic	26
2.4 Materials and Methods	28
2.4.1 Permanent Magnet Surface Coating	29
2.4.2 Microrobot Fabrication	30

2.5	Experimental Results	31
2.5.1	Experimental Setup	31
2.5.2	Levitation Capabilities	33
2.5.3	Accurate Positioning and Phase Difference Characterization . .	35
2.5.4	Motion Capabilities of microrobot	37
2.5.5	Head Bending Reaction	39
2.6	Discussion	42
2.6.1	General	42
2.6.2	Analytical Calculation and Simulation	43
2.6.3	Levitation on z-Axis	43
2.6.4	Drag Force—Lifter Magnet Effects	44
2.6.5	Center Alignment	44
2.6.6	Phase Difference	45
3	STABLE UNTETHERED MICROROBOT MOTION BEHAVIOUR	46
3.1	Mathematical Model	47
3.1.1	Head-Tilting Model	48
3.2	FEM Simulation	52
3.2.1	Orientation Effect of the Magnets	52
3.2.2	Environmental Effects on Microrobot	54
3.2.3	Microrobot Working Range	55
3.2.4	Lifter Magnet Orientation Control	56
3.3	Experimental Results	58
3.3.1	Experimental Setup	58
3.3.2	Robot Levitation	61
3.3.3	Robot Orientation Capabilities	61
3.3.4	Uncontrolled Model and Rule-Based Model	63
3.3.5	Vision-based Model	65
3.3.6	Laser Model and Hybrid Model	67
3.4	Discussion	71
4	FLOW-RELATIVE MICROROBOT OPTIMIZATION AND MOTION MOD- ELLING WITH IMPLEMENTATION	76
4.1	Microrobot with SU-8 Body	76
4.1.1	Determination of Damping and Spring Coefficients	77
4.1.2	Magnetic Force Calculation	79
4.1.3	Drag Force Calculation	81
4.1.4	Simulation Results	82
4.1.5	Experimental Results	84
4.2	Micro-magnet based robot	91

4.2.1	Materials and Methods	91
4.2.2	CAD Design	91
4.2.3	Free Body Diagram	91
4.2.4	Drag Force Calculation	95
4.2.5	Magnetic Force Calculation	97
4.2.6	Mathematical Model	100
4.2.7	Reynolds Number Effects	104
4.2.8	Stationary Microrobot in Fluidic Flow	106
4.2.9	Microrobot Motion in Fluidic Flow	108
4.3	Discussion	110
5	INCREASING MICROROBOT FLUID RESISTANCE AGAINST TO FLOW	112
5.1	Materials and Methods	112
5.1.1	A free body diagram of the microrobot	113
5.1.2	Analytical Calculations	116
5.2	Simulation Results	118
5.3	Experimental Results	122
5.4	Discussion	126
6	RESULTS AND DISCUSSION	128
	REFERENCES	130
A	Supplementary Materials	140
	PUBLICATIONS FROM THE THESIS	150

LIST OF SYMBOLS

$\ddot{\theta}$	Angular acceleration of microrobot
θ	Angular position of microrobot
$\dot{\theta}$	Angular velocity of microrobot
F_B	Buoyant force
A	Cross sectional area of microrobot
c_s	Damping coefficient
F_g	Diamagnetic force
F_0	Disturbance
c_d	Drag coefficient
F_D	Drag force
r	Drag force offset relative to the microrobot's center
ρ_f	Fluid density
g	Gravitational acceleration
F_r	Gravitational force
τ	Longitudinal displacement
H	Magnetic field strength
B	Magnetic flux density
F_m	Magnetic force
χ_d	Magnetic insulation coefficient
M	Magnetization vector
a_r	Microrobot acceleration
ρ_r	Microrobot density
m_r	Microrobot mass

V_r	Microrobot volume
I_r	Moment of inertia
w_n	Natural frequency
$\partial/\partial x$	Partial derivative with respect to x
$\partial/\partial y$	Partial derivative with respect to y
$\partial/\partial z$	Partial derivative with respect to z
U	Potential energy
μ_r	Relative permeability
k_s	Spring coefficient
\iint_S	Surface integral
n_x	Surface normal -x direction
n_y	Surface normal -y direction
n_z	Surface normal -z direction
Δ	The amount of head tilting
β	The angle between lower lifter magnet and the centerline
α	The angle between upper lifter magnet and the centerline
l_c	The characteristic length of
F_l	The longitudinal force
t_s	The settling time
T_x	Unwanted torque -x axis
T_y	Unwanted torque -y axis
T_z	Unwanted torque -z axis
μ_0	Vacuum permeability
v	Velocity of the microrobot
\iiint_V	Volume integral
V_p	Volume of a particle

LIST OF ABBREVIATIONS

ABF	Artificial Bacterial Flagella
CFD	Computational Fluid Dynamics
DOF	Degree of Freedom
DI	De-ionized
FEM	Finite Element Method
FSI	Fluid-Structure Interaction
FTIR	Fourier Transforms Infrared
MFNC	Magnetic Fields No Currents
MAH	Motion Area Highlighting
NdFeB	Neodymium Iron Boron Magnets
PDA	Polydopamine
PG	Pyrolytic Graphite
Re	Reynolds Number
TFDD	Two Frames Difference Detector

LIST OF FIGURES

Figure 2.1	Shows the whole experimental with Top-view (A), Front-view (B), and Isometric-view (C). The control of the motorized micro stage where lifter magnet is attached, is realized through a control interface programmed in Visual C#.Net platform (Microsoft Corporation, Redmond, WA, USA). Camera image is transferred to the same interface simultaneously. The data of laser displacement sensor is acquired through the sensors' own interface	12
Figure 2.2	Shows the forces acting on the micro-untethered floating object (microrobot). A free-body diagram of the system is obtained according to the z-axis levitation and lateral movement along the x-axis. Phase difference denotes the lateral movements, which can be expressed as a distance between the center of the lifter and the carrier magnet	14
Figure 2.3	Shows (A) top-view and (B) Front-view. Complete mesh consists of 63259648 domain elements, 560896 boundary elements, and 4112 edge elements	22
Figure 2.4	The effect of the magnetic field on the microrobot and the dimensions of the materials used are shown. As expected in the lifter magnet, the magnetic field is seen with a higher [T] (red color) due to the magnetic field lines' polarity in the corner regions. In the microrobot, the same situation is seen in the magnified image. It is also shown that the lines are in the z-axis direction (front view) since the magnets are placed in order. Used computer: Intel Xeon E4820 * 4 processors (32 core), 128 GB RAM	24
Figure 2.5	Shows von Mises stress on the microrobot upper surface	25
Figure 2.6	Shows vector plot of the surface stresses around the microrobot is seen for various velocities, © 2021 Journal of Magnetics, with permission, from ref [107]	26

Figure 2.7	Exhibits a parabolic drag force characteristic depending on the velocity of microrobot. The drag force change is less for the $[-2, 2]$ mm/s range, which is the microrobot motion speed. For this reason, the system can be expressed by linear equation, by performing curve fitting at the specified interval. For the equation proposed as $F_d = kV_r$, a constant coefficient was found to be $k = 7.075 \times 10^{-9} \text{ kg/s}^2$. Due to the symmetric structure of the microrobot, the force calculation is preferably shown only for x-axis	27
Figure 2.8	The net magnetic force characteristics acting on the microrobot for each of the three axes with respect to the levitation distance are presented	28
Figure 2.9	Shows the effect of the forces exerted on the microrobot depending on the distance between the "Lifter Magnet" and the "Pyrolytic Graphite"	29
Figure 2.10	Fourier transforms infrared (FTIR) spectrum of magnet coated with polydopamine (PDA). The peak between a wavelength of $1500\text{--}1650 \text{ cm}^{-1}$ indicates N–H vibrations, and the peak between the wavelength of $3200\text{--}3600 \text{ cm}^{-1}$ indicates hydroxyl groups in the structure. That proves the successful coating of the magnet surface	30
Figure 2.11	Fabrication process of the microrobot. (A) Sacrificial layer coating; (B) SUEx lamination on sacrificial layer; (C) UV Exposure; (D) Developing; (E) Assembling polydopamine (PDA) coated permanent magnet	32
Figure 2.12	(A) shows diamagnetic levitation experimental setup of microrobot with equipment. An optical microscope is used to record levitation from the lateral view. A container is used for pyrolytic graphite and microrobot with fluid inside. Motorized micro-stages are used due to manipulation of the microrobot in x, y, and z axes. Magnet holder with servo motor controls the microrobot orientation due to its parallel motion to the pyrolytic graphite's surface. (B), (C) and (D) represent the images of microrobot at different heights during the experiment, © 2021 Journal of Magnetism, with permission, from ref [107]	33

- Figure 2.13** The experimental results show the microrobot with different levitation height depending on the distance between "Lifter Magnet" and the "Pyrolytic Graphite (PG)." The experiment was recorded by acquiring the position data with the laser distance sensor in each movement step. The microrobot has been shown to operate at a maximum stabilization level of $333.8\ \mu\text{m}$ in the current system. In figure, the microrobot is shown at various levitation heights based on lifter-magnet position relative to PG; (a) $50\ \mu\text{m}$, (b) $127\ \mu\text{m}$, (c) $173\ \mu\text{m}$, (d) $258\ \mu\text{m}$, (e) $309\ \mu\text{m}$ and (f) $323\ \mu\text{m}$ 34
- Figure 2.14** Shows comparison of finite element method (FEM) and experimental results for the microrobot levitation height according to distance lifter magnet with respect to pyrolytic graphite surface. It is seen that the obtained levitation height are overlapped with each other which is an indication of simulation results are confirmed 35
- Figure 2.15** The phase difference between microrobot and lifter magnet starts from t_0 , starting moment, is shown in (A). After t_1 (B), the carrier magnet's speed will be equal with the lifter magnet: however, the phase difference reaches the maximum value. After that point, the phase difference begin to decrease. The microrobot acceleration, a_r , is already calculated by using Table 2.2 (see Figure 2.8). The phase difference can be expressed easily for this microrobot and lifter magnet with the help of velocity profile and acceleration specified 37
- Figure 2.16** (A) shows the initial position of the microrobot, (B) first delay is occurred when the microrobot is moved, (C) maximum delay is occurred between the lifter magnet and microrobot's center, and (D) motion is completed and phase difference becomes zero. The red line belongs to the laser displacement sensor which is propagating from the lifter magnet's center due to its ring-shaped structure 38
- Figure 2.17** Shows comparison of the experimental and the analytical results for the phase difference. It can be observed that the microrobot phase difference can be analytically calculated which may help to adjust maximum microrobot speed 39
- Figure 2.18** The sinusoidal and circular orbit trajectories have been successfully tracked. (A) shows the sinusoidal trajectory followed by the signal input given as amplitude 4 mm. In (B), a circular orbit with a radius of 2 mm was followed 40

Figure 2.19	The cause of the head-tilt reaction is to suspend the directional changes of the vector field forces acting on the microrobot. The head-tilt angle is a parameter proportional to the phase difference. The increase in phase difference also causes an increase in the head-tilt angle. As shown in the figure, in the experimental studies performed, the head-tilt angle of 7° is monitored. The increase in head-tilting of the microrobot can be seen from (a) to (b)	41
Figure 2.20	(A) refers to the orientation case with misalignment of microrobot as a surface graph with linear characteristic. (B) refers to the values of the lifter magnet angles to provide the prevention of undesired torque (0 approach), © 2021 Journal of Magnetism, with permission, from ref [107]	42
Figure 3.1	(A) The head-tilting reaction is introduced in the uncontrolled state of the microrobot moving in the X direction. (B) Microrobot whose dimensions are: $\varnothing 3\text{mm} \times \varnothing 1\text{ mm} \times \varnothing 0.2\text{mm}$, shown from top view	47
Figure 3.2	The angle calculation to be applied to the lifter-magnet is presented to eliminate undesired torque	49
Figure 3.3	Illustration of levitation height determination in relation to the microrobot-head-tilting angle	49
Figure 3.4	Diagram of magnetic levitation system used in experiments. Numbers represent part names. (A) shows vertical alignment of microrobot and lifter-magnet; (B) shows forces exerted on microrobot, which is aligned with lifter-magnet; and (C) illustrates isometric view of the whole experimental setup	50
Figure 3.5	The orientation of the carrier-magnet in order to avoid head-tilting reaction is presented. Accordingly, the carrier-magnet must have a direction opposite to the motion direction of the microrobot, is observed	53
Figure 3.6	Calculation of Re number is simulated at different head-tilting angles for microrobots with same thickness ($250\mu\text{m}$) and different sizes (1 mm, 2 mm, and 3 mm). COMSOL® Creeping Flow analysis is utilized in stationary liquid media. The legend on the right side, as expected, shows that the $Re \ll 1$ is not dependent on size and head-tilting angle	55
Figure 3.7	Microrobot study limits are determined. Accordingly, the minimum and maximum points are shown in the range of $31.0\mu\text{m}$ (red)– $329.1\mu\text{m}$ (blue)	56

Figure 3.8	(A) shows roll, and pitch axes control the orientation of the microrobot to eliminate head-tilting reaction. The result of the uncontrolled microrobot motion is given in (B). The head-tilting reaction can be eliminated by adjusting carrier-magnet orientation (C)	57
Figure 3.9	(A) Illustrates the experimental system with 2 servo motors, micro-stage connection apparatus, and lifter-magnet microrobot alignment. In (B) the full testing and measurement systems are shown	59
Figure 3.10	(A) Shows the rule-based model (open-loop), (B) shows the laser model (closed-loop), and (C) shows the hybrid model control block diagrams	60
Figure 3.11	The left picture shows minimum levitation height of the microrobot ($30.0\mu m$) and maximum levitation height ($333.8\mu m$) on the right picture	61
Figure 3.12	Axial orientations of the robot are shown. (e) is the initial position at $223\mu m$ levitation height, (a,c) shows negative and positive roll angle respectively, and (b,d) shows positive and negative pitch angle, respectively	62
Figure 3.13	The experimental data represents microrobot motion on a 4 mm trajectory with a sine-wave profile relative to the x-axis by the time recording changes on levitation height relative to the z-axis. Five snapshots are given to show actual location	63
Figure 3.14	Experimental results to show microrobot head-tilting reaction during implementation of uncontrolled and rule-based models at variable speeds (from 5 mm/s to 10 mm/s). While head-tilting reaction is obvious, in the case of the rule-based model, the microrobot's longitudinal motion is slightly developed	64
Figure 3.15	Microrobot head-tilting reaction during implementation of uncontrolled and rule-based models at variable speeds (from 5 mm/s to 10 mm/s) when the levitation height is changed to $100\mu m$ is presented. It can be seen that the rule-based model can be implemented in different levitation height during the microrobot's longitudinal motion since head-tilting angles do not change with the levitation height at lower speeds	65
Figure 3.16	Microrobot corner detection algorithms and their application steps are presented	66

Figure 3.17	Microrobot head-tilting reaction during implementation of visual-feedback models at variable speeds (from 5 mm/s to 10 mm/s) when the levitation height is 200 μm is presented. Head tilting angle of the microrobot is reduced to 1.926° (average). Tilting angle of the microrobot is more developed than the rule-based model during its longitudinal motion	68
Figure 3.18	The images taken by the experimental data of the laser feedback and the hybrid model controllers at six different speeds in the range of 5–10 mm/s. In order to make the laser marker visible, the experimental images of the microrobot are presented in isometric view	69
Figure 3.19	The microrobot head-tilting angle and the applied servo motor angle for the application of the laser model within a speed 5 mm/s	70
Figure 3.20	The microrobot head-tilting angle and the applied servo motor angle for the application of the laser model within a speed 6 mm/s	71
Figure 3.21	Shows the head-tilting angles of the microrobot for speeds 5 and 6 mm/s with the hybrid controller	72
Figure 3.22	Shows the head-tilting angles of the microrobot for speeds 7 and 8 mm/s with the hybrid controller	73
Figure 3.23	Shows the head-tilting angles of the microrobot for speeds 9 and 10 mm/s with the hybrid controller	74
Figure 3.24	Comparison of average head-tilting angles in the speed range of 5–10 mm/s	75
Figure 4.1	(A) In order to determine the dynamic behavior of this system, the second order system simulation in the form of mass-damping-spring is expressed in (B). The dimensions of the microrobot used in experiments is given in (C). The carrier magnet and the microrobot thicknesses are set to 250 μm	78
Figure 4.2	(A) Ring-type lifter magnet whose dimensions are $R_i = 20$ mm, $R_a = 40$ mm, $D_r = 8$ mm and (B) bar-type carrier magnet are given. These parameters are used to derive magnetic fields in (4.4) and (4.5)	81
Figure 4.3	The surface graph obtained as a result of the net magnetic force calculation is shown. The x-axis is the distance between the magnets and the graphite; y axis shows the amount of offset applied to the lower positioned lifter magnet; the z axis shows the total magnetic force values obtained. The bar above the figure shows the color map of the force change between 0-1 μN	82

Figure 4.4	The c_d values that vary depending on the Re are shown. Re converges to a value of c_d as expected at its greater values. However, it is calculated that the drag force coefficient for the predicted operating range (0-50 mm/s) for microrobot and flow rate would be between $0.58 < c_d < 1.85$	83
Figure 4.5	The analysis result is shown when the flow rate of the microrobot in a rectangular channel is 16.6 mm/s. Due to no slip boundary conditions is considered in a rectangular shape channel, velocity is generated as parabolic manner and higher magnitude of velocity field can be seen around in the middle of channel and corner of the robot (top view (B))	84
Figure 4.6	The application of different flow rates using the laminar flow-solid mechanics-moving mesh in the COMSOL [®] AC/DC module shows the relationship between c_d and Re . The markers on the graph represent each flow step of 2.5 mL/min. While the Re value increases, c_d values converge to a constant value (0.49)	85
Figure 4.7	The oscillation amplitude of the microrobot subject to laminar flow are presented. When the microrobot holds still, it exposes oscillation characteristics due to the drag force	86
Figure 4.8	The laser displacement data depending on the flow rates was recorded during microrobot movements. The 10 peaks in each graph indicate the number of experiments	87
Figure 4.9	presents a side view of this experiment at flow rate of 25 mL/min and microrobot speed of 50 mm/s. From the initial location, the microrobot travelled 4mm away. From its initial position to the final position, the microrobot performed oscillation characteristics as (1.05-1.07 sec), (2.04-2.06 sec) respectively	88
Figure 4.10	SD values of all measured lateral motion results with means for microrobot speeds from 10 mm/s to 50 mm/s are expressed. Although different flow rates and microrobot velocities are applied, displacement and error amounts are similar according to $P < 0.05$ by 1-way ANOVA ($p = 0.46$)	90
Figure 4.11	Shows an isometric view of the CAD design of the experimental setup, © 2021 IEEE, with permission, from ref [115]	92
Figure 4.12	Close-up view of the levitation mechanism, © 2021 IEEE, with permission, from ref [115]	93

Figure 4.13	A sketch that shows the primary forces acting on the microrobot for the proposed dynamic model. Here the fluidic forces are modeled as a damping element, and the magnetic forces are modeled as spring elements. Magnetic forces can be modeled as spring elements due to the stabilizing nature of the pyrolytic graphite, © 2021 IEEE, with permission, from ref [115]	94
Figure 4.14	Shows a free-body diagram of the robot. The main forces that determine the microrobot's longitudinal motion are the fluidic drag force and the combination of longitudinal components of the magnetic forces due to upper and lower magnets, © 2021 IEEE, with permission, from ref [115]	95
Figure 4.15	(A) Shows the drag coefficient's variation against the Reynolds number for the entire range of laminar flow regime. However, it is calculated that the drag force coefficient for the predicted operating range (0–100mm/s) for microrobot and flow rate would be between $0.58 < c_d < 1.85$. The drag force coefficient values in this range shown in great detail in (B), © 2021 IEEE, with permission, from ref [115]	97
Figure 4.16	(A) Shows the ring-type lifter magnet whose dimensions are $R_i = 20\text{mm}$, $R_a = 40\text{mm}$, $D_r = 8\text{mm}$ and (B) the cylinder-type carrier magnet whose dimensions are shown. These parameters are used to derive the magnetic fields given in (4.13) and (4.14), © 2021 IEEE, with permission, from ref [115]	98
Figure 4.17	The surface graph obtained as a result of the net magnetic force calculation is shown. The x-axis is the distance between the magnets and the graphite; the y-axis shows the offset applied to the lower positioned lifter magnet; the z-axis shows the total magnetic force values. The bar above the figure shows the color map of the force change between $0 - 0.8 \mu\text{N}$, © 2021 IEEE, with permission, from ref [115]	99
Figure 4.18	The longitudinal force on the microrobot increases linearly as it moves away from the center of the lifter magnets up to a certain distance. The longitudinal magnetic force can be modelled as a spring element due to its linear relationship with displacement. In light of these results, we see that for displacements lower than 7.5mm the spring coefficient can be taken $k = 21.675\text{nN/mm}$. If microrobot displacement is measured greater than 7.5mm, the spring coefficient is switched to the $k = 17\text{nN/mm}$, © 2021 IEEE, with permission, from ref [115]	102

Figure 4.19	Dynamic behavior of the microrobot at different flow rates as predicted by the analytical model. Microrobot exhibits oscillatory behavior due to the magnetic forces' nature. It converges to a stable resting position when the fluidic and magnetic forces are balanced, © 2021 IEEE, with permission, from ref [115]	103
Figure 4.20	The analysis result for a flow rate of 41.6mm/s is shown. The velocity field reaches its maximum at the center of the channel due to the no-slip boundary condition (B) and (C), © 2021 IEEE, with permission, from ref [115]	105
Figure 4.21	The application of different flow rates using the laminar flow-solid mechanics-moving mesh in the COMSOL [®] AC/DC module shows the relationship between c_d and Re . The drag force coefficient is calculated for increasing flow rates with an interval of 0.5mL/min. As the Re value increases, c_d value converges to a constant value (~ 0.49), © 2021 IEEE, with permission, from ref [115]	106
Figure 4.22	The oscillation amplitude of the microrobot subject to laminar flow are presented. When the microrobot reaches its final position, it exhibits an oscillatory motion characteristic due to the interaction of drag and magnetic forces. The oscillation amplitude varies depending on the applied flow rate. The amplitude of oscillation relative to the resting position is shown in (A) 1mL/min, (B) 1.5mL/min, (C) 2mL/min, (D) 2.5mL/min, (E) 3mL/min, (F) 3.5mL/min, (G) 4mL/min, (H) 4.5mL/min. For lower flow rates the oscillation amplitudes were insignificant, © 2021 IEEE, with permission, from ref [115]	107
Figure 4.23	Displacement of the microrobot for different flow rates as measured by the laser displacement sensor, © 2021 IEEE, with permission, from ref [115]	108
Figure 4.24	Presents a side view of this experiment at a flow rate of 2.8mL/min and a microrobot speed of 50mm/s. From the initial position, the microrobot traveled 4mm in the longitudinal axis. From its initial position to the final position, the microrobot performed oscillatory characteristics, © 2021 IEEE, with permission, from ref [115] . . .	109
Figure 4.25	Standard deviation values of all measured longitudinal motion results with means for microrobot speeds from 10mm/s to 50mm/s are expressed. Although different flow rates and microrobot velocities are applied, displacement and error amounts are similar according to $P < 0.05$ by 1-way ANOVA ($p=0.46$), © 2021 IEEE, with permission, from ref [115]	110

Figure 5.1	The CAD models for four different magnetic levitation configurations named (A) "single," (B) "double," (C) "kerkan," and (D) "double-double" are given in isometric view, respectively. All the equipment's list is given in the bottom left corner of (A), and their dimensions are also available on the figure's right side. W, h, l, d, t, od, id denote width, height, length, diameter, thickness, outer diameter, and inner diameter, respectively	114
Figure 5.2	A free body diagram of the microrobot during its longitudinal motion is presented with a front view. This diagram can be used for every proposed configuration. For example, all the terms related to the bottom magnet should be removed when single configuration is applied. The magnetic force's magnitude varies for the rest of the configurations only. τ denotes the longitudinal distance from the centerline of the magnets. According to the flow rate, which generates drag force on the microrobot, τ changes exponentially .	115
Figure 5.3	Shows the drag coefficient's variation against the relative velocity which is between fluid flow and microrobot for the laminar flow regime. It is calculated that the drag force coefficient for the predicted operating range 10-150 mm/s for microrobot and flow rate would be between $0.95 < c_d < 4.49$	118
Figure 5.4	Here the longitudinal force on the microrobot is given for four different configurations. Since in the other configurations, the microrobot is subjected to magnetic fields both from above and below, the single configuration generates lower longitudinal forces in comparison. Rest of the magnetic forces' which have another magnet positioned below the channel, pull the microrobot to both sides and make its motion more stable. The magnetic force difference of a maximum of 20% was observed between double and double-double configurations. The reason for this is that there are more magnets in the double-double configuration. Thus, its magnetic field magnitude cause such a difference; however, it can be seen at higher displacement only. In the Kerkan configuration, the magnetic force increases of 43% is observed compared to the double-double configuration. Also, it can be seen that the Kerkan configuration can be effective from the initial position of the microrobot up to 20 mm	120
Figure 5.5	Simulation result is obtained with respect to Eq. (5.1) in the COMSOL [®]	122

Figure 5.6	(A), (B), (C) and (D) show the general frontal-view of the magnetic field distributions for each configuration respectively. Their close-up view for the magnetic streamlines are demonstrated in (A-1), (B-1), (C-1) and (D-1) when the microrobot is displaced 10 mm from the magnet's centerline. As can be seen from the upper and bottom part of the streamlines, the magnetic field lines are more linear for the Kerkan configuration. Lastly, magnetic field force lines are presented in (A-2), (B-2), (C-2) and (D-2). As can be seen here, the magnetic field lines are given as three dominant vectors that have two horizontal components and one perpendicular. In the Kerkan configuration, horizontal components of the magnetic field force lines are slightly upwards compared to others. Thus, the levitation can be maintained with a more intense and linear magnetic field that is achieved with the Kerkan configuration	123
Figure 5.7	Microrobot is shown for four different configurations under 0.5 mL/min flow rate (10.3 mm/s velocity) and at a levitation height of 100 μm . In (A) the initial position of the microrobot is shown for each experiment. (B), (C), (D), and (E) represent magnetic configurations named "Single," "Double," "Double-Double," and "Kerkan" respectively. Analogous to the simulation results, it is observed that the microrobot moved backwards lesser for the Kerkan configuration. The reason for this are the magnetic field lines over the microrobot and the longitudinal forces acting on the microrobot are increased	124
Figure 5.8	For all configurations between 0.5 mL/min and 4 mL/min the displacement values for the microrobot are given. The single configuration was able to withstand the lowest flow rate (2.5 mL/min) due to its low longitudinal force. For all flow rates, higher displacement values were observed	125
Figure 5.9	(A) shows error as percentage between experimental and simulation results. Also, the mean errors as follows: Single 3.7%, Double 3.9%, Double-Double 3.6%, and Kerkan 3.5%. (B) shows absolute error and their mean as follows: Single 152.1 μm , Double 232.1 μm , Double-Double 140.6 μm , and Kerkan 179.5 μm . As we can see, Kerkan configuration can withstand higher flow rates at almost same amount of error	126

Figure 5.10	(A) shows initial starting position of the microrobot for the all magnetic configuration. (B), (C), (D), and (E) represent magnetic configurations named "Single," "Double," "Double-Double," and "Kerkan" respectively. As we can see that Kerkan configuration can withstand at higher flow rate with lower displacement rather than other configurations	127
Figure A.1	Dynamic behavior of the microrobot with SU-8 body at different flow rates as predicted by the analytical model. Microrobot exhibits oscillatory behavior due to the magnetic forces' non-linear nature. After period of time when the fluidic and magnetic forces are balanced, then microrobot displacement can converge to a stable resting position.	140
Figure A.2	This figure shows the flow profile around the microrobot for 50, 75 and 100 μm levitation heights. It was used to determine if there is a correlation between flow velocity and levitation height.	141
Figure A.3	This figure shows the flow profile around the microrobot for 125, 150 and 175 μm levitation heights. It was used to determine if there is a correlation between flow velocity and levitation height. .	142
Figure A.4	This figure shows the flow profile around the microrobot for 200, 225 and 250 μm levitation heights. It was used to determine if there is a correlation between flow velocity and levitation height. .	143
Figure A.5	This figure is used to determine the point at which the drag force is applied on the robot surface. The offset of this point from the microrobot center, which was denoted as "r" was calculated. As such, the effect of this phenomenon on the microrobot orientation was determined.	144
Figure A.6	This figure was used to show the impact of the hydrodynamic entrance effect on the microrobot movement. The velocity magnitude at the center of the channel gradually increases and attains a parabolic shape as it gets to the fully-developed state. This interval between the start of the channel and the point where the flow is fully developed is called the hydrodynamic entrance interval. During our calculations, the effect of this hydrodynamic entrance was taken into consideration.	145
Figure A.7	This figure shows the results of the flow simulation. These results were used to determine the microrobot displacement magnitude for different flow rates.	145

Figure A.8	This figure shows the close-up version of the flow simulation results. These results show the flow profile around the microrobot at steady-state conditions for (A) 1 (mL/min), (B) 1.5 (mL/min), (C) 2 (mL/min) and (D) 2.5 (mL/min).	146
Figure A.9	This figure shows the close-up version of the flow simulation results. These results show the flow profile around the microrobot at steady-state conditions for (E) 3 (mL/min), (F) 3.5 (mL/min), (G) 4 (mL/min) and (H) 4.5 (mL/min).	147
Figure A.10	This figure shows the levitation height measurements at different flow rates. The desired levitation height was 100 μm , and for the flow rates at 1 (mL/min), 2 (mL/min), 3 (mL/min) and 4 (mL/min). The deviation was less than 1.5 μm . Thus, it can be seen that the microrobot successfully operated under stable conditions when a constant flow was applied.	148
Figure A.11	This figure shows the levitation height measurements at different flow rates. The desired levitation height was 100 μm , and for flow rates at 1.5 (mL/min), 2.5 (mL/min), 3.5 (mL/min) and 4.5 (mL/min). The deviation was less than 1.5 μm . Thus, it can be seen that the microrobot successfully operated under stable conditions when a constant flow was applied.	149

LIST OF TABLES

Table 2.1	System Model Parameters	13
Table 2.2	Micro-untethered floating object (microrobot) properties and nonmagnetic forces	20
Table 2.3	Mesh structure of the experimental system	23
Table 3.1	System Model Parameters	71
Table 4.1	Parameters of the microrobotic setup	80
Table 4.2	Microrobot 4000 μm longitudinal motion experimental results . . .	89
Table 4.3	Parameters of the microrobotic setup	96
Table 4.4	Microrobot 4000 μm longitudinal motion experimental results . . .	109
Table 4.5	Comparison of the displacement values determined from the analytical calculations, simulation results and experimental measurements are given at the upper part of the table. Error values in comparison with the experimental results are given at the bottom part of the table	111
Table 5.1	Parameters that were used in the calculation of the forces	116
Table 5.2	Simulation Results of the major parameters with respect to flow rates	121

Investigation and Experimental Verification of Untethered Microrobot Motion Behavior Subject to Laminar Flow

Ali Anil DEMIRCALI

Department of Mechatronics Engineering
Doctor of Philosophy Thesis

Advisor: Asst. Prof. Huseyin UVET

Untethered manipulation of microrobots is emerging as a promising field of research in medical and biological applications. This study presents an untethered micromanipulation technique to control magnetic microrobot with high precision positional accuracy inside a microfluidic channel. It is aimed to develop an untethered microrobotic platform that can operate on high flow rate microfluidic channels for in vitro applications. Firstly, a novel diamagnetic untethered levitation configuration is used in order to eliminate the friction force between the substrate's surface and the microrobot. Secondly, the drag force acting on the microrobot is decreased to move the microrobot longitudinally towards and against the flow. After that, the liquid media's hydrodynamic effects on microrobot is optimized by finite element method (FEM) simulations in COMSOL[®] (version 5.3, COMSOL Inc., Stockholm, Sweden). Analytical and simulation studies are conducted, which are then validated by experimental results to demonstrate the advantages of the developed platform. Experimental results are on par with analytical and simulation studies, and this platform significantly improves the longitudinal forces on the microrobot. Moreover, this platform also provides a more stable longitudinal motion in fluidic channels, where a high rate flow is present. An increase in flow rate exponentially increases the drag force on the microrobot and negatively impacts its positioning accuracy. Increasing the longitudinal force generated by the microrobot's driving apparatus helps disrupt the fluid flow and increases longitudinal motion stability. No prior study exists investigating the longitudinal motion of a microrobot for high flow velocities

(~ 5 mm/s). Longitudinal force investigation is an important topic for increasing the applicability of microrobots in many areas such as cell research, micromanipulation, and lab-on-a-chips. The following points are achieved in the relevant study, and their details are given:

- The microrobot can move in three dimensions and two orientations in a liquid environment.
- The microrobot stable levitation range is determined between $30\text{ }\mu\text{m}$ to $330\text{ }\mu\text{m}$. This range is also confirmed with simulation and experimental studies. Furthermore, the microrobot capable of tracking the desired trajectory with the accuracy of $<1\text{ }\mu\text{m}$ at varying speed. Also, the levitation height can be adjusted in the stable working range.
- Different controllers are used such as "rule-based", "laser-feedback", "visual-feedback", and "hybrid model" to reduce the microrobot orientation at higher speeds.
- The microrobots' ability in a square-shaped microfluidic channel is demonstrated by following a linear trajectory with a relative flow velocity of up to 132.6 mm/s .

Keywords: Microrobot motion, Motion in flow, Diamagnetic levitation, Reynolds number, Laminar flow

Laminer Akış Altındaki Temassız Bir Mikrorobotun Hareket Davranışının İncelenmesi ve Deneysel Doğrulanması

Ali Anil DEMIRCALI

Mekatronik Mühendisliği Anabilim Dalı
Doktora Tezi

Danışman: Dr. Öğr. Üyesi Hüseyin ÜVET

Mikrorobotların temassız manipülasyonu, tıbbi ve biyolojik uygulamalarda umut verici bir araştırma alanı olarak ortaya çıkmaktadır. Bu çalışmada, bir mikroakışkan kanal içerisinde bulunan ve yüksek hassasiyette temassız bir şekilde kontrol edilebilen manyetik mikrorobota ait mikromanipülasyon tekniği anlatılmıştır. In-vitro uygulamalar için yüksek akış hızlı mikroakışkan kanallar üzerinde çalışabilen ve temassız hareket edebilen mikrorobotik bir platform geliştirilmesi hedeflenmektedir. İlk olarak, substratın yüzeyi ile mikrorobot arasındaki sürtünme kuvvetini ortadan kaldırmak için yeni bir diyamanyetik levitasyon konfigürasyonu kullanılmaktadır. İkinci olarak, mikrorobot üzerine etki eden sürüklenme kuvveti azaltığı için mikrorobot akışa doğru ve akışa karşı hareket edebilmektedir. Daha sonra, sıvı ortamın mikrorobot üzerindeki hidrodinamik etkileri, COMSOL[®] (sürüm 5.3, COMSOL Inc., Stockholm, İsveç) içindeki sonlu elemanlar yöntemi (FEM) simülasyonları ile optimize edilmektedir. Analitik ve simülasyon çalışmaları önerilen tekniğin avantajlarını göstermek için deneysel sonuçlarla doğrulanmaktadır. Deneysel sonuçlar, analitik ve simülasyon çalışmaları ile aynı olması; bu çalışmanın mikrorobot üzerindeki yanal kuvvetleri önemli ölçüde geliştirdiğini ve yüksek hızlı akışın mevcut olduğu akışkan kanallarda daha kararlı bir yanal hareket sağladığını göstermektedir. Akış hızındaki bir artış, mikrorobot üzerindeki sürüklenme kuvvetini üssel olarak artırmakta ve konumlandırma doğruluğunu olumsuz yönde etkilemektedir. Mikrorobotun yanal kuvvetinin arttırılması, sıvı akışının etkilerinin azaltılmasına yardımcı olur ve yanal hareket stabilitesini artırmaktadır. Yüksek akış hızları 5 mm/s için bir mikrorobotun

yanal hareketini arařtıran nceki bir alıřma bulunmamaktadır. Yanal kuvvet alıřmaları, mikrorobotların hcreler zerindeki arařtırmalarda, mikromaniplasyon ve ip-st-laboratuvar (lab-on-a-chip) gibi birok alanda uygulanabilirliėini artırmak konusunda nemli bir yer almaktadır. İlgili alıřmada ařaėıdaki noktalar bařarılmıř ve detaylarına yer verilmektedir:

- Mikrorobot, sıvı bir ortamda  boyutlu doėrusal ve iki ynde aısal hareket edebilmektedir.

- Mikrorobotun kararlı alıřma aralıėı 30 μm ile 330 μm arasındadır ve hem simlasyonlarda hem de deneysel sonularda doėrulanmıřtır. Verilen yrngeyi, deėiřen hızlarda ve farklı levitasyon yksekliklerinde yksek doėrulukla ($<1 \mu m$ hata ortalaması) takip edebilmektedir.

- Kural tabanlı, lazer geri beslemeli, grsel geri beslemeli ve hibrit model denetleyicileri tasarlanması ile mikrorobotun yksek hızlardaki aısal problemi iyileřtirilmiřtir.

- Kare řeklindeki bir mikroakıřkan kanal ierisinde 132.6 mm/s greceli bir hızla doėrusal bir yrngeyi takip etme bařarısı gstermektedir.

Anahtar Kelimeler: Microrobot hareketi, Akıř iinde hareket, Diyamanyetik levitasyon, Reynolds sayısı, Laminer akıř

1

INTRODUCTION

1.1 Literature Review

Recently, microrobots have been used widely for a variety of biological and medical applications such as artificial insemination [1], biopsy [2], biosensing [3], cell manipulation [4–7], cellular treatment [8], chemical synthesis [9], diagnostics [10, 11], drug delivery [12, 13], marking [14], measuring systems [15], microparticle transport [16–18] with minimal damage to the desired site. Furthermore, helical swimmers [19], micro grippers [20], and soft microparticles [21] are developed to use in the in-vitro applications. Microrobots can also be used in biomedical engineering because of their untethered controllability capabilities [18, 22, 23]. The microrobots' motion precision in such applications can be more advantageous when the liquid conditions are considered [10]. The microrobots can be mostly used in microfluidic systems due to their high precision controllability [24]. The forces acting on the microrobot is effected by the liquid environment and the flow characteristics due to diminishing dimensions. In the microfluidic chip platforms, creeping ($Re < 1$) or laminar flow ($Re < 2100$) can be observed according to the Reynolds number (Re). Micro-objects' transfer and movement become crucial in the laminar flow environment since the microfluidic system presents high viscous medium behaviour [25]. Different approaches can also be used in such a laminar flow environment in order to move micro-objects. Some of these approaches are based on optical, thermal, electrostatic, and chemically manipulated [26, 27]. However, the microrobots' usage can be promising since their motion accuracy, the longitudinal force capability and the spatial effects [3].

Microrobot actuation studies have primarily focused on electromagnetic methodologies associated with different control structures. The main reasons are ease of use for biomedical applications, energy efficiency, and minimal collateral damage at the operated region [28]. Their locomotion techniques have a crucial role in invasive diagnostics, targeted drug and living cell delivery. Due to the nonlinear nature of the magnetic field, the microrobots' precise localization in the in-vitro/vivo

application become a challenging area for researchers [29]. Promising solutions can be developed by implementing material-based solutions and a combination of sensors and control models. Miniaturization strategies of existing robotic technologies and bio-mimetic approaches make an effort towards moving microrobots in a predefined trajectory in different medias [19, 30]. Microfluidic environments render the inertial terms of viscous force and surface tension more significant at a smaller scale. Moreover, precise position control of the microrobot become more important in this scale [31]. Thus, these terms should be taken into account in such applications [32]. Different microrobot levitation techniques have been deployed to achieve such precise control ability despite the challenging operating conditions. Moreover, their actuation mechanisms, power consumption, and precision of movement should also be optimized [33–39]. In these studies, electrical forces [33], acoustic forces [35], combination of permanent magnet and Helmholtz coil [36], electromagnetic [37], optical tweezers [38], light-based manipulation [34] and chemically controlled [39] tethered and untethered levitation techniques are used. These techniques are then combined with different controller techniques. Examples of such techniques are; electromagnetic [40–44], permanent magnet-based [45], ultrasonic [46], air cushion [47], thermally actuated [48] and optically driven [49] levitation. These techniques have been used under a variety of working conditions such as in air [50, 51], water [52, 53], oil [54] and blood [36], glycerine [53], and in channels with different flow characteristics [41]. In these studies, the effects of drag force and Re (Reynolds number) on the microrobots during their locomotion and motion profiles are examined. The medium's viscosity is an essential factor due to its relationship with the Reynolds number (Re). This number is used in the drag coefficient calculation, determining the necessary longitudinal forces produced on the microrobot for withstanding the environmental conditions. The problems related to the microrobot and its manipulation are addressed as follows: precision, dimension, drag Force, control, and motion against to flow. They are explained in the following sections in detail.

1.1.1 Microrobot Precise Motion Capability

High-accuracy motion control is crucial for many applications such as tissue engineering, cell analysis, cell manipulation, drug delivery, micro-assembly, and protein-crystal handling [18, 22, 24, 55–67].

Sub-micron resolution is required to move and transfer micro-objects, especially in biomedical applications. Although using microrobots have advantages compared to other methods, there are still ongoing studies to develop their precise movement

capability. The main challenges of microrobot manipulation are the ability to move it precisely, and the force exerted on it must be increased. Moreover, the medium's viscosity in a microfluidic chip and the friction forces between microrobot and substrate should also be considered [68]. For example, Bradley Nelson et al. were inspired by the artificial bacterial flagella (ABF) to fabricate their microrobot. This ferromagnetic microrobot has a helical structure, and it can move by rotating magnetic fields. In such a structure, the tail's rotational motion allows high efficient motion with low magnetic fields requirement [19]. In this type of microrobot design, the helical structure appears to be a restriction and limiting the design of different robot geometries; however, microrobot designs should be flexible since they can be used in various microfluidic applications. Furthermore, the microrobot cannot maintain its position when the applied magnetic force is stopped. Arai et al. were studied microrobot control with magnetic field effect using permanent magnets on the microrobot body. In their work, focusing on force and microrobot position sensitivity are addressed [3]. The design of microrobots was modified in order to decrease friction forces, leading to an improvement in accuracy of motion [4]. Nevertheless, there was still contact between substrate and microrobot as a limiting factor. Thus, ultrasonic vibrations were also introduced to microfluidic chips in order to reduce surface friction forces [69]. The effort was to reduce surface contact and had a high force to provide precise manipulation. However, ultrasonic vibrations also reveal a new problem, which is the main reason for micro-objects vibrations and movement.

1.1.2 Challenge in Miniaturization of Magnetic Microrobots

Barbot and his team considered Reynolds' effects on helical microrobot with its rolling, spin top motion, and swimming motion capabilities [70] by comparing milli-, micro-, and nano-robots. Carlo has described inertial microfluidic systems with essential fluid dynamic effects such as Reynolds number, drag force, and size [30]. In these studies, the ultrasonic waves are applied to the surface to reduce the friction force and increase the end-effector positioning accuracy of a microrobot. Movement accuracy can be achieved at a few microns level. Even though this improved method is a successful example of the "oocyte enucleation", it causes cell-immobilization problems in smaller cells and objects than the oocyte cell ($\approx 100 \mu m$). During the microrobot movement, there is an ultrasonic wave in the medium, which causes the object in the medium to change its position or displacement. Xie and his team have worked on the programmable generation and motion control of a snakelike magnetic microrobot swarm [71]. Four coils are used to generate the electromagnetic force on peanut shape microrobots. Though robot sizes are too small, the fluid's viscous drag effects are also mentioned; however, operational speeds are too slow.

1.1.3 Drag Force Effect in Liquid Media

The fluidic environment shows either creeping or laminar flow characteristics while working with micro-nano scale robots. At this level, the fact that the environment exhibits laminar flow characterization causes Re (Reynolds Number) cannot be ignored. Nelson and his team investigated the effects of drag force during electromagnetic levitation [14]. However, they could not get adequate results in the robot's control due to a lack of modeling of environmental effects. Similarly, Sitti and his team had difficulties controlling microrobots due to a lack of theoretical calculation of net magnetic force [72]. Assumptions made about the drag force hindered their accuracy of motion. Khamesee and his team obtained similar results, even though they added drag force into their control model [73]. Arai and his team applied high-frequency ultrasound vibrations on the surface upon which the microrobot moves and consequently achieved better results [46]. However, the drag force on the microrobot still exists, and their motion control strategy does not answer it. Feng Lin and his team manufactured a microrobot using pyrolytic graphite and a diamagnetic material and levitated it using an electromagnet with four poles [52]. However, their motion range was limited to 1mm, and no accuracy of motion was studied. Also, since the study does not contain any mathematical model of the motion characteristics, the deviation of experimental results from the theoretical calculations cannot be seen.

1.1.4 Microrobot Control in Liquid Media

Recent studies by Metin Sitti and Arai show magnetic levitation and acoustic levitation provide precise positioning and generate high force, respectively. Their design offers unstable motion control due to the nonlinear distribution of electromagnetic field [72]. Unfortunately, it is hard to obtain time effective motion control. In their other work, a robot with 5 degrees of freedom (DOF) can be moved at higher speeds (>20 mm/s) by eight electromagnets. However, the microrobot orientation can be made with a high positioning error of 2.83 mm [74]. They also performed microrobot control without avoiding experimental uncertainty in the friction coefficients' measurements, and the adhesive force [75]. Arai et al., external ultrasonic forces applied for levitating microrobots appeared once again as a restricting factor. The existence of the ultrasonic waves is still present in the liquid environment [46]. They have also achieved successful results by applying ultrasonic vibrations [46, 69, 76]. Munoz and his team have done a capsule robot's 3-D torque transmitted analysis that is included a small permanent magnet [73]. However, there is still room for improvement due to an analytical error is %8.8. Also, Lucarini et al. investigated teleoperated and autonomous controls of a microrobot in a liquid environment. Even though they developed a robust control algorithm with high reproducibility to manipulate it at

a low speed of 2 mm/s, the mean error is as high as 250–300 μm . Besides, the control response's effect was not mentioned in higher speeds [77]. Moreover, Nelson and his team have performed precise position control with three electromagnets. In the work they produce by the inspiration of bacterial manipulation, they have observed drag force and Low-Reynolds effects [19]. Feng Ling and his team performed passive diamagnetic levitation using 4-pole magnets. However, the orbits can be 1 mm at most, and no motion sensitivities or control strategies are mentioned in their work [52]. Accordingly, various levitation techniques for stabilizing and controlling the horizontal movements of microrobots are existed [19, 30, 73]. Based on these studies, active levitation techniques that use an electromagnet give better results compared to passive levitation techniques that use permanent magnets. However, active levitation application requires expensive and complicated feedback mechanisms and has a higher energy consumption rate. Passive levitation is generally more favorable since it is compact, consumes less energy, and can be applied at room temperature [71, 78, 79]. Furthermore, it is observed that open-loop control methods yield good results when applied to passively levitated microrobots. It is possible to obtain satisfactory results in microrobot studies using various control methods such as single-degree-of-freedom models [80, 81]. With these methods, even with simple control strategies, good results can be observed. Moreover, previous studies exist in which passive levitation was applied to living cells and water bubbles to levitate them to a target position [82–84]. In another study, Perline and his team applied open-loop controllers to colonies of diamagnetically levitated microrobots [71].

Those efforts have shown that microrobot levitation studies had increasing demand to maintain better positioning accuracy and force output. In contrast, all those studies required constant energy consumption to drive piezo vibrator or run bulky electromagnets in order to provide continuous suspension of the microrobot. At this point, the diamagnetic levitation emerges as a powerful method for the precise positioning of a microrobot with a suspension mechanism. With the aid of a permanent magnet embedded in the microrobot, which is positioned above a diamagnetic material, the microrobot can be levitated without an active control mechanism. In the studies on diamagnetic levitation, it is seen that the dipole-dipole [85] interaction could be used by dividing the bismuth [86] and the permanent magnet into two halves, respectively. Unlike Pigot's set-up, which works on a magnetic array, our system is in liquid, which is more suitable for lab-on-chip systems, and has higher control accuracy [86]. According to Profijt and his team, the levitation height is much lower than our proposed method [85]. To the best of our knowledge, the first diamagnetically floating microrobot application was developed by Ron Pelrine et al. [71, 87]. In their work, impressive motion repeatability and speed results are demonstrated on the trajectory

designed by the microrobot printed circuit board (PCB). However, it is necessary to regulate the PCB and the 4-pole magnet for levitating the microrobot in the proposed method. Also, how to control the levitation height on the z-axis has not been specified. Despite a microrobot levitation technique, which moves horizontally very fast, there is no theoretical calculation. Also, minimum and maximum levitation ranges are not specified. Also, the proposed levitation system is not in the liquid medium, so the potential for lab-on-a-chip applications has not been discussed. The current on the PCB affects the positioning accuracy of the passing path. In our case, the positioning resolution of the linear stage shows the same effect.

1.1.5 Microrobot Motion Behaviour Subject to Laminar FLOW

Particularly, single-cell applications such as cell injection [88], or cell cutting [69] require increased longitudinal forces. Higher longitudinal forces are also required to obtain a more stable microrobot motion under unsteady flow conditions. Nevertheless, microrobots that can accurately move in longitudinal flow profiles are not studied adequately [89–92].

Khalil and his team levitated a microrobot inside a fluidic channel using four electromagnets [41]. However, they could move the robot against a low rate flow of $7.5 \mu\text{L}/\text{min}$. Using a similar levitation technique, they were able to control the position of a micro-bead inside a fluidic channel with a $584 \mu\text{L}/\text{min}$ flow rate [93]. Generated force by their levitation system was not high; thus, it can be observed that this system cannot be used in applications that required high flow rates. They also studied the locomotion of an object in a microfluidic channel in the creeping flow regime ($Re < 1$) [94]. They used four electromagnets for levitation and examined the effects of different controller techniques on the robot's speed, system rise time, and motion sensitivity. Although rate of the applied flow is low ($< 0.6 \text{ mL}/\text{min}$), the positioning error is reported as $\sim 16 \mu\text{m}$. Belharet and his team manipulated a spherical microrobot ($\varnothing 500 \mu\text{m}$) in water and glycerin with different viscosity values under laminar flow regime [53]. Applied flow rates varied in the range of $2.8 \text{ mL}/\text{min}$ and $10 \text{ mL}/\text{min}$ and the reported positioning error was approximately $100 \mu\text{m}$. This margin of error renders the accurate positioning of the microrobot impossible. Sanchez and his team used permanent magnets to control the movement of a catalytic microrobot in a $150 \mu\text{m}$ wide microfluidic channel [95]. They were able to achieve a lateral velocity of $78 \mu\text{m}/\text{s}$ when the applied flow velocity was $73 \mu\text{m}/\text{s}$. However, this technique requires the use of a catalyst for self-propulsion, which compromises the viability of the environment for cell studies and reduces the application's repeatability. Sitti and his team showed that a robot with dimensions

of $250\ \mu\text{m} \times 130\ \mu\text{m} \times 100\ \mu\text{m}$ can produce a longitudinal force of 52 nN when it is moved in contact with the surface [96]. When driven in non-contact mode, the robot could only produce a longitudinal force of 1.7 nN. Hao Li and his team were able to perform folding and unfolding motions at various pH values in order to trap and release drug-carrying microbeads for targeted drug delivery [6]. However, the microrobot was able to reach a maximum velocity of $600\ \mu\text{m}/\text{s}$. This velocity renders the configuration useless for delivering larger and heavier particles at higher flow rates. Ke Meng and his team studied the navigation of a microrobot in a cardiovascular environment [97]. In this study, fluidic properties of blood flow inside the circulatory system are considered, and a robot that can achieve 5 mm positioning accuracy inside a 10 mm/s fluidic flow is designed. It can again be seen from this study that the optimization of longitudinal forces is critical for a microrobotic system. Since the motion property, velocity, and 3DOF (Degree of freedom) positioning accuracy of a microrobot are predominantly dependent on its longitudinal forces.

1.2 Objective of the Thesis

Lab-on-a-chip based micro-sensor and micro-actuator devices have been rapidly progressing in the state-of-the-art in Micro-ElectroMechanical System (MEMS) technologies due to integration possibility to complex tasks. Untethered biomedical microrobots and their applications can perform minimally invasive surgical techniques to the desired site by providing sub-micron resolutions with several new procedures. These robots' benefits are even less injury to the patient, faster recovery times, and diagnostic with higher resolution. Micro-needles, micro-pumps, force, and chemical sensors based MEMS can be carried on-board for various surgical and diagnostic tasks. This thesis's overall goal is to create micro/nano robots with novel functions and are committed to establishing analysis and design technology for them by emphasizing the micro-nano world. Sub-millimeter sized microrobots are intended for high-precision positioning, longitudinal and parallel motion to the surface. Their levitation height and motion control can be achieved with 5 DOF(degrees of freedom) mobilization in the laminar flow.

For example, in the literature, 3D controlled microrobots promise in-vitro or in-vivo applications; they have not yet been successfully applied to closed microfluidic environments. The main reason is their high surface-to-volume ratio, which is a handicap for robustness as they can be stuck on the substrate/channels walls or carry away by external flow (e.g., in a blood vessel). Indeed, it is required to have innovative methodologies for micro-nano robots to make them robust enough to be applied in such environments. A novel diagnosis, treatment, and identification

of many medical/bio-medicine science areas in the interdisciplinary subject area of micro-nano robotics in biomedical applications. As such, for microfluidic researches that require continuous flow operations such as circulated tumor cell (CTC) detection, cell separation or sorting, etc., a microrobot is a potential candidate to develop new generation analysis systems. The microrobot, capable of robust localization in a time-varying flow regime, can quickly investigate a large amount of testing samples and enable cell reuse for downstream applications. In these studies, using liquid in stationary or very low flow profiles is that the drag force is more effective on the robot, and the lateral forces acting on the robot can not be increased enough. Therefore, higher lateral forces must be applied to the robot in order to increase motion sensitivity and to move against high flow rates. These problems are expected to be solved in the micro-nano world urgently and can therefore be considered as a priority.

As a contribution to the Micro-Nano robotic field;

- It leads the innovative research field of micro-nano robotics and promotes collaborative researches between industry and the laboratory.
- Develop novel micro-nano robotics platforms for medical robotics/bio-medicine with due consideration of legal, ethical, and technical challenges
- Develop lab-on-a-chip, organ-on-a-chip, and robot-on-a-chip applications use in biological, chemical, and medical researches
- Develop new and novel magnet configuration which makes the lateral force of microrobot is increased, and the microrobot can be moved faster (132.3 mm/s)
- Realization of the motion of the untethered microrobot in laminar flow regime in liquid(DI-water) media for the first time

are achieved.

1.3 Hypothesis

Many microfluidic applications, such as cell separation and sorting, cell immobilization, CTC (circulated tumour cell) detection, require a continuous flow to be present. In order for a microrobotic platform to be functional in the context of such applications, it needs to be able to withstand the disturbance due to flow inside the channel. Such platforms hold the potential to be used as an analysis platform upon which many techniques can be developed. Mostly, a microrobot, which is capable of precise positioning in a time-varying flow regime, can investigate

large amounts of sample in a short time and can enable cell reuse for downstream applications [98–101].

In previous studies on the use of microrobot inside microchannels, characteristic of the fluid flow is either stationary or has a very low flow velocity ($\sim 557.4 \mu\text{m/s}$ at up to 35 mL/h). The levitation techniques used in these studies cannot generate sufficient longitudinal forces on the microrobot. Therefore, they can not resist the exponentially increasing drag force of the flow in higher flow velocities [94, 102]. Therefore, the development of a levitation technique that can generate higher longitudinal forces is needed in order to increase the precision of locomotion and stabilize the robot against higher flow rates. The microrobot's levitation and orientation under higher flow rates can be used in lab-on-a-chip platforms such as cell-culture and cell-harvesting. According to the proposed a novel permanent magnet (NdFeB) based micromanipulation method that can produce higher lateral forces compared to previously reported techniques [94, 102] and enables the positioning and locomotion in a laminar flow ($Re < 2000$). A microrobot driving configuration is used to increase longitudinal forces acting on an untethered microrobot. The basis of the proposed configuration is the concentration of the magnetic field force lines on the microrobot and the formation of a force vector on both sides of the robot's vertical axis. The proposed methodology enables microrobots to carry out manipulation tasks that require continuous-flow microfluidic applications.

This study's main contribution is the proposal of a novel magnetic manipulation configuration, named Kerkan configuration, based on diamagnetic levitation. The longitudinal forces on a microrobot are increased compared to the state-of-the-art methods. Kerkan configuration is a potential candidate for applications that require a continuous flow, high velocity, and precise positioning capability due to its various advantages. The ability to withstand longitudinal disturbance forces allow more robust and effective cell manipulation methods to be developed. One of the most exciting aspects of this manipulation method is using microrobots for continuous-flow applications, such as; on-chip diagnostic methods, lab-on-a-chip applications, and organ-on-a-chip applications where a dynamic cell culture with the continuous medium flow is required.

MAGNETICALLY LEVITATED UNTETHERED MICROROBOT DESIGN

2.1 Background Information

In this study, a diamagnetic microrobot levitation system in a liquid environment is presented. It provides a three-dimensional linear and two-dimensional orientation control in higher accuracy. In this system, a single carrier magnet and a lifter magnet is used. In this way, it does not require current control due to permanent magnets feature. So, unwanted physical effects such as heat and noise can be eliminated. According to the similar approaches, our system can be more compact, and its size can be reduced by $1/4$. In the future, it will allow the construction of different polymer microrobots in which the buoyant force can be used effectively. This study shows includes analytical calculation, numerical and experimental studies. The microrobot's positioning accuracy, phase differences due to higher speed manipulation and their effects such as head tilting are presented. The analytically presented magnetic force equations are solved numerically by FEM (Finite Element Method) analysis. Design steps of the system are demonstrated by multi-physics analysis before the experimental stage. Different physic modules should be paired due to the nature of the system. Such a problem requires multiple physic modules since the system includes magnetic and motion-based calculations.

Moreover, the proposed approaches are then experimentally confirmed. Besides, it is shown that the microrobot is ability to move in a submicron error for complex trajectories. In this way, high precision of untethered microrobot manipulation technique can be obtained without using bulky electromagnetic setup or extra sensory attachments to increase manipulation accuracy. Our system has one ring-shaped permanent magnet and one cylindrical-shaped magnet that is inserted to the microrobot center. To determine the system's working regime, the mathematical model of the three-dimensional motion in the liquid environment is calculated via analytically and experimentally. Every calculation steps are shown in detail in the

following sections.

2.2 Mathematical Models

In this section, the mathematical model of the diamagnetic levitation system is given. Forces acting on the microrobot during its levitation and the motion are presented using a free body diagram. All of the equations are calculated analytically with the help of simulation to determine unknown parameters. They all are then confirmed and compared with the experimental results. At the end of this section,

- microrobot minimum and maximum levitation points,
- Drag force as a function of microrobot velocity,
- Magnetic forces acting on the microrobot on x, y, z axes

are addressed.

2.2.1 Schematic of microrobot

Precise levitation and contactless manipulation of the micro-untethered floating object (microrobot) can be performed using diamagnetic force [103–105]. The reason for this is that pyrolytic graphite can stabilize the magnetic field, which imposes on microrobot. Furthermore, it is capable of generating a force in the upwards direction. This force can change with respect to the distance between the microrobot and the pyrolytic graphite's upper surface. Thus, the magnetic force acting on the microrobot can be balanced with graphite, and stable levitation can be achieved.

Figure 2.1 shows that the microrobot is positioned in a deionized (DI) water container with pyrolytic graphite on its surface. The ring-shaped magnet (lifter magnet), which generates the magnetic force required for levitation, is positioned above the container. It is necessary to position the lifter magnet on the DI water container parallelly to achieve stable and micro precise levitation. To do this, PI Micro Stage (M-126.PD2/20mm × 20mm × 20mm, Physik Instrumente (PI) GmbH & Co. KG, Karlsruhe, Germany) with 3-axis linear micro/nano movement sensitivity was equipped. A manual micro-stage was used to position the DI water container parallel to the floor and to move in 3 axes when it is necessary. Nano-sensitive laser distance sensor (optoNCDT-ILD2300-50, Micro-Epsilon, Raleigh, NC, USA) was preferred for instant measurement of levitation height within the system. At the same time, the microscope camera–lens system (Olympus SZX-7, Olympus Corporation, Tokyo,

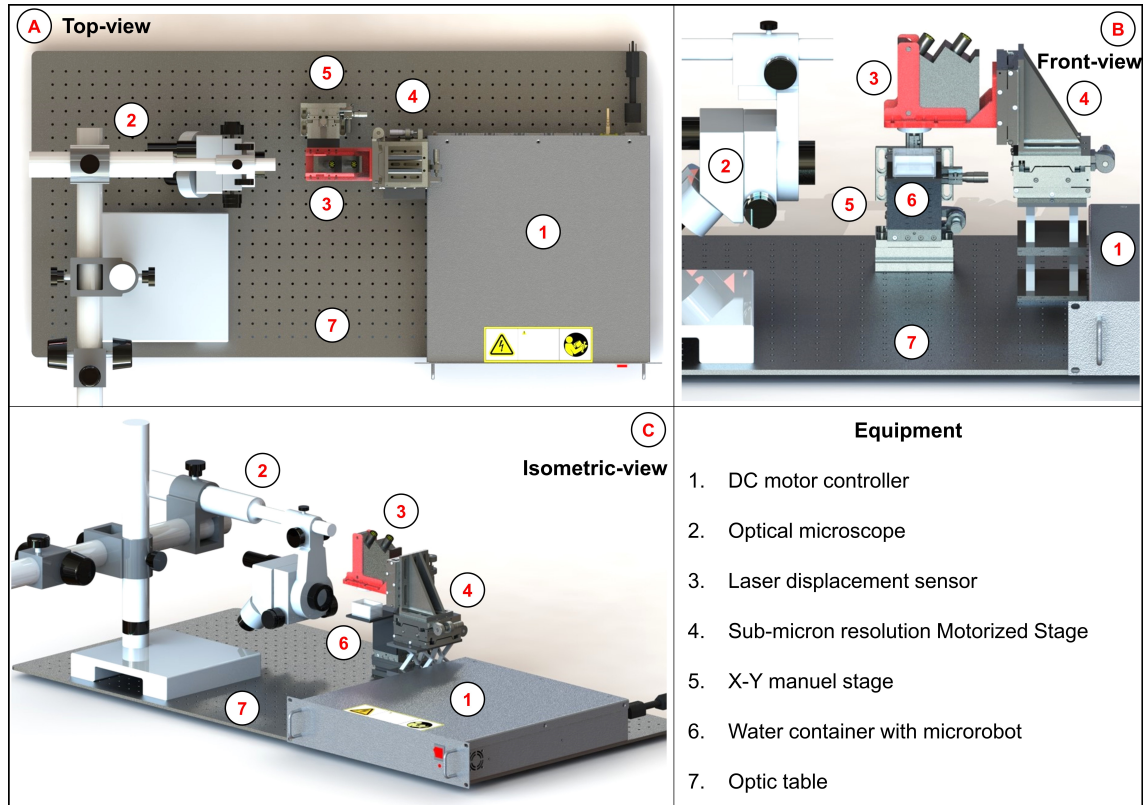


Figure 2.1 Shows the whole experimental with Top-view (A), Front-view (B), and Isometric-view (C). The control of the motorized micro stage where lifter magnet is attached, is realized through a control interface programmed in Visual C#.Net platform (Microsoft Corporation, Redmond, WA, USA). Camera image is transferred to the same interface simultaneously. The data of laser displacement sensor is acquired through the sensors' own interface

Japan and PointGrey GS3-U3, FLIR Integrated Imaging Solutions Inc., Richmond, BC, Canada) was positioned perpendicularly from the side profile. In this way, the mechanical contact of the microrobot with the pyrolytic graphite surface can be observed easily. microrobot levitation was performed with an external ring-shaped N48 grade "lifter magnet" and an N52 grade "carrier magnet" located at the SU-8 body center. In the microrobot levitation system, an acrylic container with DI-water were experimented. Pyrolytic graphite was placed on the surface of the vessel and the microrobot was placed above it.

According to Newton's Second Law, the motion characteristics are determined by the forces which are exerted on the carrier magnet (shown in Figure 2.2). Firstly, system dynamics of the microrobot was modelled to find out locomotion limits under the proposed condition. The point where the microrobot is suspended by the forces exerted on it in the liquid environment can be demonstrated by the mathematical model. In this model,

Table 2.1 System Model Parameters

Symbol	Quantity	Units
F_B	Buoyant force	N
F_g	Diamagnetic force	N
F_D	Drag force	N
F_m	Magnetic force	N
F_r	Gravitational force	N
T_x	Unwanted torque	Nm
B	Magnetic flux density	T
H	Magnetic field strength	A/m
M	Magnetization vector	A/m
χ	Magnetic insulation coefficient	—
μ_r	Relative permeability	—
V_p	Volume of a particle	m^3
m_r	Robot mass	kg
g	Gravitational acceleration	m/s^2
V_r	Robot volume	m^3
ρ_f	Fluid density	kg/m^3
ρ_r	Robot density	kg/m^3
a_r	Robot acceleration	mm/s^2

- The interaction between lifter magnet and carrier magnet is shown as magnetic force,
- The interaction between water and microrobot is shown as buoyant force,
- The interaction between pyrolytic graphite and microrobot is shown as diamagnetic force,
- The interaction between water and microrobot during the motion is shown as drag force,
- The gravitational force is also considered.

Parameters used in the model are given in Table 2.1, and relevant forces are shown on the schematic in Figure 2.2. According to the configuration of the experimental

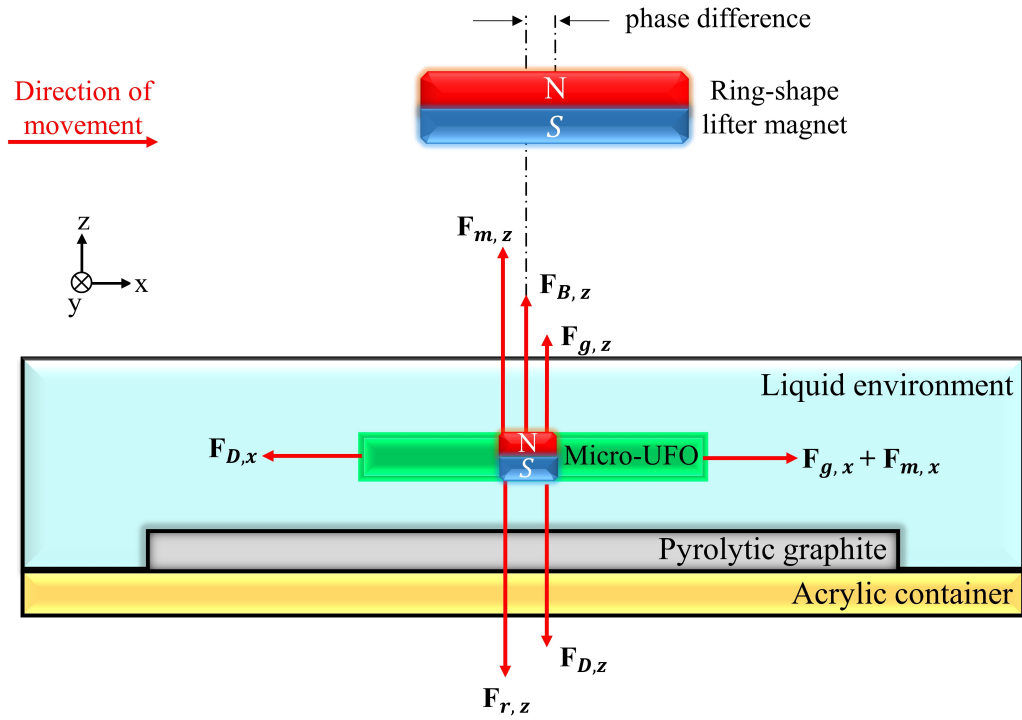


Figure 2.2 Shows the forces acting on the micro-untethered floating object (microrobot). A free-body diagram of the system is obtained according to the z-axis levitation and lateral movement along the x-axis. Phase difference denotes the lateral movements, which can be expressed as a distance between the center of the lifter and the carrier magnet

setup shown in this figure, non-magnetic and magnetic forces acting on the microrobot during its movement on the x-axis in the liquid environment are shown in Figure 2.2. During the microrobot's lateral motion, it is subject to a drag force originating from the liquid in which the microrobot is located. Due to the liquid's hydrodynamic structure, drag force is influenced by the direction of microrobot motion. This effect causes a phase difference between the lifter magnet and the carrier magnet centers. This is because the acceleration of the microrobot is counteracted by the drag force lower than that of the lifter magnet. Moreover, drag coefficient is different due to environmental conditions. Ring-shaped lifter magnet is moving in the air whereas microrobot in the DI-water. Because of the drag force changes proportional to the square of the microrobot's speed, the amount of phase difference is higher at higher speed. These are the reasons why the microrobot design and lower drag coefficient are crucial factors to achieve more efficient manipulation.

2.2.2 Theoretical Background

Non-magnetic forces, which are gravitational, buoyant, and drag forces, are shown in Figure 2.2, and can be expressed individually as,

$$F_r = m_r g \quad (2.1)$$

$$F_B = V_r (\rho_r - \rho_f) g \quad (2.2)$$

$$F_D = \frac{1}{2} c_d \rho_f A v |v| \quad (2.3)$$

where the forces are denoted as F_r , F_B , and F_D , respectively. Vortexes are circular patterns in the microrobot's corner points that are mainly observable in turbulent flow with a higher Reynolds number. However, flow speed is increased corners due to area can be taken into account as a point. Smaller areas tend to increase flow speed, which also affects on Reynolds number. For this reason, rather than using the "linear damping term" in Equation (2.3), the "quadratic viscous term" is preferred to calculate drag force more precisely. Then, attractive magnetic force induced by lifter magnet, $F_{m,x}$, $F_{m,y}$, and $F_{m,z}$ can be expressed respectively in the volume of the suspended magnet [78],

$$F_{m,x} = m_x \iiint_v \frac{\partial B_x}{\partial x} dv \quad (2.4)$$

$$F_{m,y} = m_y \iiint_v \frac{\partial B_y}{\partial y} dv \quad (2.5)$$

$$F_{m,z} = m_z \iiint_v \frac{\partial B_z}{\partial z} dv \quad (2.6)$$

where m_x , m_y , and m_z are the magnetization of the volume element dv of the carrier magnet. Alternatively, the differential form is derived by Thomson's formulation as,

$$F_{m,x} = \frac{V_p \chi}{2\mu_0 \mu_r} (B_x \nabla) B_x \quad (2.7)$$

$$F_{m,y} = \frac{V_p \chi}{2\mu_0 \mu_r} (B_y \nabla) B_y \quad (2.8)$$

$$F_{m,z} = \frac{V_p \chi}{2\mu_0 \mu_r} (B_z \nabla) B_z \quad (2.9)$$

Stable levitation can be satisfied by stability conditions in (2.7–2.9), and some of the boundary conditions should be calculated. In this equation when $\nabla B^2 > 0$ and $(\mu_r - 1) < 0$, are satisfied then stability at the equilibrium point can be ensured. A magnetic field gradient is needed from this equation so that a linear force can be generated on the microrobot. The position of the microrobot can be controlled by positioning the magnetic field gradient relative to the microrobot. The magnetic force induced by pyrolytic graphite is the diamagnetic repulsive force on the microrobot. It can be derived by assuming the material is uniform. In this case, the diamagnetic force of per unit volume dv on the magnetic field of the carrier-magnet can be expressed as,

$$df = M_{dia}(\nabla B)dv \quad (2.10)$$

where M_{dia} is the magnetization at the location of the diamagnetic material in the magnetic field of the carrier magnet, respectively. Since χ_{dia} value is so small, it can be expressed as

$$M_{dia} = \frac{\chi_{dia}}{\mu_0} B \quad (2.11)$$

The Equation (2.11) is substituted in to (2.10), and the volume integral for all the diamagnetic material can be taken. Therefore, the force between the diamagnetic material and the carrier magnet can be obtained as follows:

$$F_{dia,x} = \frac{\chi_{dia}}{2\mu_0} \iiint_V \left(\frac{\partial \|B\|^2}{\partial x} \right) dv \quad (2.12)$$

$$F_{dia,y} = \frac{\chi_{dia}}{2\mu_0} \iiint_V \left(\frac{\partial \|B\|^2}{\partial y} \right) dv \quad (2.13)$$

$$F_{dia,z} = \frac{\chi_{dia}}{2\mu_0} \iiint_V \left(\frac{\partial \|B\|^2}{\partial z} \right) dv \quad (2.14)$$

Furthermore, it is possible to simplify the diamagnetic force components in x, y, z directions according to Ostrogradsky's divergence law [106] as $F_{dia,x}$, $F_{dia,y}$, $F_{dia,z}$, for

d_s , which is the surface area unit of the diamagnetic material,

$$F_{dia,x} = \frac{\chi_{dia}}{\mu_0} \iint_S \|B\|^2 n_x ds \quad (2.15)$$

$$F_{dia,y} = \frac{\chi_{dia}}{\mu_0} \iint_S \|B\|^2 n_y ds \quad (2.16)$$

$$F_{dia,z} = \frac{\chi_{dia}}{\mu_0} \iint_S \|B\|^2 n_z ds \quad (2.17)$$

where n_x , n_y , n_z are the surface normal vector component of the diamagnetic material in x, y, z direction, respectively. The diamagnetic force between the pyrolytic graphite and the carrier magnet can be obtained through Equations (2.15–2.17). After determination of the magnetic forces which are given in the equation set (2.7), (2.15–2.17), the dynamic model can be expressed by (2.18–2.20),

$$\ddot{x} = \frac{1}{2m_r} c_d \rho_f A_x v_x |v_x| + \frac{(F_{m,x} + F_{g,x})}{m_r} \quad (2.18)$$

$$\ddot{y} = \frac{1}{2m_r} c_d \rho_f A_y v_y |v_y| + \frac{(F_{m,y} + F_{g,y})}{m_r} \quad (2.19)$$

$$\ddot{z} = \frac{1}{2m_r} c_d \rho_f A_z v_z |v_z| + \frac{V_r g}{m_r} (\rho_r - \rho_f) - g + \frac{(F_{m,z} + F_{g,z})}{m_r} \quad (2.20)$$

According to the dynamic model of the microrobot, state-space models can be represented for x, y, and z axes in general form (2.21) and (2.22).

$$\dot{x} = \mathbf{Ax} + \mathbf{Bu} \quad (2.21)$$

$$\dot{y} = \mathbf{Cx} + \mathbf{Du} \quad (2.22)$$

(2.21) and (2.22) can be rewritten in the Laplace form as,

$$s\mathbf{X}(s) = \mathbf{A}\mathbf{X}(s) + \mathbf{B}\mathbf{U}(s) \quad (2.23)$$

$$\mathbf{Y}(s) = \mathbf{C}\mathbf{X}(s) + \mathbf{D}\mathbf{U}(s) \quad (2.24)$$

Also, state equation can be obtained as,

$$s\mathbf{X}(s) - \mathbf{A}\mathbf{X}(s) = [s\mathbf{I} - \mathbf{A}]\mathbf{X}(s) = \mathbf{B}\mathbf{U}(s) \quad (2.25)$$

where $s\mathbf{I}$ denotes an $n \times n$ with all elements are zero except diagonal part. $[s\mathbf{I} - \mathbf{A}]$ is a square $n \times n$ matrix, and its elements are directly related to the \mathbf{A} matrix. (2.26) can be satisfied by using the Cramer's rule, Gaussian elimination, the matrix inverse etc.

$$[s\mathbf{I} - \mathbf{A}] = \begin{bmatrix} (s - a_{11}) & -a_{12} & \cdot & \cdot & \cdot & -a_{1n} \\ -a_{21} & (s - a_{22}) & \cdot & \cdot & \cdot & -a_{2n} \\ \cdot & \cdot & \cdot & & & \cdot \\ \cdot & \cdot & & \cdot & & \cdot \\ \cdot & \cdot & & & \cdot & \cdot \\ -a_{n1} & -a_{n2} & \cdot & \cdot & \cdot & (s - a_{nn}) \end{bmatrix} \quad (2.26)$$

Since all of the equations conducted with the model are second-order in (2.18–2.20), their state space models include the following transformations:

$$x = x_1 \quad (2.27)$$

$$\dot{x} = x_2 \quad (2.28)$$

$$y = y_1 \quad (2.29)$$

$$\dot{y} = y_2 \quad (2.30)$$

$$z = z_1 \quad (2.31)$$

$$\dot{z} = z_2 \quad (2.32)$$

State-space model of the microrobot motion can be represented in the $\dot{\mathbf{x}} = \mathbf{A}\mathbf{x} + \mathbf{B}\mathbf{u}$, where \mathbf{A} is an $n \times n$ square matrix, \mathbf{B} is an $n \times m$, \mathbf{x} is the state vector n , and the

input vector u is a column vector of length m . The output equations are commonly written in the form of $\dot{y} = \mathbf{C}\mathbf{x} + \mathbf{D}u$. In this equation, y is a column vector, C is an $m \times n$ matrix that includes weight of coefficients, D is an $m \times r$ matrix which is the null matrix because of there is no direct relationship between controller to outputs.

$$\begin{bmatrix} x_2 \\ \dot{x}_2 \end{bmatrix} = \begin{bmatrix} 0 & 1 \\ 0 & \frac{c_d \rho_f A_x}{2m_r} |\dot{x}| \end{bmatrix} \begin{bmatrix} x_1 \\ x_2 \end{bmatrix} + \begin{bmatrix} 0 \\ \frac{1}{m_r} \end{bmatrix} u \quad (2.33)$$

$$\begin{bmatrix} y_1 \\ \dot{y}_1 \end{bmatrix} = \begin{bmatrix} 0 & 1 \\ 0 & \frac{c_d \rho_f A_y}{2m_r} |\dot{y}| \end{bmatrix} \begin{bmatrix} y_1 \\ y_2 \end{bmatrix} + \begin{bmatrix} 0 \\ \frac{1}{m_r} \end{bmatrix} u \quad (2.34)$$

$$\begin{bmatrix} z_2 \\ \dot{z}_2 \end{bmatrix} = \begin{bmatrix} 0 & 1 \\ 0 & \frac{c_d \rho_f A_y}{2m_r} |\dot{y}| \end{bmatrix} \begin{bmatrix} z_1 \\ z_2 \end{bmatrix} + \begin{bmatrix} 0 \\ \frac{1}{m_r} \end{bmatrix} u + \begin{bmatrix} 0 & 0 \\ \frac{V_r g}{m_r} & -1 \end{bmatrix} \begin{bmatrix} (\rho_r - \rho_f) \\ g \end{bmatrix} \quad (2.35)$$

where $u = F_m + F_g$ is the control signal of the system. In addition, the sum of the magnetic forces acting on the microrobot can be collected into a single expression to simplify as a net force in Equation (2.36),

$$F_{net} = F_m + F_g \quad (2.36)$$

FEM simulations are used to determine c_d by using time-dependent FSI (Fluid-Structure Interaction), and F_{net} , stationary MNFC (Magnetic Field No Currents). The parameters of microrobot and its environment, which are used in both simulation and experimental studies, are given in Table 2.2 (microrobot mass, cross-sectional areas, and volume values are obtained by SOLIDWORKS[®]).

2.3 FEM Analysis

In this section, the drag force and the magnetic force imposed on the microrobot are calculated. According to the values given in Table 2.2, analytically, drag force and magnetic force cannot be calculated due to the complex geometry of the microrobot. The precise calculation of microrobot can be achieved by integrating a magnetic field around it because a convergence problem may occur during the magnetic field's integration due to non-uniformity. There is also no further simplification in the analytical formulations to determine c_d and F_{net} as numerically. Since each force acting on the microrobot cannot be calculated analytically, it is necessary to reduce the processing load by utilizing numerical methods. For this reason, COMSOL[®] MFNC

(Magnetic Field No Currents) module for magnetic force calculation and COMSOL[®] FIS (Fluid-Structure Interaction) module for drag force calculation are used. In this way, the surface stress and force exerted on the surface of microrobot can be determined. The microrobot has a full circle design with four half-moon shape pockets for possible future cell-separation and manipulation studies.

2.3.1 Mesh Structure

The microrobot levitation system is designed and is imported to the simulation environment, which is shown in Figure 2.3. In this figure, (1) Air domain, (2) Permanent magnet and (3) pyrolytic graphite are presented with mesh-render. Assigning appropriate mesh to the system is crucial for precise results since the magnetic field module is very mesh-sensitive. To overcome such a mesh problem, it is required to incorporate meshes as follows:

- The minimum and maximum mesh values in tetrahedral meshes should be close to each other. The ratio between them should be less than 1/10.
- Regular refinement feature can be used to increase mesh intensity. Level 1 or 2 can be selected but it requires more CPU power.
- Corner refinement might be good consideration for complex geometries and

Table 2.2 Micro-untethered floating object (microrobot) properties and nonmagnetic forces

Symbol	Quantity	Units
m_r	2.929751×10^{-6}	N
g	9.81	m/s^2
ρ_r	1798.374	kg/m^3
ρ_f	998.2071	kg/m^3
A_x	1.229066×10^{-6}	m^2
A_y	1.229066×10^{-6}	m^2
A_z	8.15402×10^{-6}	m^2
V_r	1.61911×10^{-6}	m^3
I	23.62×10^{-6}	kgm^2
$F_{B,z}$	12.788	μN
$F_{r,z}$	28.741	μN

sharp turns/edges. Especially the magnitude of stress around corners can be computed with higher errors.

- Pyrolytic graphite structure can be assumed uniform and smooth. Mapping mesh feature can be applied to the upper surface and assigned to the whole material by the "swept mesh" method.
- Convert and insert center/diagonal points can be used to combine meshes all together; otherwise, it would be better to use one single mesh type.
- Free triangular mesh structure is ideal for entire system if there is no huge size difference.

According to the suggestions mentioned earlier, the magnetic levitation system mesh is shown in Figure 2.3. In this figure (A) shows top view of the system include with (1) Air domain, (2) Permanent magnet, and (3) Pyrolytic graphite. The same system is also given in (B) as front-view. Three different mesh types are used in this system which are triangular, mapping, and tetrahedral. The reason is that magnetic field lines and their direction should not be affected by the mesh. Every mesh in the system is calculated separately and then finalized by combining them. Mesh structure detail is also given in the Table 2.3. The mesh number should be carefully adjusted according to the computer since computational time is affected exponentially, not linearly.

After assigning an appropriate mesh structure, the drag force can be calculated more precisely. Because of the non-symmetrical and complex shape of the microrobot, F_d should be determined first. In this way, c_d can be calculated since the rest of the terms are all known numerically. Accordingly, computational fluid dynamics (CFD) must be computed F_d while the microrobot is moving in an enclosed fluidic environment. Parametric analysis is necessary in order to compare the drag coefficient at different levitation height. Also, different microrobot speeds are tested. The analysis is done in the FSI module in COMSOL[®]. As a result of the analysis, the c_d calculation is completed. In this calculation, external surface stress on the microrobot body includes gravitational and hydrodynamic effects of the microrobot z-axis. In the analysis, c_d calculations are performed by the comparison of two results. These results are the microrobot's levitation in the z-axis in the fluid channel and moving mesh along the x-axis. The overall view of the computational fluid dynamics (CFD) model, the materials' settings, and their dimensions are shown in Figure 2.4. In this figure, magnetic flux density can be observer outer part of the lifter magnet. The reason is that permanent magnet is axially magnetized along its geometric axis. Magnetization direction of this magnet is along the z axis. As we can see in the front-view that

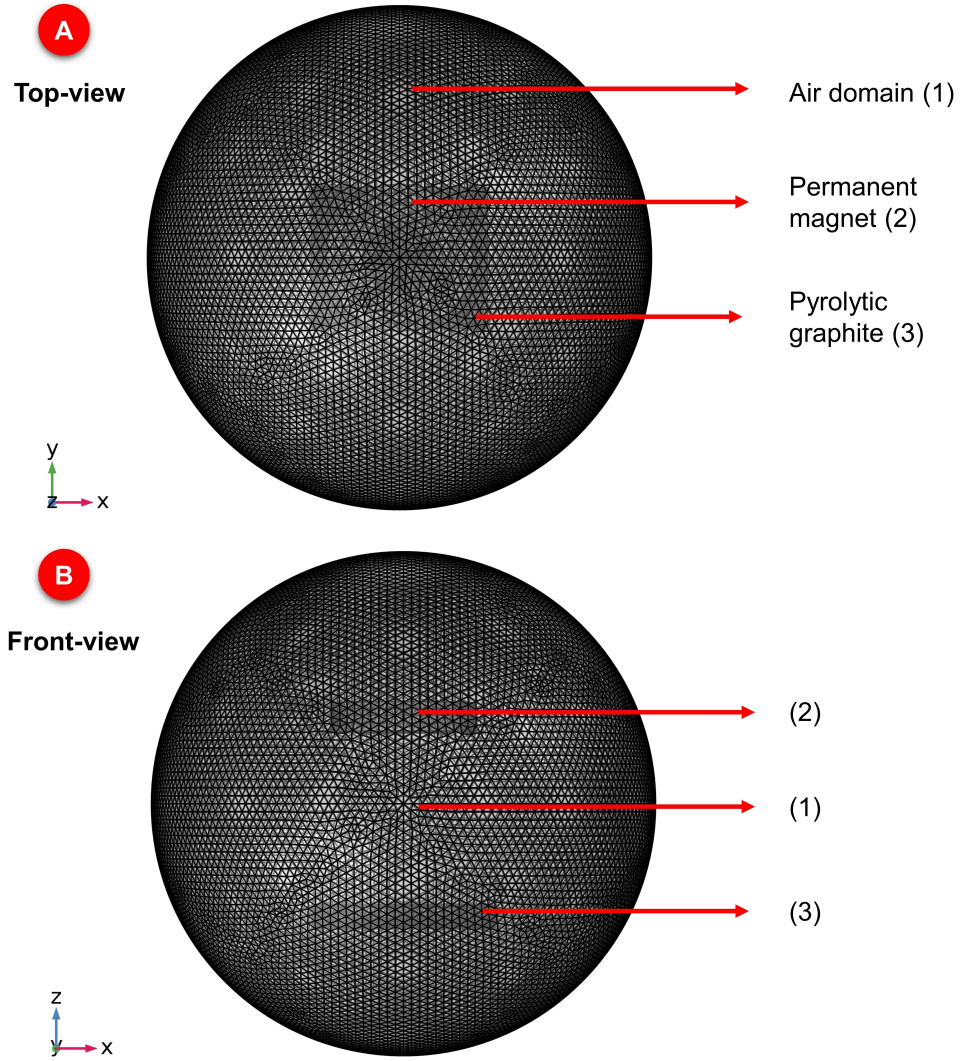


Figure 2.3 Shows (A) top-view and (B) Front-view. Complete mesh consists of 63259648 domain elements, 560896 boundary elements, and 4112 edge elements

magnetic field propagates on the $+z$ direction. Moreover, magnetic flux on the microrobot is intensified around its outer surface, as expected.

After confirmation of the N-S-N-S order is completed, the drag force should be calculated first. In the calculation of this force, it is expected to obtain dependent variable is velocity only. If the flow characteristic can be affected by the microrobot position, it is challenging to compute. This is the reason that we assume, drag force and its coefficient would only be dependent on the cross-sectional area, fluid medium, and microrobot velocity. The F_D is obtained with respect to microrobot's velocity, that is obtained from the analysis shown in Figure 2.5. In this figure, the surface stress plot at the velocity of 5 mm/s. F_D is calculated by integrating the external surface stresses generated on the microrobot during its movement on the z-axis. Velocity values of microrobot are in the range of 0–7 mm/s, and represented by the upper legend.

Table 2.3 Mesh structure of the experimental system

Mesh feature	Number of mesh
Number of vertex elements	4
Number of edge elements	90
Number of vertex elements	8
Number of edge elements	188
Number of boundary elements	1180
Number of elements	1000
Minimum element quality	1
Number of vertex elements	46
Number of edge elements	4112
Number of boundary elements	560896
Number of elements	63259648
Free meshing time	5.86s
Minimum element quality	0.03109

According to contour lines on the microrobot, the lower legend represents surface stress on the microrobot. It can be seen more intensively at corner and intersection points between SU-8 and stabilizer magnet, same as mentioned in Figure 2.4. The reason is that the different properties of the intersection point of SU-8 and carrier magnet hardness affect the homogeneous distribution in stresses. So, the intersection point of SU-8 and magnet has more stress. Moreover, there is more stress in the microrobot corner areas as well. This is due to the smaller areas increase the high flow rates and it causes more stress at the corner areas.

2.3.2 Drag Coefficient Calculation

Using simulation results of the Figure 2.4–2.5, surface stresses can be calculated numerically. To do this, positive and negative expressions for the microrobot moving in the range of $[-2 \ 2]$ mm/s represent the direction of movement. Also, the surface stress can be observed on the microrobot surface for this range, and it is shown in Figure 2.6. When the microrobot velocity is selected as 3 mm/s, light blue-green colors can be observed more intensively around the microrobot. Colour intensity is also given in the upper legend. Surface stress can be seen in the lower legend in the range of 16.6-348 Pa. microrobot body (SU-8) and carrier magnet have different mechanical

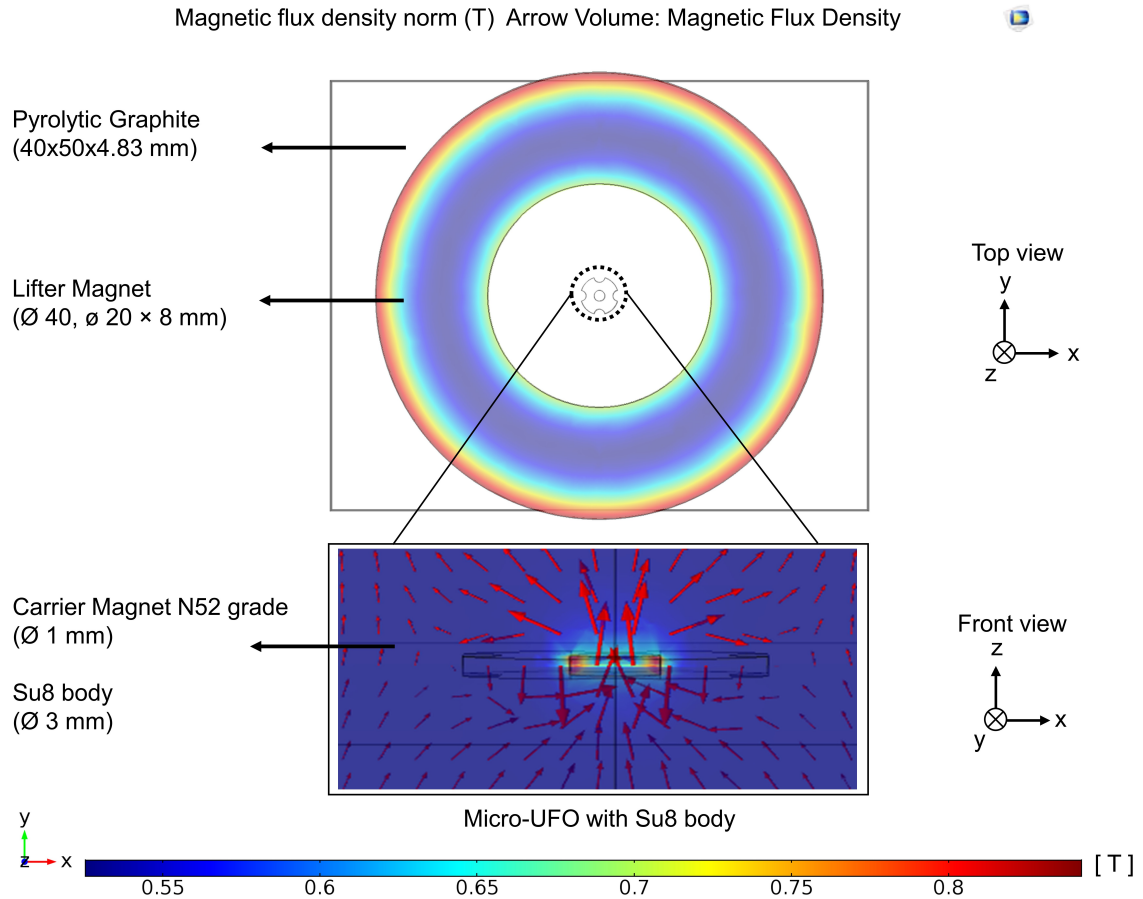


Figure 2.4 The effect of the magnetic field on the microrobot and the dimensions of the materials used are shown. As expected in the lifter magnet, the magnetic field is seen with a higher [T] (red color) due to the magnetic field lines' polarity in the corner regions. In the microrobot, the same situation is seen in the magnified image.

It is also shown that the lines are in the z-axis direction (front view) since the magnets are placed in order. Used computer: Intel Xeon E4820 * 4 processors (32 core), 128 GB RAM

hardness. Thus, surface stress is seen more intensively at the corner and intersection points between SU-8 & stabilizer magnet. Thus, the surface's stress is higher in the intersection regions, while the stress in the magnet center is less and homogeneously distributed.

In the beginning, when the microrobot starts moving from its initial state named "stationary state," inertial forces should be overcome first. After that, the drag force is affected as a function of velocity exponentially. According to Newton's 1st law of inertia and the dynamic principle of Newton's 2nd law are exposed to friction and viscous forces on the opposite side of the magnetic forces acting on the microrobot in the x-axis. Besides, during the movement of the "lifter magnet," there is almost no friction in the air environment, which is assumed to be negligible. As a result, different accelerations occur in the lifter magnet and microrobot motions. In the

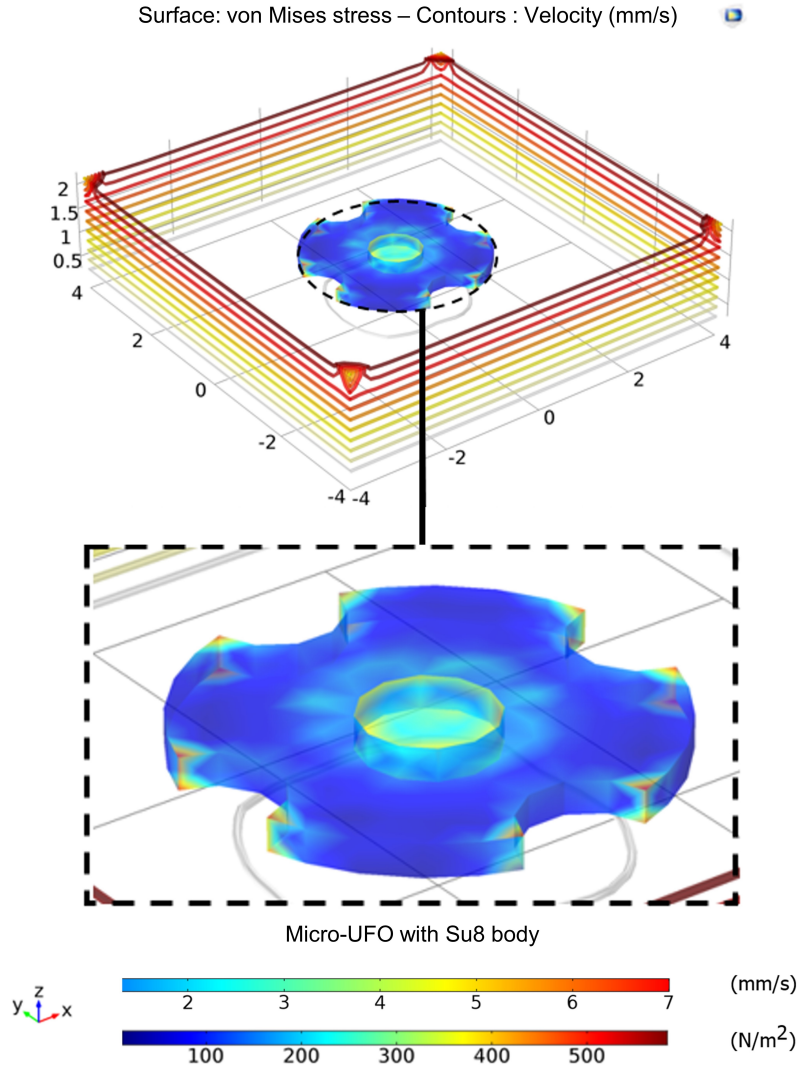


Figure 2.5 Shows von Mises stress on the microrobot upper surface

starting position, the microrobot and lifter magnet is aligned with each other with respect to the magnet's center. Because the ring-shaped magnet is used in the system, the alignment can be confirmed using a laser displacement sensor before levitation and microrobot manipulation. Though, their motion parallelity disrupts with the misalignment of their centers during their movement longitudinally. The drag force imposed on the microrobot cross-sectional area is given in Figure 2.7. In this figure, drag force due to microrobot velocity is shown. This force is the main reason for the misalignment that can be observed during the motion. This force, which depends on the square of the velocity, can not be neglected, especially at higher velocities. This is because, the drag force highly depends on velocity such as $0.1 \mu N$ at 5 mm/s and $0.5 \mu N$ at 10 mm/s .

After the determination of the c_d , the magnetic and diamagnetic forces are left to calculate only. For this reason, as a second step after drag force calculation, the net

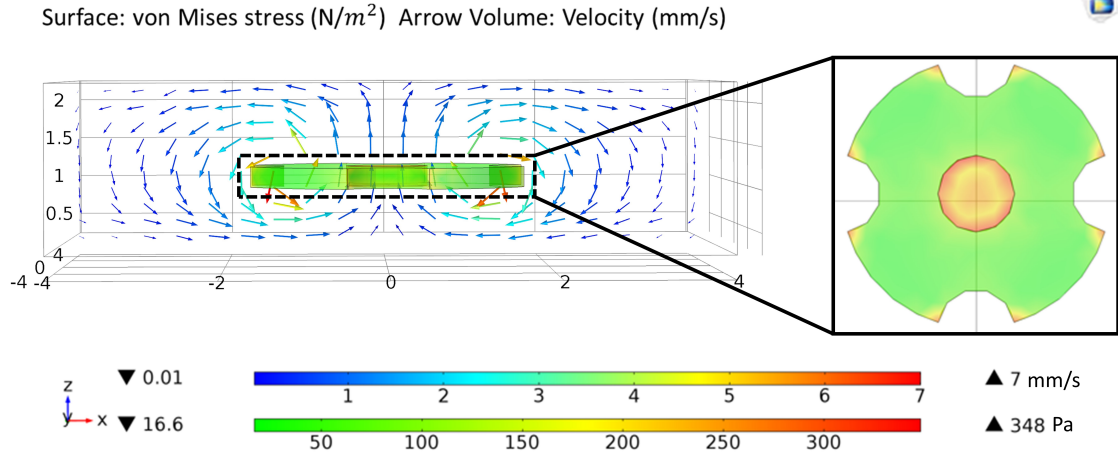


Figure 2.6 Shows vector plot of the surface stresses around the microrobot is seen for various velocities, © 2021 Journal of Magnetics, with permission, from ref [107]

magnetic force, F_{net} , shall be calculated. F_{net} varies with the lifter magnet's levitation height from the pyrolytic graphite surface. The distance between the microrobot and the pyrolytic graphite surface represents the levitation point when the total net magnetic forces acting on the microrobot are equal to zero. Furthermore, there can be more than one levitation point as long as stability conditions are satisfied. Simulation results of the levitation distance with respect to the net magnetic force is given in Figure 2.8. In this figure, the magnetic forces that are generated by the x and y axes are lower than the z-axis. There is a 1/103 ratio between their magnetic force due to axially magnetized ring-shaped lifter magnet. Thus, the magnetic force imposed on the microrobot in the z-axis more dominant than other axes. However, when the acting forces on the x and y axes of the microrobot are small, 40-50 nN, the motion that occurs can be due to x, y forces being more significant than the drag force (Figure 2.7).

The lifter magnet position effect on levitation characteristic is demonstrated in Figure 2.9. In this figure, the total net magnetic forces on the z-axis decrease exponentially when the lifter magnet is moved away. Minimum levitation point when lifter magnet distance is 60 mm, 31.02 μm ; maximum levitation point is 54 mm, 329.1 μm are calculated. The experimental setup analysis is solved using the COMSOL[®] direct solver method to obtain more accurate results.

2.3.3 Determination of Levitation Characteristic

The result of the analysis is calculated by using both the Maxwell stress tensor and global matrix evaluation methods, and it is seen that the results are the same. Lifter magnet is far away from the microrobot so that the magnetic field force lines can occur

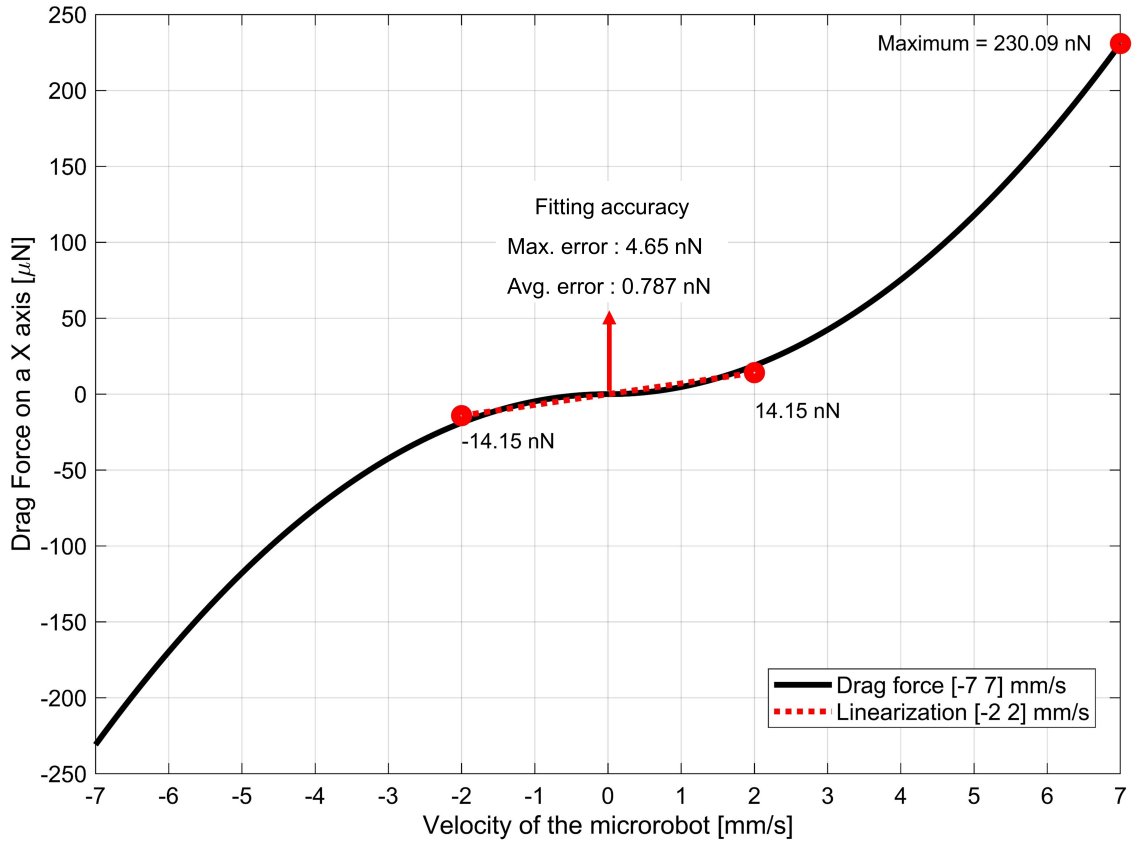


Figure 2.7 Exhibits a parabolic drag force characteristic depending on the velocity of microrobot. The drag force change is less for the $[-2, 2]$ mm/s range, which is the microrobot motion speed. For this reason, the system can be expressed by linear equation, by performing curve fitting at the specified interval. For the equation proposed as $F_d = kV_r$, a constant coefficient was found to be $k = 7.075 \times 10^{-9} \text{kg/s}^2$. Due to the symmetric structure of the microrobot, the force calculation is preferably shown only for x-axis

symmetrically. Since the sufficient length of the lifter magnet is larger than the physical length by an amount roughly equal to the air gap, the forces generated in the x- and y-axes are weaker than the z-axis. During levitation on the z-axis, net magnetic forces generated are in the order of micrometers. In x and y axes, the forces falling in the nano order are about $1/10^3$. Figure 2.8 shows the net magnetic force values calculated when the phase difference is 0.1 mm and the pyrolytic graphite-lifter magnet distance is about 54 mm. Along with the net magnetic force, drag force, buoyant force, and gravitational force are acting on the microrobot simultaneously. Thus, they can be summed as F_T (total force), as it is shown in Equation (2.37).

$$F_T = F_{net,z} - F_{D,z} + F_{B,z} - F_{r,z} \quad (2.37)$$

In addition, $F_D = 14.15 \text{ nN}$ is calculated when the microrobot velocity is about 2

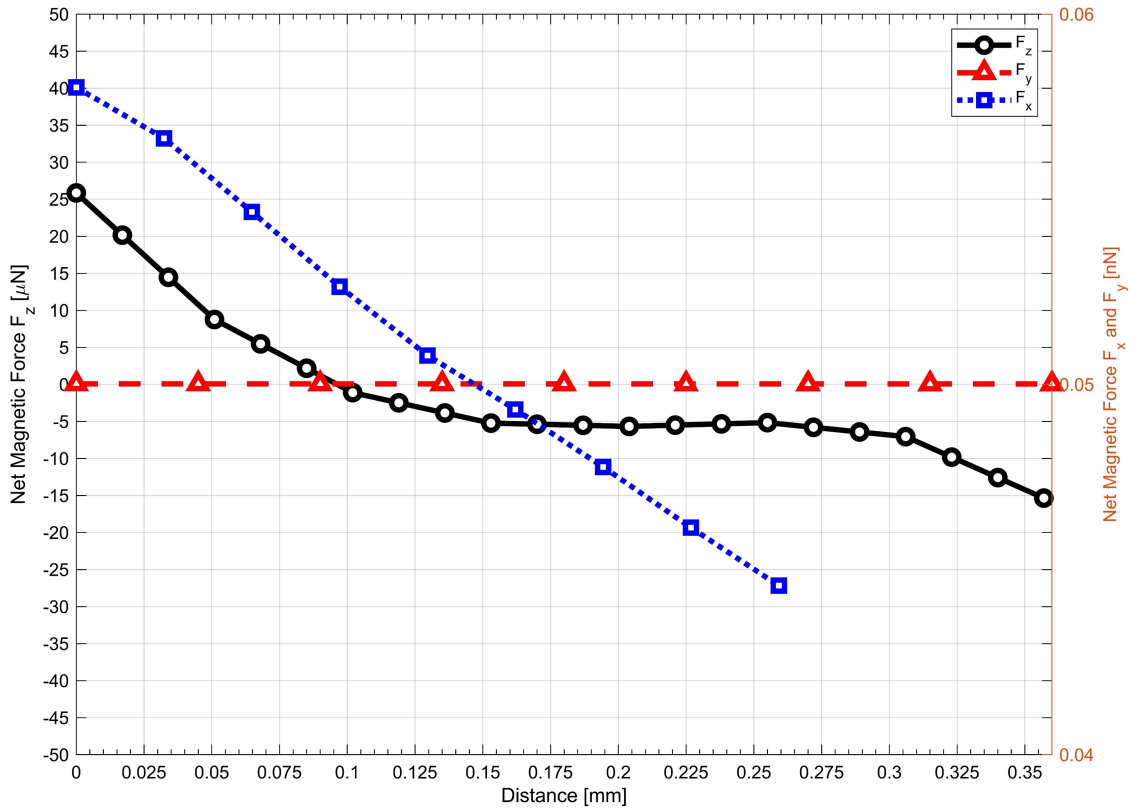


Figure 2.8 The net magnetic force characteristics acting on the microrobot for each of the three axes with respect to the levitation distance are presented

mm/s. The required magnetic force $F_{net,z}$ for the levitation is calculated as $15.967 \mu\text{N}$. The corresponding force value given in Figure 2.8 is shown as marked on the surface graph. As a result of the analysis, the robot is separated from the stabilization point at the levitation height of $333.8 \mu\text{m}$. Besides, there is a flat profile with a linear slope at the levitation height: $100\text{--}300 \mu\text{m}$. The area outside the region concerned may be called the region of instability; within this region, the microrobot can be stably operated. The total force obtained on the z-axis is shown as the surface plot in Figure 2.9. The maximum levitation height relative to pyrolytic graphite is shown in Figure 2.9. According to this, when the z-axis distance between the "lifter magnet" and the "pyrolytic graphite" is more than 54 mm , microrobot reaches instability and detaches from suspension at the height of $329.1 \mu\text{m}$. The reason is that the required magnetic force $F_{net,z}$, which is calculated as $15.967 \mu\text{N}$, cannot be obtained after 54 mm .

2.4 Materials and Methods

In this section, the materials used and microrobot fabrication are presented. In the lifter and carrier magnets, neodymium N52 and N48 magnets are used, respectively. For avoiding corrosion effects due to water and magnet interaction, permanent magnet

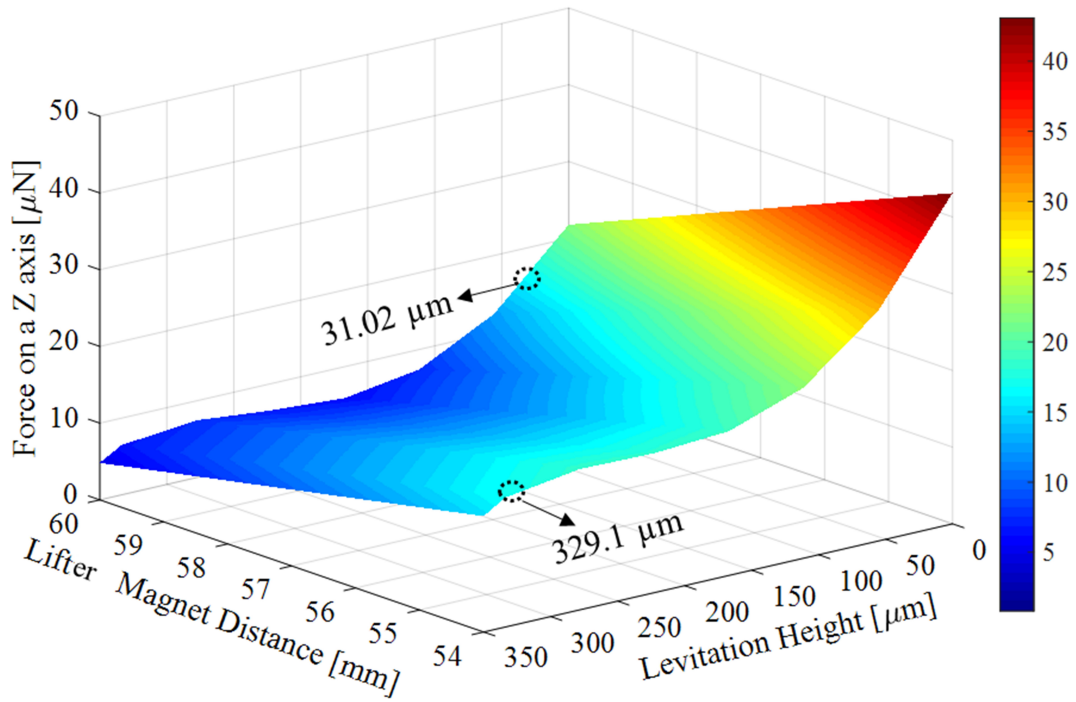


Figure 2.9 Shows the effect of the forces exerted on the microrobot depending on the distance between the "Lifter Magnet" and the "Pyrolytic Graphite"

surfaces are coated.

2.4.1 Permanent Magnet Surface Coating

Since most of the microrobot's target application areas are biomedical applications, the microrobot surface is coated with polydopamine (PDA), which is a suitable material for biomedical applications [108]. Accordingly, after adding 100 mg of dopamine powder (Merck & Company, Inc., Kenilworth, NJ, USA) in 50 mL of purified water, Tris powder (100 mg) was dissolved in the prepared mixture. Starting with the beginning of the coating, the color of the solution gradually gets darker. The magnet is coated with the PDA is separated from the solution using another magnet. After coating the magnet, Fourier transform infrared (FTIR) measurements were applied by Perkin Elmer Spectrum 100 (PerkinElmer, Inc., Waltham, MA, USA) contains diamond crystals for reflection. After placing coated magnet in accessory, peaks of the spectrum were measured at the wavelength of $1500\text{--}1650\text{ cm}^{-1}$ and $3200\text{--}3600\text{ cm}^{-1}$; these peaks indicate atomic vibrations of the hydroxyl groups and N-H vibrations in the structure which is shown in Figure 2.10. In this figure, the presence of the coating layer is confirmed by the FTIR spectrum observed. This demonstrates that the robot's body's permanent magnet is successfully coated with PDA for biomedical applications.

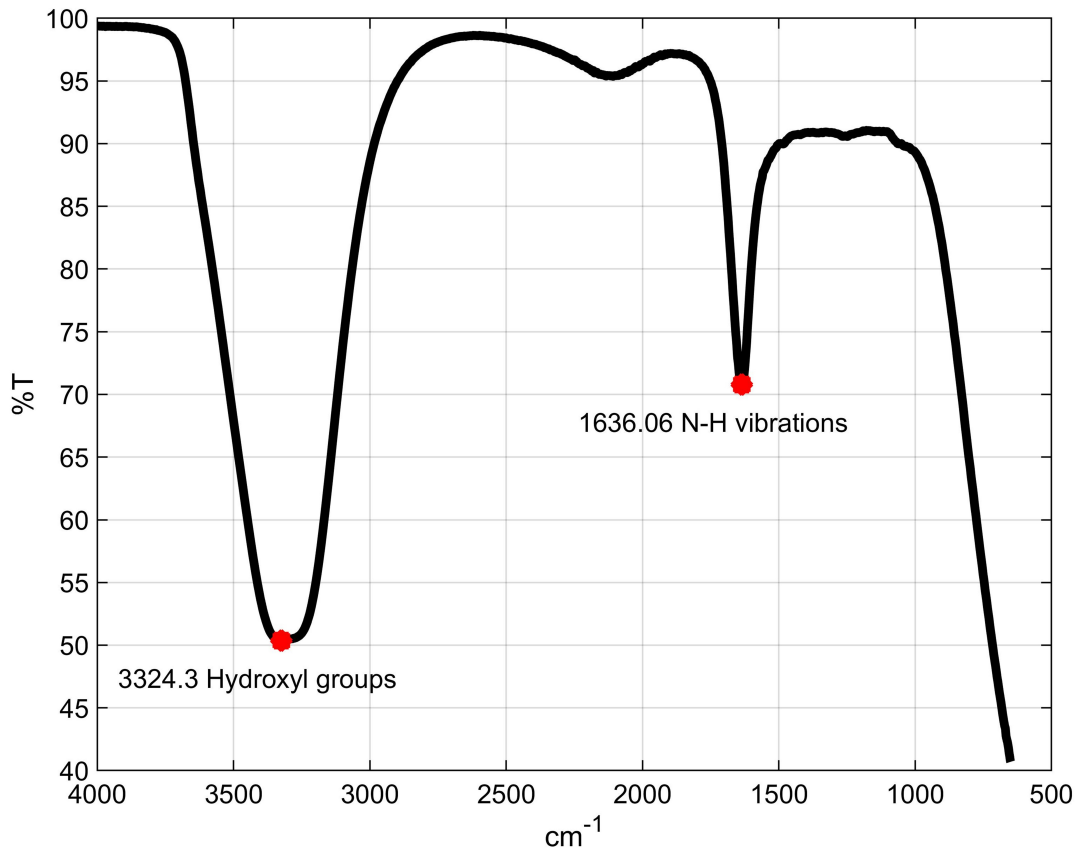


Figure 2.10 Fourier transforms infrared (FTIR) spectrum of magnet coated with polydopamine (PDA). The peak between a wavelength of $1500\text{--}1650\text{ cm}^{-1}$ indicates N-H vibrations, and the peak between the wavelength of $3200\text{--}3600\text{ cm}^{-1}$ indicates hydroxyl groups in the structure. That proves the successful coating of the magnet surface

2.4.2 Microrobot Fabrication

Basic lithography techniques are used for microrobot SU-8 body production. These operations can be listed as follows:

- Silicon wafer coating with photoresist is done by using a spin coater. The spin coating allows having homogeneous distributions according to target thickness. Every SU-8 material has its receipt, and accordingly, coating speed can be adjusted to have appropriate photoresist thickness AZ1505 (positive photoresist). In this way, thin layers of the viscous material can be turned into a smooth surface.
- Masking is used to produce microrobot body.
- Developer removing from the related zone can be achieved by using UV light. In this process, UV light is propagating through the photoresist on the mask. Some of the part does not allow light to be propagated due to photoresist. So, the

shape of the robot body can be obtained at the end of this process.

- PDMS preparation,

Completion of the microfluidic system by plasma treatment microrobot manufacturing steps are shown in Figure 2.11. In this figure, (A) shows AZ 1505, that is a positive photoresist with the high resolution and adhesion, is firstly coated onto a substrate surface as a sacrificial layer (MicroChemicals GmbH, Ulm, Germany). (B) shows a negative adhesive film with a thickness of $200\ \mu\text{m}$ is laminated on the sacrificial layer by rolling at $90\ ^\circ\text{C}$ on a hot plate (SUEx 200, DJ MicroLaminates, Inc., Sudbury, MA, USA). (C) the exposure process on film is applied, and then the final polymer microrobot body is obtained by the pattern development process. In (D), neodymium ($\text{Nd}_2\text{Fe}_{14}\text{B}$) circular permanent magnet (N52 grade) with the dimensions of $1\ \text{mm} \times 0.25\ \text{mm}$ (diameter-thickness) is coated with PDA. (E) As a final step is that PDA-coated bio-compatible permanent magnet was assembled in the microrobot body.

microrobot production has been completed in this way. Using the steps mentioned above, different microrobots can be produced, such as thicker, thinner, or complex geometry, as long as they can be extruded 2D to 3D.

2.5 Experimental Results

In the previous sections, calculations of the drag force, the magnetic force, diamagnetic force, and the microrobot production are presented in detail. In this section, essential factors that should be taken into consideration for the experimental setup is given.

2.5.1 Experimental Setup

According to the diamagnetic based levitation system, the microrobot levitation is shown with the optimal parameter. These parameters are as lifter and carrier magnet size, pyrolytic graphite thickness, and microrobot shape. First of all, preliminary experiments of the microrobot, which is designed and determined by the analysis results, are studied. The experimental system set up in accordance with the selected parameters, as shown in Figure 2.12-(a). Preliminary experimental results are shown that the microrobot levitation can be performed using calculated parameters. For the lifter magnet's orientation, a high precise micro-nano stage (PI M-126.PD2) is equipped, and a container with thick pyrolytic graphite is placed right under it. A camera system attached to a microscope lens (Olympus SZX-7 and PointGrey GS3-U3) is utilized to confirm the levitation. In (B), (C), and (D) represent the different image of the microrobot during its manipulation

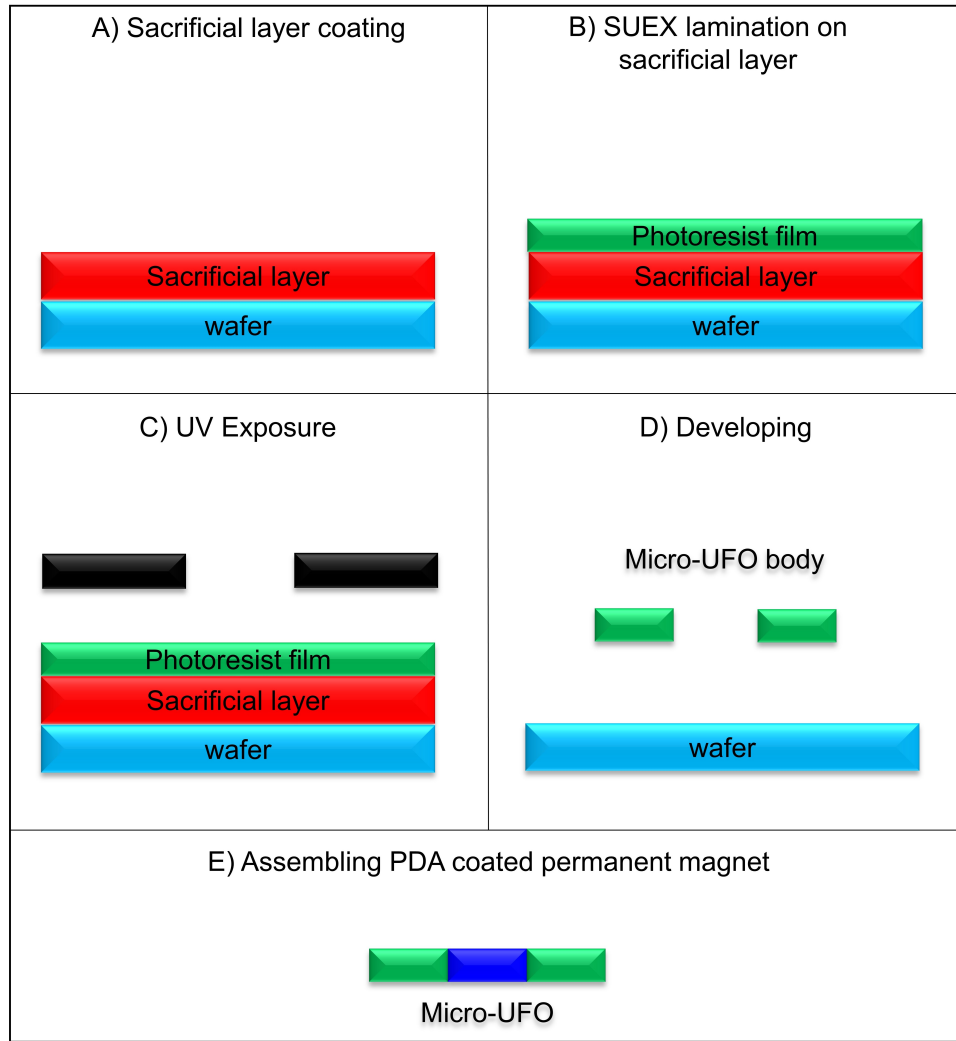


Figure 2.11 Fabrication process of the microrobot. (A) Sacrificial layer coating; (B) SUEX lamination on sacrificial layer; (C) UV Exposure; (D) Developing; (E) Assembling polydopamine (PDA) coated permanent magnet

Precise positioning of the lifter magnet in the z-axis relative to the pyrolytic graphite is achieved by using the motorized micro stage. The results of the analyzes are tested to compare whether the robot is levitated at the calculated range from 54 mm to 62 mm. Firstly, the microrobot which has a higher density than (Deionized) DI water is allowed to sink into the graphite surface. It is observed that the mechanical contact of the microrobot from the graphite surface can be removed by adjusting the lifter magnet in proper position. When microrobot and lifter magnet is aligned and the distance between them is adjusted then levitation is done. As expected, (b), (c), (d) refer to the microrobot levitation is confirmed and results are given in Figure 2.12. As shown in this figure and simulation results, the microrobot levitation height can be adjusted according to the relative position of the lifter magnet.

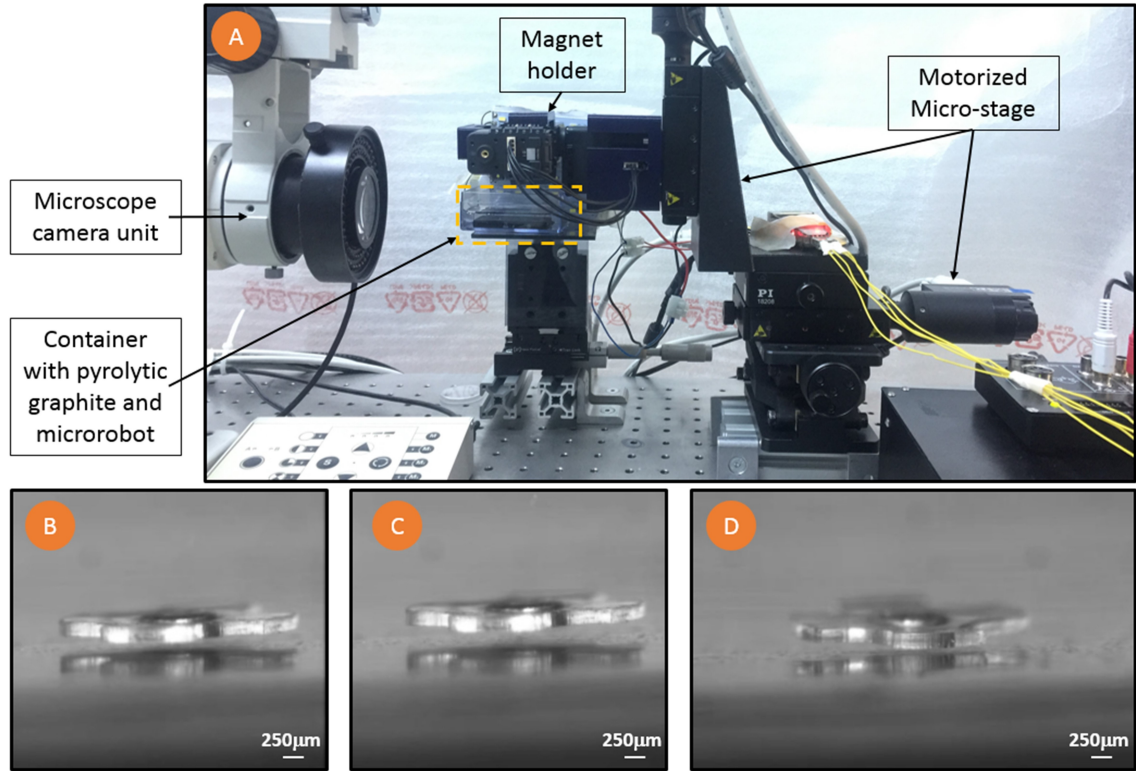


Figure 2.12 (A) shows diamagnetic levitation experimental setup of microrobot with equipment. An optical microscope is used to record levitation from the lateral view.

A container is used for pyrolytic graphite and microrobot with fluid inside. Motorized micro-stages are used due to manipulation of the microrobot in x, y, and z axes. Magnet holder with servo motor controls the microrobot orientation due to its parallel motion to the pyrolytic graphite's surface. (B), (C) and (D) represent the images of microrobot at different heights during the experiment, © 2021 Journal of Magnetism, with permission, from ref [107]

2.5.2 Levitation Capabilities

The whole experimental setup and the microrobot's levitation and motion characterization experiments are already given. The microrobot levitation height can be controlled by moving the lifter magnet in microns' order along the z-axis. It exhibits the levitation characteristic depending on the magnets and properties use within the system. The reason for using a ring-shaped lifter magnet is that it has a hole in its center, which is required for laser measurement. The laser sensor is aligned with the microrobot since the gap in the middle of the ring-shaped structure ($\varnothing 20 \text{ mm}$). The PI Stage, which we control through the interface, is moved by $50 \mu\text{m}$ on the z-axis, followed by $10 \mu\text{m}$ steps as the first levitation is achieved. When the microrobot is in the levitation state, the lifter magnet's force characteristics in the motion range of about 6 mm are observed. The measurements are made in terms of the distance between different levitation heights, and the microrobot positions are given in Figure 2.13. In this figure, the experimental results of the microrobot with different levitation

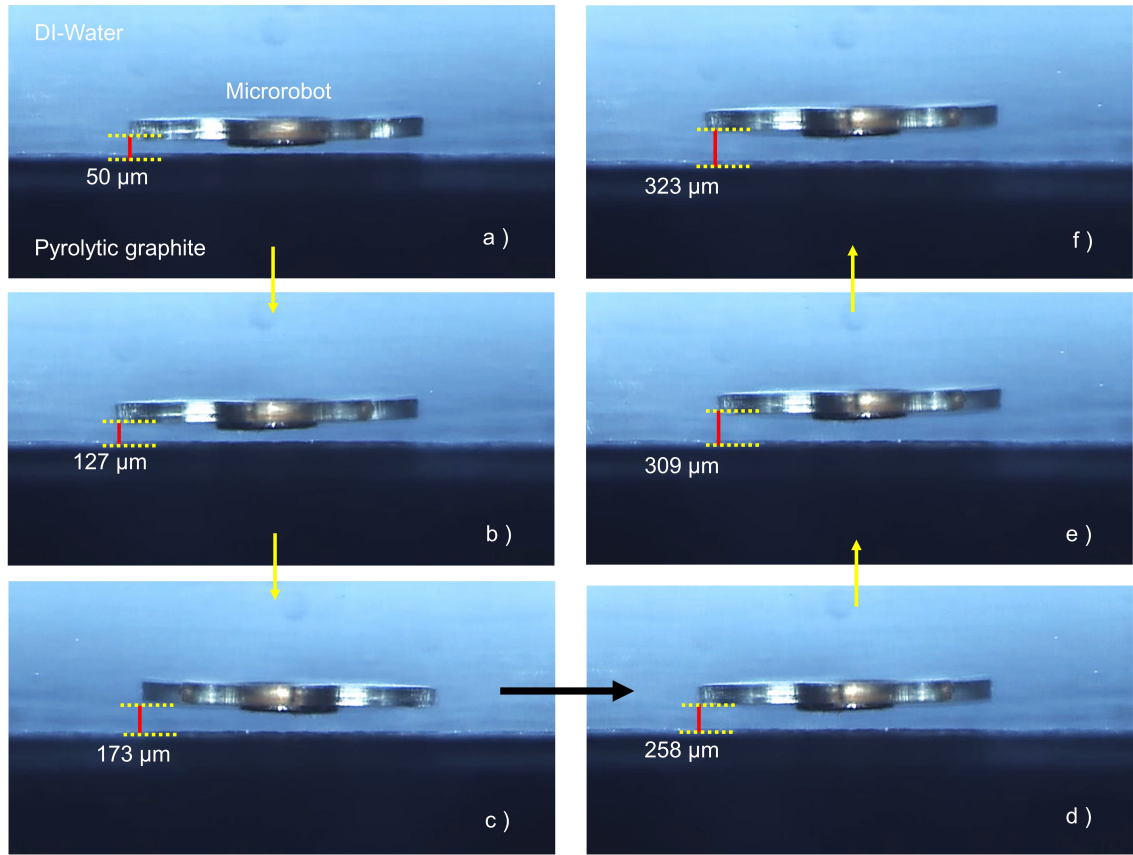


Figure 2.13 The experimental results show the microrobot with different levitation height depending on the distance between "Lifter Magnet" and the "Pyrolytic Graphite (PG)." The experiment was recorded by acquiring the position data with the laser distance sensor in each movement step. The microrobot has been shown to operate at a maximum stabilization level of $333.8 \mu\text{m}$ in the current system. In figure, the microrobot is shown at various levitation heights based on lifter-magnet position relative to PG; (a) $50 \mu\text{m}$, (b) $127 \mu\text{m}$, (c) $173 \mu\text{m}$, (d) $258 \mu\text{m}$, (e) $309 \mu\text{m}$ and (f) $323 \mu\text{m}$

heights depending on the distance between "Lifter Magnet" and the "Pyrolytic Graphite (PG)." The optical microscope records the experiment, and the levitation height is measured with the laser displacement sensor. The microrobot can be operated at a maximum stabilization level of $333.8 \mu\text{m}$ in the existing experimental system. The microrobot is also shown at various levitation heights based on lifter-magnet position relative to PG; (a) $50 \mu\text{m}$, (b) $127 \mu\text{m}$, (c) $173 \mu\text{m}$, (d) $258 \mu\text{m}$, (e) $309 \mu\text{m}$ and (f) $323 \mu\text{m}$.

In the following experiment, the lifter magnet and the pyrolytic graphite distance effects are observed. Same as the simulation, the lifter magnet position is changed to 6 mm. Therefore, microrobot's levitation height is changed, and it is shown in Figure 2.14. In this figure, the x-axis denotes lifter magnet height relative to the pyrolytic graphite's surface. Y-axis represents microrobot levitation height as an order of μm .

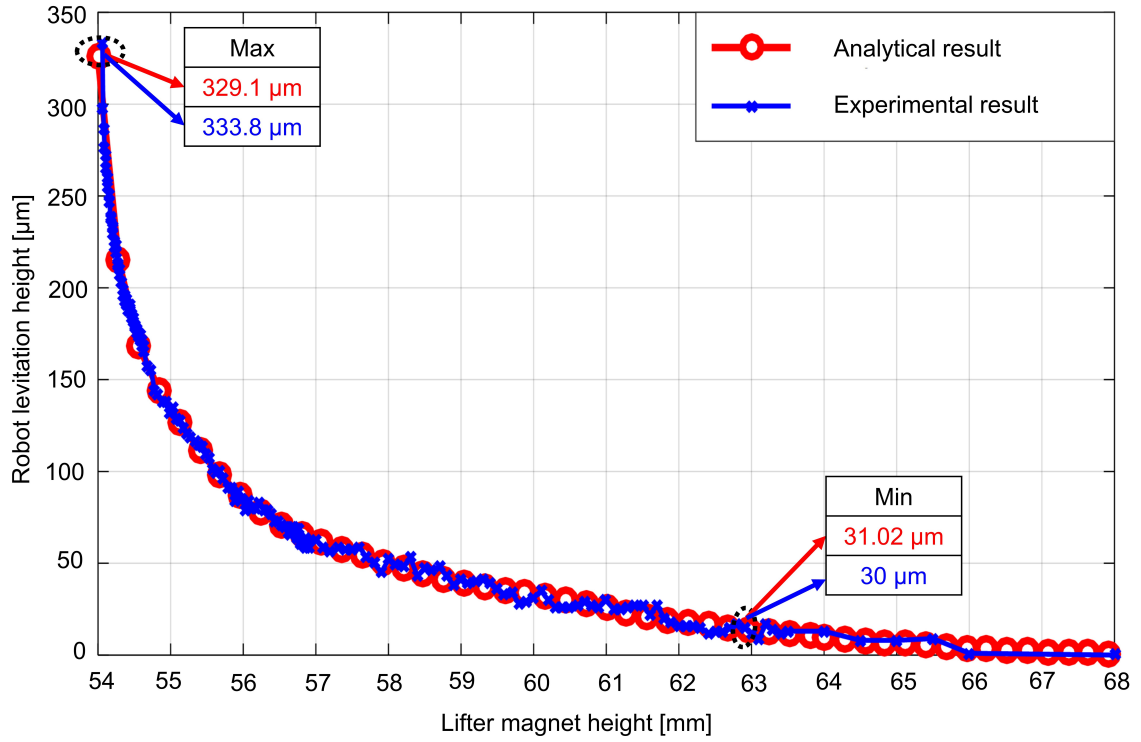


Figure 2.14 Shows comparison of finite element method (FEM) and experimental results for the microrobot levitation height according to distance lifter magnet with respect to pyrolytic graphite surface. It is seen that the obtained levitation height are overlapped with each other which is an indication of simulation results are confirmed

As shown in the figure, levitation height is changed exponentially rather than the linear function of the lifter magnet height. The reason is that the net magnetic force imposed on the microrobot is also changed exponentially and the magnets' non-linear nature.

As we can see in the figure, the maximum of 329.1 μm and a minimum of 30 μm levitation height obtained. This levitation range is sufficient for biomedical applications such as lab-on-a-chip. That is because cell manipulation, drug delivery, and pick and place robotic applications may require different objects to be used. The diamagnetic levitation methodology that we developed may vary according to these system configurations. The proposed manipulation method allows us to configurable microrobot design and driving magnet properties. In this way, achieve specific levitation intervals for different anticipations.

2.5.3 Accurate Positioning and Phase Difference Characterization

After levitation range determination is completed, then positioning accuracy and phase difference should be measured. In our system, the lifter magnet attached to the micro-stages is moving in the air by using motorized stages. Thus, the stage speed

is equal to the speed of the lifter magnet due to friction being neglected. Also, lifter magnet speed is a constant profile due to its acceleration keeps the same. However, the microrobot is located in the fluidic environment, and its velocity profile is varying. microrobot speed is zero at the starting position, and it increases until reaching the desired speed. It takes an amount of time which is depending on the desired speed. If the desired speed is high, microrobot requires more time to overcome inertial effects and drag forces until it reaches the same speed as the lifter magnet. Thus, the delay is occurred by the different speed profiles between the lifter magnet and robot. This problem is named "phase difference." The microrobot speed profile can be investigating in there different phases, which are as follows:

- Accelerating to the target speed: phase difference is getting higher,
- Constant speed: maximum phase difference,
- Decelerating to the zero speed and stop: phase difference becomes zero at the end of the motion.

The corresponding phase difference is shown in Figure 2.15-A, and the motion profile is shown in Figure 2.15-B. This figure (A), microrobot and lifter magnet are aligned when $t_0 = 0$ s. When lifter magnet moves, then microrobot follows slightly behind it, and the phase difference occurs. The maximum phase difference is observed when microrobot reaches at the same speed as the lifter magnet. They both move with a little bit offset to the same direction at the same speed. When the lifter magnet movement is completed, then microrobot speed is descending and zero at t_{end} . With the magnetic force's parameter values, it is possible to calculate the phase difference analytically in the further studies.

As a result of experimental studies and observations, the microrobot can precisely move and position in the proposed system. microrobot performed smooth motion at the desired speeds, ending its movement at the point where it would be coincident with the lifter magnet, as expected. During the microrobot motion, it is exposed to fluid-induced frictional resistance in the fluid. Besides, it has inertial effects originating from its own mass. The microrobot follows the trajectory in x and y axes with a delay because of all these factors. The difference between the lifter magnet center and microrobot is measured by the laser displacement sensor, which is shown in Figure 2.16. In this figure, (A) shows the initial microrobot position. (B) right after its motion is started, (C) maximum difference is occurred, and (D) at the end of the motion. The offset (delay) from the center of the lifter magnet is defined as "phase difference." The phase difference is a parameter controlled by the computer

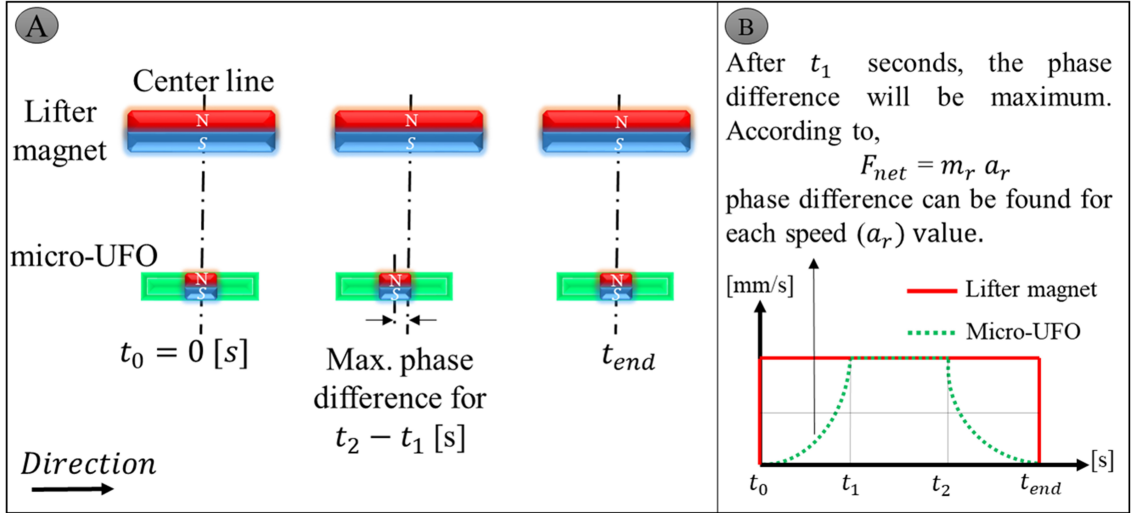


Figure 2.15 The phase difference between microrobot and lifter magnet starts from t_0 , starting moment, is shown in (A). After t_1 (B), the carrier magnet's speed will be equal with the lifter magnet: however, the phase difference reaches the maximum value. After that point, the phase difference begin to decrease. The microrobot acceleration, a_r , is already calculated by using Table 2.2 (see Figure 2.8). The phase difference can be expressed easily for this microrobot and lifter magnet with the help of velocity profile and acceleration specified

interface and depends on the speed of the moving ring-shape lifter magnet on the micro-motorized stages. As the speed of the magnet increases, the phase difference also increases as a result of experiments. The fact that the phase differences are on the move does not cause a situation to hinder precise speed and position control. The microrobot follows the same trajectory as the lifter magnet on x and y-axes. After the motion is finished, the microrobot ends its movement in the concentric state with the lifter magnet.

The amount of delay due to the micro-stage speed is experimentally determined and shown in Figure 2.17. At higher velocities of about 1.4 mm/s, the phase difference is characterized by an exponentially increasing trend, and at lower speeds with linearized phase difference characterization, as expected. The phase difference falls below $150 \mu\text{m}$ as the same linear change is likely to continue even at low speeds of 0.5 mm/s. It indicates that non-delayed positioning can be performed by neglecting the phase difference at the nanometer range's speed requirements, which will be needed, especially in lab-on-a-chip applications.

2.5.4 Motion Capabilities of microrobot

The microrobot motion in an untethered manner is illustrated in the x axis for variable levitation height. In the second experiment which is conducted with the different

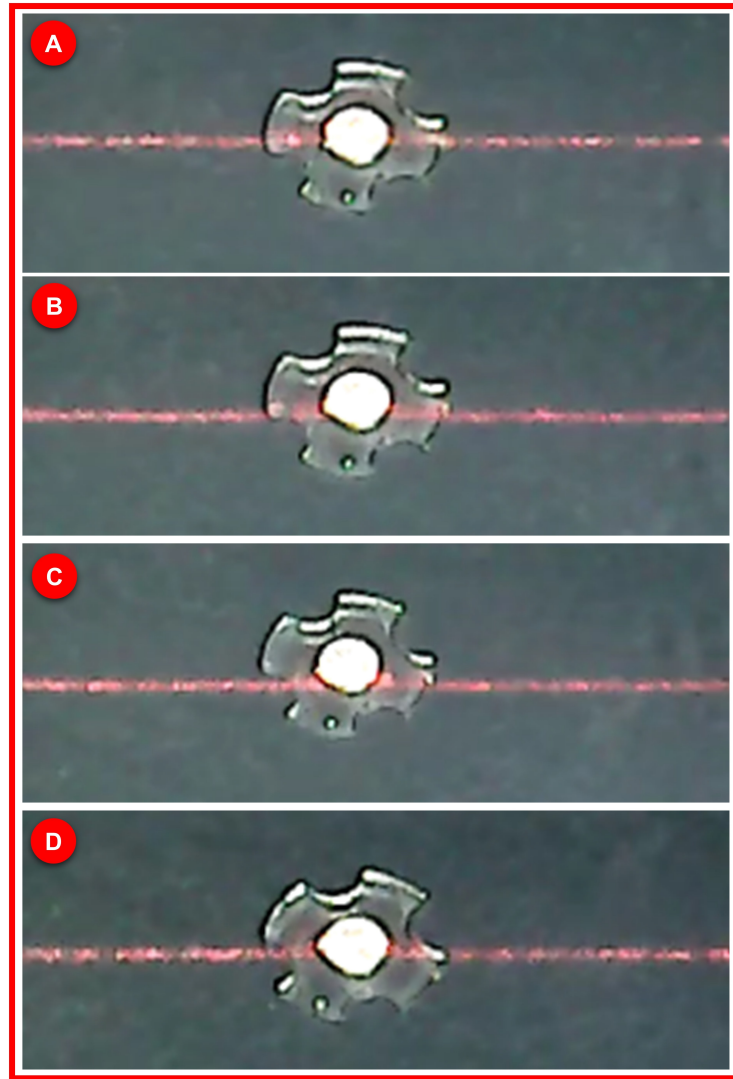


Figure 2.16 (A) shows the initial position of the microrobot, (B) first delay is occurred when the microrobot is moved, (C) maximum delay is occurred between the lifter magnet and microrobot's center, and (D) motion is completed and phase difference becomes zero. The red line belongs to the laser displacement sensor which is propagating from the lifter magnet's center due to its ring-shaped structure

motion characteristics such as sinusoidal and circular motion. To do this, the following trajectories are followed:

- sinusoidal motion with 4 mm amplitude,
- circular motion with 2 mm radius

These trajectories are successfully followed at a constant levitation height of $250 \mu\text{m}$. The experimental result with the actual trajectory is given in Figure 2.18. In this figure, (A) the maximum $7.91 \mu\text{m}$, and average $0.75 \mu\text{m}$ errors for sinusoidal motion are calculated for a high speed as 2 mm/s . In (B), the maximum $13.48 \mu\text{m}$ and average

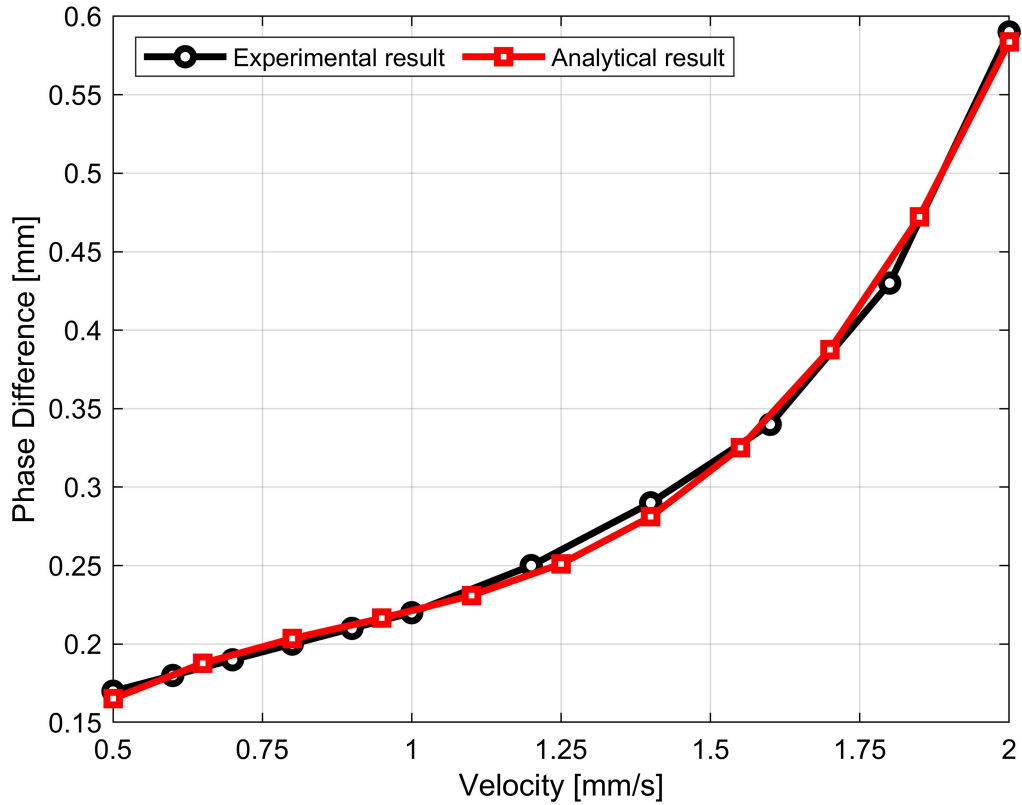


Figure 2.17 Shows comparison of the experimental and the analytical results for the phase difference. It can be observed that the microrobot phase difference can be analytically calculated which may help to adjust maximum microrobot speed

0.89 μm errors for circular motion are obtained at the same speed as (A). It can be observed that the maximum error level increases when the trajectory has a sudden turn and sharp movements. The reason is that the lifter magnet's magnetic field through to the microrobot is not linear or point-wise. Because of its effect on the microrobot as a volume, sharp turns are hard to follow. Significantly, the sinusoidal motion has two peak points: $\pi/2$, and the other one is $3\pi/2$. The circular motion has four different sharp points, which are $n\pi/2$ where $n = 1, 2, 3$, and 4 . Microrobot size should be reduced in order to experience fewer errors when following its trajectory. In this way, different trajectories can be followed more robustly and the ability to follow sharp edges and peaks is increased.

2.5.5 Head Bending Reaction

Because of the phase difference effects, microrobot can not be moved parallel to the pyrolytic graphite's surface. The reason is that magnetic field force lines between the lifter magnet and the carrier magnet should be the same. This is why microrobot makes non-parallel itself to follow the same magnetic field gradient. This problem is named "head-tilting." Since phase difference is increased by microrobot speed,

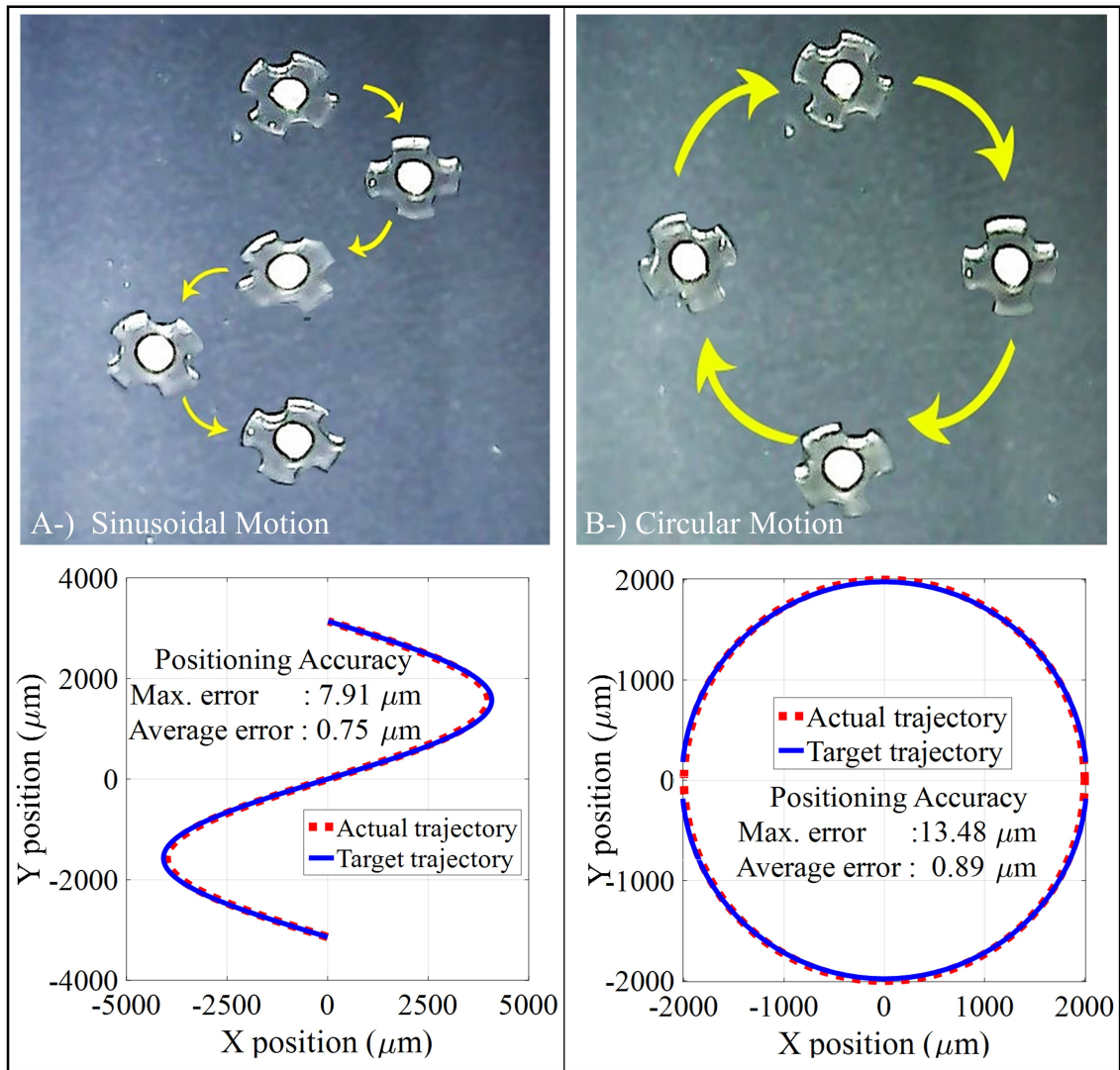


Figure 2.18 The sinusoidal and circular orbit trajectories have been successfully tracked. (A) shows the sinusoidal trajectory followed by the signal input given as amplitude 4 mm. In (B), a circular orbit with a radius of 2 mm was followed

head-tilting is also increased due to high phase difference, and this is shown in Figure 2.19. (A) shows microrobot starting position and (B) is the image during the movement as can be seen from the figure that microrobot can not achieve parallel movement and head-tilting angle is calculated as 7° .

The phase difference is a parameter controlled by the computer interface and depends on the moving ring-shape lifter magnet's speed on the micro stage. As the speed of progression increases, the phase difference increases as a result of experiments. The fact that the phase differences are on the move does not cause a situation to hinder precise speed and position control. The microrobot follows the same trajectory as the lifter magnet on x- and y-axes. After the motion is finished, the microrobot ends its movement in the concentric state with the lifter magnet. The amount of delay

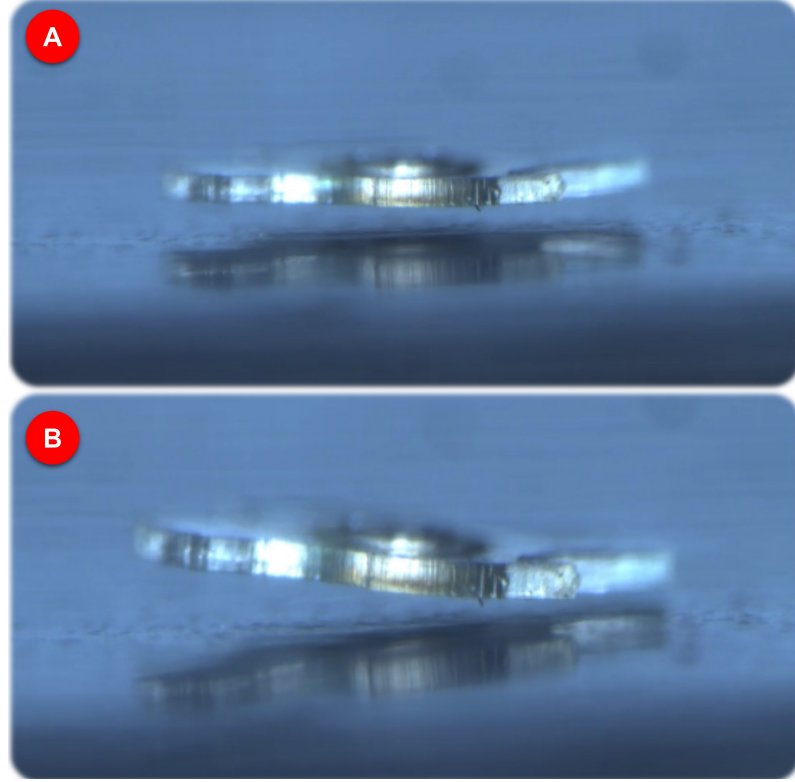


Figure 2.19 The cause of the head-tilt reaction is to suspend the directional changes of the vector field forces acting on the microrobot. The head-tilt angle is a parameter proportional to the phase difference. The increase in phase difference also causes an increase in the head-tilt angle. As shown in the figure, in the experimental studies performed, the head-tilt angle of 7° is monitored. The increase in head-tilting of the microrobot can be seen from (a) to (b)

due to the micro-stage speed is experimentally determined and shown in Figure 2.17. The amount of head tilting angle was also be analyzed for different orientation of the microrobot in the range of $\pm 10^\circ$, and it is seen in Figure 2.20. In this figure, (A) shows the orientation and misalignment of the resultant undesired torque, which can be prevented by the lifter magnet's angle. In this analysis, it can be seen that -1.96° negative rotation of the lifter magnet is required to obtain $0 \mu Nm$ torque on a y-axis when a 0.5 mm misalignment and 8° positive orientation is observed on the microrobot. Here, for example, when the microrobot performs an 8° positive angular orientation, unwanted torque can be observed. Besides, the orientation of the lifter magnet to avoid undesired torque is calculated. As a result of this analysis, the lifter magnet must be rotated opposite the microrobot direction. We aim to move microrobot in parallel with respect to the pyrolytic graphite's surface. Since microrobot has a symmetrical design, other torques generated on x and y axes must be equal, so the y-axis is preferred to be shown only.

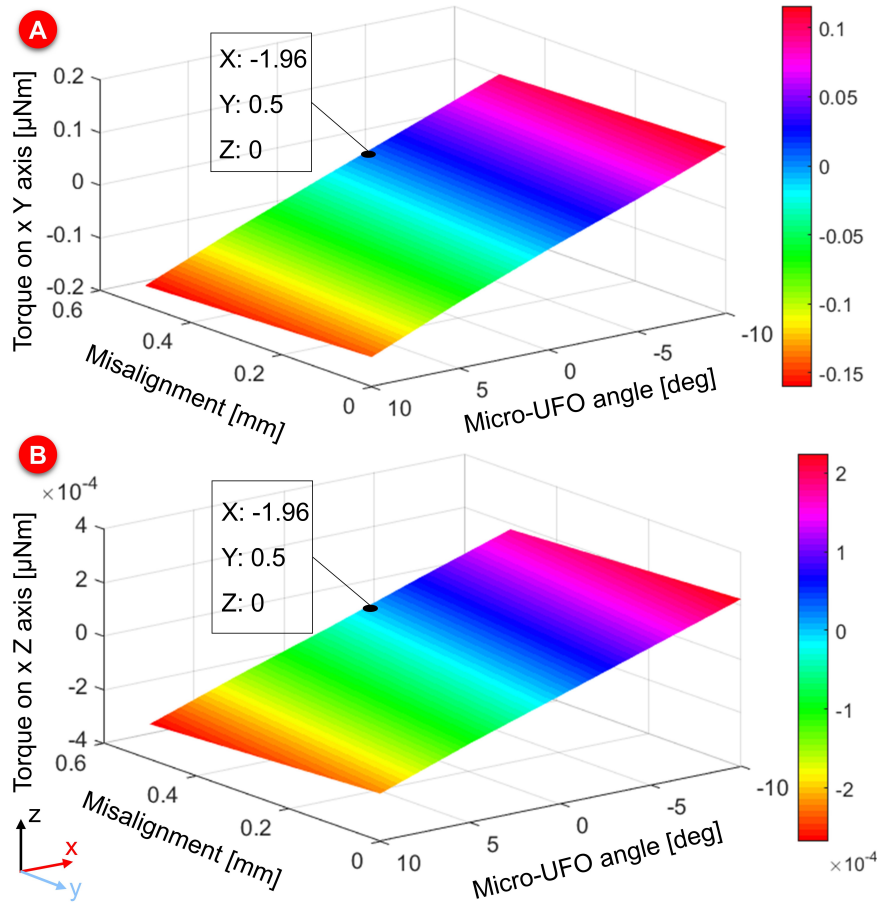


Figure 2.20 (A) refers to the orientation case with misalignment of microrobot as a surface graph with linear characteristic. (B) refers to the values of the lifter magnet angles to provide the prevention of undesired torque (0 approach), © 2021 Journal of Magnetics, with permission, from ref [107]

2.6 Discussion

2.6.1 General

In general, it is shown that the proposed microrobot levitation technique can be used in liquid media at higher velocities up to 10 mm/s. Since the drag force is changed proportional to the relative velocity between microrobot and fluid, head-tilting angle can be dangerous due to non-parallel motion to the pyrolytic graphite surface. Accordingly, microrobot can hit the surface during the longitudinal motion if its levitation height is low. For this reason, to show microrobot orientation stability and drive it at higher velocities with less head-tilting angle, further experiments, which are the combination of linear, interpolation, and complex reference tracking motions and control techniques, are needed.

2.6.2 Analytical Calculation and Simulation

In this study, optimum parameter values such as "mesh selection," "lifter magnet size," "pyrolytic graphite thickness" to be used in the COMSOL[®] analysis prepared to precisely levitate a microrobot have been determined. The different COMSOL[®] physics modules such as FSI and AC/DC can be reliably merged and run with proper mesh generation. Errors discovered after simulations can be eliminated successfully via proposed methodologies, formulations, and calculation techniques. In the COMSOL[®] analysis, it is seen that large differences and error values may occur in the results depending on the mesh selection. For this reason, the most accurate endorers are shared by experimenting with different mesh methods for each analysis. For example, in the COMSOL[®] FSI analysis, the min and max values of tetrahedral meshes should be close to each other. For this reason, "regular refinement level 2" and "corner refinement" have been applied, and especially stress values calculated in corner areas have been taken successfully. Therefore, on the resulting c_d graph, the "drag force coefficient" can be calculated by obtaining a smooth exponential graph.

In the MFNC, pyrolytic graphite thickness determination analysis, "mapping mesh" is applied to the upper surface and assigned to all components by the "swept" method. By applying "convert - insert center points" entirely to graphite, graphics with increasing characteristics according to their thickness have been obtained. Moreover, In the MFNC lifter magnet sizing analysis, the "free triangular" mesh structure was applied to the surface and then "swept" to the entire component. From the COMSOL[®] "distributions menu," symmetrical mesh structure is given to the component by adjusting the number of generated meshes based on the selected edge. Thus, the expected graphical characteristics were taken so that the experimental setup of the simulation was established. After successful analysis and simulation, it is shown that the proposed microrobot levitation technique, whose equipment is optimized, can be used. To show microrobot orientation stability and drive it at higher velocities, further experiments that combine linear, interpolation, and complex reference tracking motions, are needed. Optimized parameters and equipment are chosen in this work, can be used in the next step.

2.6.3 Levitation on z-Axis

It is possible to control the movement of x-y and z-axes within the microfluidic channel of the microrobot. Utilizing finite element analysis in COMSOL, the microrobot's levitation height limits were successfully determined and compared with the experimental results. The magnetic analysis showed that the microrobot showed linear surface behavior in the range of 90–280 μm according to the surface force graph

on z-axis direction. Experimentally, it was determined that the current microrobot levitation characteristic has an unstable structure in the range of 0 to 30 μm and 290 to 333.8 μm . In contrast, the system's stable working range is in the range of 30 to 290 μm . Accordingly, compared with the experimental results, the analysis results were within the experimental limits. If the analytical findings obtained are used on the system, it has been proved that a safe and linear behavior range can be studied.

2.6.4 Drag Force—Lifter Magnet Effects

The distance between the lifter magnet and the pyrolytic graphite is calculated numerically. Also, the range of levitation and its calculation steps are given in detail. Compared to the experimental results, it has been shown that the operating range of 54–58 mm is expected with the current experimental setup. Although the microrobot can be controlled beyond this range, it has been shown that the linear zone is the better working range. The experimental and the numerical analysis results show that the microrobot has more stable characteristics in the determined range. The drag force analysis result shows that the water's viscous effect is not much higher than microrobot. It is calculated that the maximum value of drag force is about 5% of the force required to levitate the robot. If micro-stages' operating speed range is set to $\pm 2(\text{mm/s})$, it is estimated that the drag force will be less than 0.75%. Thus, we can say that the drag force can be neglected, and the system can be linearized by neglecting the drag force effect. For future studies, a linear control technique can be potentially utilized in this application.

2.6.5 Center Alignment

Precise position control is also provided on the x- and y-axes of the microrobot in the experimental data direction. microrobot mobility has been tested in motion trajectories that may be encountered in different scenarios and work areas. The microrobot has successfully followed the sinusoidal and circular orbits, in addition to the linear motion. As can be seen in COMSOL[®] analysis, when 0.1 mm phase difference occurs between lifter-carrier magnets' center, it is calculated that forces generated in x- and y-axes are about $1/10^3$ of the force in the z-axis. Therefore, the predominant z-axis force cannot be affected by x- and y-axes forces dramatically, and levitation height does not change during the microrobot motion. Furthermore, it is always centralized with lifter magnet poles that provide stable trajectory tracking.

2.6.6 Phase Difference

According to levitation characteristics with the help of motorized micro-stage motions, the phase difference during the movements is seen as a factor that will force us to do real-time position control. On the other hand, for many biomedical applications, nanometric speeds are being used. In this case, the phase difference was found to be negligible as a result of our experimental studies. According to the analysis and experimental results regarding the phase difference, the torque and force values applied to the robot were not affected. The micro-stage is moving at a maximum speed of 2 mm/s. In this case, an offset of 0.6 mm is calculated and shown in Figure 2.17. It can be seen that the calculated phase difference is tiny ($1/66$) compared to the lifter magnet size. Thus, it is observed that there will be no effect on the magnetic force and torque produced. When the phase difference is high, the head-tilting reaction observed at high-speed levels is likewise observed to be negligible within the applications' operating speed requirements. However, the possibility of giving capillary damage to the head-tilt reaction's surface boundaries cannot be overlooked, especially in low run-up working conditions. In this regard, in future studies, closed-loop control-based studies will be carried out to prevent the head-tilt reaction.

3

STABLE UNTETHERED MICROROBOT MOTION BEHAVIOUR

In this section, an untethered microrobot's longitudinal motions are controlled based on the passive diamagnetic levitation technique in a fluidic environment. A cylindrical magnet (N48 grade neodymium) with $\varnothing 1\text{mm}$ and $250\mu\text{m}$ thickness, called the "carrier-magnet," is used at the center of a microrobot. It is also placed above on a pyrolytic graphite surface in a liquid medium. The reason is that magnetic field density can be increased over the carrier-magnet due to the pyrolytic graphite stabilizing feature. A ring-shaped magnet (N48 grade neodymium) with dimension of $\varnothing 40\text{mm} \times \varnothing 20\text{mm} \times \varnothing 8\text{mm}$, called the "lifter-magnet", is attached on a micro-stage and aligned with the microrobot in order to provide stable magnetic levitation. Compared to others, this setup is more compact and requires less energy to operate than actively controlled magnetic levitation systems. While the microrobot moves along the longitudinally, it cannot accelerate parallel to the ground. The head-tilting reaction starts and develops depending on the microrobot's longitudinal speed and increases exponentially in time. Furthermore, the drag force also increases exponentially as a function of the microrobot's speed, and its effect cannot be negligible. Before determining control parameters, the speed, mechanical delay between permanent magnets, and carrier-magnet orientation are modeled in COMSOL[®] (version 5.3, COMSOL Inc., Stockholm, Sweden). Afterward, control strategies are applied to minimize the drag force's effect to realize stable locomotion characteristics even at a much higher speed ($> 5\text{ mm/s}$). Experimental results show that the microrobot may successfully have followed a sinusoidal trajectory of $150\mu\text{m}$ amplitude and a 4mm period with an average error of $1.73\mu\text{m}$.

In this study, a 4 different controller models are compared by taking hydrodynamic effects on the microrobot. For the first time, the problem of head-tilting reaction is investigated and solutions are presented based on these three control models: the rule-based model, the laser model, and the hybrid model. The primary purpose of the developed control techniques is to minimize the drag force's effect on the microrobot,

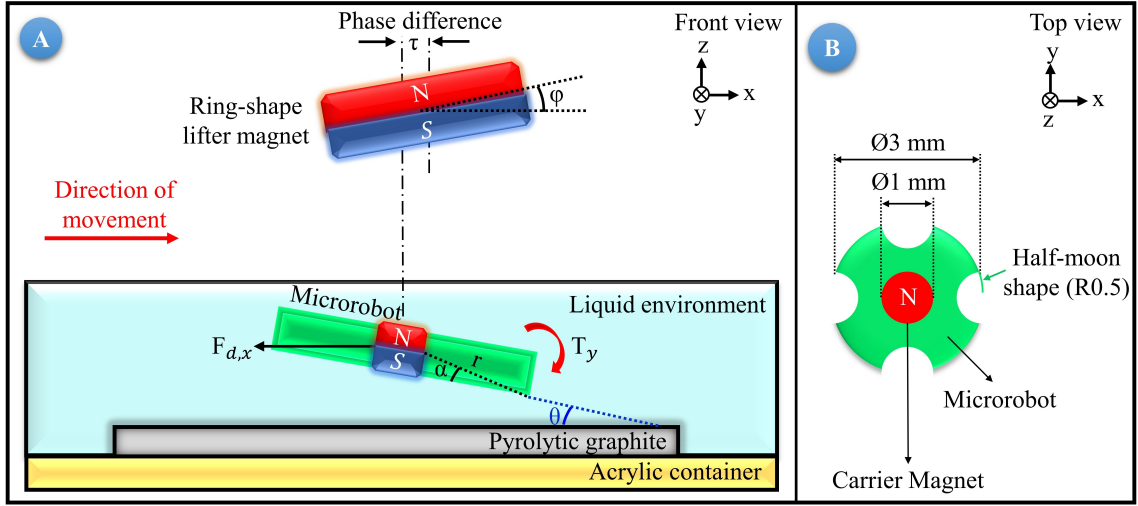


Figure 3.1 (A) The head-tilting reaction is introduced in the uncontrolled state of the microrobot moving in the X direction. (B) Microrobot whose dimensions are: $\varnothing 3\text{mm} \times \varnothing 1\text{ mm} \times \varnothing 0.2\text{mm}$, shown from top view

which moves inside a fluidic environment in an untethered manner. Thus, they can be utilized in any application that requires complex trajectory tracking and precise transportation of micro and nanostructures. The rule-based model uses a constant angle, which is calculated via the projected duration of motion and motion speed, as input parameters. The control input frequency changes between 15 (66.7 ms) Hz and 58 (17.2 ms) Hz for the laser model. On the other hand, the hybrid model takes advantage of those two previous strategies and combines them into a single model. In the experimental results section, these three models' reliability is verified, and the results are presented. All control techniques are compared to the uncontrolled head-tilting reaction.

3.1 Mathematical Model

Calculating the microrobot's minimum and maximum levitation heights, speed-phase difference of the stage, and head-tilting angle equations are presented. In experiments, we observe that the microrobot's longitudinal motion causes a head-tilting reaction; consequently, it is unable to move parallel to the surface. Two main reasons are concluded for this situation. These reasons are the "phase difference" between the center of the microrobot and the "carrier-magnet." Second, the drag force that acts on the robot due to its hydrodynamic structure. The phase difference occurs because the acceleration of the microrobot is lower than the carrier-magnet. This acceleration difference is caused by the air resistance acting only on the lifter-magnet, which is connected to the micro-stages during its movement. While air resistance is negligible, the drag force acting on the microrobot in the fluid cannot be omitted.

For this reason, while the lifter-magnet follows a step function as a motion profile with sharp edges, the microrobot has a parabolic motion profile with smoother edges [109]. Figure 3.1 shows the schematic diagram of the head-tilting reaction and phase difference for the microrobot moving in the x-axis. In this figure, pyrolytic graphite is placed on the surface of an acrylic container. The microrobot is located above the pyrolytic graphite in liquid media. For our model and further experiments, the liquid media is chosen as De-Ionized (DI) water. The pyrolytic graphite is a diamagnetic material with a magnetic permeability of $\mu_r=0.999992$. That is the reason it encloses the microrobot within the boundaries of magnetic field lines of the lifter-magnet. We can achieve more stable levitation characteristics inside the liquid [109, 110].

3.1.1 Head-Tilting Model

An undesired torque T_y in the y axis is exerted on the microrobot during microrobot longitudinal motion. It causes the microrobot to tilt in the direction of motion. Also, a phase difference, τ , is observed, caused by the reasons mentioned above. The lifter magnet's position is controlled in three-axes using micro stages, and its orientation is controlled in two axes by using two servo motors. The orientation angle of the lifter-magnet in the direction of motion is expressed by ϕ_y . The microrobot radius is shown by r and the angle between the corner point and the center by α . Also, the angle between the corner point and the pyrolytic graphite is denoted by θ . Lastly, the drag force acting on the x-axis direction movement is represented by $F_{d,x}$. As shown in Figure 3.1, the microrobot moving in the x-direction is not parallel to the surface during its motion due to the undesired torque T_y acting on it. For a microrobot, for which the moment of inertia is taken as $I=23.62 \text{ } (\mu gmm^2)$, a relation between the angular acceleration and undesired torque can be determined [107, 109, 111]. Accordingly, (3.1) will be used to calculate the angle value at which the lifter-magnet should be held in order to avoid the generation of undesired torque values as shown in Figure 3.2. In this figure, the x-axis represents phase difference, the y-axis is the lifter magnet orientation angle, and the z-axis shows undesired torque, which causes non-parallel motion. The phase difference is expected to be less than 0.6 mm; that is why it is preferably selected as the maximum in this axis. Lifter magnet angle range is -10° to 10° due to avoiding microrobot surface contact at higher orientation. The slope of the desired torque line is the torque, which can eliminate undesired torque by applying proper lifter magnet orientation.

$$\ddot{\theta} = \frac{T_y + (-F_{D,x} + F_{m,x} + F_{g,x})\sin(\theta)r}{I} \quad (3.1)$$

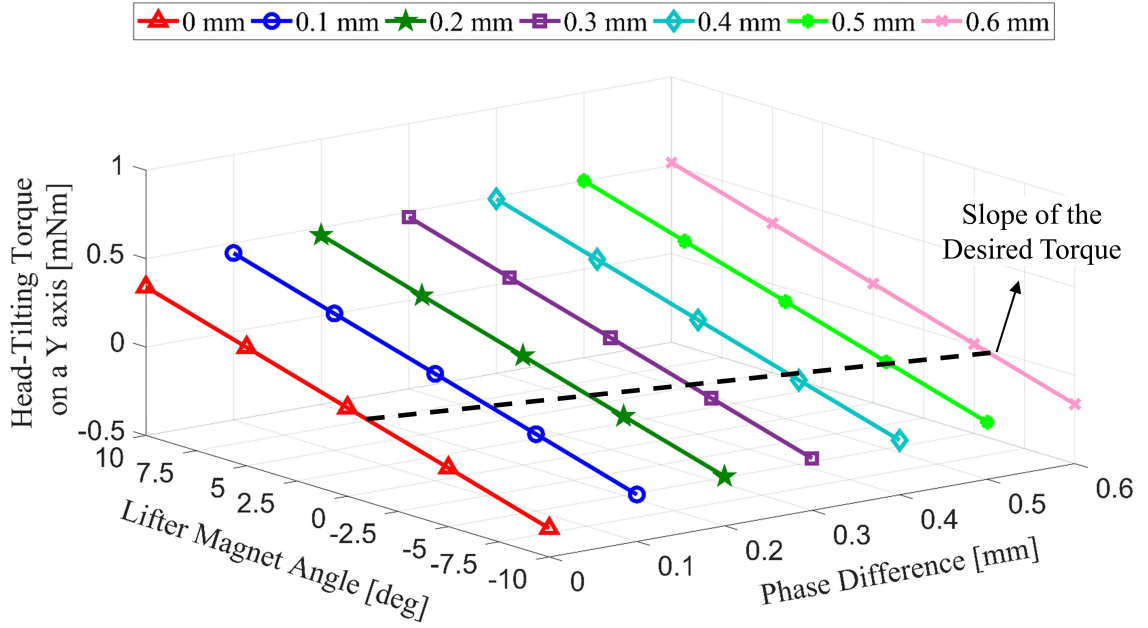


Figure 3.2 The angle calculation to be applied to the lifter-magnet is presented to eliminate undesired torque

The head-tilting angle, θ , increases with the motion speed, and it has some implications for robot levitation. Increasing head-tilting angles can cause the microrobot to hit the surface during its motion. In Figure 3.3, the head-tilting amount, Δ , can be calculated for a microrobot with $\alpha = 3.814^\circ$, $\theta = 10^\circ$, $h = 300 \mu m$, and $r = 1503.33 \mu m$,

$$\Delta = h - r \cos(\alpha) \sin(\theta) \quad (3.2)$$

where $\Delta = 39.528 \mu m$ is obtained for $h = 300 \mu m$, which is the instantaneous levitation height. According to this calculation, if the angle of diversion of the

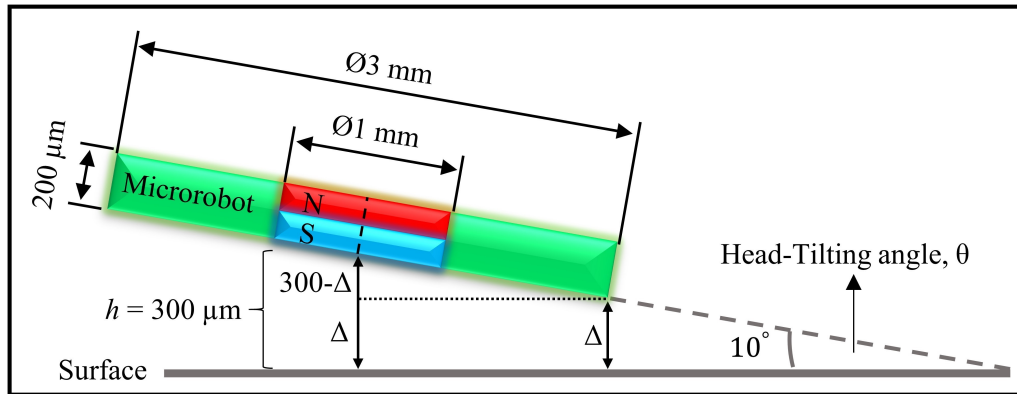
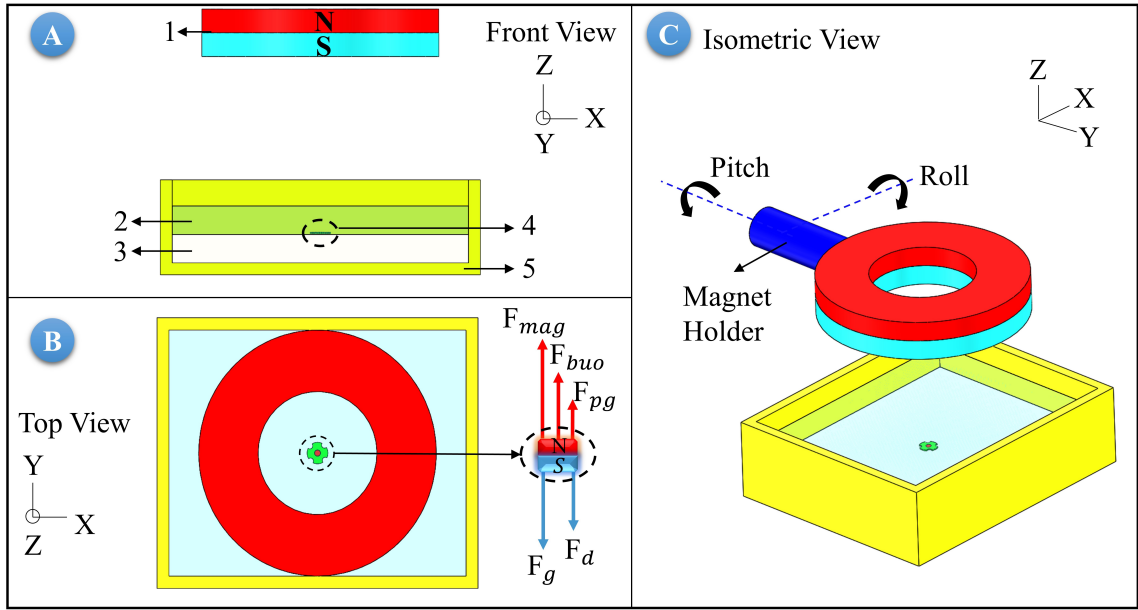


Figure 3.3 Illustration of levitation height determination in relation to the microrobot-head-tilting angle



1 : Lifter Magnet | 2 : DI – Water | 3 : Pyrolytic Graphite | 4 : Microrobot | 5 : Acrylic Container

Figure 3.4 Diagram of magnetic levitation system used in experiments. Numbers represent part names. (A) shows vertical alignment of microrobot and lifter-magnet; (B) shows forces exerted on microrobot, which is aligned with lifter-magnet; and (C) illustrates isometric view of the whole experimental setup

microrobot is 10° , and if the levitation height is lower than $260\mu m$, it is determined that the robot is likely to be hit the surface. If the instantaneous levitation height is lower than the required tolerance between the microrobot and the surface, the robot may hit the surface. For this reason, the operational working range of the microrobot should firstly be determined. To find these boundaries, a free-body diagram needs to be generated, and each force acting on the robot needs to be calculated.

The forces acting on the microrobot should be determined in order to obtain free-body of the microrobot levitation system. To do that, the levitation system of the microrobot is given in Figure 3.4. In (A), it shows the front view of the system with the equipment used. In (B), the system's top view and the forces acting on the robot are shown. Moreover, forces acting on the microrobot is illustrated as follows:

- the magnetic force of the lifter-magnet F_{mag} ,
- the buoyant force due to liquid media as F_{buo} ,
- the diamagnetic force induced by the pyrolytic graphite, which is located on the surface of the acrylic container (shown in Figure 3.1-A and Figure 3.4-A), as F_{pg} ,
- the gravitational force as F_g ; and the drag force as F_d .

In (C), the isometric view of the lifter-magnet and the test setup is shown. The second-order mathematical representation of this model is expressed in 3.3–3.5, in which the robot mass is m_r [107, 109, 111]. The forces exerted on the microrobot are shown in Figure 3.4-B. For a robot with a mass of $2.92 \mu g$, robot acceleration can be determined for known values of lifting force ($12.788 \mu N$), speed-dependent friction force [107], and gravitational force ($28.741 \mu N$). The relationship between phase difference and the microrobot acceleration has been investigated in a previous study [109].

$$\ddot{x} = F_{d,x} + \frac{(F_{mag,x} + F_{pg,x})}{m_r} \quad (3.3)$$

$$\ddot{y} = F_{d,y} + \frac{(F_{mag,y} + F_{pg,y})}{m_r} \quad (3.4)$$

$$\ddot{z} = F_{d,z} + F_{buo,z} - F_{g,z} + \frac{(F_{mag,z} + F_{pg,z})}{m_r} \quad (3.5)$$

It is calculated that the net magnetic force should be $16.74 \mu N$ in order to levitate the microrobot [107, 109, 111] in accordance with the mathematical model. Applying this net magnetic force on the microrobot causes it to levitate in the fluidic environment. It is necessary to calculate the robot and lifter-magnet accelerations so that the approximate values for phase difference can be found during the robot's longitudinal motion. The experiments aimed to control microrobot motion in high accuracy to complete a predetermined trajectory in a repeatable manner at the desired speed. Also, how fast this task can be accomplished is another important criterion. Since the lifter-magnet speed profile is determined (step function), the acceleration value can also be found. However, the acceleration of the microrobot depends on the speed of the lifter-magnet. The lifter-magnet is capable of completing a trajectory of 5 mm in 1 sec with a speed of 5 mm/s. However, it requires more time for the microrobot to reach a speed of 5 mm/s due to the drag force. It has been shown that the value of $F_{d,x}$ is $0.125 \mu N$ for 5 mm/s speed [107]. For a microrobot with a constant mass, it has been stated that the speed profile, and thus the acceleration, maybe of parabolic increasing-decreasing characteristic against the variable drag force [109]. The value of the microrobot acceleration can be determined according to (3.6).

$$F_{mag,x} - F_{d,x} = m_r a_r \quad (3.6)$$

For the microrobot whose acceleration is determined, instantaneous speed values can be found by assuming it has an acceleration characteristic. Using the microrobot speed, V_r , (3.7) can be used to calculate the time required to reach a speed of 5 mm/s.

$$v_r = v_0 + \int_0^t a dt \quad (3.7)$$

The drag force, which is equal to about 1/134 of the net magnetic force [110], causes the microrobot to have a delay of 103.1 ms in total because the starting values are 7.46 ms and 5 mm/s. As a result, according to the speed value, it is expected that the robot will move with $\tau = 515.5 \mu m$. Besides, a linear expression can be obtained from previous works done with the phase difference, and approximate phase difference expression can be related to the speed by (3.8) [107, 109].

$$\tau = 0.134v_r - 0.146 \quad (3.8)$$

3.2 FEM Simulation

In section 3.1, it is shown that the microrobot head can hit the surface if the levitation height is not sufficient. Also, the definitions for head-tilting and phase difference are described in detail. Besides, a method for determining the acceleration of the microrobot in order to find the phase difference is given. In this section, the simulation studies are conducted to develop a method for improving the head-tilting action that acts during the microrobot's longitudinal movements.

3.2.1 Orientation Effect of the Magnets

Using the simulation results, we obtain the following microrobot control parameters via orientation equations, the operation limits, and the expression for surface impact condition. In addition to them, a first-order linear equation for the phase difference is calculated. The aim is to perform the robot motion parallel to the surface, as shown in Figure 3.4-C. In the analyses made on the COMSOL[®] AC/DC module, the orientation that must be applied on the lifter-magnet should firstly be determined. Figure 3.5 shows that the magnetic field force lines that pass through the lifter-magnet and microrobot surface are shown when they are parallel to the surface. (A) shows microrobot right movement with carrier magnet positive orientation. According to the vectors, carrier-magnet magnetic field can be perpendicular to the ground when the lifter magnet has an opposite orientation. A similar effect can also be seen in

Orientation scheme for Microrobot parallel movement

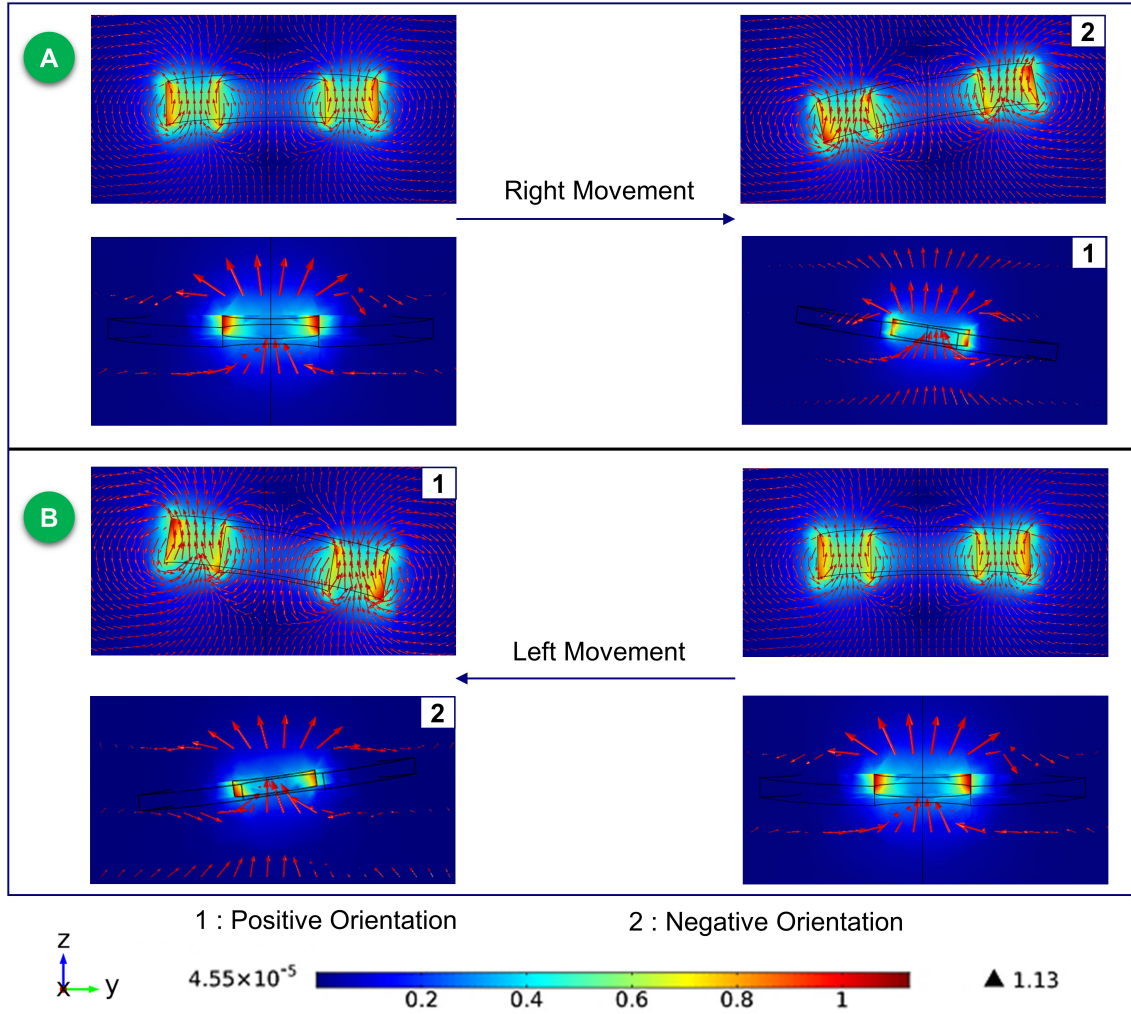


Figure 3.5 The orientation of the carrier-magnet in order to avoid head-tilting reaction is presented. Accordingly, the carrier-magnet must have a direction opposite to the motion direction of the microrobot, is observed

(B), which illustrates the microrobot's left movement. It has a negative orientation that can be stabilized with the positive orientation of the lifter magnet. Orientations are also denoted where the angular images' right corners as 1, positive orientation and 2, negative orientation. Lastly, magnetic flux detail is given with the horizontally positioned bottom legend.

It is observed from Figure 3.5 that the magnetic field lines on the robot with levitation on the z-axis are perpendicular to the robot. A parametric analysis on the tilting angle of the microrobot is performed in order to determine the direction of the force applied during right and left movements. As a result of the analysis, it is found that the robot and the lifter-magnet must have opposite orientations. In this case, the active force lines on the robot are observed to remain perpendicular to its surface. So, the microrobot linear motions with higher speed can be achieved more parallel than

uncontrolled case (without any lifter-magnet orientation).

3.2.2 Environmental Effects on Microrobot

Reynolds number is affected by operational speeds, fluid properties, and size. Microrobot and fluidic chip size are also important to determine the characteristic length of the entrance. It determines the flow profile steady and transient conditions. Flow profile becomes parabolic when the hydrodynamic entrance length is ended. There is a velocity condition which is zero near the walls and maximum in the center after the characteristic length. Because of the microrobots have a small characteristic length, L , and a small characteristic velocity V_s . It leads to a small Reynolds (Re) number (3.9) and Stokes flow (3.10) [110].

$$Re = \frac{\rho_f V_s L}{\mu} \ll 1 \quad (3.9)$$

At low Re, the Navier-Stokes Equation becomes time-independent [112],

$$\rho \left(\frac{\partial \mathbf{v}}{\partial t} + (\mathbf{v} \cdot \nabla) \mathbf{v} \right) = -\nabla p + \mu \nabla^2 \mathbf{v} \quad (3.10)$$

in which \mathbf{v} is the velocity vector field, and p is the hydrodynamic pressure scalar field. A low Re number can be due to a slower motion, a small working environment, or high viscosity [40]. Navier can be omitted since $Re \ll 1$ [113] and inertial terms of fluid become negligible, while viscous force and surface tension are more dominant at the small length scale. In the studies with a low Re regime, it can be seen that dimensional effects can be neglected, and locomotion of a microrobot can be achieved by vibrating it. Depending on the vibration frequency, the p-value is changed, and motion under low Re can be obtained [40, 110, 112, 113]. In our work, the microrobot velocity determines the flow characteristic since DI-water remains stationary in the container. Thus, the motion characteristics of the microrobot in a low Re flow regime is investigated depending on its scale and with a head-tilting angle, which varies between $0^\circ - 10^\circ$ (Figure 3.6). Creeping Flow Physics in COMSOL[®] is used for three different sizes of microrobot (1 mm, 2 mm, and 3 mm). In this case, when the experimental conditions are kept constant, the Reynolds number's change depends on the speed of the robot, not its size and head-tilting angle. Also, for microrobots of different sizes with the same flow characteristics, the drag force does not change in the movements parallel to the surface [107, 109, 111]. However, the drag force can change proportionally with microrobot cross-sectional area for the

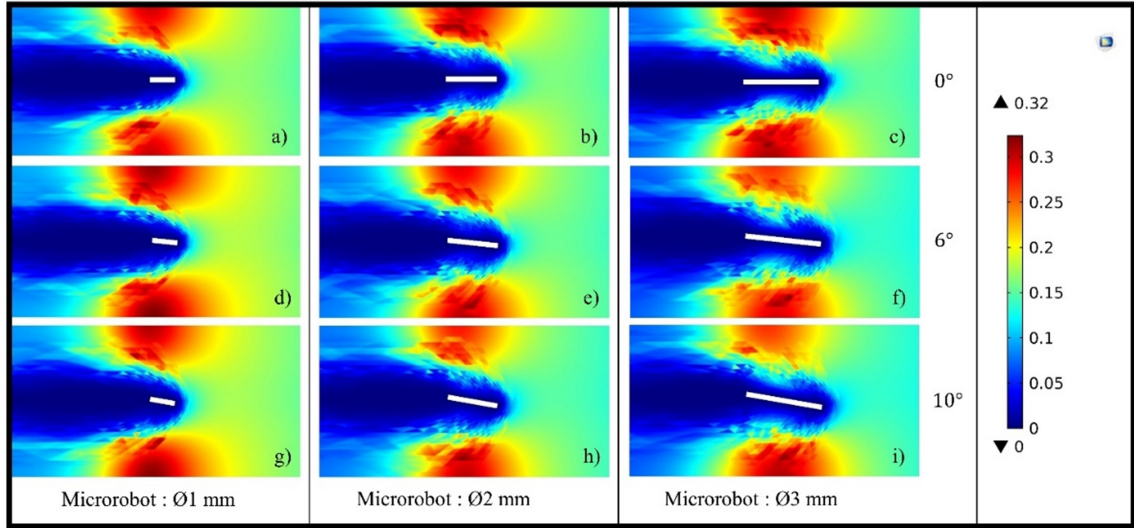


Figure 3.6 Calculation of Re number is simulated at different head-tilting angles for microrobots with same thickness ($250\mu\text{m}$) and different sizes (1 mm, 2 mm, and 3 mm). COMSOL[®] Creeping Flow analysis is utilized in stationary liquid media. The legend on the right side, as expected, shows that the $Re \ll 1$ is not dependent on size and head-tilting angle

identical experimental conditions. This condition is valid when the same speed and head-tilting angle are the same with different sizes. From (3.1), the torque value that should be applied to the microrobot can also be calculated.

3.2.3 Microrobot Working Range

After the lifter-magnet orientation problem is solved, it is also essential to determine the microrobot's operation limits. As indicated in Section 3.1, the robot has a risk of surface collision, depending on its levitation height and speed. There is a risk of the microrobot surfacing in an uncontrolled manner due to proximity to the lifter-magnet. These situations can be addressed by setting a lower and an upper limit to the levitation height. Figure 3.7 represents a graph for the net magnetic force exerted on the microrobot. In this figure, the y-axis shows the distance between microrobot and lifter-magnet at different levitation heights. The levitation height is shown x-axis, which ranges from $0\mu\text{m}$ to $350\mu\text{m}$. The reason is that the maximum microrobot levitation height is found as lower than $350\mu\text{m}$ in the previous studies. According to the net magnetic force value of $16.74\mu\text{N}$ [107, 109, 111], the microrobot is observed to be at the maximum levitation height of $329.1\mu\text{m}$. The lifter-magnet is at a distance of 54 mm (marked with a blue dot) from the pyrolytic graphite.

On the other hand, the microrobot is at the minimum $31.0\mu\text{m}$ levitation height when the lifter-magnet is located at 60 mm height (marked with a red dot). It can be seen that the microrobot can be controlled within this distance, which is also found in FEM

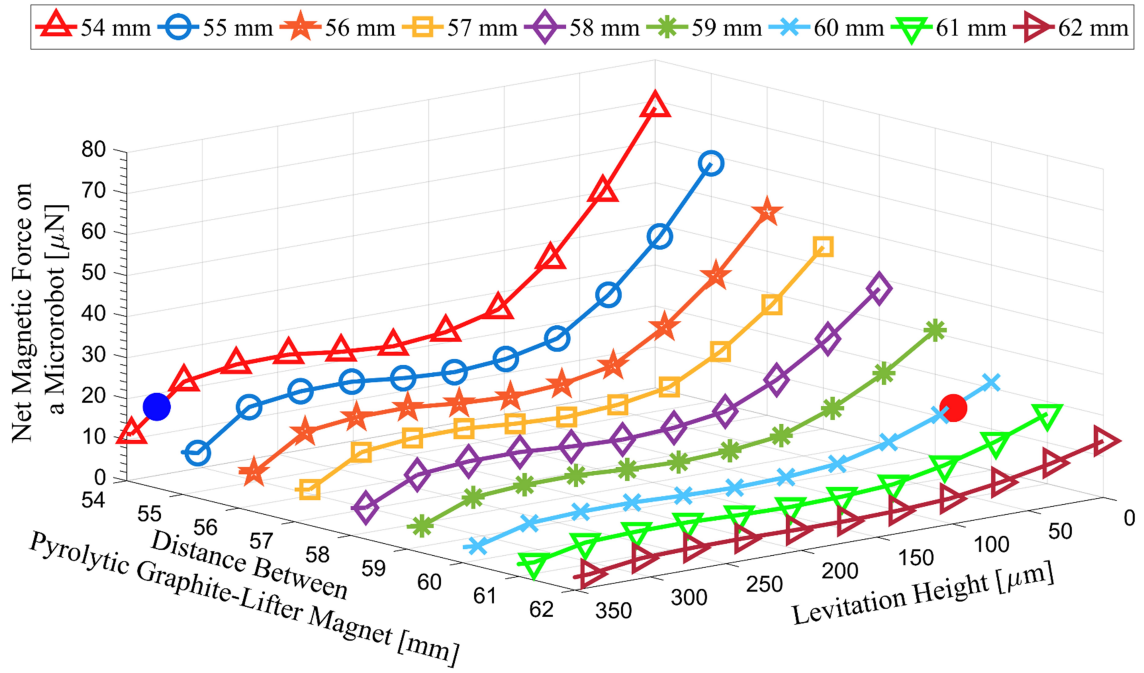


Figure 3.7 Microrobot study limits are determined. Accordingly, the minimum and maximum points are shown in the range of 31.0 μm (red)–329.1 μm (blue)

analysis. The lifter magnet is getting closer to the pyrolytic graphite, magnetic force non-linearity increases. It is a challenging task to control microrobot efficiently beyond this range. Moreover, when the distance is higher than 60 mm, the net magnetic force cannot levitate to the microrobot. Distance effects can also be observed in the levitation height. The magnetic force exhibits an exponential characteristic; the linear region of 100–300 μm is chosen as the operating limits. In particular, this region is affected less by the nonlinear magnitudes for experimental speed ranges.

3.2.4 Lifter Magnet Orientation Control

After determining operation limits, the head-tilting reaction after specific time intervals is examined, and results are presented. By the time the microrobot reaches the desired speed with a specific delay parameter due to a lower acceleration, the tilting angle is also found to be dependent on this parameter. Figure 3.8-A shows the top view of the system and the lifter-magnet orientation. Figure 3.8-B shows a depiction of the microrobot that is starting to move by tilting its head gradually in the x-direction at t_1 until it reaches the desired speed at t_4 . At t_4 , the microrobot is depicted as hitting the surface due to its higher speed. Moreover, the simulation data presented in Figure 3.8-C shows that the lifter-magnet is given an opposite orientation relative to microrobot. It is observed that the head-tilting angle of the microrobot is reduced, starting from time t_2 . At the time t_4 , instantaneous speeds are equal, and the motion characteristic is depicted as being parallel to the surface.

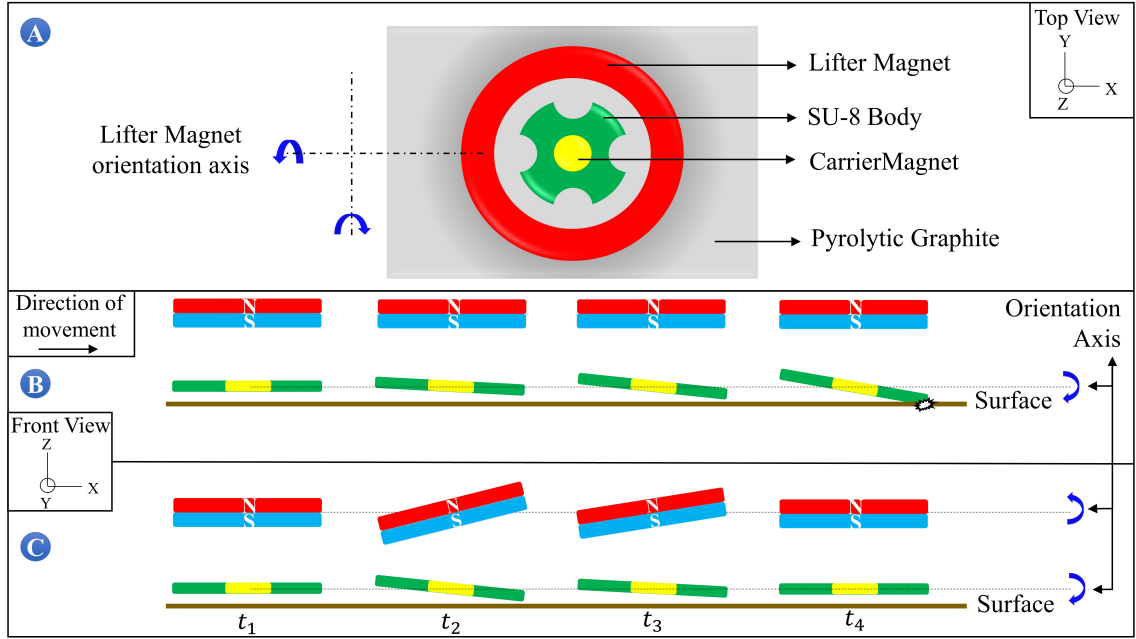


Figure 3.8 (A) shows roll, and pitch axes control the orientation of the microrobot to eliminate head-tilting reaction. The result of the uncontrolled microrobot motion is given in (B). The head-tilting reaction can be eliminated by adjusting carrier-magnet orientation (C)

For all cases mentioned in the mathematical model section, the finite element method (FEM) studies are conducted, and their results are given in this section. After determining these results, we need to derive the equations necessary for the rule-based model design. To this end, various tilting angle values of microrobot are studied in COMSOL[®] by parametric analysis. Different phase difference values are presented relative to the x-axis with the upper legend in Figure 3.8, while different microrobot angles are given on the y-axis. On the z-axis, undesired torque values for different phase differences and carrier-magnet angles are shown. In this graph, a black dashed line shows the values where the torque equals zero. This line shows the angle that must be applied to the lifter-magnet in order to overcome the undesired torque. (3.11) and (3.12) are derived using the dashed line shown in Figure 3.8. These equations are related to the micro-stage's speed and its tilting angle to be applied to the rule-based model and the laser model, respectively.

$$\theta = 1.323v - 0.529 \quad (3.11)$$

$$\theta = 1.8761\phi + 0.541 \quad (3.12)$$

The head-tilting angle can be improved by using these equations with a specific time

delay depending on the speed. It is also presented with the results in the experimental study section.

3.3 Experimental Results

In this section, the experimental studies are presented in accordance with the simulation results, which are grounded on the mathematical models obtained in Section 3.1. In the light of simulations and mathematical models, the lower and upper limits of magnetic levitation are determined, and the control algorithms are created. Afterwards, microrobot is tested for different scenarios such as following a complex sinusoidal trajectory and longitudinal motion control at a constant levitation height, and results are then compared.

3.3.1 Experimental Setup

Based on the derived mathematical model and conducted simulations, it is found that the microrobot can be levitated in the range of 31.0–329.1 μm , and the undesired torque on the robot can be overcome when the orientation of the lifter-magnet is opposite to that of microrobot in the direction of motion. Also, the approximate linear equation of the phase difference is given as a function of the horizontal speed of the microrobot in (3.8). In this section, the theoretical and simulation results are compared with the experimental results, and the experiments for each control algorithms are explained. Pyrolytic graphite is placed on the surface of an acrylic container filled with deionized water (DI-water). The lifter-magnet is placed on top of the microrobot, which consists of an N48 neodymium magnet and an SU-8 frame. The component that connects the carrier-magnet to the micro-stage is printed in a 3D printer. This component is designed to enable controlling of the orientation of the microrobot using two servo motors (Figure 3.9-A). An optical microscope (Olympus SZX-7, Olympus Corporation, Tokyo, Japan and PointGrey GS3-U3, FLIR Integrated Imaging Solutions Inc., Richmond, BC, Canada) is used for imaging the experiment (Figure 3.9-B). On the z axis, the head-tilting angle and levitation height are measured by a sub-micrometer-resolution laser sensor (optoNCDT-ILD2300-50, Micro-Epsilon, Raleigh, NC, USA).

With the experimental setup shown in Figure 3.9, it is possible to control the microrobot with 5 degrees of freedom (5 DOF). In all systems in which a microrobot is intended to be levitated in a fluidic environment using a lifter-magnet, it is inevitable for a phase difference to occur due to the hydrodynamic structure of the system. For this reason, the first control problem we worked on is orienting the lifter-magnet at

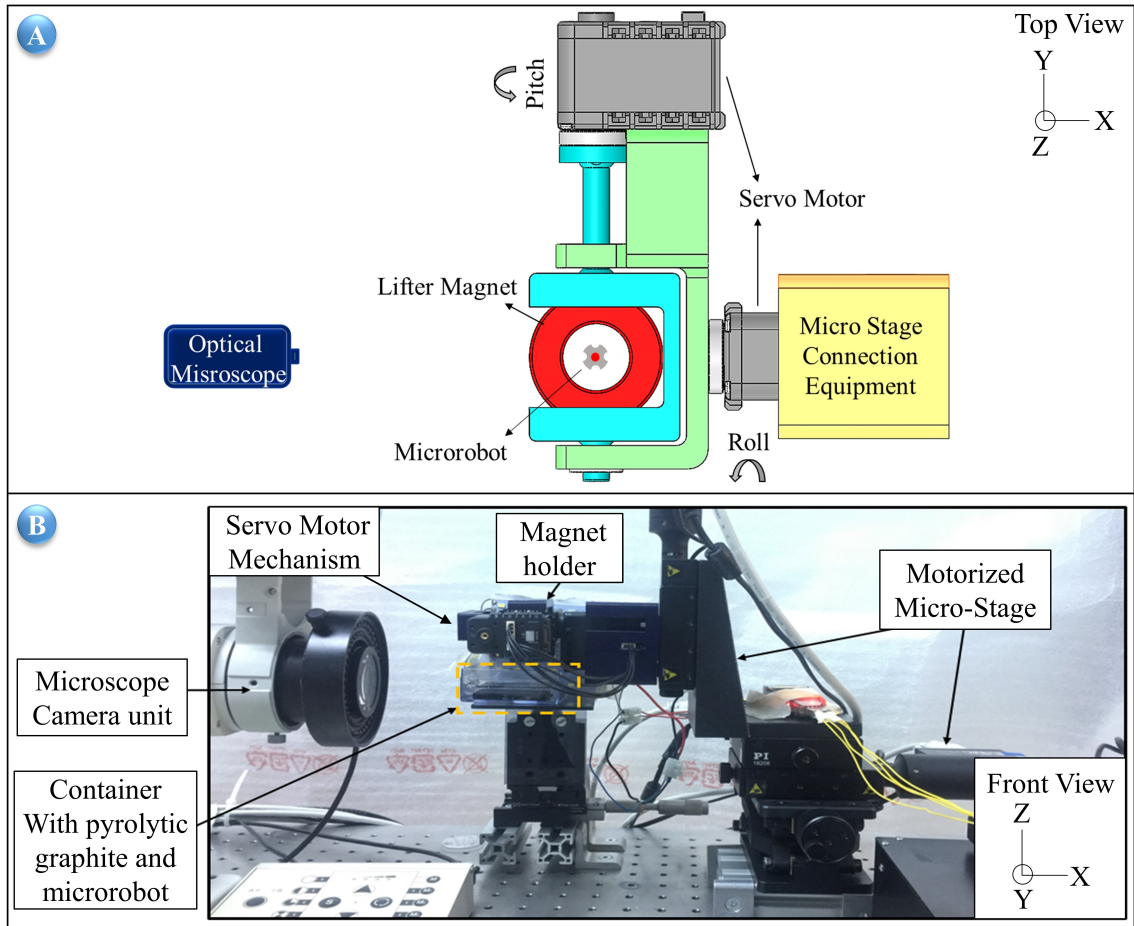


Figure 3.9 (A) Illustrates the experimental system with 2 servo motors, micro-stage connection apparatus, and lifter-magnet microrobot alignment. In (B) the full testing and measurement systems are shown

the optimal angle depending on the horizontal speed of the microrobot such that it will move parallel to the surface (Figure 3.10-A).

The inputs of the control system are determined as micro-stage speed (mm/s) and length of trajectory (mm). The motion completion time, t_y , can be calculated easily for a given trajectory using its length and microrobot speed. However, orientation control of the lifter-magnet should not be applied until the microrobot reaches a desired speed so that an undesired torque is not induced on the microrobot. This requirement is explained in a previous study in detail [109]. For this reason, orientation control of the lifter-magnet is applied after a certain time delay, t_g , when the microrobot reaches the desired speed. Before the trajectory is completed, the lifter-magnet should return to the parallel position by reducing the angle as shown in time periods t_3 , t_4 in Figure 3.8B. This ensures that the robot will remain parallel to the surface at the start and at the end. By controlling the lifter-magnet angle according to (3.11), during the time period t_u as shown in Figure 3.10, head-tilting angle of the microrobot can be reduced. The second control problem we work on is reducing the head-tilting

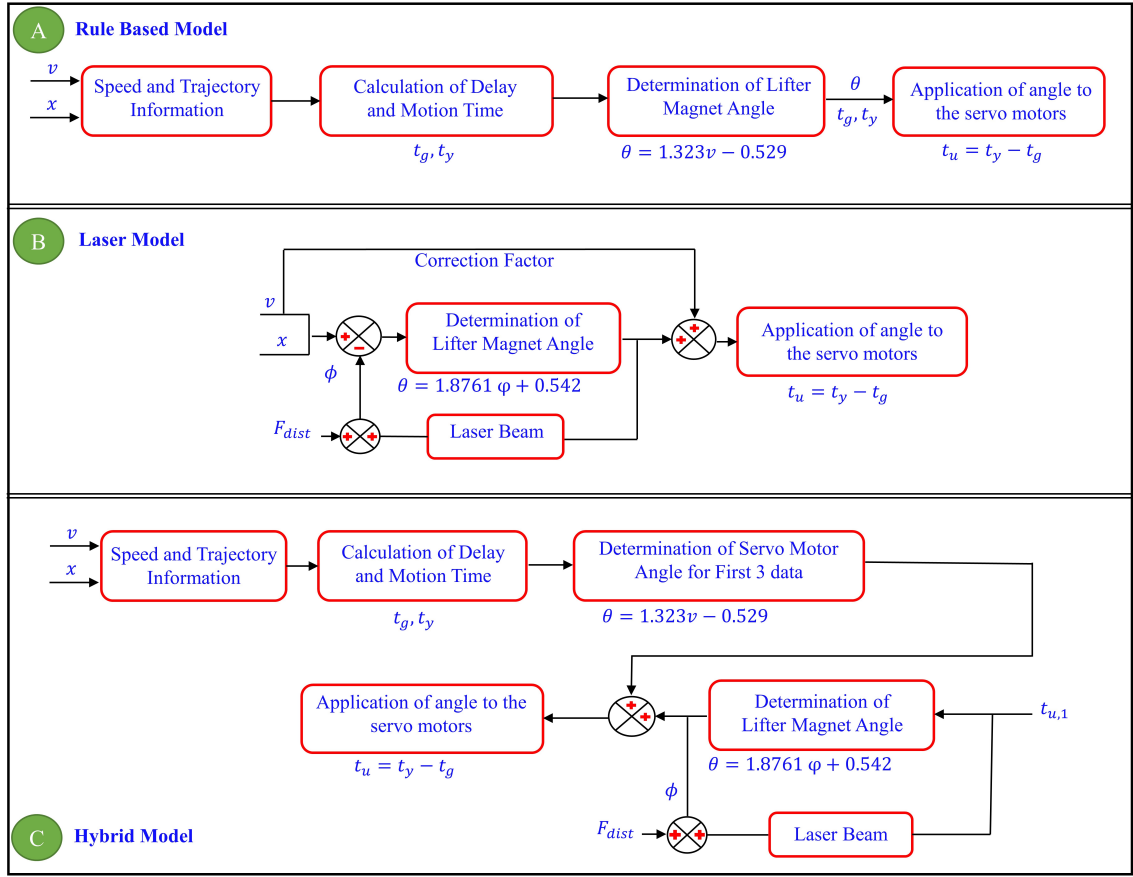


Figure 3.10 (A) Shows the rule-based model (open-loop), (B) shows the laser model (closed-loop), and (C) shows the hybrid model control block diagrams

angle using a closed loop control algorithm (Figure 3.10-B). This time, the head-tilting angle of the microrobot is measured with a laser sensor and (3.12) is applied. A feed-forward approach is also added to improve the transient response, in accordance with the horizontal speed of the microrobot. The hybrid model is used in the last controller structure. In this model, development of a better control structure is aimed for, which could achieve lower tilting rates and a more stable motion by combining the advantages of the rule-based model and the laser model shown in Figure 3.10-A and B. Initially, the rule-based model shown in Figure 3.10-A is applied in order to improve the transient response. Then, the laser model shown in Figure 3.10-B is used in order to eliminate the steady-state error. The $t_{u,1}$ value shown in Figure 3.10-C represents the elapsed time after the first three angle commands are applied.

It is possible to obtain displacement measurements at the sub-micron level using the OptoNCDT-ILD2300-50 laser sensor. However, it needs to be calibrated first in order for it to be able to measure the head-tilting angle and the levitation height inside the fluidic container, because the laser beam emitted from the laser sensor will exhibit different characteristics inside the fluid and in the air. If the laser beam does not enter into the fluid in a perfectly perpendicular manner, it will diffract, and the accuracy of

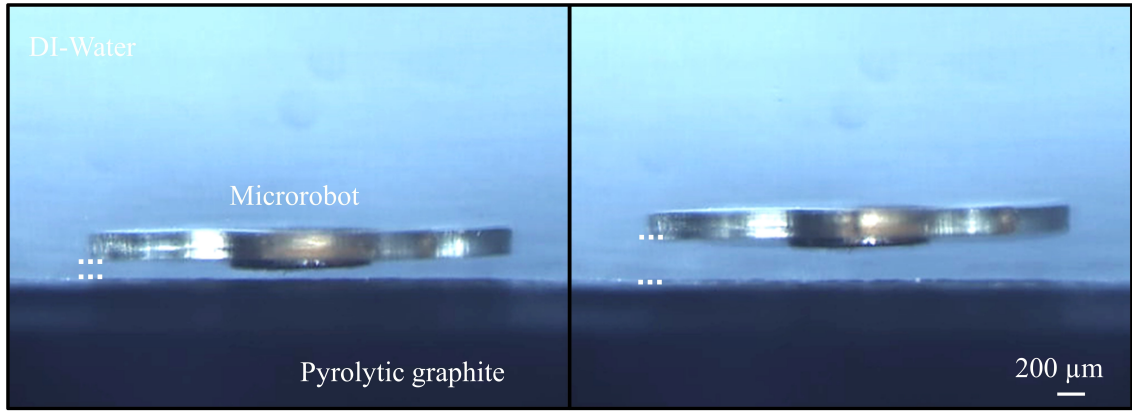


Figure 3.11 The left picture shows minimum levitation height of the microrobot ($30.0\mu m$) and maximum levitation height ($333.8\mu m$) on the right picture

measurements will lower. For this reason, blocks with different sizes, manufactured in accordance with the DIN EN ISO 3650 standard, are used to calibrate the laser sensor. Different blocks that have different increasing heights of $1\mu m$, $10\mu m$, and $100\mu m$, starting from 0.5 mm , are used. The error rates obtained from the measurement of these blocks are later incorporated into the control structure as F_{dist} (Figure 3.10-B and C).

3.3.2 Robot Levitation

Robot levitation is preferred, especially for applications in which very high precision (nano-level) is required. The operation range of the microrobot is affected by various parameters such as the density of the media, temperature and so on. According to the simulations and analytical calculations made, the operating limits of the microrobot are found to be minimum $31.0\mu m$ (by analysis)– $30.0\mu m$ (by experiments) and maximum $329.1\mu m$ (by analysis)– $333.8\mu m$ (by experiments) [107, 109, 111]. The minimum and maximum operation points are also determined in Figure 3.11. The difference in analysis and experiments is caused by the homogeneity of the neodymium magnets used, and the uncertainty in the magnetic flux densities within the given range.

3.3.3 Robot Orientation Capabilities

Orientation of the microrobot is controlled by changing the orientation of the lifter-magnet using the 2 attached servo motors (Figure 3.12). Its longitudinal movements and control are enabled through the positioning of the lifter-magnet. Angular motions, such as rolls and pitches, are also taken into account to control the orientation of the lifter-magnet with high precision. The greatest advantage of

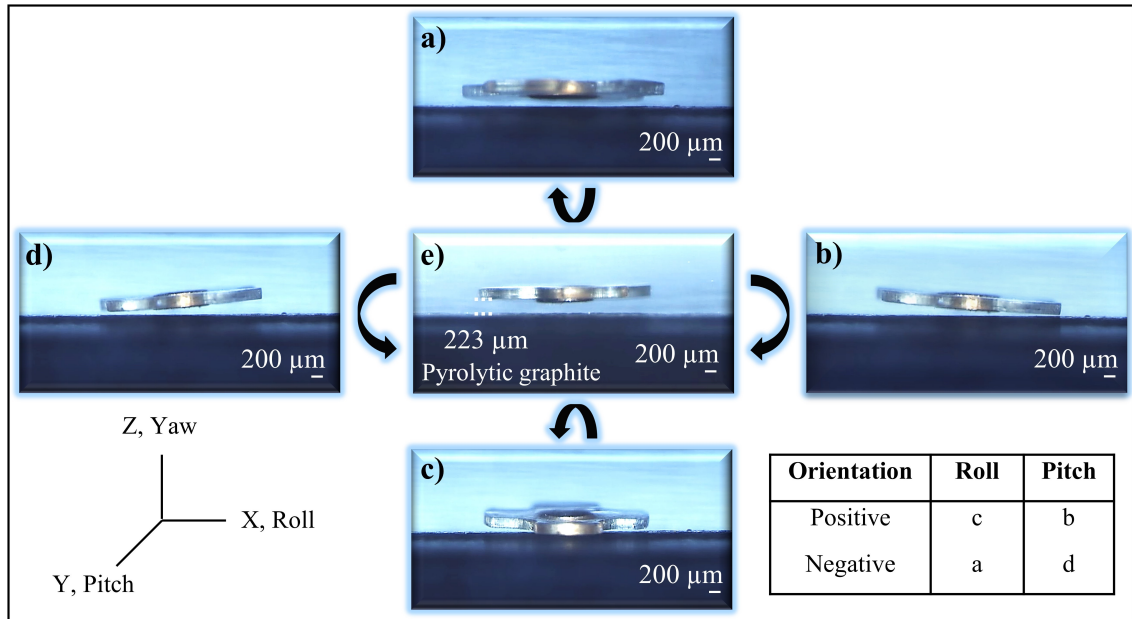


Figure 3.12 Axial orientations of the robot are shown. (e) is the initial position at $223 \mu\text{m}$ levitation height, (a,c) shows negative and positive roll angle respectively, and (b,d) shows positive and negative pitch angle, respectively

high-precision orientation ability is that the robot can avoid the increase in head-tilting reaction that occurs due to the drag forces during its longitudinal motion. Figure 3.12-A presents the negative roll, Figure 3.12-B the positive pitch, Figure 3.12-C the positive roll, and Figure 3.12-D the negative pitch orientations. Correspondingly, Figure 3.12-E indicates the stable positioning of the microrobot at certain levitation height ($223 \mu\text{m}$) parallel to the surface.

After successfully performing magnetic levitation and 2-axis orientation control of the microrobot, the sine-wave-shaped trajectory is followed to demonstrate the motion capabilities of the microrobot. For the first time, a motion profile with a variable levitation height is applied, and the results are given in Figure 3.13. With an initial levitation height of $200 \mu\text{m}$, the robot is able to follow a trajectory of 4 mm horizontal length and $150 \mu\text{m}$ amplitude at a speed of 5 mm/s with an average error of 0.536%. It is observed that this margin of error is due to the need for sharp turns at minimum and maximum levitation heights. To calculate testing errors, microrobot motion is recorded at 100 fps(frames per second), and the levitation height is calculated. An optical microscope unit, which has a wide focal area, has a fixed position such that it records the longitudinal localization at given frame rate. Additionally, the proximity profiles acquired from the laser sensor are compared to determine maximum and average errors.

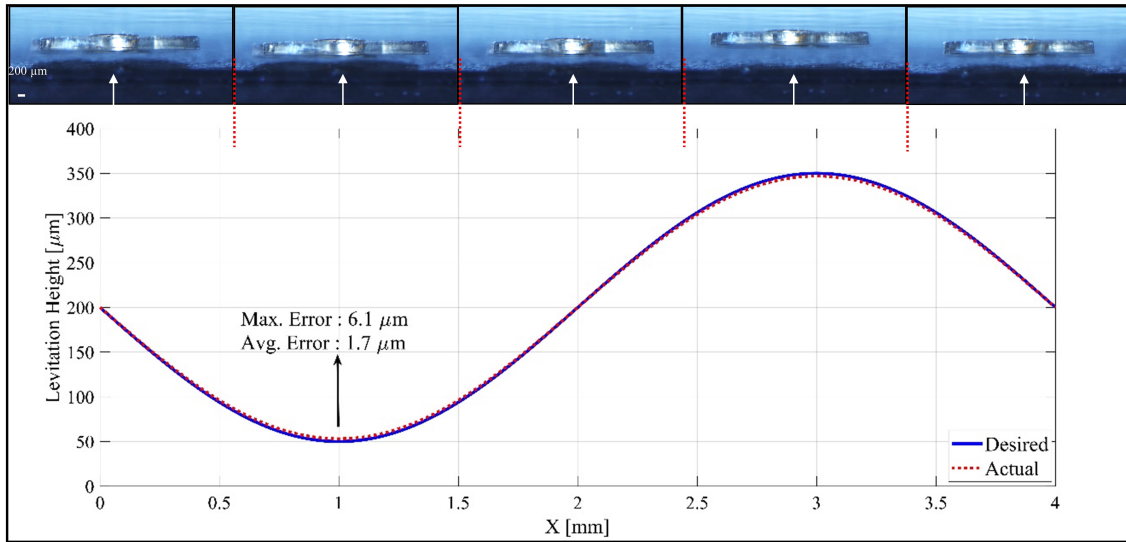


Figure 3.13 The experimental data represents microrobot motion on a 4 mm trajectory with a sine-wave profile relative to the x-axis by the time recording changes on levitation height relative to the z-axis. Five snapshots are given to show actual location

3.3.4 Uncontrolled Model and Rule-Based Model

Uncertainties due to laser calibration, the sampling processes and the deviations observed during the control of the microrobot led us to design a controller. The controller that make the microrobot levitation system more stable, and reduce the errors while following the desired trajectories. The rule-based model, which is an open-loop controller, is an ideal choice for stabilizing the tilting of the microrobot. The non-linearities that are influential on these effects during the longitudinal motion of the robot can be eliminated efficiently. Microrobot velocity and reference trajectory is the user inputs in the rule-based model. According to the velocity, mechanical delay and motion time is calculated. Delay is occurred due to microrobot inertia in the fluid and the acceleration to the desired velocity. Then, determination of the lifter magnet and its orientation are calculated according to (3.11). In this formula, θ is calculated to determine the time period that is controlling the lifter-magnet angle. As shown in Figure 3.14, the rule-based model is applied to reduce the head-tilting angle, and it corrected up to a few degrees, depending on the microrobot's speed (Table 3.1). In this figure, microrobot speeds are adjusted in the range from 5 mm/s to 10 mm/s with the increment of 1 mm/s. In the uncontrolled case, microrobot head-tilting angle is proportional with respect to its speed and orientation angles are as follows: 6.8° , 8.3° , 9.1° , 9.6° , 10.4° , and 11.5° respectively. In the rule-base model, microrobot head-tilting angle is stabilized; however, there is steady-state error at the end of the motion is observed. These errors are as follows: 1.8° , 2.0° , 2.6° , 2.8° , 3.1° , and 3.8° respectively. Because of the head-tilting angle is reduced during the

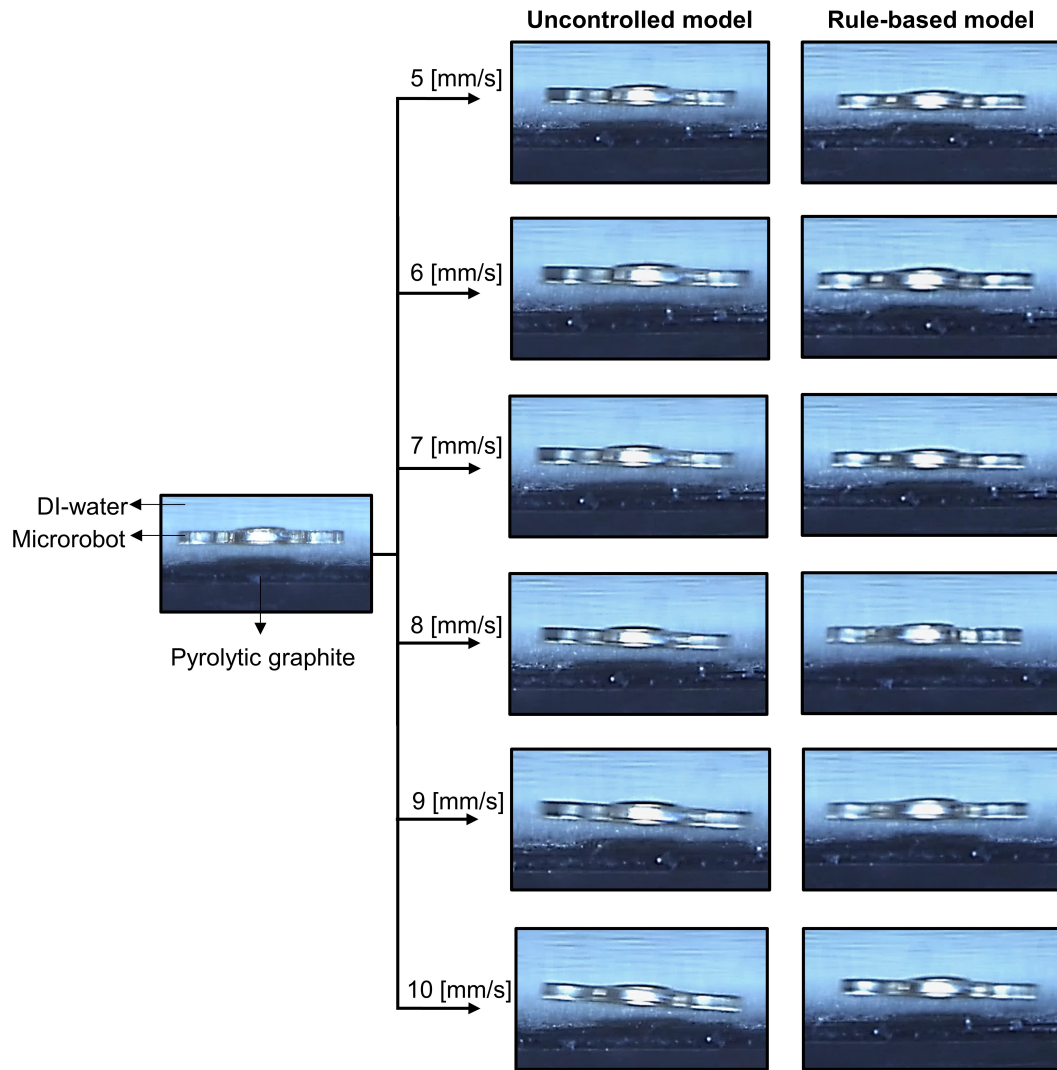


Figure 3.14 Experimental results to show microrobot head-tilting reaction during implementation of uncontrolled and rule-based models at variable speeds (from 5 mm/s to 10 mm/s). While head-tilting reaction is obvious, in the case of the rule-based model, the microrobot's longitudinal motion is slightly developed

longitudinal motion of the microrobot, it is possible to control it at lower levitation height.

Steady-state error is occurred in the rule-based model due to the absence of a sensory feedback mechanism. Moreover, to improve robustness of the control structure, it is necessary to develop closed-loop control models, which are based on the vision-based, laser, and hybrid models. Another experiment which is conducted with the open-loop controller is also shown in Figure 3.15. In this figure, the levitation height is changed from $200 \mu m$ to $100 \mu m$, and images are given slightly isometric view. As the same with the previous experiment, microrobot head-tilting angle is proportional with respect to its speed and orientation angles are as follows: 6.8° , 8.3° , 9.1° , 9.6° , 10.4° , and 11.5° respectively. On the other hand, microrobot head-tilting angle is reduced;

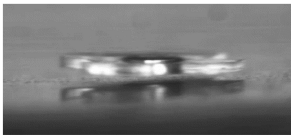
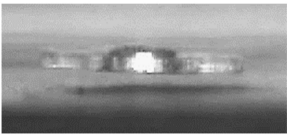
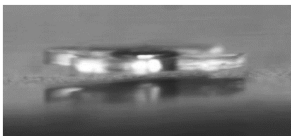
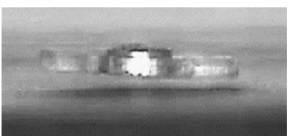
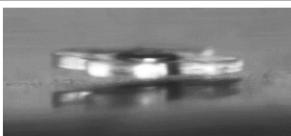

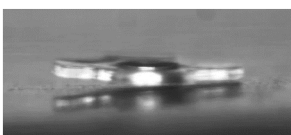
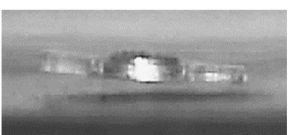
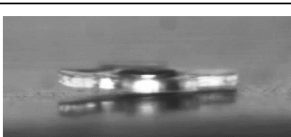
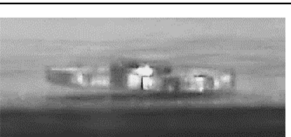
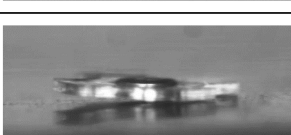

	Uncontrolled	Open-Loop Control
5 mm/s		
6 mm/s		
7 mm/s		
8 mm/s		
9 mm/s		
10 mm/s		

Figure 3.15 Microrobot head-tilting reaction during implementation of uncontrolled and rule-based models at variable speeds (from 5 mm/s to 10 mm/s) when the levitation height is changed to 100 μm is presented. It can be seen that the rule-based model can be implemented in different levitation height during the microrobot's longitudinal motion since head-tilting angles do not change with the levitation height at lower speeds

however, there is steady-state error at the end of the motion is observed. These errors are measured as follows: 1.8°, 2.0°, 2.6°, 2.8°, 3.1°, and 3.8° respectively in the rule-base model.

3.3.5 Vision-based Model

For the closed-loop controller design, the feedback mechanism is established from the image taken from the fixed positioned optical microscope. Following functions are used to detect microrobot corner via optical microscope from the side-view:

- TwoFramesDifferenceDetector
- MotionAreaHighlighting algorithms

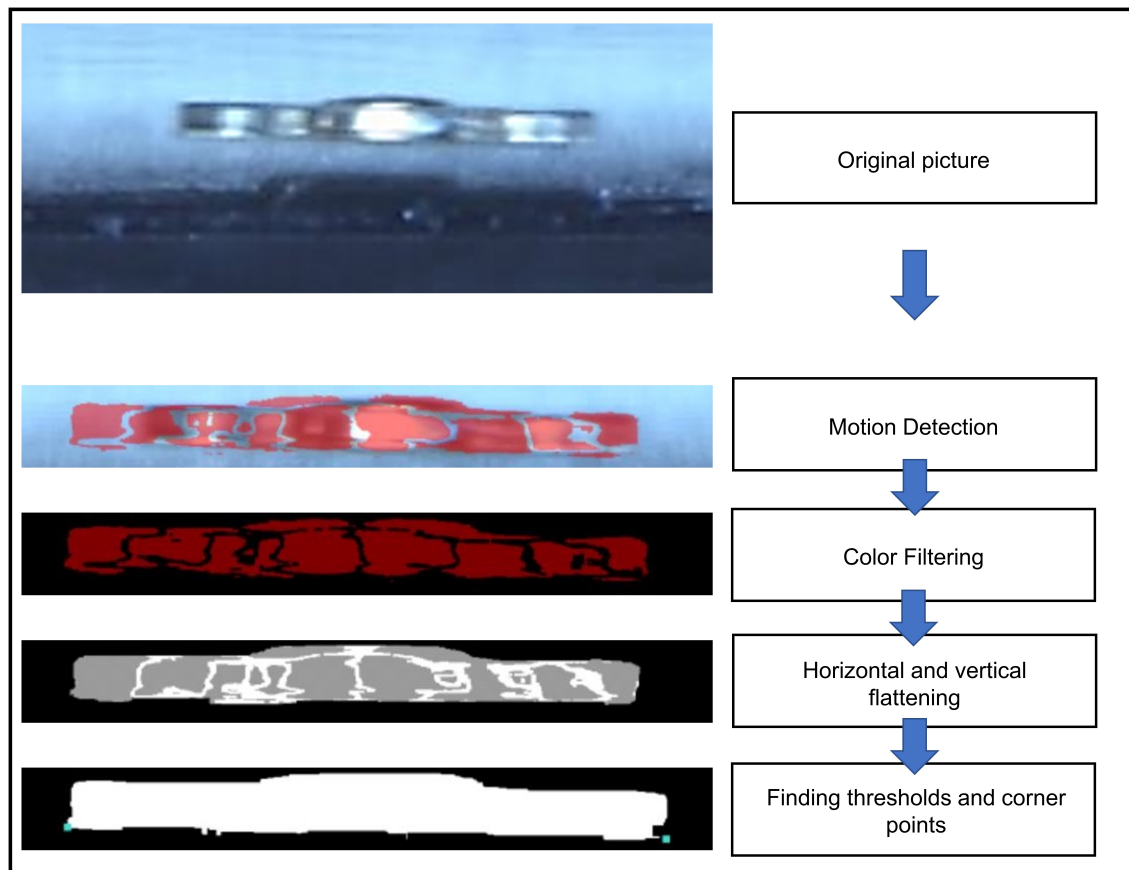


Figure 3.16 Microrobot corner detection algorithms and their application steps are presented

- Euclidian color filtering algorithm
- Horizontal and vertical flattening
- Threshold
- Corner point detection
- Bottom left and Right corner detection
- Calculation of $\text{atan2}(x, y)$

In order to calculate the angle, any two points moving at the same direction on the object are taken. Figure 3.16 shows the algorithm flow of the visual-feedback controller. Euclidean color filtering algorithm is used since color scale of the object is very narrow and the object cannot be distinguished from the environment without this filter. In motion detection, Two Frames Difference Detector (TFDD) algorithm and Motion Area Highlighting (MAH) algorithm are used for motion detector and motion processing respectively. TFDD and MAH are chosen for their fastest computational time and capability of the object detection, respectively. In order to calculate the

head-tilting angle, any two points moving that are on the microrobot in the same direction shall be taken. To do this,

- Detecting the movement and processing the motion area as in the Figure 3.16
- Drawing the perimeter of the detected object with Graham Convex Hull (Graham Convex Shell) algorithm
- The corner points of this convex shell by using (A) Get Furthest Point (Farthest point) and (B) Calculating the tilting angle of the object by taking the angle between the two points determined by the new algorithm.

According to the mentioned algorithms, the microrobot head-tilting angle is measured at varying speed values in the Figure 3.17. The maximum head tilting angle is shown in the figure for each speed and the controller frequency is calculated at 11 Hz. The average head tilting angle is reduced to 1.926° .

3.3.6 Laser Model and Hybrid Model

Following the open-loop control model that is used to improve the transient response, the closed-loop models, which are the laser and hybrid models, are tested to decrease steady-state error. The position and orientation information of the microrobot is obtained from a laser sensor placed on top of the experimental setup. The head-tilting angle is calculated from the slope of the line that intersects the lower corner points of the microrobot. It is observed that the transient response of the microrobot can be developed with the laser model, which uses sensory feedback from a laser sensor. The scanning frequency of this sensor varies between 15 Hz and 58 Hz, due to the laser sensor being sensitive to hardware limitations and other dynamic external factors such as ambient light conditions or low-frequency vibrations. The microrobot follows the lifter-magnet with a minimum delay of around 100 ms. Thus, the frequency of the controller needs to be at least 20 Hz. The transient response of the head-tilting angle does not satisfy this requirement at high speeds. Therefore, the laser model is not robust enough to correct the head-tilting angle at higher speeds (above 15 mm/s). For this reason, a hybrid model is developed in order to make a more robust controller to adapt to different environmental conditions and in order to have a speed-independent model (Figure 3.21, 3.22, 3.23). In this model, the transient response is improved by adapting the rule-based model to the laser model. As a result, the control system can reduce steady-state errors and can be used independently of microrobot speed.

Head-tilting angles of the microrobot and the lifter-magnet are shown in Figure 3.19–3.20 in a speed range of 5–10 mm/s when the laser model is used. Orientation

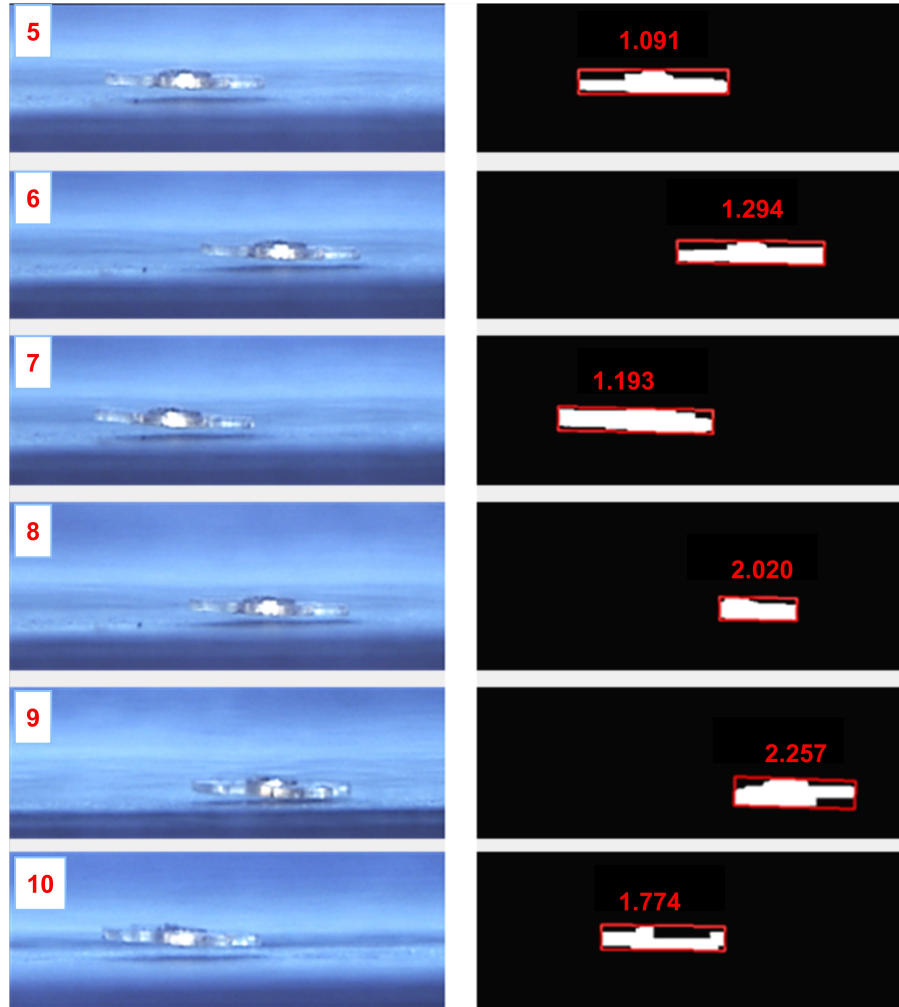


Figure 3.17 Microrobot head-tilting reaction during implementation of visual-feedback models at variable speeds (from 5 mm/s to 10 mm/s) when the levitation height is $200\ \mu\text{m}$ is presented. Head tilting angle of the microrobot is reduced to 1.926° (average). Tilting angle of the microrobot is more developed than the rule-based model during its longitudinal motion

control of the microrobot with only laser feedback causes it to exhibit a rolling motion due to the drag force exerted on it along the z-axis. Thus, the steady-state error cannot be eliminated. By using only laser feedback, it can be observed in Figure 3.19–3.20 that the head-tilting reaction sometimes surpasses the servo angle and causes inconsistencies in the number of samples and results. For this reason, directing the microrobot using only laser feedback cannot be regarded as a reliable control technique.

In the next experiment, the change in head-tilting angle is investigated by running the micro-stage at a speed of 15 mm/s. Results of this experiment are given in Figure 3.20. The first six data points show unstable changes in head-tilting angle at the beginning of the motion. After the sixth data point, the head-tilting angle stabilizes at around

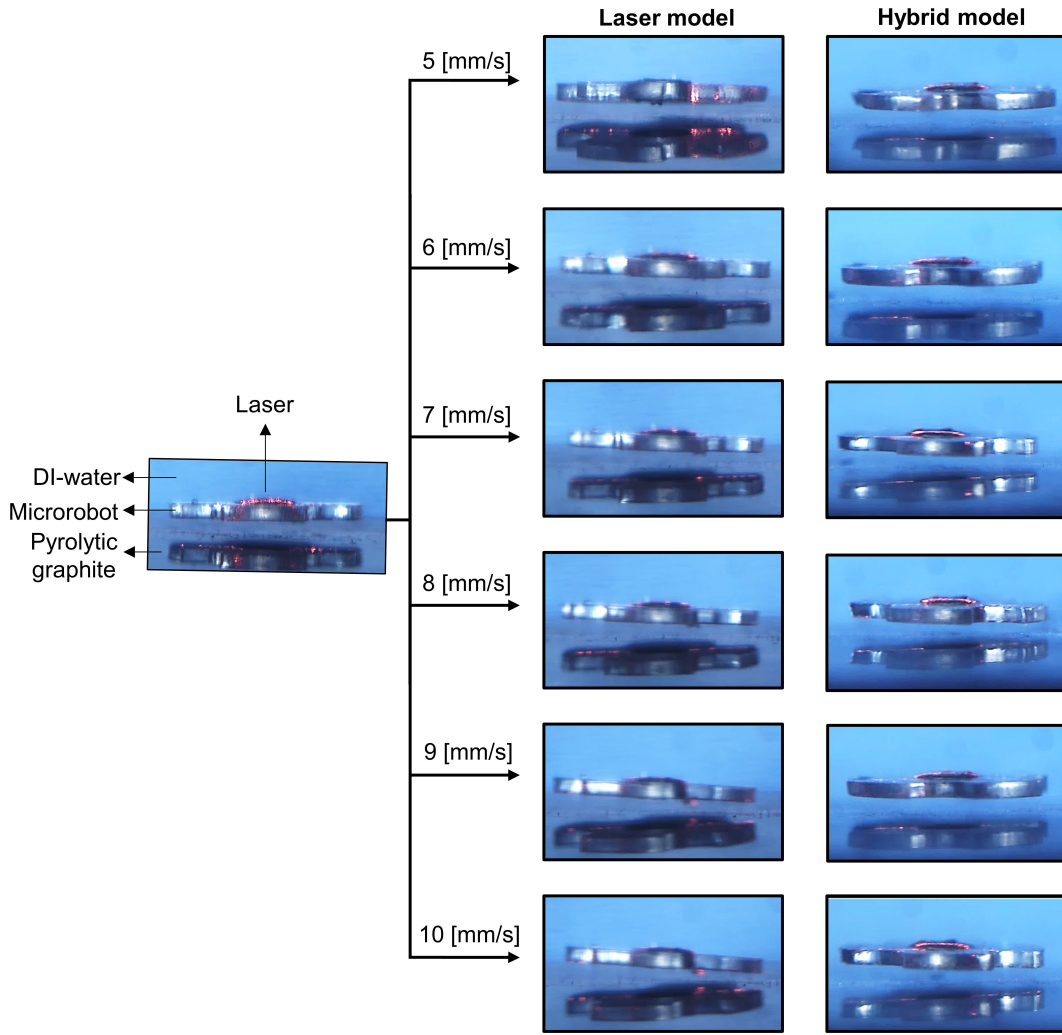


Figure 3.18 The images taken by the experimental data of the laser feedback and the hybrid model controllers at six different speeds in the range of 5–10 mm/s. In order to make the laser marker visible, the experimental images of the microrobot are presented in isometric view

3°. The reason for the first six errors is related to the microrobot acceleration process [109]. Chattering occurs at the head-tilting angle until it reaches the desired speed. Although a faster and more stable motion profile can be obtained compared to the uncontrolled and rule-based models, the steady-state error could not be eliminated, and the head-tilting angle remains at 3°.

The main reason to develop the hybrid model is the unstable change observed in the head-tilting angle during the acceleration phase when the laser model is used. A hybrid model that combines laser model and rule-based model is used to obtain better motion characteristics throughout the whole trajectory. In the experimental results given in Figure 3.21, 3.22 and 3.23 a trajectory of 5 mm length is successfully followed by the microrobot in a speed range of 5 mm/s to 30 mm/s. As can be seen from these figures, the unstable change that is observed for the laser model during the

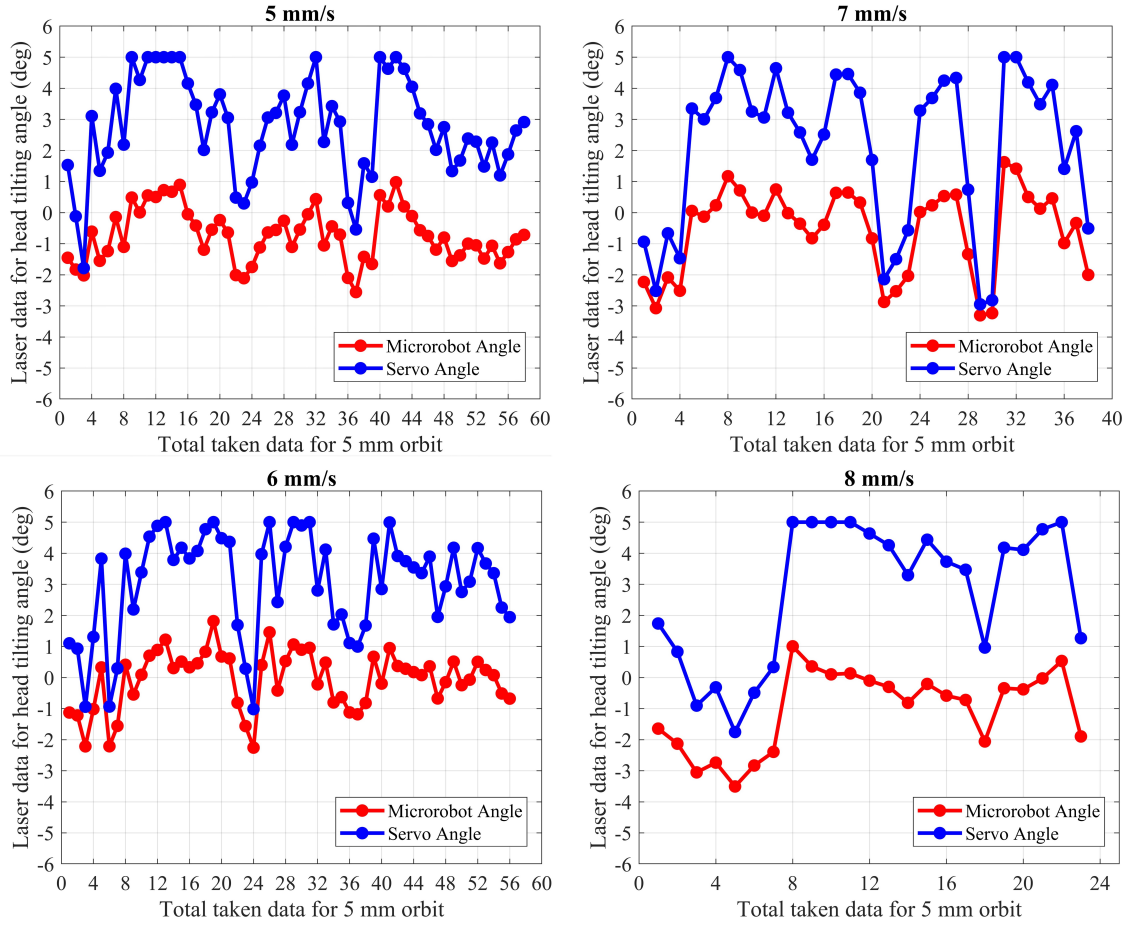


Figure 3.19 The microrobot head-tilting angle and the applied servo motor angle for the application of the laser model within a speed 5 mm/s

acceleration phase is eliminated. This enabled higher speed control to be achieved as a result of stabilization of microrobot motion. Likewise, the steady-state error is mostly eliminated, even at higher speeds. Here, the results indicate that the angle of head-tilting can be reduced independently of the speed of the motion. They also show that microrobot is capable of tracking different trajectory profiles for different applications that require high mobility, high speed, and precise localization.

Average head-tilting angles for each controller for the speed range in which the experiments are conducted are given in Figure 3.24. As expected, high head-tilting angles that increase with microrobot speed are observed for the uncontrolled case. For the rule-based, laser, and hybrid models, ever-increasing controller performances are obtained. The average head-tilting angle values are shown in detail at Table 3.1 based on the comparison shown in Figure 3.24. As can be seen here, the head-tilting angle obtained with the hybrid model, in contrast to the uncontrolled model, is lower than 1° throughout this speed range. This average value is lower than that for the uncontrolled case, and even than the values obtained at 5 mm/s for each controller.

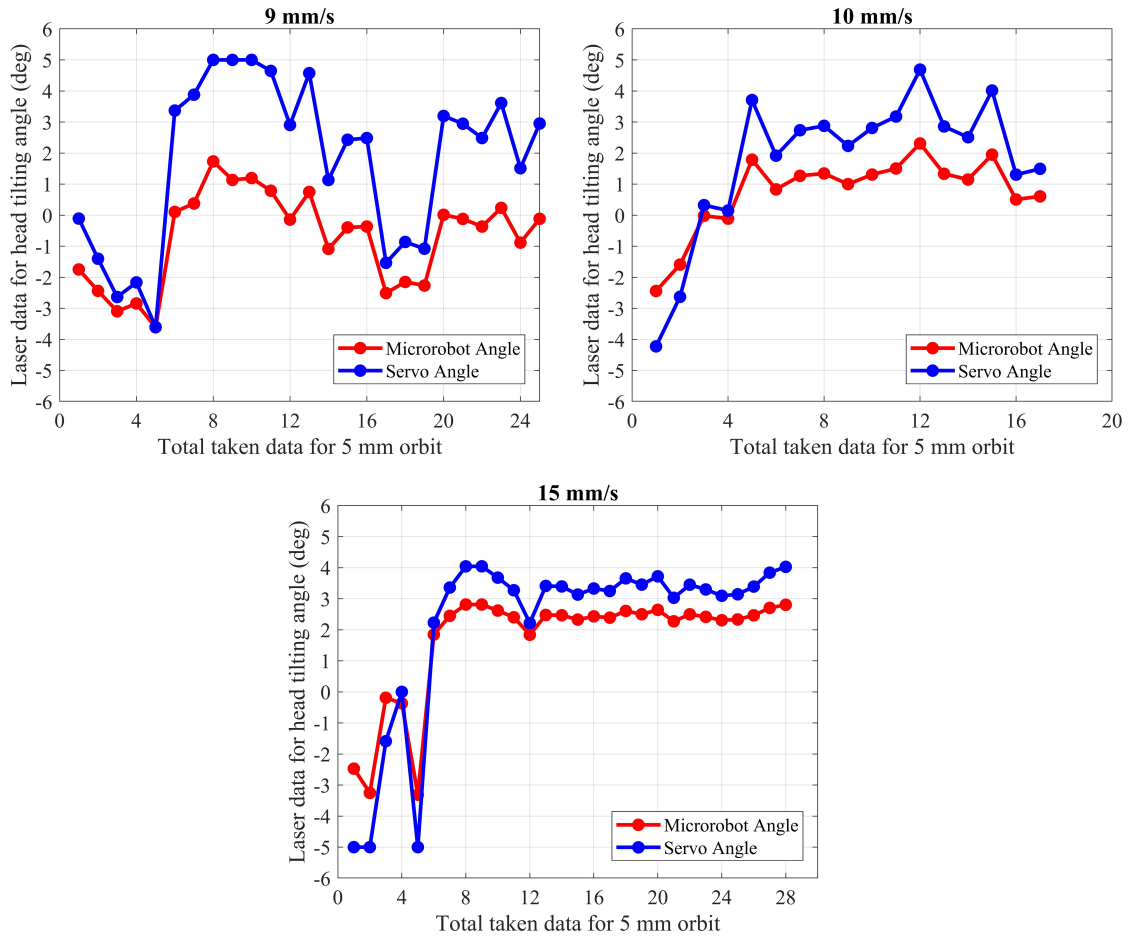


Figure 3.20 The microrobot head-tilting angle and the applied servo motor angle for the application of the laser model within a speed 6 mm/s

3.4 Discussion

The microrobot is intended to track a 5 mm linear trajectory at $200\mu\text{m}$ levitation height to compare the controller performances of different models. All conducted

Table 3.1 System Model Parameters

Speed(mm/s)	Uncontrolled	Rule-Based	Laser	Hybrid
5	6.8	1.8	0.9	0.7
6	8.3	2.0	0.7	0.6
7	9.1	2.6	1.1	0.6
8	9.6	2.8	1.2	0.9
9	10.4	3.1	1.3	0.5
10	11.5	3.8	1.2	0.6
Mean (Deg)	9.3	2.7	1.1	0.7

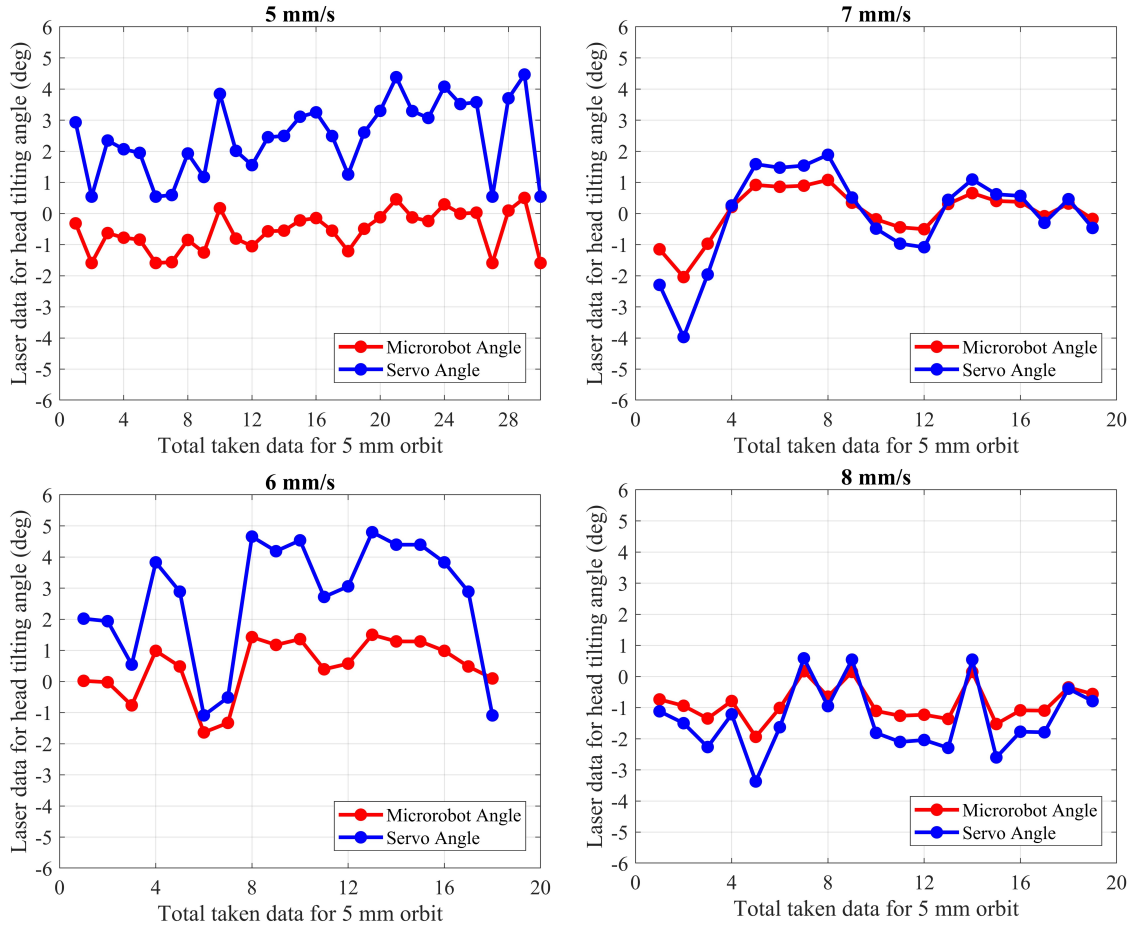


Figure 3.21 Shows the head-tilting angles of the microrobot for speeds 5 and 6 mm/s with the hybrid controller

experiments are repeated at different speeds for each control model separately, while the trajectories and levitation heights remain constant. Firstly, the microrobot movement is performed at a speed range of 5–10 mm/s in the uncontrolled model. We found that the head-tilting angle increases with respect to speed of the microrobot. At higher speeds, the robot is likely to hit the surface of the pyrolytic graphite. In experiments with the uncontrolled model, the reason for the head-tilting reaction in the z-axis is the drag force generated by the DI-water medium. Thus, to reduce the head-tilting angle, we developed a rule-based controller model. However, during the experimental test, it is observed that steady-state error cannot be eliminated with this model, whereas transient response can be improved. Since the rule-based model is an open-loop controller and non-linearities in the system are not taken into account for simplicity, the obtained results are unsatisfactory. Moreover, when the microrobot moves faster than 10 mm/s, the steady-state error is more likely to increase, and as a result, the microrobot head hits the surface. In the laser model, although steady state error is less than the steady-state error of the rule-based model, due to hardware limitation of sensing speed, this technique is not reliable enough for a closed-loop

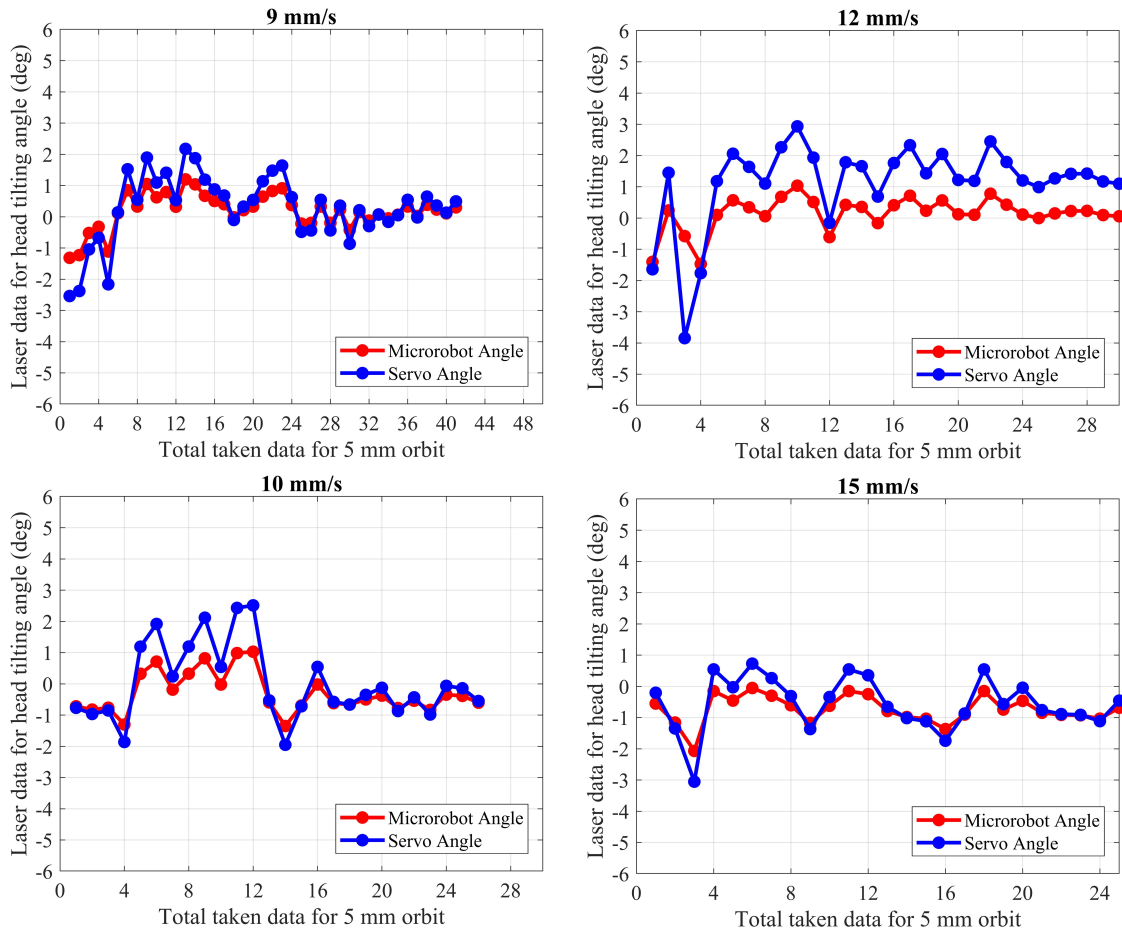


Figure 3.22 Shows the head-tilting angles of the microrobot for speeds 7 and 8 mm/s with the hybrid controller

controller. This model can be used to control the microrobot up to speeds of 15 mm/s in stable conditions. Thus, it is not suitable for applications in which higher speeds are required. Therefore, the rule-based control system and laser calibration are merged to create a hybrid control model, resulting in a more stable control at high speeds of up to 30 mm/s. It is verified that the microrobot with the hybrid model enabled one to achieve more precise localization over a number of test results. Furthermore, in the hybrid model, the aggressiveness and the transient system response can be tuned via the rule-based model. This ensures a speed-independent, stable, closed-loop control structure and low steady-state error.

In this study, we developed various control algorithms based on discussed three models for the stabilization of the longitudinal motion of microrobots. There exists no prior study for the solution to this problem. By taking into consideration the complex motion tasks of microrobots in 3D space, a sinusoidal trajectory with $150\mu\text{m}$ amplitude and 4 mm length is also tested, with an average error rate of $1.73\mu\text{m}$. The fact that this motion did not take place at a constant levitation height and that the microrobot

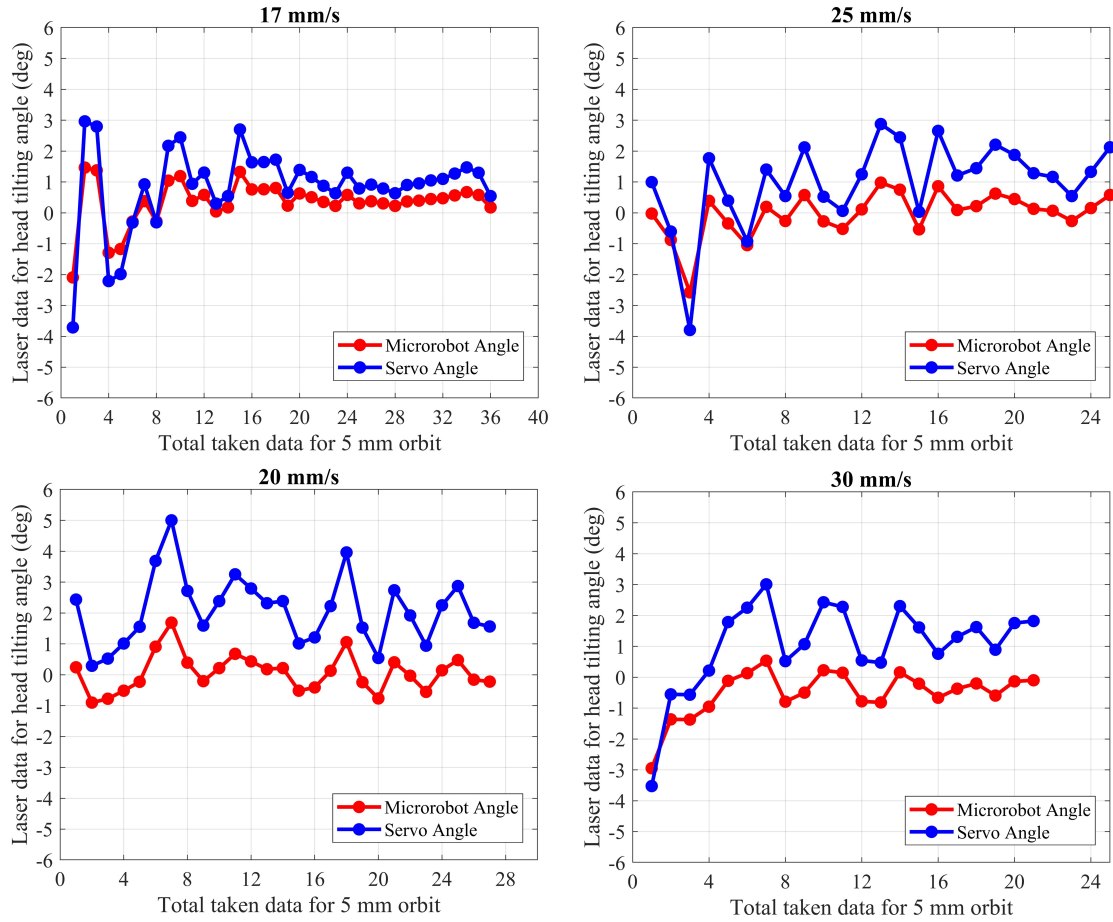


Figure 3.23 Shows the head-tilting angles of the microrobot for speeds 9 and 10 mm/s with the hybrid controller

has a wide range of levitation height shows the high performance of the microrobot design and orientation control. In the mathematical model section, starting from a free body diagram with head-tilting angle, the relation between the head-tilting angle and levitation height and phase difference equation depending on the micro-stage speed are derived. Thus, the mechanical delays in the controller are calculated based on the differences in the accelerations of the lifter-magnet and the microrobot. According to the calculated delay, the time required for the lifter-magnet to be held at the target orientation is determined, which in turn allowed the control of the longitudinal motion of the microrobot. By conducting parametric FEM analyses in COMSOL[®], the equations that depend on micro-stage speed and microrobot head-tilting angle are determined for open-loop and closed-loop controllers. The head-tilting reaction, which can be determined using the first-order equations of angle-correction, generated undesired torque on the microrobot. It brought out, as a result, average 9.3° head-tilting angle in the case of uncontrolled model. On the other hand, by using control strategies, we achieved following results:

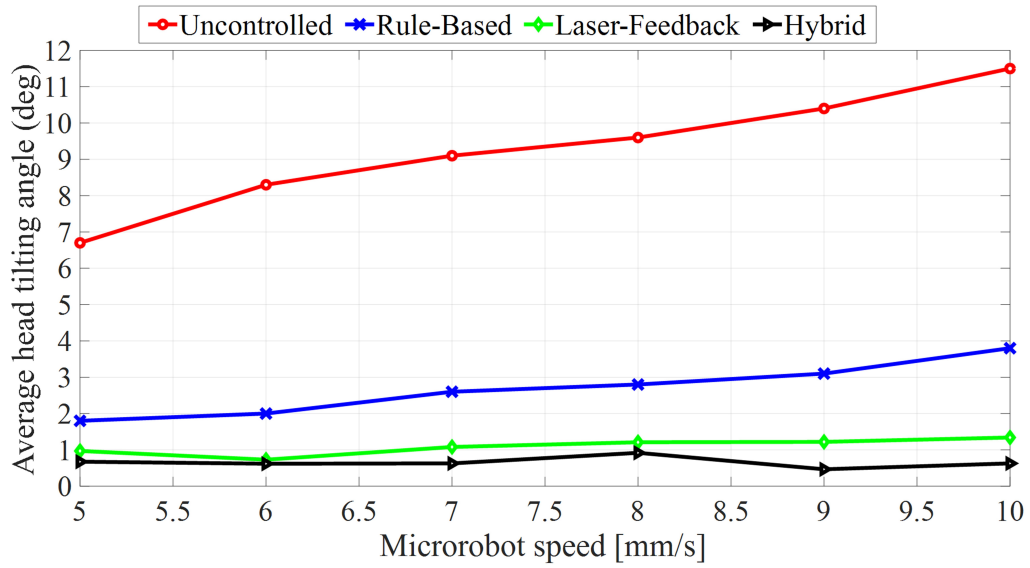


Figure 3.24 Comparison of average head-tilting angles in the speed range of 5–10 mm/s

- 2.7° head-tilting angle for the Rule-based Model
- 1.1° head-tilting angle for the Laser Model,
- 0.7° head-tilting angle for the Hybrid Model

Moreover, the hybrid model is also experimented with at a speed of 30 mm/s and received an average angle error of 1°. This result proved that the microrobot can be used in cases in which a high speed and a complex and long trajectory are necessary. Furthermore, since the microrobot is capable of 5 axes orientation, its head position can also be utilized in various object manipulation tasks.

As a result, through the developed control models, a solution methodology for the head-tilting problem is developed and implemented for different tasks that require high-speed and low positioning error rates. The presented control models are particularly important for the purposes of cell and particle manipulation applications. In future studies, we will focus on developing fully autonomous control techniques and longitudinal motion in laminar flow. To do so, microrobot longitudinal forces which is generated by permanent magnets need to be increased.

FLOW-RELATIVE MICROROBOT OPTIMIZATION AND MOTION MODELLING WITH IMPLEMENTATION

A novel permanent magnet (NdFeB) based micromanipulation method which produces higher lateral forces compared to previously reported techniques [94, 102] and enables the positioning and locomotion in a laminar flow ($Re < 2000$) is proposed. A microrobot driving configuration with pyrolytic graphite which is a diamagnetic material and two ring-type permanent magnets were used to increase lateral forces acting on an untethered microrobot. The basis of the proposed configuration was concentration of the magnetic field force lines on the microrobot and the formation of a force vector on both sides on the vertical axis of the robot. We report the motion characteristics of our microrobot at different flow rates with simulation results and confirm them with experimental results.

4.1 Microrobot with SU-8 Body

In this section, the proposed micromanipulation technique is described in detail. This technique is based on the interaction of a ferromagnetic microrobot, two ferromagnetic outer magnets and a diamagnetic pyrolytic graphite layer. It enables the positioning of a microrobot inside a microfluidic channel in which a continuous laminar flow is present. In Figure 4.1-A, F_p represents the diamagnetic force, F_m the magnetic force, F_g the gravitational force, F_b the buoyancy force and F_d the drag force. The 2 lifter magnets were positioned above and under the channel and aligned along with z-axis. They are N52 grade and have dimensions of $\varnothing 20 \text{ mm} \times \varnothing 40 \text{ mm} \times 8 \text{ mm}$. The dimensions of the pyrolytic graphite on the surface was 7 mm width, 30 mm depth and 0.5 mm thickness. It was expected that the levitated microrobot would not be able to maintain its position relative to the "center line" due to drag force caused by stream flow applied in the x-axis direction (A and B). Since the microrobot would have a certain displacement during flow, the carrier magnet in microrobot's center would also have a displacement, τ , relative to the centers of the magnets. Because of this

displacement, the angle between the upper lifter magnet with the "center line" was indicated as α . Under these circumstances, the proposed model turns into a second order mathematical system (Figure 4.1-B). In this model, the drag force exerted on microrobot's surface was modeled as disturbance input and microrobot was modeled as a mass, the robot-liquid environment pair was modeled as a damping element and the robot-magnets pair was modeled as a spring. The reason behind using damping and spring elements in the model was to show the mathematical determination of the hydrodynamic structure of the liquid and the relationship between the robot and liquid environment in the model. The same parameters α and τ in Figure 4.1-B are also valid here and are not shown again for a clearer representation. The microrobot's dimensions are given in C. A cube-shaped magnet was placed in the microrobot body, made by SU-8 based polymer material. It has semicircular front-head, designed for object manipulation in future studies. The gray colored ground depicts pyrolytic graphite on the surface, that is also illustrated in this figure.

The forces shown in Figure 4.1-B, the Brownian force and the Atomic forces were not shown. Since these forces were more dominant at the nano level, their effects on sub-millimeter would be very low (<1 nN). Hence, they were neglected during modeling. F_b and F_g forces considered as constant terms; for F_d , F_m and F_p forces, no simplified or empirical formulas were reported [32, 107]. Therefore, a FEM (finite element method) program, COMSOL[®] (version 5.3a, COMSOL Inc., Stockholm, Sweden) was used to calculate these forces.

4.1.1 Determination of Damping and Spring Coefficients

The sketch of proposed dynamic model which was designed to explain the behavior of the microrobot in laminar flow was shown in Figure 4.1-C. Since the dynamic model of the system was expressed as mass-damping-spring elements, the general expression of a transfer function of a second-degree system on x axis can be represented (4.1)

$$\ddot{\tau}(t) + \frac{c_s}{m_r} \dot{\tau}(t) + \frac{2k_s}{m_r} \tau(t) = \frac{(F_{m,ux} + F_{m,lx} - F_d)}{m_r} \quad (4.1)$$

Viscous damping coefficient acting on a particle within the channel which has the height of $h = 3.5$ mm, can be solved using (4.2),

$$c_s = \frac{\mu A_c}{h} \quad (4.2)$$

where, $c_s = 3.127 \times 10^{(-7)}$ (Ns/m). To calculate spring coefficient; total magnetic force,

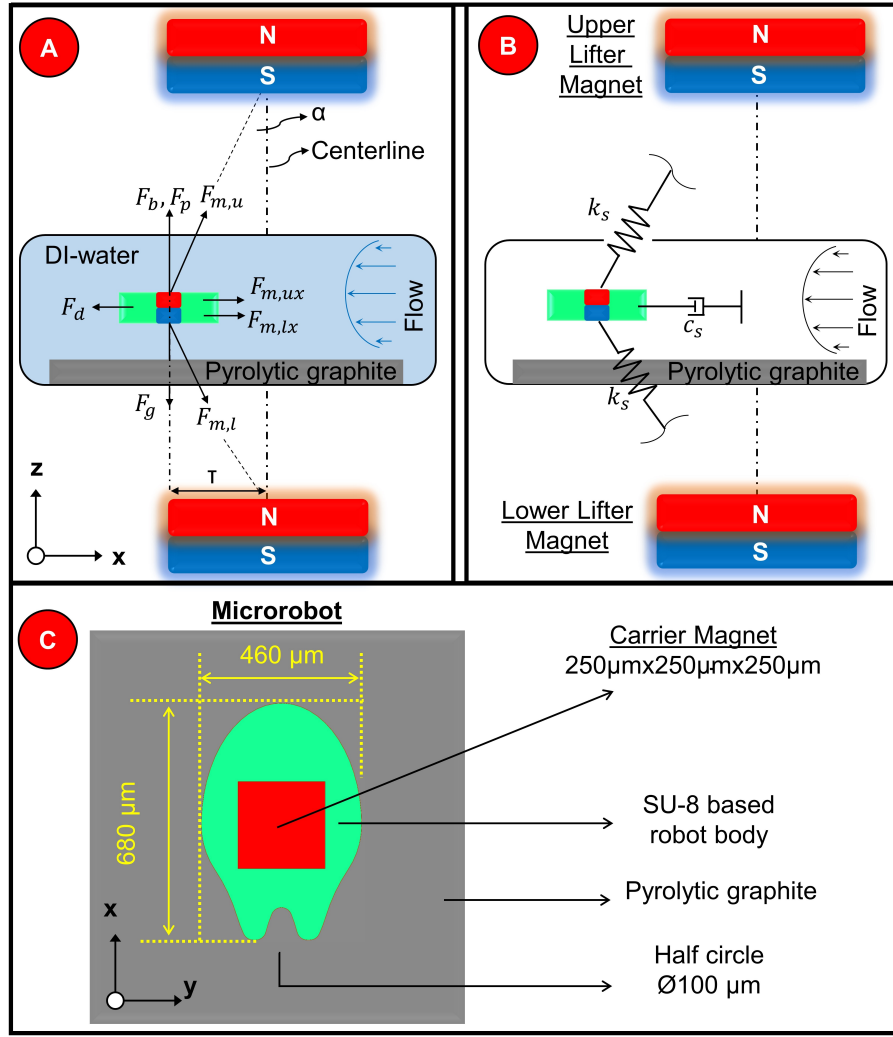


Figure 4.1 (A) In order to determine the dynamic behavior of this system, the second order system simulation in the form of mass-damping-spring is expressed in (B). The dimensions of the microrobot used in experiments is given in (C). The carrier magnet and the microrobot thicknesses are set to 250 μm

drag force, velocity and displacement of the microrobot were required. These values were used in calculating k_s based on the free-body diagram in Figure 4.1-C and when put in equation (4.1) its value is determined as $k_s = 2.658 \times 10^{(-4)}$ (N/m). In this calculation, the acceleration of the robot was neglected, so that the spring coefficient was made independent of the robot mass. Such an approach was considered since high acceleration values were not expected during the motion of the robot in the liquid. Thus, the spring coefficient value was found and it can be used in similar studies. Consequently, assuming that a single force source was applied, the robot motion equation is obtained as;

$$\ddot{\tau} + 1.936\dot{\tau} + 1645.4\tau = F_0 \quad (4.3)$$

where the maximum disturbance amplitude is F_0 (Appendix Figure A.1). The natural resonance frequency of this system for the motion equation is expressed according to (4.3) was calculated as $w_n = 6.456$ Hz.

4.1.2 Magnetic Force Calculation

There are some simplified formulas that model the attractive forces two identical magnets exert on each other. However, there were no such formulas that model the attractive forces two permanent magnets with different sizes and geometric shapes exert on each other. For the calculation of attractive forces on carrier magnet, which was used on the microrobot, due to ring-type lifter magnets following points are emphasized:

- The ring-type lifter magnets were considered as solid. Magnetic force values were calculated for larger diameter (outer) and smaller diameter (inner) values separately. By taking the difference of the calculated force values for larger and smaller diameters, magnetic force can be calculated.
- The magnet on the microrobot considered as bar type while the calculation was made.
- The magnetic force of the magnets on the robot was calculated by taking the geometric average of the force values produced for the lifter magnet and microrobot.

Parameters required for magnetic force calculations, buoyancy and gravitational force values were also given in Table 4.1.

The lifter magnets, and carrier magnet which was located in the center of microrobot were given in Figure 4.2-A and Figure 4.2-B respectively. Here, the remanence magnetic field which changes with respect to the distance from magnet were illustrated and they are also used in (4.4) and (4.5) to calculate unknown parameters, respectively.

Magnetic field on the symmetry axis of an axially magnetized ring magnet, B_h [114] is,

$$B_h = \frac{B_r}{2} \left[\frac{D_r + z}{\sqrt{R_a^2 + (D_r + z)^2}} - \frac{z}{\sqrt{R_a^2 + z^2}} \left(\frac{D_r + z}{\sqrt{R_i^2 + (D_r + z)^2}} - \frac{z}{\sqrt{R_i^2 + z^2}} \right) \right] \quad (4.4)$$

Table 4.1 Parameters of the microrobotic setup

Symbol	Quantity	Value
ρ_r	Robot density	2882 kg/m^3
m_r	Robot mass	$0.162 \times 10^{-3} \text{ kg}$
A_c	Projected surface area	$1.09 \times 10^{-6} \text{ m}^2$
F_b	Buoyant force	$1.036 \text{ }\mu\text{N}$
F_g	Gravitational force	$1.5838 \text{ }\mu\text{N}$
μ_r	Magnetic permeability	0.999991
μ_0	Vacuum permeability	1
B_r	Remanence field	1.43 T
χ	Magnetic susceptibility (\perp)	450×10^{-6}

Magnetic field on the symmetry axis of an axially magnetized block(cube) magnet, B_b [114] is,

$$B_b = \frac{B_r}{\pi} \left[\text{atan} \left(\frac{LW}{2z\sqrt{4z^2 + L^2 + W^2}} - \frac{LW}{2(D+z)\sqrt{4(D+z)^2 + L^2 + W^2}} \right) \right] \quad (4.5)$$

According to Table 4.1, the net magnetic force required for the levitation of the microrobot on z axis was calculated as $F_t = 548 \text{ nN}$. In order to obtain this force, it was necessary to move the upper and lower lifter magnets vertically with respect to the graphite surface in the configuration shown in Figure 4.1-A. However, if these two magnets were equidistant from the robot, the total magnetic force on the robot would be 0. Therefore, during the calculation, two magnets were moved simultaneously. In each step, the upper magnet's position was held constant, while the lower magnet was offset in the range of 0-10 mm in $1 \text{ }\mu\text{m}$ steps. Moreover, a distance graph was obtained by combining both distance and offset values for each magnet movement. In Figure 4.3, microrobot can be levitated at every point corresponding to 548 nN value on the z axis. The bar on the upper side of this figure showed the change in force values between 0-1 μm and the corresponding colors. As expected, if there was no offset value between the magnets (offset = 0, y axis), the magnetic force value also became 0. It was also seen that the magnets have an exponential characteristic due to magnetism, and net magnetic force converged to a certain value as they move away simultaneously. As a result, the robot can be levitated for different distance and offset values in the green-yellow color range.

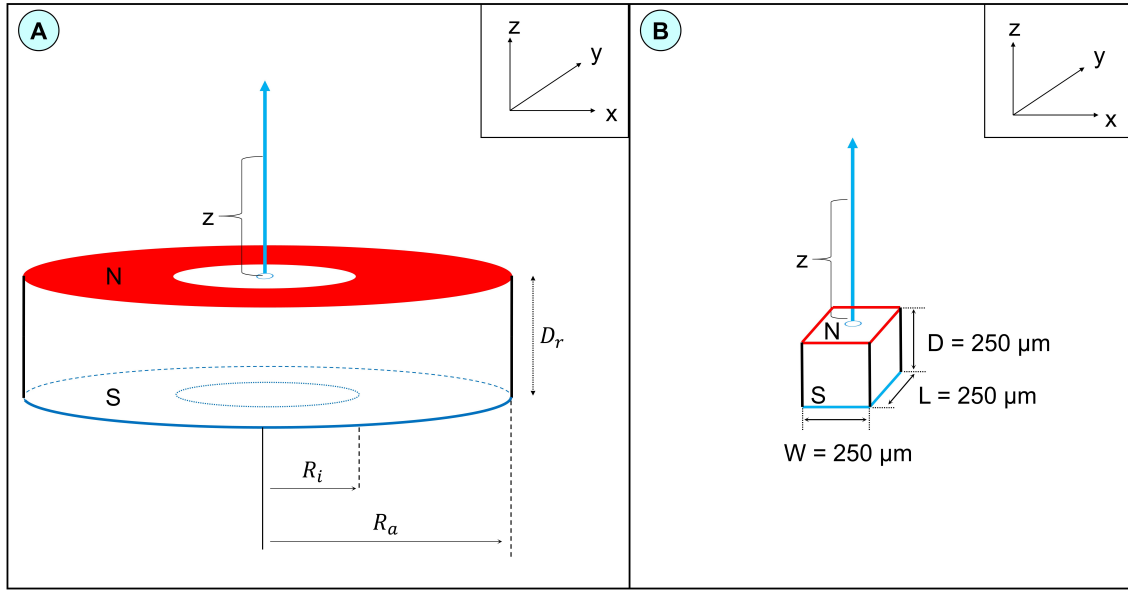


Figure 4.2 (A) Ring-type lifter magnet whose dimensions are $R_i = 20$ mm, $R_a = 40$ mm, $D_r = 8$ mm and (B) bar-type carrier magnet are given. These parameters are used to derive magnetic fields in (4.4) and (4.5)

4.1.3 Drag Force Calculation

For the drag force calculation, cross-sectional area of microrobot, which was taken perpendicular to the flow direction during the lateral movements of the robot, was designed as a rectangular shape with an area $460 \mu m \times 250 \mu m$. However, it has an elliptical surface which can be seen in detail in Figure 4.1-C. Therefore, a rectangular shape approach should not be adopted directly. In this case, 3D analysis and complex formulas must be required to precise calculation of c_d . Re (Reynolds number) working range was determined based on equation (4.6) by considering flow rate and microrobot speed. Here, to calculate Re, liquid density, $\rho_f = 998.29$ (kg/m^3 , $25^\circ C$), hydraulic diameter $D = 4.67$ mm, flow rate v , dynamic viscosity, $\mu = 0.001003$ (Pa.s) for,

$$Re = \frac{\rho_f D v}{\mu} \quad (4.6)$$

where it was substituted in (4.7) for $d_A/d_n = 0.806$, $c = 0.847$ then,

$$c_d = \frac{24}{Re} \frac{d_A}{d_n} \left[1 + \frac{0.15}{c^{0.5}} \left(\frac{d_A}{d_n} Re \right)^{0.687} \right] + \frac{0.42 \left(\frac{d_A}{d_n} \right)^2}{c^{0.5} \left[1 + 4.25 \times 10^{-4} \left(\frac{d_A}{d_n} Re \right)^{-1.16} \right]} \quad (4.7)$$

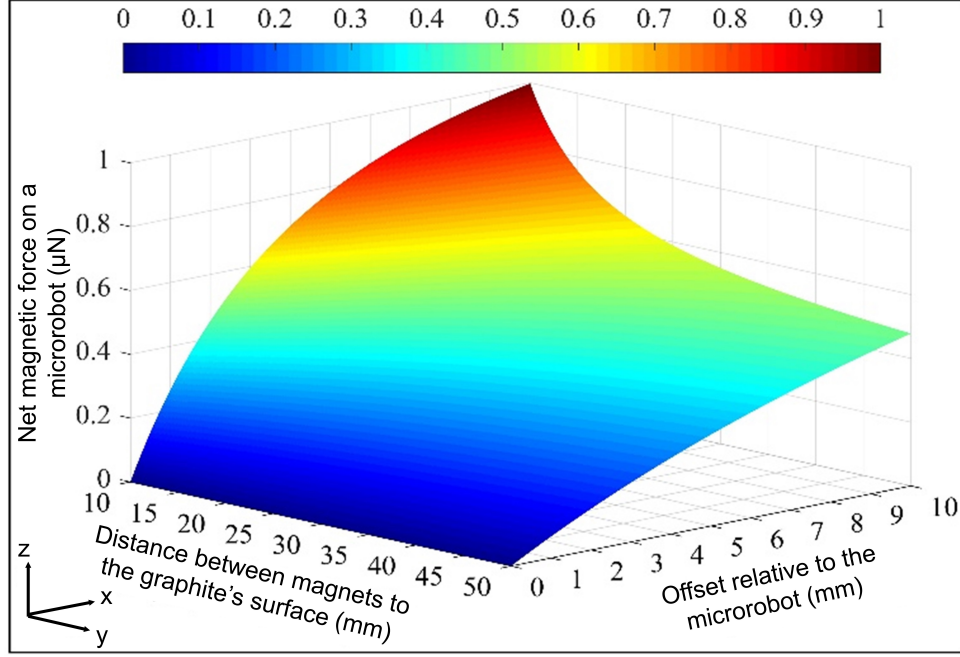


Figure 4.3 The surface graph obtained as a result of the net magnetic force calculation is shown. The x-axis is the distance between the magnets and the graphite; y axis shows the amount of offset applied to the lower positioned lifter magnet; the z axis shows the total magnetic force values obtained. The bar above the figure shows the color map of the force change between 0-1 μN

c_d was calculated for different velocities depending on Re value and it was shown in Figure 4.4. In the laminar flow regime, c_d cannot be converged to a constant value.

Using the values calculated in this section and the robot cross-sectional area, $A_c = 1.091 \text{ mm}^2$, with different robot speeds, v_r , drag force can be calculated according to (10)

$$F_d = 0.5c_d\rho_f A_c v_r |v_r| \quad (4.8)$$

4.1.4 Simulation Results

In this section, analysis results, that were obtained by COMSOL[®] for net magnetic force (Figure 4.3) and c_d (Figure 4.4) values, are compared with theoretical results. A parametric and time-dependent analysis was performed for different flow speeds from 0 mL/min to 100 mL/min. In this analysis, microrobot performance were simulated in a rectangular-shaped channel (3.5 mm \times 7 mm). With the analysis, changes in Re, c_d and τ in the channel were observed and compared with the results calculated. Overlapping of theoretical and analysis results shows the accuracy of the proposed model, all results were recalculated in this section before experimental studies. All

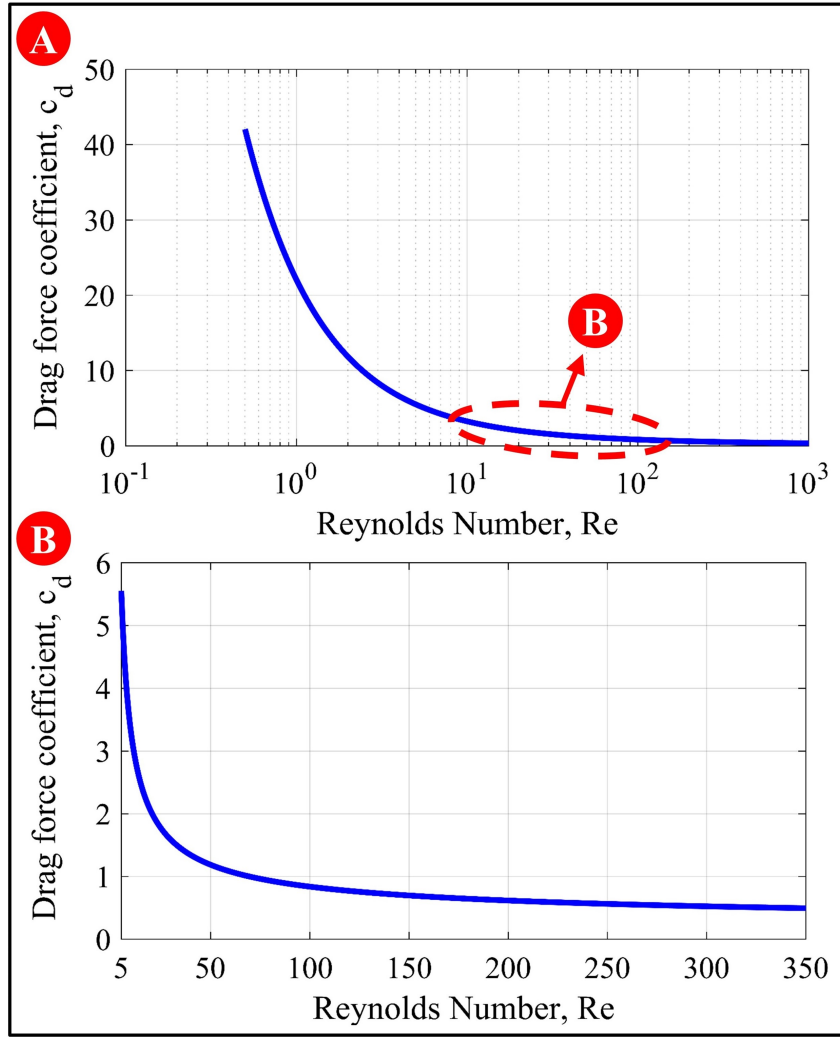


Figure 4.4 The c_d values that vary depending on the Re are shown. Re converges to a value of c_d as expected at its greater values. However, it is calculated that the drag force coefficient for the predicted operating range (0-50 mm/s) for microrobot and flow rate would be between $0.58 < c_d < 1.85$

simulations, which were utilized by a workstation that has AMD Threadripper 1950x (16 real cores) processor with 96 GB RAM and with a Windows-10 64-bit operating system, are performed using the software COMSOL[®] Multiphysics Version 5.3 (CPU License No: 17076072). AC/DC module of the software COMSOL[®] was implemented for investigating effects of magnetic field lines over microrobot and to observe system dynamics behavior under different flow conditions by using a combination of laminar flow-solid mechanics-moving mesh structure. In Figure 4.5, the variation of the flow rate in the channel in the -x direction was isometrically shown when the flow was 10 mL/min. The black arrows on the figure showed the flow direction and the characteristic of flow, and the velocity vectors at the level of the robot were shown in the top view in detail. The slices on the right and left ends of the channel on the y-z axes refer to the inlet and outlet respectively. No slip boundary condition and

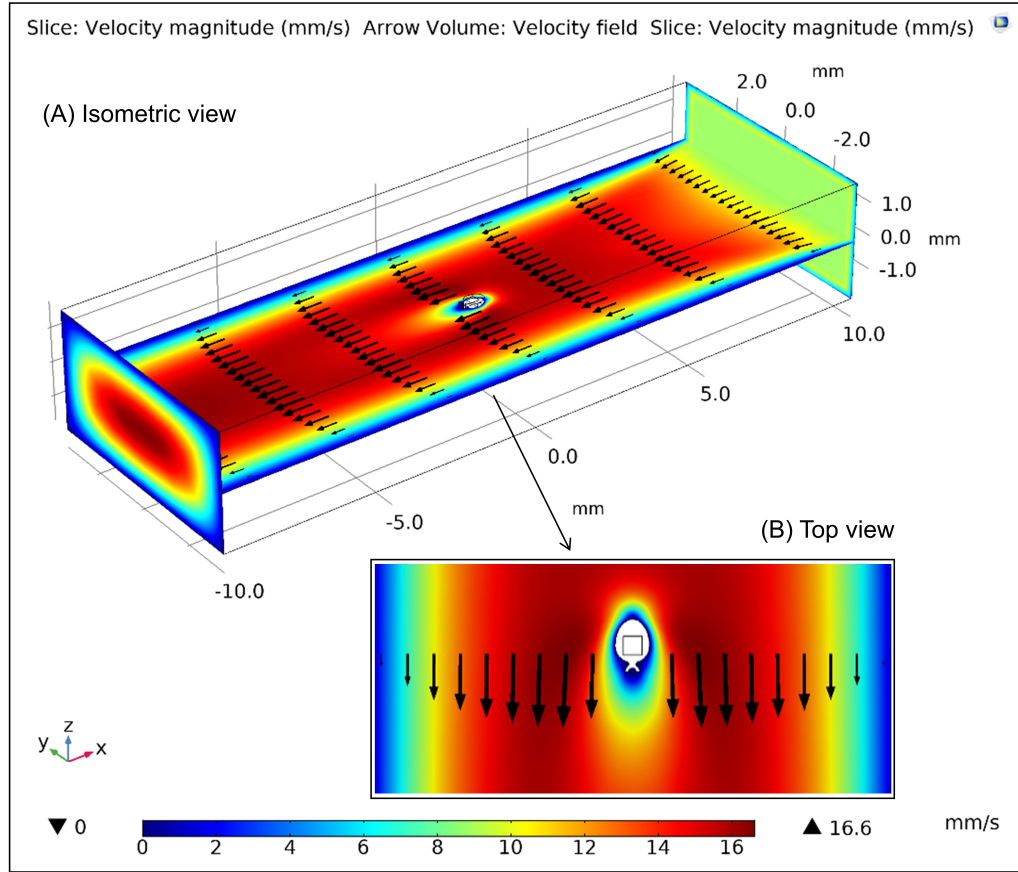


Figure 4.5 The analysis result is shown when the flow rate of the microrobot in a rectangular channel is 16.6 mm/s. Due to no slip boundary conditions is considered in a rectangular shape channel, velocity is generated as parabolic manner and higher magnitude of velocity field can be seen around in the middle of channel and corner of the robot (top view (B))

gravity are also considered. Mesh consists of 37251 domain elements, 3738 boundary elements, and 534 edge elements.

In the simulation shown in Figure 4.5, the $Re - c_d$ was calculated as a result of the parametric analysis. It was performed for 2.5 mL/min steps in the range of 0-100 mL/min (Figure 4.6). According to the theoretically calculated c_d values shown in Figure 4.4-B, it can be observed that there was an absolute error value of 0.0388(%2.26) in simulation results given in this figure. On the other hand, both theoretical and simulation results were converged to the same number ($c_d = 0.49$) at higher Re .

4.1.5 Experimental Results

After theoretical and simulation analysis, experiments were conducted on microrobot motion behavior in laminar flow regime with the proposed setup. Immobilization

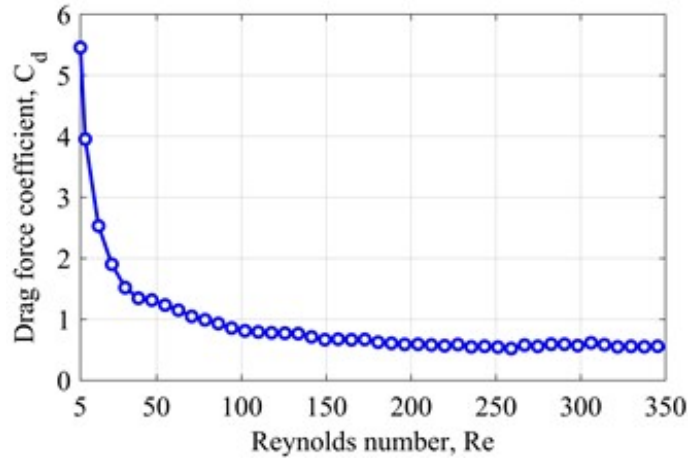


Figure 4.6 The application of different flow rates using the laminar flow-solid mechanics-moving mesh in the COMSOL[®] AC/DC module shows the relationship between c_d and Re . The markers on the graph represent each flow step of 2.5 mL/min. While the Re value increases, c_d values converge to a constant value (0.49)

characteristics and lateral motion results towards or against flow direction were examined. The dynamic behavior of the robot was studied based on the τ and lateral force calculations. Here, the microrobot behavior and its motion accuracy at different speeds were investigated under the different flow rates. For this purpose, the robot was moved 4 mm along the channel forward and backward, in other words, towards/against the flow. The microrobot lateral motion characteristics were experimented at different flow rates (5-65 mL/min) and recorded by the optical microscope system. The microrobot was levitated in a 3.5mm \times 7 mm microfluidic channel. A syringe pump capable of applying a flow rate from 0 to 2120 mL/h was used to provide higher flow rates through the channel. For robot levitation, ring type $\varnothing 20$ mm \times $\varnothing 40$ mm \times 8 mm N52 grade magnets were used below and above the channel. The magnet positions were controlled by a high accuracy 3 axes positioning stage. The dynamic behavior of the robot during laminar flow was shown from the side-view in Figure 4.7.

In this figure, the tested microrobot flow rates are: (A) 5 mL/min, (B) 15 mL/min, (C) 25 mL/min, (D) 35 mL/min, (E) 45 mL/min, (F) 55 mL/min, (G) 65 mL/min. Moreover, the oscillation amplitudes of 585.6-1125.9 μm in (A), 1775.6-2281.3 μm in (B), 2757.8-3120.6 μm in (C), 3494.4-3843.5 μm in (D), 4400.1-4780.7 μm in (E), 6027.8-6556.7 in (F) and 9727.9-10388.0 μm in (G) respectively. In case of (A) and (B), the microrobot had more amplitude due to flow velocity inside of the channel are very low level. Between (C) - (F), a lower amplitude and lower oscillation frequency can be seen (Figure 4.8). At (G), 65 mL/min flow rate is applied and the microrobot reveals more unstable behavior, and the levitation control is lost at $\tau = 10388.0 \mu m$. Due to the nature of stream flow and magnetic field, the displacement



Figure 4.7 The oscillation amplitude of the microrobot subject to laminar flow are presented. When the microrobot holds still, it exposes oscillation characteristics due to the drag force

was increased exponentially for higher flow rates. The experiment was repeated 10 times to demonstrate repeatability. During the experiments, laminar flow profile is applied as a step-wise function with two distinct y values. Therefore, displacement of the microrobot converges on two distinct values at different time periods depending on whether or not the flow is applied. The aim of step-wise flow was to test whether or not the microrobot levitation was affected by discontinuities in the flow and drag force. By this way, we were also able to observe and measure that whether the application of flow rates at different time intervals over an experimental period had an effect on the microrobot motion behavior. The results shown that microrobot answered similarly to step-wise discontinuities flow and demonstrated stable behavior. Moreover, the detachment point of the microrobot was also determined. Although the microrobot was resistant to flow at 65 mL/min, the stability of levitation began to deteriorate at

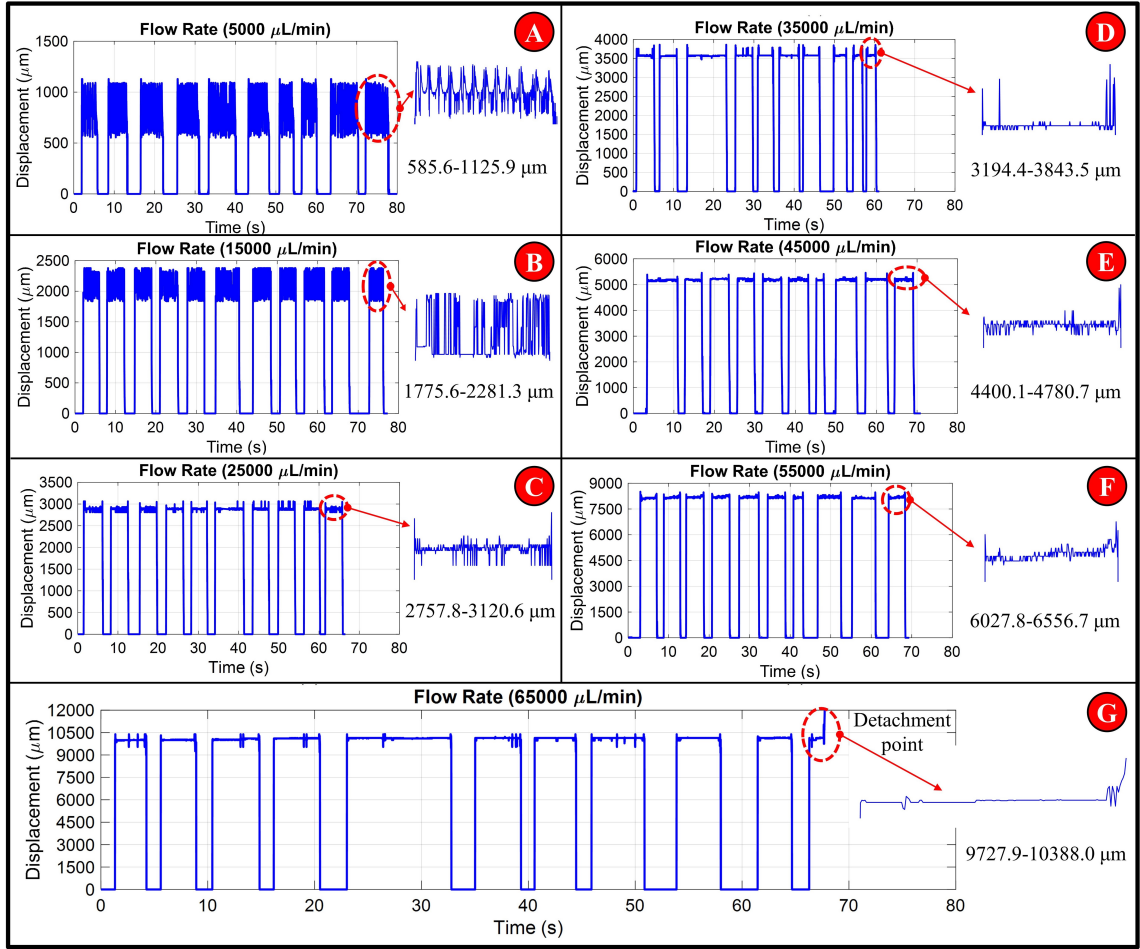


Figure 4.8 The laser displacement data depending on the flow rates was recorded during microrobot movements. The 10 peaks in each graph indicate the number of experiments

this flow rate. It was calculated that the distance from the point where the detachment occurs to the center of the carrier magnet was 10388.0 μm . At this point, the upper lifter magnet is 20 mm from the graphite surface and the lower carrier magnet at 25 mm away from graphite surface.

All experiments were performed with the robot at a constant levitation height of 100.0 μm . In the experiments carried fluidic channel, 7 different flow rates in ascending order with 10 mL/min intervals were applied to channel and repeated 10 times for each experiment. The data acquired by a laser displacement sensor were plotted in Figure 4.8. Here, the oscillation response of the microrobot depending on varying flow rates was observed. However, while an oscillation response with increasing amplitude was expected, more stable motion and decreasing in oscillation amplitude were observed at the flow rates higher than 15 mL/min in Figure 4.8-C, D, E, F, G. This abnormality can be explained with the resonance width of the system. Forces due to electric charges at rest are more dominant in micro-scale systems than gravitational forces.

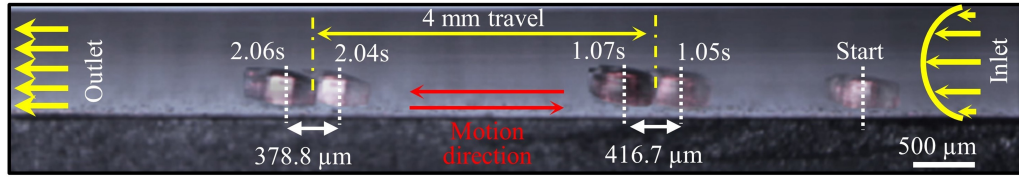


Figure 4.9 presents a side view of this experiment at flow rate of 25 mL/min and microrobot speed of 50 mm/s. From the initial location, the microrobot travelled 4mm away. From its initial position to the final position, the microrobot performed oscillation characteristics as (1.05-1.07 sec), (2.04-2.06 sec) respectively

Vibrations and second order system responses are generated in this case. From the robotic perspective, another reason for not being able to hold microrobot at a single location under a constant stream flow was that our system did not have any active or passive controller.

Microrobot could not remain in a single fixed position and several peaks were observed at displacement values especially below 15 mL/min flow rate. The continuous oscillation hindered our ability to position the microrobot precisely. On the other hand, at higher flow rates the microrobot had more stable characteristics by the means of lower oscillation amplitudes. In Figure 4.7-G and Figure 4.8-G, it can also be also observed that although the microrobot has lower oscillation, instantaneous peak values scaled up and the robot went back and forth till 10388.9 μm then detachment occurred.

The second experiment was conducted where the microrobot was moved 4 mm laterally both towards/against the laminar flow. This experiment was also repeated 10 times for each microrobot speed in the range of 10-50 mm/s for each flow rate (Table 4.2). In each experiment, the speed was increased by 10 mm/s and the microrobot was moved backward and forward. Figure 4.9 presents a side view of this experiment at flow rate of 25 mL/min and microrobot speed of 50 mm/s. In the beginning, the microrobot was standing in the levitation state in the initial position. With flow, the first oscillation had been observed (1.05-1.07 s) and it was successfully moved to 4000 μm away from the initial location. After 4000 μm displacement, the microrobot demonstrated the same oscillation interval (2.04-2.06 s). By the same scenario, Table 4.2 was obtained by measuring lateral displacement of the microrobot subject to different flow rates when it was intended to move 4000 μm . Each value at the intersection of each row & column was averaged over 10 experiments. Here, there is no data available for when the flow speed reaches the detachment point (65 mL/min) and microrobot speed reaches 50 mm/s. Because, it is due to drag force rise at the higher microrobot speeds as it drops resistance against to flow. In Table 4.2, this point was represented as "x".

Table 4.2 Microrobot 4000 μm longitudinal motion experimental results

		Microrobot Speed (mm/s)				
		10	20	30	40	50
Flow Rate (mL/min)	5	4075,4	4024,9	4054,1	3946,6	3988,8
	15	4047.3	3926.5	3973.6	4058.9	4070.7
	25	4030.5	3990.7	3942.4	4054.1	4042.5
	35	3973.9	4004.7	4069.2	3990.5	3982.8
	45	4015.2	4009.9	4127.4	4033.2	3962.6
	55	4014.9	3893.3	4071.9	4081.8	4069.1
	65	4124.4	3942.9	4075.5	3977.9	x

For different microrobot speeds (10-50 mm/s), each distance data was grouped under the respective flow rates. These rates were then shown in Figure 4.10 with means \pm SD (Standard Deviation) values. Data were normalized by flow rate, expressed as means \pm SD, and compared with respect to the microrobot speed by 1-way ANOVA and unpaired t-test (Statview v.5.0, SAS, Cary NC). A P value of <0.05 was considered significant. The results show that there was no major difference between the displacements obtained from different flow rates since p was found as 0.46. The minimum error measured for the lateral displacement of 4000 μm was 0.951% at 35 mL/min and the maximum was 2.106% for 65 mL/min. When the distance between upper lifter magnet and robot was 20 mm (where it was calculated that $\alpha > 27.449^\circ$), in this case, the magnetic force required to levitate the microrobot in the z axis could produce a maximum lateral force of 284.65 nN according to $F_t \tan(\alpha)$. Depending on the magnetic force exerted on the microrobot on the z axis, the rate of lateral force could be found as 51.94%.

After obtaining the theoretical and analysis results of all required parameters, experiments were conducted in the liquid flow regime. First of all, limits of standing microrobot subject to laminar flow were tested in order to find out its detachment point. For this purpose, increasing flows were applied in 5-65 mL/min range and with 10 mL/min intervals. During these experiments, we also have observed that the microrobot had oscillations behavior depending on the flow rates. It had oscillations ranging from 585.6-1125.9 μm at 5 mL/min, 1775.6-2281.3 μm at 15 mL/min, 2757.8-3120.6 μm at 25 mL/min, 3494.4-3843.5 μm at 35 mL/min, 4400.1-4780.7 μm at 45 mL/min, 6027.8-6556.7 at 55 mL/min and 9727.9-10388.0 μm at 65 mL / min. Moreover, It was also observed that the microrobot had higher oscillation frequency at the slower flow rates (5 mL/min and 15 mL/min), in other words, the

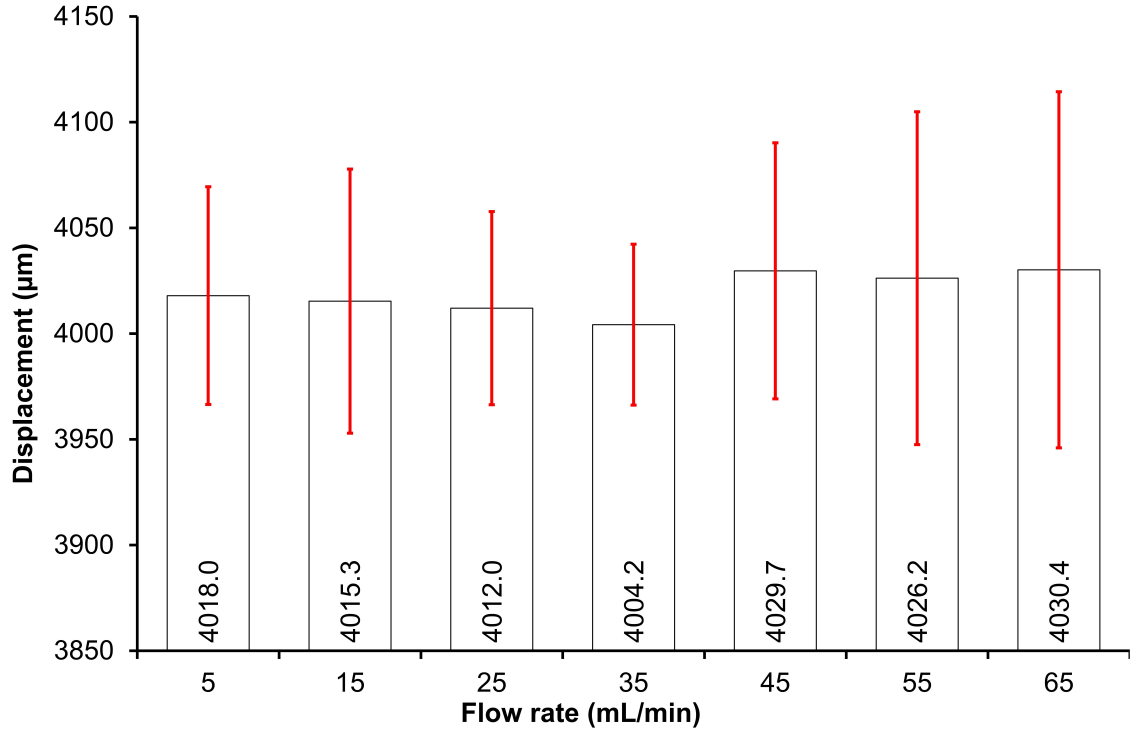


Figure 4.10 SD values of all measured lateral motion results with means for microrobot speeds from 10 mm/s to 50 mm/s are expressed. Although different flow rates and microrobot velocities are applied, displacement and error amounts are similar according to $P < 0.05$ by 1-way ANOVA ($p = 0.46$)

oscillation frequency fallen off as the flow rate risen up. However, some distortions (peaks) were detected in the microrobot position momentarily, which was due to the non-linearity of the magnetic field and flow. These peaks at 65 mL/min distorted the microrobot levitation and shifted from the lifter magnets' central region and caused loss of control. The distance of this point to the center was calculated as $10388.0 \mu\text{m}$ and called as detachment point. This behavior can be explained with the oscillating band width of the system. Electric charges at rest are more dominant in micro-scale systems than gravitational forces.

The longitudinal motion of the microrobot was monitored again under the same flow rates after the displacement experiment. For this purpose, the microrobot was followed up a longitudinal trajectory of 4 mm with 5 different speed values varies between 10-50 mm/s. When the drift force acting on the microrobot increases due to laminar flow, the microrobot can move against flow rate of 65 mL/min at a velocity of 40 mm/s. However, when trying to move the microrobot at a speed of 50 mm/s, the levitation distortion followed the rupture. Furthermore, microrobot's motion accuracy was obtained with a maximum error of 2.106% when it travelled 4 mm distance at different motion speeds (10-50 mm/s). As a result of these experiments, it can be demonstrated that the proposed microrobot is capable of positioning under the

laminar flow regime and follow a longitudinal trajectory in a microchannel.

4.2 Micro-magnet based robot

4.2.1 Materials and Methods

the experimental setup is given in Figure 4.11 in an isometric view. Initially, the microrobot is levitated at the designated starting position, and then a steady-state flow is applied to the channel using a syringe pump. Displacement of the microrobot is then measured by a laser displacement sensor. In Figure 4.12 close-up view of the levitation mechanism is illustrated. A model of the proposed levitation technique is given in Figure 4.13. All calculation steps and assumptions to obtain the corresponding mathematical model are given in detail in this section. Also, free-body diagram of the system, calculation of the forces acting on the microrobot (Figure 4.14) and longitudinal motion model (along the x-axis) are described. Throughout the manuscript, longitudinal motion is the motion of the microrobot along the x-axis, which corresponds to the length of the robot and vertical motion is motion along the z-axis, which acts in the direction of gravitational forces.

4.2.2 CAD Design

In the proposed microrobot manipulation technique, the flow inside the channel is generated by a syringe pump. The position of the microrobot is measured using the laser displacement sensor. The CCD camera, coupled with the optical microscope, is used to obtain the channel's side-view. The motorized linear stage controls the vertical position of the upper and lower magnets. Controlling the vertical position allows us to adjust the microrobot's levitation height inside the channel. A detailed view is shown in Figure 4.12. The pyrolytic graphite layer generates a repulsive force on the microrobot due to its diamagnetic properties ($\mu_r = 0.999991$). The lower magnet is used to increase the longitudinal forces on the robot. With the lower magnet present, the vertical force that the upper magnet needs to generate is higher. The servomotors are used to control the orientation of the upper and lower magnets in 2-DOF, which enables us to control the orientation of the microrobot.

4.2.3 Free Body Diagram

A free body diagram of the proposed technique during longitudinal motion (along the x-axis) is presented in Figure 4.14. In this figure, the two lifter magnets were positioned above and under the channel and aligned along the z-axis. They are N52 grade (Remanence $B_r = 1.43T$, no coating, axially magnetized, Hangzhou YangYi

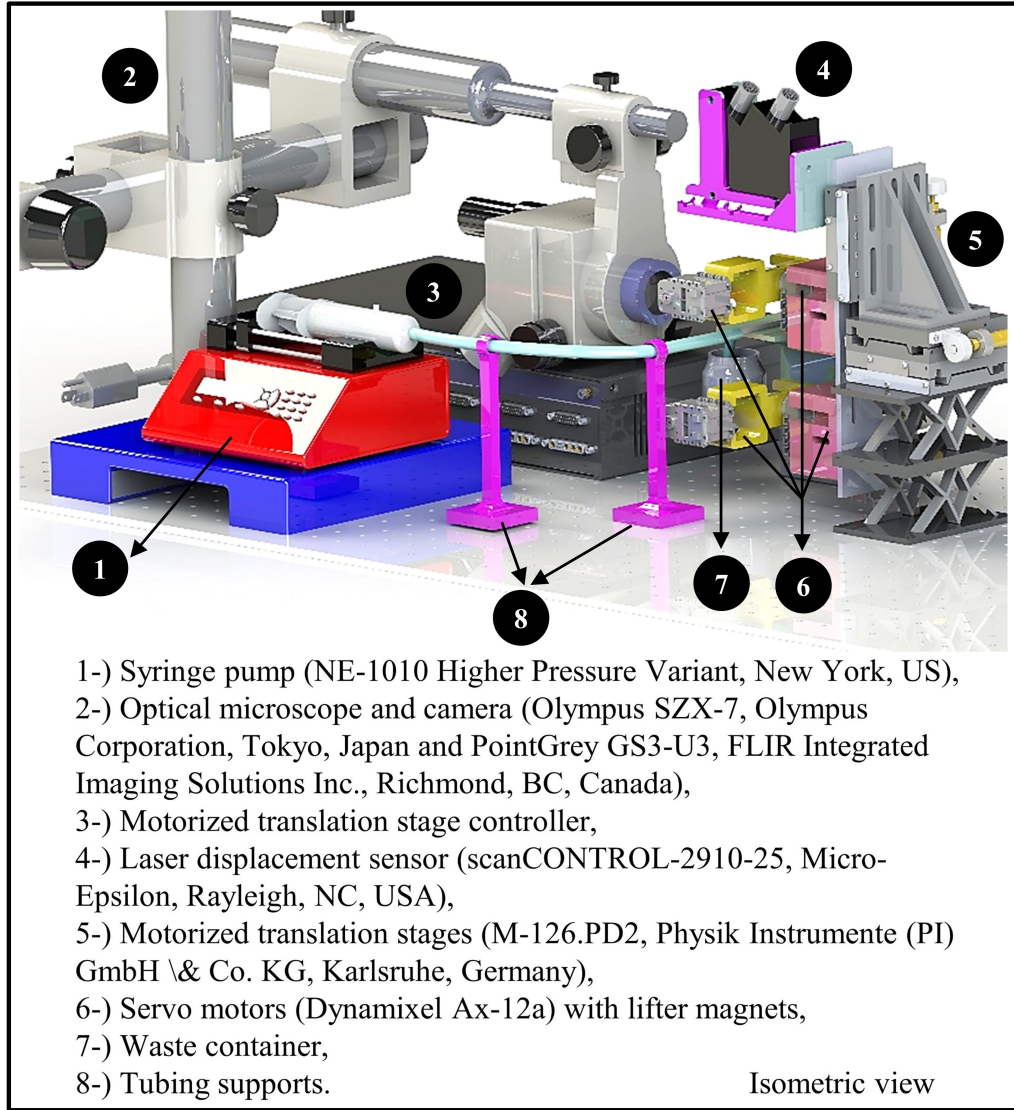


Figure 4.11 Shows an isometric view of the CAD design of the experimental setup,
 © 2021 IEEE, with permission, from ref [115]

Magnetics Co., Ltd) NdFeB and have dimensions of $\varnothing 20\text{mm} \times \varnothing 40\text{mm} \times 8\text{mm}$. N52 grade was used due to its higher concentration of magnetic flux compared to other grades. The N52 grade robot which is called “carrier magnet” has dimensions of $\varnothing 250\mu\text{m} \times 250\mu\text{m}$. The microfluidic channel has a square-shaped cross-section with the dimensions of $900\mu\text{m} \times 900\mu\text{m}$. The pyrolytic graphite on the surface is $7\text{mm} \times 30\text{mm} \times 0.5\text{mm}$. It was expected that the levitated microrobot would not align itself in its initial position due to the drag force caused by the flow applied along the longitudinal axis (-x axis). Thus, microrobot displacement is measured along with the upper lifter and lower lifter magnets center, which is shown as "centerline" in Figure 4.14. The microrobot would have a certain displacement during flow, τ , relative to the magnets' centers. The angles between the upper lifter magnet and lower lifter magnet with the "centerline," which is due to this displacement, were denoted as α

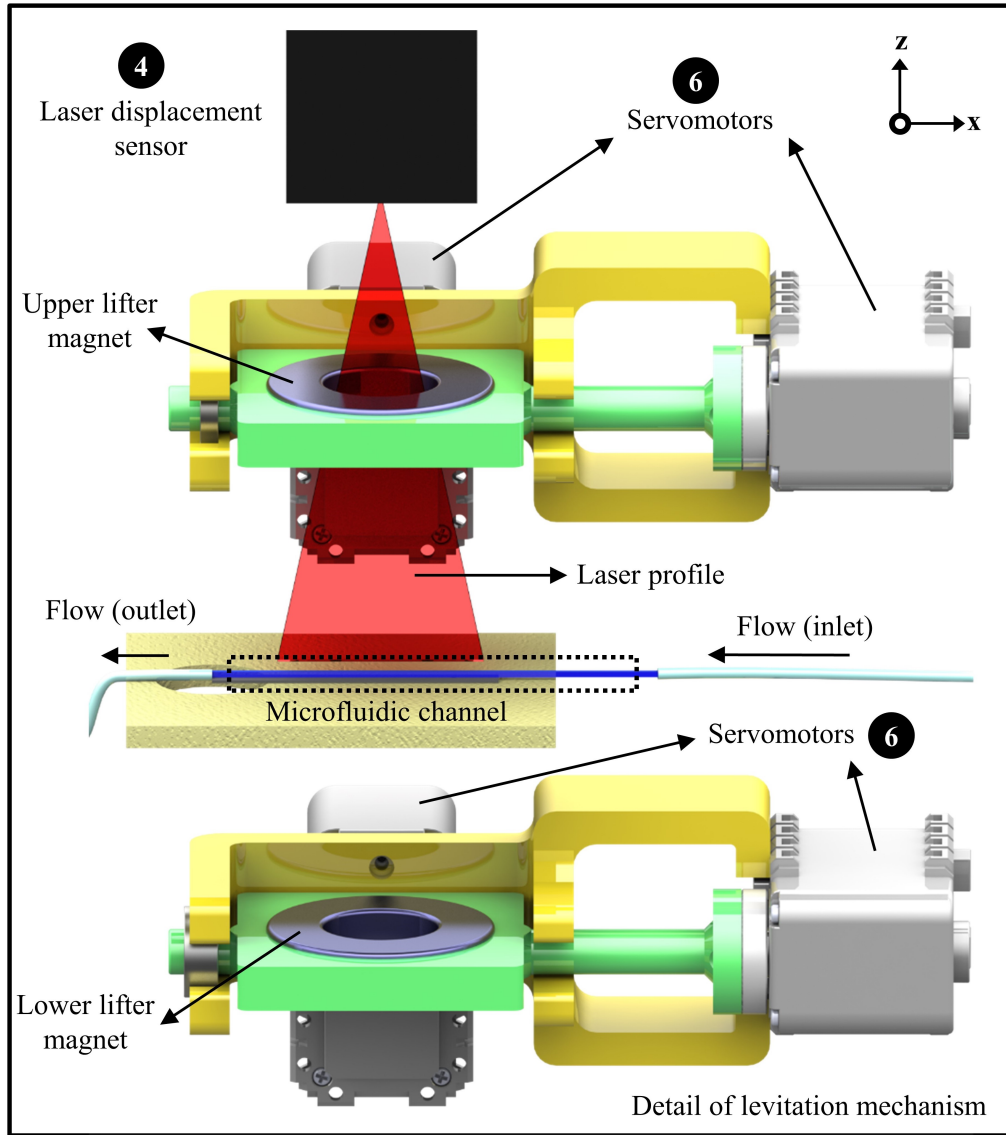


Figure 4.12 Close-up view of the levitation mechanism, © 2021 IEEE, with permission, from ref [115]

and β , respectively.

In Figure 4.14, F_p represents the diamagnetic repulsive force generated by pyrolytic graphite, F_m the magnetic force, F_b the buoyant force, F_g the gravitational force. The drag force, F_d , is shown at a distance, r , from the microrobot center. This offset is a result of the drag force profile acting on the microrobot due to the flow in the channel. This profile, which has a parabolic characteristic, produces different drag forces at different points on the robot surface (Appendix Figure A.2, A.3, A.4 and Figure A.5). By averaging these velocities the microrobot surface; a single resultant force can be obtained which is formed a few microns (denoted as r) down from the center of gravity of the microrobot. Details of the calculation of this force is given in Section 4.2.4. According to free body diagram buoyant and gravitational forces are, $F_b =$

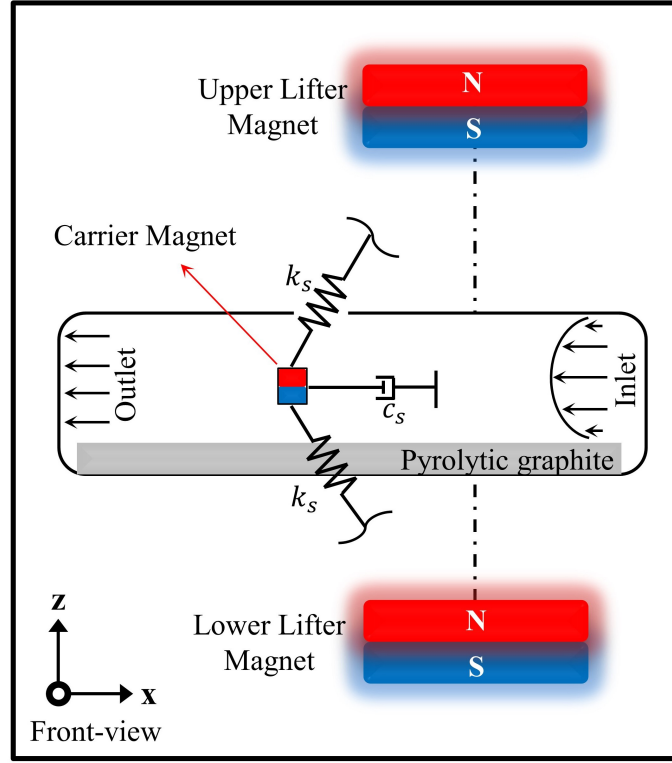


Figure 4.13 A sketch that shows the primary forces acting on the microrobot for the proposed dynamic model. Here the fluidic forces are modeled as a damping element, and the magnetic forces are modeled as spring elements. Magnetic forces can be modeled as spring elements due to the stabilizing nature of the pyrolytic graphite, © 2021 IEEE, with permission, from ref [115]

$V_r(\rho_r - \rho_f)g$ and $F_g = m_r g$, and the moment force is;

$$M_r = F_d r = I_r \ddot{\theta} \quad (4.9)$$

where $I_r = m_r \tau^2$ and θ represents orientation angle of microrobot to the pyrolytic graphite surface and $\ddot{\theta}$ represents angular velocity. The orientation angle of the microrobot can be calculated as

$$\theta(t) = \iint \ddot{\theta}(t) = \iint \frac{F_d r}{m_r \tau(t)^2} \quad (4.10)$$

To calculate θ , F_d and τ must be known. Detailed calculations are shown in Section 4.2.4. Also, for the calculation of F_m and F_p , no explicit analytic formulas were reported [116]. However, detailed calculation steps and the analysis of magnetic forces exerted on microrobots in a fluid medium, was previously reported [32, 109, 117]. The robot was located above pyrolytic graphite and balanced with two lifter

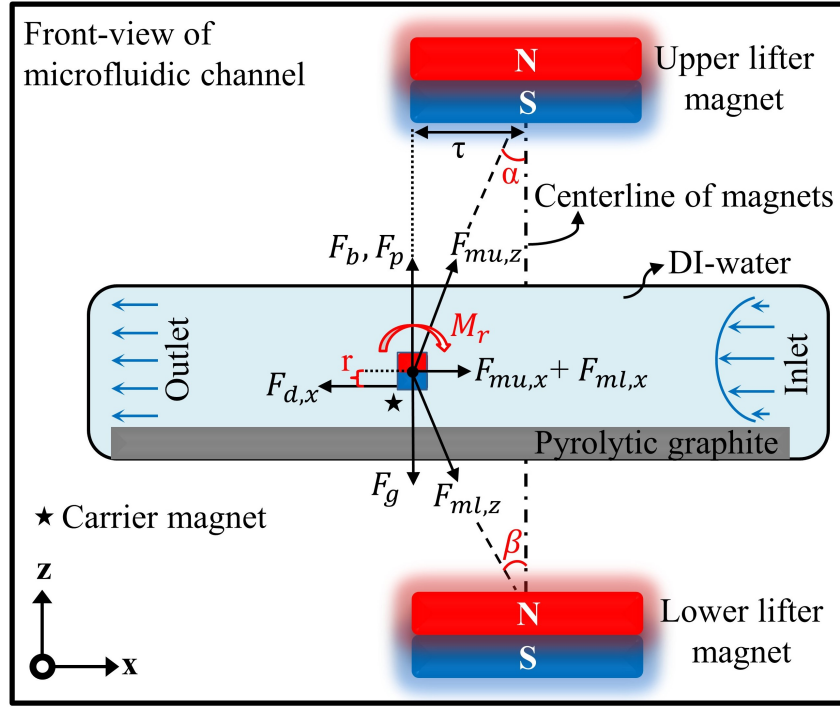


Figure 4.14 Shows a free-body diagram of the robot. The main forces that determine the microrobot's longitudinal motion are the fluidic drag force and the combination of longitudinal components of the magnetic forces due to upper and lower magnets, © 2021 IEEE, with permission, from ref [115]

magnets above and below the channel as described in Section 4.2.2. In this model, the effects of flow and additional lower lifter-magnet were also added to the mathematical model in accordance with previous works. Brownian and atomic forces are neglected in our model since their effects on the micro-scale are insignificant ($< 1\text{nN}$) [118].

4.2.4 Drag Force Calculation

For calculating the drag force, the cross-sectional area of the microrobot during longitudinal movements should be used. Reynolds number was determined based on (4.11) by considering flow rate and microrobot speed.

$$Re = \rho_f D v / \mu \quad (4.11)$$

Here, density of the fluid is denoted by $\rho_f = 998.29(\text{kg/m}^3, 25^\circ\text{C})$, hydraulic diameter by $D = 0.9\text{mm}$ for square-shaped channel, fluid velocity by v , and dynamic viscosity by $\mu = 0.001003\text{ Pas}$. Laminar flow conditions begin to deteriorate when $Re > 2000$, for which the fluid velocity is calculated as $v = 2232.7\text{mm/s}$. For fluid velocities below this value, obtained Reynolds number guarantees that the flow regime stays in

Table 4.3 Parameters of the microrobotic setup

Symbol	Quantity	Value
ρ_r	Robot density	7400kg/m ³
m_r	Robot mass	9.081 × 10 ⁻⁸ kg
V_r	Robot volume	1.2272 × 10 ⁻¹¹ m ³
A_c	Projected surface area	4.9087 × 10 ⁻⁸ m ²
F_b	Buoyant force	0.7703μN
F_g	Gravitational force	0.8904μN
μ_r	Magnetic permeability	0.999991
μ_0	Vacuum permeability	1
B_r	Remanence field	1.43T
χ	Magnetic susceptibility (⊥)	450 × 10 ⁻⁶

the laminar region. Drag force coefficient c_d was calculated in (4.7), $d_A = \sqrt{4A_c/\pi}$ denotes spherical diameter, $d_n = \sqrt[3]{6V_r/\pi}$ denotes nominal diameter, and c denotes the surface sphericity (shape factor) [116]. Calculating these values accordingly, we obtain $d_A/d_n = 0.8736$ and $c = 0.5531$. Using these values and substituting (4.11) in (4.7) for different velocities depending on the respective Re value gives the graph shown in Figure 4.15-A. Since we are working in a laminar flow regime, variations in the c_d value are large at lower flow rates ($c_d \approx 0.49$, $Re > 1000$). Therefore, assuming that the working speed of the robot is in the range of 0–100mm/s, the relevant region of the c_d graph is shown in more detail at Figure 4.15-B. Drag force can be calculated by using the c_d , which is calculated in this figure and for different microrobot speeds, v_r , according to (4.12).

$$F_d = 0.5c_d\rho_f A_c v_r |v_r| \quad (4.12)$$

To determine the robot orientation described in Section 4.2.3, the distance between the microrobot center and the center of drag force, r , needs to be calculated (as shown in Figure 4.14). This calculation is done for 100 μm levitation height, and 1-5 mL/min flow velocity where no-slip boundary conditions were applied (Appendix Figure A.2, A.3, A.4). Additionally, mean velocity values are calculated for each flow rate. The r -value is assumed to be unaffected by changes in flow rate because the standard deviation of this parameter over each flow rate value was determined as ±0.089 mm/s. The maximum error value was thus calculated as %0.3, which is a negligible value (Appendix Figure A.5).

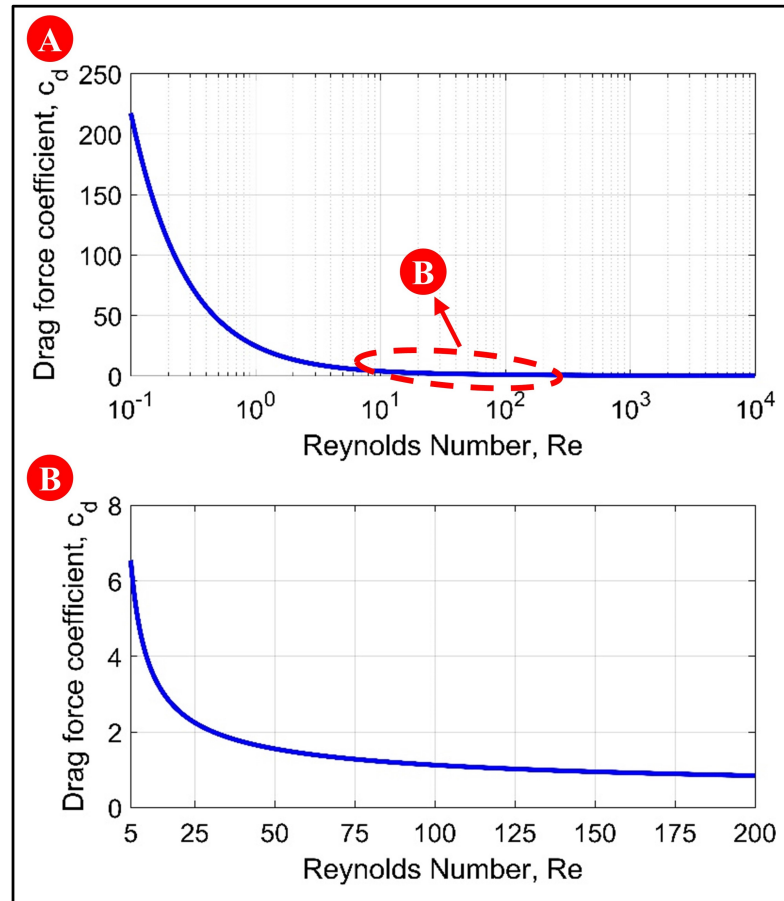


Figure 4.15 (A) Shows the drag coefficient's variation against the Reynolds number for the entire range of laminar flow regime. However, it is calculated that the drag force coefficient for the predicted operating range (0 – 100mm/s) for microrobot and flow rate would be between $0.58 < c_d < 1.85$. The drag force coefficient values in this range shown in great detail in (B), © 2021 IEEE, with permission, from ref [115]

4.2.5 Magnetic Force Calculation

Various formulas in the literature can be used for determining the interactions between identical magnets; however, they can't be utilized for non-identical magnets, as in the case of our configuration [119]. The following procedure was used for the calculation of the magnetic forces between the carrier magnet and the lifter magnets. Firstly, the ring-shaped lifter magnets (Figure 4.16-A) were both assumed as two disc-shaped magnets. The outer diameter of one of these magnets was equal to the outer diameter of the original magnet. The outer diameter of the other magnet was equal to the inner diameter of the original magnet. The magnetic field around the microrobot was calculated for both disc-magnets. The geometric mean of the magnets' resulting magnetic fields was then taken to determine the particular magnetic field of a ring-magnet. As such, the magnetic force acting on the microrobot (Figure 4.16-B) was determined by taking the mathematical integration of the magnetic field magnitude

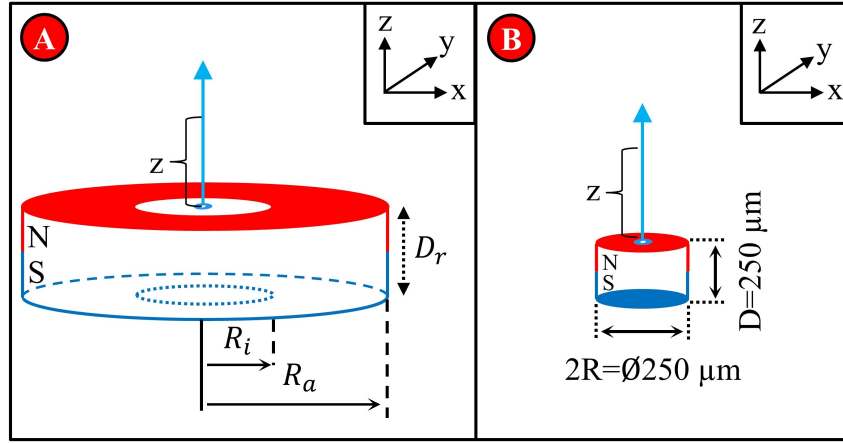


Figure 4.16 (A) Shows the ring-type lifter magnet whose dimensions are $R_i = 20\text{mm}$, $R_a = 40\text{mm}$, $D_r = 8\text{mm}$ and (B) the cylinder-type carrier magnet whose dimensions are shown. These parameters are used to derive the magnetic fields given in (4.13) and (4.14), © 2021 IEEE, with permission, from ref [115]

over the microrobot body (4.16).

The lifter and carrier magnets were illustrated in Figure 4.16-A and 4.16-B respectively. The remanence magnetic field changes with the distance from magnets' center and can be formulated as in (4.13) and (4.14). The magnetic field on the symmetry axis of an axially magnetized ring magnet, B_h [114] is,

$$B_h = \frac{B_r}{2} \left[\frac{D_r + z}{\sqrt{R_a^2 + (D_r + z)^2}} - \frac{z}{\sqrt{R_a^2 + z^2}} \left(\frac{D_r + z}{\sqrt{R_i^2 + (D_r + z)^2}} - \frac{z}{\sqrt{R_i^2 + z^2}} \right) \right] \quad (4.13)$$

where z is the distance from the center of the magnet. The magnetic field on the symmetry axis of an axially magnetized cylinder magnet, B_b [114] is,

$$B_b = \frac{B_r}{2} \left[\frac{D + z}{\sqrt{R^2 + (D + z)^2}} - \frac{z}{\sqrt{R^2 + z^2}} \right] \quad (4.14)$$

To ensure the stability of the microrobot at the levitation point, following criteria (4.15) must be met,

$$\nabla^2 U = -\frac{\chi V}{2\mu_0} \nabla^2 B^2 > 0 \quad (4.15)$$

where potential energy is represented by U , vacuum permeability by μ_0 , magnetic

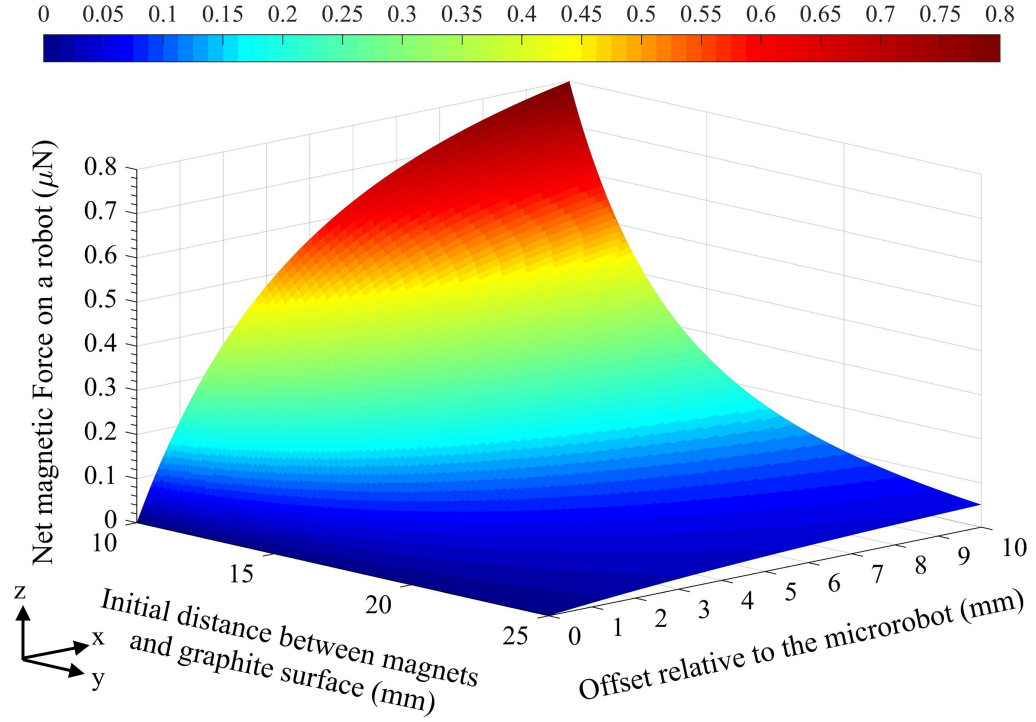


Figure 4.17 The surface graph obtained as a result of the net magnetic force calculation is shown. The x-axis is the distance between the magnets and the graphite; the y-axis shows the offset applied to the lower positioned lifter magnet; the z-axis shows the total magnetic force values. The bar above the figure shows the color map of the force change between 0 – 0.8 μN , © 2021 IEEE, with permission, from ref [115]

susceptibility by χ , and volume by V . Only a diamagnetic material can satisfy this stability condition [120]. The attractive magnetic force, which was applied by a lifter magnet, acting on the microrobot, was expressed in (4.16) in a volumetric form [32, 107, 109],

$$F_m = \frac{\mu_r - 1}{2\mu_0\mu_r} \iiint_v \nabla B^2 dV \quad (4.16)$$

By using parameters in Table 4.3, the net magnetic force required for the levitation of the microrobot on z-axis can be calculated by (4.17),

$$F_t = F_p + F_{mu,z} \cos \alpha - F_{ml,z} \cos \beta \quad (4.17)$$

where $F_t = 0.120 \mu\text{N}$. To obtain F_t , it was necessary to move the upper and lower lifter magnets vertically to the pyrolytic graphite surface in the configuration shown

in Figure 4.12. However, if these two magnets were equidistant from the microrobot, the total magnetic force would be 0 N. The net magnetic force acting on microrobot can be calculated by using (4.13), (4.14), (4.15), (4.16), and it is shown as a surface graph in Figure 4.17. Here, the x-axis represents the lower magnet's displacement from its initial position. The y-axis represents the initial distance between upper and lower magnets and pyrolytic graphite's upper surface at the beginning of the parameter sweep with a constant offset value. In the simulations, the upper and lower magnets initially had the same distance to the microrobot such that the net magnetic force on it was zero. Then, the lower magnet was displaced downward with $1\ \mu\text{m}$ steps in the range of 0-10 mm. This displacement causes the net force on the microrobot to increase exponentially at each step. The F_t value, calculation of which is given in (4.17), corresponds to the net magnetic force required to achieve levitation. The microrobot can be levitated at every point on the surface graph shown in Figure 4.17 corresponding to this value ($0.120\ \mu\text{N}$) on the z-axis. Thus, it can be observed that levitation can be achieved for different initial distance and offset values.

4.2.6 Mathematical Model

In this section, a dynamic motion model of the longitudinal motion of the microrobot is given. The conceptual diagram of the microrobot manipulation technique is given in Figure 4.12. The model of the proposed technique is illustrated in Figure 4.13. This system yields a second-order mathematical model for which the free-body diagram is given in Figure 4.14. In this model, the microrobot is modeled as a mass. The microrobot and fluid interactions are modeled as a damping element. The interactions between magnets, pyrolytic graphite, and microrobot are modeled as a spring element. Damping and spring elements represent the liquid media's hydrodynamic structure and the interactions of permanent magnets with diamagnetic material, respectively.

The spring nature of the magnetic forces can be understood by observing the vertical levitation distance between graphite and microrobot. When microrobot moves downwards (-z-direction in Figure 4.13), pyrolytic graphite generates a higher lifting force on it. Thus, the microrobot can move to its stable position. Similarly, if the microrobot moves upwards, a decrease in the lifting force can compensate for this disturbance and pull the robot downwards.

When the flow is applied through the microrobot, it causes a fluidic pressure on its surface. So the microrobot moves longitudinally (through -x-axis) to the centerline. As the microrobot translates to this pressure, its movement is damped by the water due to its viscosity. The effect of fluidic medium on magnetic interactions can be neglected since the DI-water's magnetic permeability is almost identical to that of air

($\mu_r = 0.999991$). Consequently, drag force exerted on microrobot's surface due to applied flow can be modeled using a damping element. Since the system's dynamic model is constructed using mass-damping-spring elements, the transfer function of a general second-degree system can be used to model the system's dynamic response, as shown in (4.18), where τ is the displacement on the x-axis.

$$\ddot{\tau}(t) + \frac{c_s}{m_r} \dot{\tau}(t) + \frac{2k_s}{m_r} \tau(t) = F_0(t) \quad (4.18)$$

Here, m_r , c_s , k_s and F_0 represents mass, damping, spring coefficients, and disturbance respectively. For this dynamic system; damping ratio, ζ (4.19) and natural resonance frequency, ω_n (rad/s) (4.20), can be calculated as,

$$\zeta = \frac{c_s}{2\sqrt{k_s m_r}} \quad (4.19)$$

$$\omega_n = \sqrt{k_s/m_r} \quad (4.20)$$

where microrobot mass is $m_r = 9.081 \times 10^{-8}$ kg. Viscous damping coefficient acting on a particle within the channel which has a height of $h = 900 \mu\text{m}$, can be determined using (4.21) [121],

$$c_s = \mu A_c / h = 5.4705 \times 10^{-8} (\text{Ns/m}) \quad (4.21)$$

where the projected surface area of the microrobot $A_c = 4.9087 \times 10^{-8} \text{ m}^2$. According to (4.18), k_s is required to determine the dynamic response of the system. In this case, the relationship between the longitudinal force acting on the robot and the robot distance to upper and lower magnets center, τ , should be calculated. In this way, microrobot moves away from the center of the lifter magnets up to a certain distance, and it gives the longitudinal force as shown for the fixed levitation height $h = 100 \mu\text{m}$ in Figure 4.18. In this figure it can be seen that the longitudinal magnetic force has a linear characteristic for small displacements (up to 7.5 mm). This plot has an exponential characteristic when the microrobot moves away from the center of the lifter magnet greater than 7.5 mm. So, the second spring coefficient should be used by curve fitting in the first order. That is why we use two spring coefficients for displacements lower than 7.5 mm and between 7.5 mm and 15 mm by using (4.22).

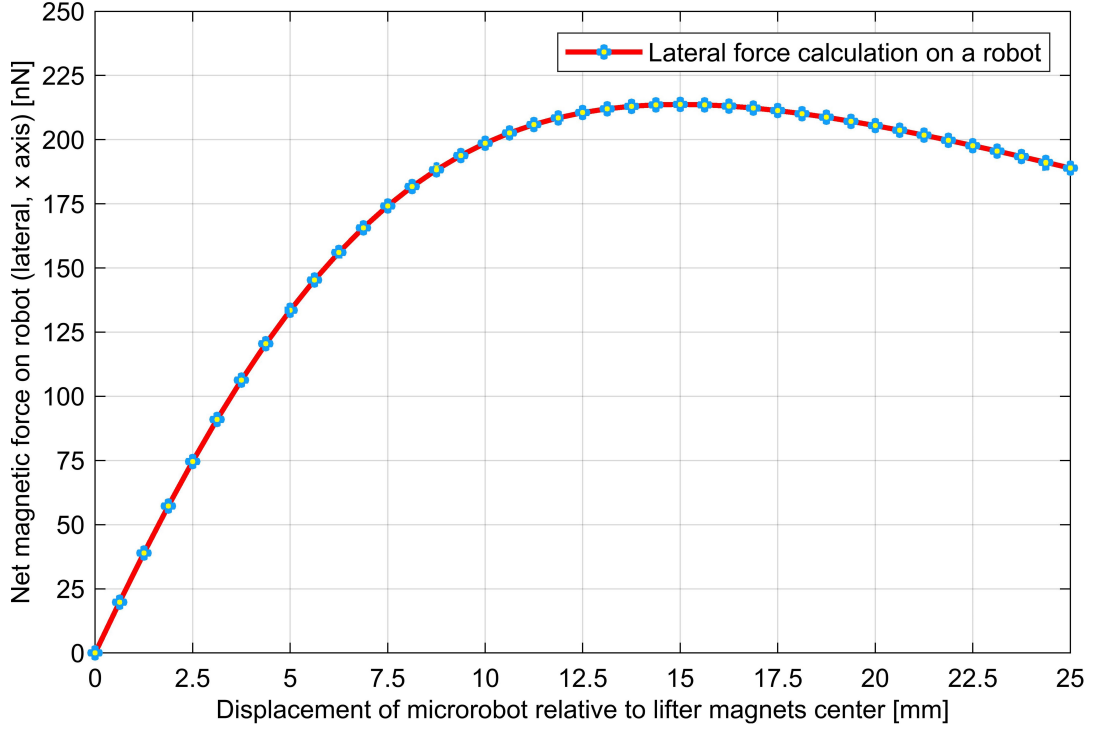


Figure 4.18 The longitudinal force on the microrobot increases linearly as it moves away from the center of the lifter magnets up to a certain distance. The longitudinal magnetic force can be modelled as a spring element due to its linear relationship with displacement. In light of these results, we see that for displacements lower than 7.5mm the spring coefficient can be taken $k = 21.675\text{nN/mm}$. If microrobot displacement is measured greater than 7.5mm, the spring coefficient is switched to the $k = 17\text{nN/mm}$, © 2021 IEEE, with permission, from ref [115]

$$k_s = F_l / \tau \quad (4.22)$$

where F_l is the longitudinal force which can be seen in Figure 4.18. In our case, $k_s = 21.675 \text{ nN/mm}$ and $k_s = 17 \text{ nN/mm}$ is calculated, respectively. After determinations of c_s (4.21) and k_s (4.22) are completed, we can assume that a single external force is applied and equations of the microrobot motion for both values of k_s are obtained from (4.18) as,

$$\ddot{\tau}(t) + 0.602\dot{\tau}(t) + 238.69\tau(t) = F_0(t) \quad (4.23)$$

$$\ddot{\tau}(t) + 0.602\dot{\tau}(t) + 187.13\tau(t) = F_0(t) \quad (4.24)$$

where the maximum disturbance amplitude is F_0 and robot mass, $m_r = 9.081 \times 10^{-8}$

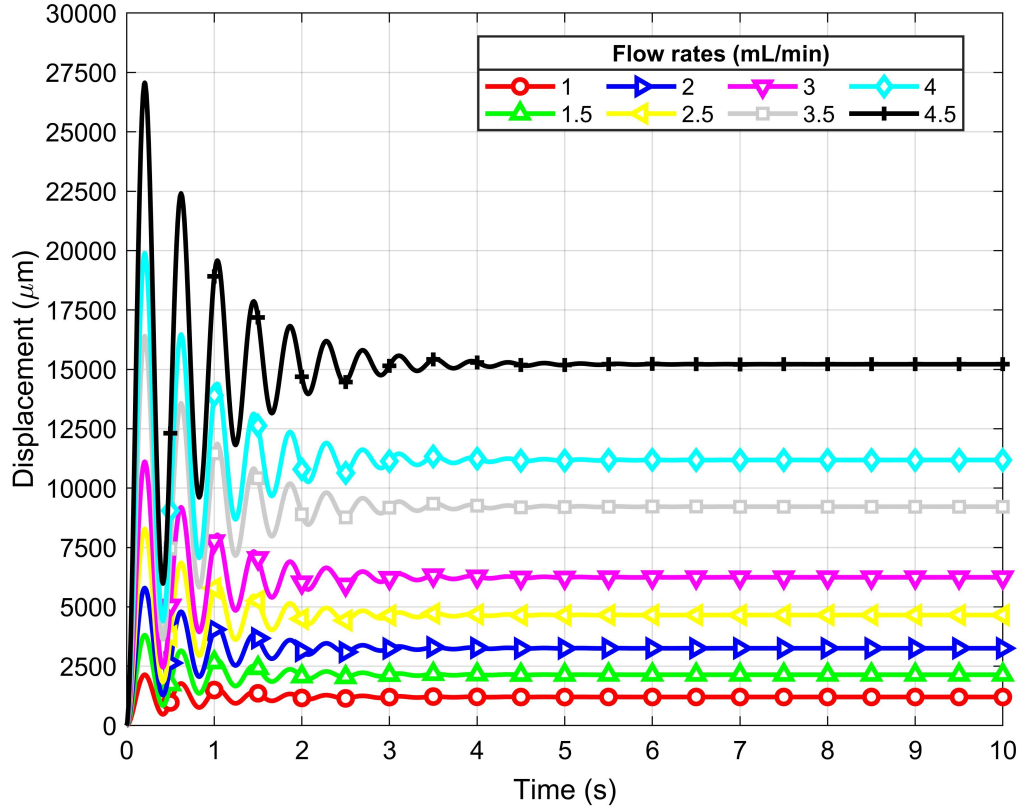


Figure 4.19 Dynamic behavior of the microrobot at different flow rates as predicted by the analytical model. Microrobot exhibits oscillatory behavior due to the magnetic forces' nature. It converges to a stable resting position when the fluidic and magnetic forces are balanced, © 2021 IEEE, with permission, from ref [115]

kg. To obtain the transfer function of the robot motion, time domain equations in (4.23) and (4.24) should be converted to the frequency domain. When initial conditions are set as $\tau(0) = 0$ and $\dot{\tau}(0) = 0$ following transfer function is obtained,

$$\frac{\tau(s)}{F_0(s)} = \frac{1}{s^2 + 0.602s + 238.69} \quad (4.25)$$

$$\frac{\tau(s)}{F_0(s)} = \frac{1}{s^2 + 0.602s + 187.13} \quad (4.26)$$

Responses of these transfer functions to different disturbance amplitudes, F_0 , due to fluid flow are given in Figure 4.19. The natural resonance frequency of (4.23) and (4.24) and the settling time of the system were calculated as $\omega_n = 2.458\text{Hz}$, $\omega_n = 2.177\text{Hz}$ and $t_s = 3.145\text{sec}$ respectively.

The drag force values for different robot velocities are calculated using (4.12).

Subsequently, the r value is substituted in (4.9) and θ values are calculated using (4.10). The orientation angles for flow velocities between 1-4.5 mL/min with 0.5 mL/min steps are calculated as 0.643° , 0.598° , 0.579° , 0.578° , 0.571° , 0.489° , 0.494° and 0.436° respectively. These angles were calculated for the robot's steady-state dynamic solution. As such, the theoretical longitudinal positioning error was determined as $11.015 \pm 3.231 \text{ nm}$. Additionally, a positioning error of $1.161 \pm 0.178 \mu\text{m}$ was calculated in the z-axis due to the deterioration in the parallelity of the microrobot to the surface. However, since the position of the mass center of the robot and the height of its geometrical center doesn't change the effect of this orientation during the robot's movement can be ignored.

In this section, drag force coefficient, c_d , was obtained by using a Finite Element Method (FEM) based program, COMSOL[®] in order to confirm the analytical results (Figure 4.15). Overlapping of analytical and simulation results show the accuracy of the proposed model. For this reason, it is important to determine the relationship between Re and c_d for calculating the drag force more accurately since the rest of the parameters are known in (4.27).

4.2.7 Reynolds Number Effects

A parametric and time-dependent analysis was performed for different flow rates from 0 mL/min to 10 mL/min. In this analysis, fluidic flow around the microrobot was simulated in a square-shape channel ($900 \mu\text{m} \times 900 \mu\text{m}$). No-slip boundary condition is considered in the channel walls (Hydrodynamic entrance length is also given in Appendix Figure A.6). All simulations conducted with a workstation with an AMD Threadripper 1950x (16 real cores) processor with 96 GB RAM and a Windows-10 64-bit operating system using the software COMSOL[®] Multiphysics Version 5.3 (CPU License No: 17076072).

In this analysis, to compare c_d with the analytical results, the microrobot position was kept constant in the channel. The microrobot is assumed to be stationary in the channel. It is a valid simplification since c_d is only affected by the relative velocity between the fluid and microrobot when the cross-sectional area is fixed. Therefore, analyzing a range of flow rates also accounts for when the robot moves inside the channel with the same relative velocity. Assuming the robot is stationary helps reduce the computational time and decrease the complexity of analysis. Drag force coefficient can be calculated by integrating surface tension, F_d , on the robot cross-sectional area, and rest in (4.27).

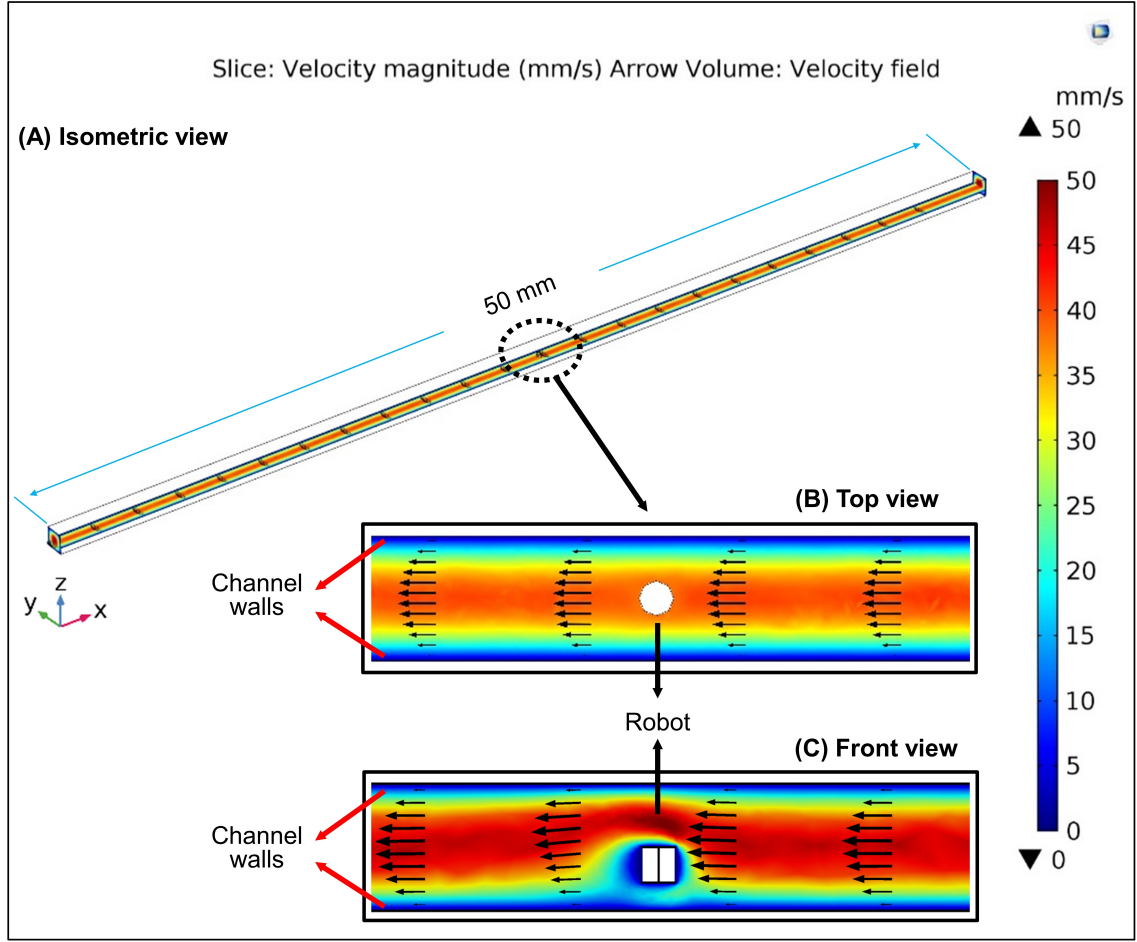


Figure 4.20 The analysis result for a flow rate of 41.6mm/s is shown. The velocity field reaches its maximum at the center of the channel due to the no-slip boundary condition (B) and (C), © 2021 IEEE, with permission, from ref [115]

$$c_d = 2F_d/(\rho_f A_c v_r |v_r|) \quad (4.27)$$

In Figure 4.20, the variation of the flow rate in the channel (longitudinal direction) was isometrically shown when the flow rate was selected as 2.5mL/min. The right and left ends of the channel parallel to the y-z axes refer to the inlet and outlet, respectively. No-slip boundary conditions and gravity are also considered. The black arrows on the figure showed the flow direction, and the characteristic of flow and the velocity vectors at the level of the microrobot was shown in the top view (B) and front view (C) in detail. In (C), it can be observed that the velocity profile acting on the microrobot has exponential characteristics, and it generates a non-symmetrical drag force on the cross-sectional body of the robot. In this way, a different magnitude of the drag force is produced on each point on the robot surface. That is why drag force is shown acting on the robot a few microns down from its center of gravity in Figure 4.14. The change

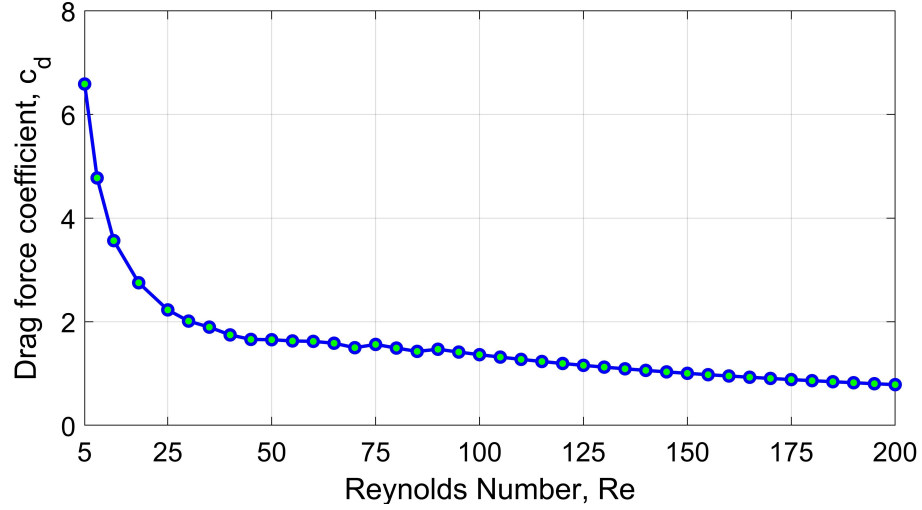


Figure 4.21 The application of different flow rates using the laminar flow-solid mechanics-moving mesh in the COMSOL[®] AC/DC module shows the relationship between c_d and Re. The drag force coefficient is calculated for increasing flow rates with an interval of 0.5mL/min. As the Re value increases, c_d value converges to a constant value (~ 0.49), © 2021 IEEE, with permission, from ref [115]

of drag force coefficient with Re is shown in Figure 4.21, which gives the results of the parametric analysis shown in Figure 4.20. The parametric analysis was performed for every 0.5mL/min step in the range of 0–10mL/min. At each step, F_d and v_r were substituted in (15) and c_d was calculated. The results obtained as such are shown in Figure 4.21. According to the theoretically calculated c_d values shown in Figure 4.15-B, it can be observed that there was an absolute average error value of ± 0.0388 (2.26%) in simulation. On the other hand, both theoretical and simulation results were converged to the same ($c_d = 0.49$) at higher Re ($Re > 2000$).

The microrobot's dynamic behavior inside the fluidic channel is simulated using COMSOL[®] to determine its motion pattern and compare it with the analytical results. In addition to Figure 4.20; the moving mesh, deformable-body, laminar flow, and fluid-structure interaction modules of the COMSOL[®] are utilized in longitudinal motion simulation (Appendix Figure A.7 and detailed Figure A.8 and A.9.)

After analytical and simulation results were obtained, experiments were conducted to analyze microrobot longitudinal motion in the laminar flow regime with the proposed setup.

4.2.8 Stationary Microrobot in Fluidic Flow

The microrobot's longitudinal motion characteristics and immobilization response were studied when the lifter magnets moved towards or against the flow direction.

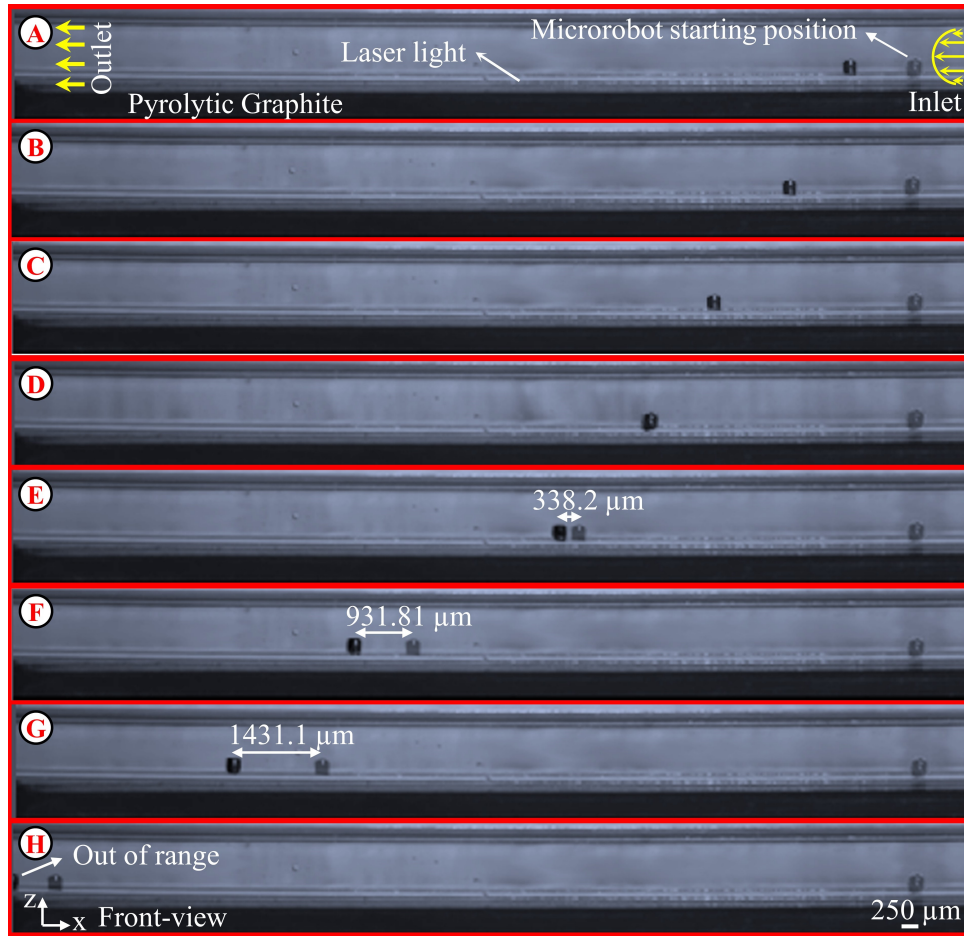


Figure 4.22 The oscillation amplitude of the microrobot subject to laminar flow are presented. When the microrobot reaches its final position, it exhibits an oscillatory motion characteristic due to the interaction of drag and magnetic forces. The oscillation amplitude varies depending on the applied flow rate. The amplitude of oscillation relative to the resting position is shown in (A) 1mL/min, (B) 1.5mL/min, (C) 2mL/min, (D) 2.5mL/min, (E) 3mL/min, (F) 3.5mL/min, (G) 4mL/min, (H) 4.5mL/min. For lower flow rates the oscillation amplitudes were insignificant, © 2021 IEEE, with permission, from ref [115]

In section 4.2.6, the dynamic behavior of the microrobot was studied based on the τ and longitudinal force calculations. Here, the microrobot motion and its accuracy at different speeds were investigated under different flow rates. In the first experiment, the microrobot longitudinal motion characteristics were evaluated at different flow rates ranging from 0.5mL/min to 4.5mL/min with 0.5mL/min intervals when microrobot velocity is zero (Figure 4.22). An optical microscope system records the longitudinal position of the microrobot, and its displacement is measured using the laser displacement sensor given in Figure 4.23. Due to the nature of streamflow and magnetic field, the displacement increased exponentially for higher flow rates. The experiment was repeated 10 times to demonstrate the repeatability of the proposed methodology. Although the microrobot was resistant to flow at 4 mL/min, levitation

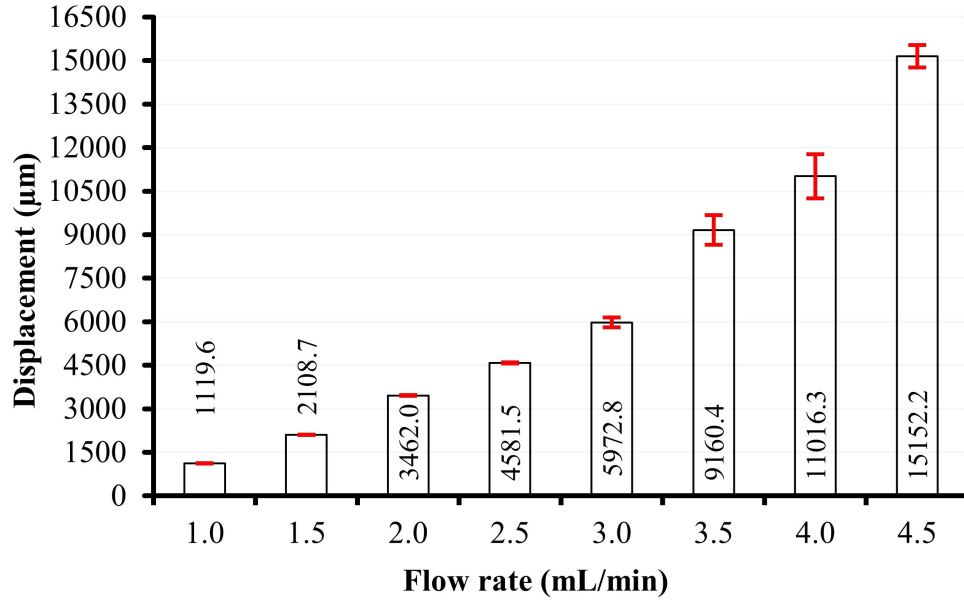


Figure 4.23 Displacement of the microrobot for different flow rates as measured by the laser displacement sensor, © 2021 IEEE, with permission, from ref [115]

stability began to deteriorate at this flow rate. For this reason, the detachment point of the microrobot was also determined. It was calculated that the distance from the detachment point to the starting position was $15152.2\mu\text{m}$. At this point, upper lifter magnet is 19.7mm and lower carrier magnet is 22.8mm away from the graphite surface. All experiments were performed with the robot at a constant levitation height of $100.0\mu\text{m}$ (Appendix Figure A.10 and A.11).

Here, the oscillation response of the microrobot depending on varying flow rates was reported. At flow rates higher than 2.5mL/min , an oscillation response with increasing amplitude and a less stable motion was observed as shown in Figure 4.22-E, F, G, H. Because of non-contact motion and low environment stiffness, the vibrational response of the microrobot approaches the resonance frequency of the system [122]. From the robotic perspective, another reason for not holding microrobot at a single location under a constant stream flow was that our system did not have any active or passive controller. The continuous oscillation hindered our ability to position the microrobot precisely. The microrobot had less stable characteristics due to higher oscillation amplitudes at higher flow rates.

4.2.9 Microrobot Motion in Fluidic Flow

The second experiment was conducted where the microrobot was moved $4000\mu\text{m}$ longitudinally towards and against the flow. It is shown from the side-view in Figure 4.24. Initially, the microrobot was in a levitation state at the starting position. The first oscillation was observed with the flow, and it was successfully moved to $4000\mu\text{m}$ away

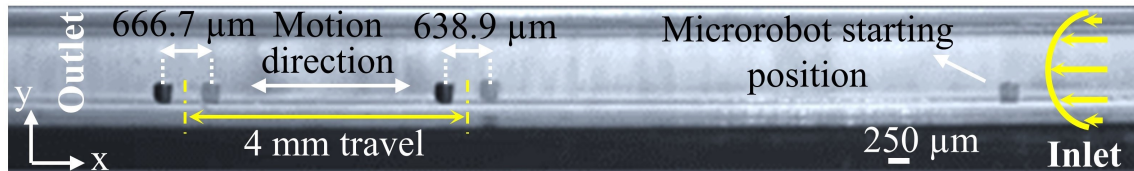


Figure 4.24 Presents a side view of this experiment at a flow rate of 2.8mL/min and a microrobot speed of 50mm/s. From the initial position, the microrobot traveled 4mm in the longitudinal axis. From its initial position to the final position, the microrobot performed oscillatory characteristics, © 2021 IEEE, with permission, from ref [115]

from its initial position. After 4000 μm displacement, the microrobot demonstrated the same oscillation interval. By the same scenario, Table 4.5 was obtained by measuring the longitudinal displacement of the microrobot subject to different flow rates when it was intended to move 4000 μm . Each value at the intersection of each row & column was averaged over 10 experiments. Here, there is no data available for when the flow speed reaches the detachment point (4.5 mL/min) and microrobot speed reaches 50 mm/s. In Table 4.4, this point was represented as "x".

For different microrobot speeds (10–50mm/s), each distance data was grouped under the respective flow rates. These rates were then shown in Figure 4.25 with means \pm SD (Standard Deviation) values. Data were normalized by flow rate, expressed as means \pm SD, and compared to the microrobot speed by 1-way ANOVA and unpaired T-test (Statview v.5.0, SAS, Cary NC). A P value of < 0.05 was considered significant. The results show no major difference between the displacements obtained from different flow rates since P was found as 0.46. The minimum error measured for

Table 4.4 Microrobot 4000 μm longitudinal motion experimental results

		Microrobot Speed (mm/s)				
		10	20	30	40	50
Flow Rate (mL/min)	1	4015,4	4024,9	4004,1	3996,6	3988,8
	1.5	4026,1	3986,7	3993,6	4011,3	4010,2
	2	4047,3	3986,5	3973,6	4058,9	4020,7
	2.5	4030,5	3990,7	3942,4	4054,1	4042,5
	3	3973,9	4004,7	4069,2	3990,5	3982,8
	3.5	4015,2	4009,9	4127,4	4033,2	3962,6
	4	4014,9	3893,3	4071,9	4081,8	4069,1
	4.5	4124,4	3942,9	4075,5	3977,9	x

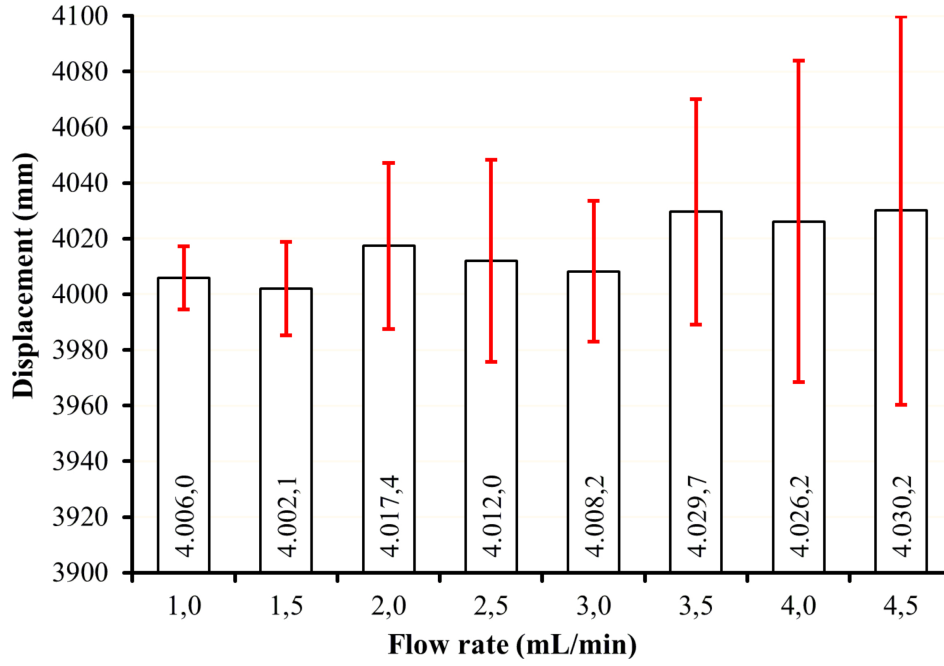


Figure 4.25 Standard deviation values of all measured longitudinal motion results with means for microrobot speeds from 10mm/s to 50mm/s are expressed. Although different flow rates and microrobot velocities are applied, displacement and error amounts are similar according to $P < 0.05$ by 1-way ANOVA ($p=0.46$), © 2021 IEEE, with permission, from ref [115]

the longitudinal displacement of $4000 \mu\text{m}$ for flow rates higher than 2.5mL/min was 0.951% at 2.5mL/min and the maximum was 2.106% for 4mL/min . Comparison of the displacement values determined from the analytical calculations, simulation results, and experimental measurements and error values in comparison with the experimental results are given in Table 4.5.

4.3 Discussion

This study investigates the motion profiles of an untethered microrobot subject to laminar flow. For a microrobot that is intended to be moved towards or against the flow direction, the total net magnetic force's longitudinal component plays a critical role. According to the analytical, simulation, and experimental results, the magnetic field was intensified by our new micromanipulation method. Consequently, the microrobot successfully followed a linear trajectory of 4mm length back and forth at a flow rate of 4.5mL/min (92.6mm/s) and with a velocity of 40 mm/s . At a velocity of 50mm/s , the levitation of the microrobot was distorted. The distance of this point, at which detachment occurred, to the starting point, was calculated as $15152.2\mu\text{m}$. The results of these experiments indicate that the proposed configuration can be used to control the motion of a microrobot under laminar flow conditions and follow a linear trajectory

Table 4.5 Comparison of the displacement values determined from the analytical calculations, simulation results and experimental measurements are given at the upper part of the table. Error values in comparison with the experimental results are given at the bottom part of the table

		Displacement (μm)			Error (%)	
		Analytical	FEM	Experimental	Analytical	FEM
Flow Rate (mL/min)	1	1119.7	1113.8	1196.6	6.43	6.92
	1.5	2139.9	2171.5	2108.7	1.48	2.98
	2	3365.3	3297.7	3462.0	2.79	4.75
	2.5	4676.2	4638.3	4581.5	2.07	1.24
	3	6243.3	6389.8	5972.8	4.53	6.98
	3.5	9217.5	8563.1	9160.4	0.62	6.52
	4	11182.3	11402.2	11016.3	1.51	3.50
	4.5	15217.9	15179.4	15152.2	0.43	0.18

in a microchannel.

One of the most exciting aspects of this manipulation method is that microrobots can be used for continuous-flow microfluidic applications such as on-chip diagnostic methods, liquid biopsy, and hemodialysis. Remarkably, cell manipulation tasks inside microfluidic channels such as cell separation and sorting require a continuous flow to be present. This manipulation technique's ability to withstand substantial longitudinal disturbance forces might be used to increase the ability to perform these tasks accurately. We believe that this method will enable the development of more robust and effective cell manipulation methods.

INCREASING MICROROBOT FLUID RESISTANCE AGAINST TO FLOW

5.1 Materials and Methods

In this section, four different microrobot manipulation methods are presented and compared. Proposed magnetic configurations are based on ferromagnetic permanent ring-shaped magnets (N52 grade, Remanence $B_r = 1.43$ T, no coating, axially magnetized, Hangzhou YangYi Magnetism Co., Ltd) and a thin pyrolytic graphite layer ($500 \mu m$). The aim of this section is to compare the ability of these configurations' ability to increase the stability and the magnetic force imposed on the microrobot during its longitudinal motion. These diamagnetic levitation configurations can be listed as,

- (A) a single magnet above the channel,
- (B) two magnets one of which is below and the other is above the channel,
- (C) two combined magnets both below and above the channel with a smaller magnet concentric to a bigger one,
- (D) two combined magnets both below and above the channel comprising of two identical bigger magnets.

These configurations are tested at the same experimental conditions to validate that "Kerkan configuration" gives a better result. Dimension effect of the lifter magnets was investigated in the previous study, where it was observed that a linear magnetic force could be obtained for an outer diameter range of 25-45 mm [107]. In this study, we compare four configurations in order to demonstrate that the magnetic field lines are more linear and concentrated around the microrobot with the proposed configuration (Kerkan). However, magnetic field orientation is not affected by the size of the magnets. The desired effect of linearized magnetic field lines can only be achieved

when a smaller magnet is used in conjunction with a bigger magnet. The proposed configurations were tested when the microrobot, which is inside a fluidic chip, is levitated at a constant levitation height of $100\ \mu m$. Levitation height is confirmed and monitored in real-time using a laser displacement sensor that is placed above the top ring-shaped magnet. The reasons for using a ring-shaped magnet are as follows:

- Disc-type, cylindrical and cube-shaped magnets are larger than the microrobot size. Since these magnets are axially magnetized and have a more homogeneous magnetic field, it is challenging to align the microrobot to their center. The microrobot can align itself in anywhere of these magnets due to the homogeneous magnetic field distribution. Thus, it is hard to manipulate the microrobot by moving the lifter magnets in 5 DOF. However, the microrobot can be aligned in the ring-type magnets easily. It can be controlled in high precision due to the fact that a ring-shaped magnet creates a higher magnetic gradient that is directed towards the center. In contrast, a solid magnet creates a uniform magnetic field throughout the center of the magnet.
- The ring-shaped magnets have a hole in their center through which the laser beam that was used for measuring the position of the microrobot can pass through. The laser displacement sensor is aligned with the microrobot through the gap in the middle of the ring-shaped structure. In this way, real-time monitoring of the levitation height and longitudinal displacement relative to the magnet's center was realized successfully.

5.1.1 A free body diagram of the microrobot

All of the magnetic configurations and equipment used, including their dimensions, are shown in Figure 5.1. In Figure 5.1-(A), a flow is applied (1) to a microrobot inside the microfluidic channels. The microrobot (2) is positioned $100\ \mu m$ above the channel surface and at the permanent magnet's center named as "bigger magnet" (5). This magnet is connected to the servo motor (6) using a 3D printed holder (4). This servomotor is used for adjusting the microrobot orientation by holding the magnet parallel to the channel surface. Also, microrobot (2) is given by closed-view at the corner. In Figure 5.1-(B), two permanent magnets (5) are used above and below the microfluidic channel. In Figure 5.1-(C), the Kerkan configuration is shown. The difference of this configuration is that smaller diameter permanent magnets (7) are added to the bigger magnets (5). Thus, this configuration makes magnetic field lines more linear on the microrobot surface (please see Figure 5.6). In Figure 5.1-(D), two permanent magnets shown with (5) are placed above and below the fluidic channel.

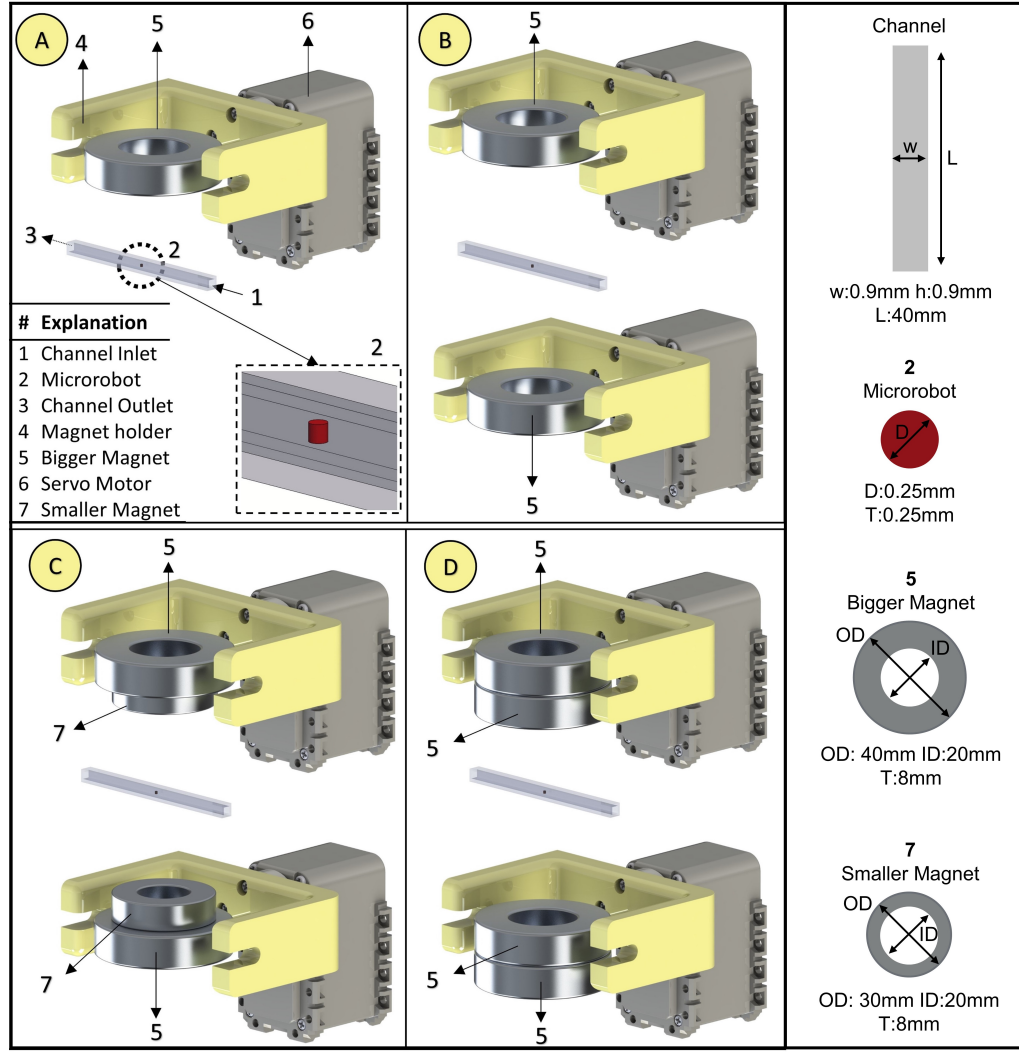


Figure 5.1 The CAD models for four different magnetic levitation configurations named (A) "single," (B) "double," (C) "kerkan," and (D) "double-double" are given in isometric view, respectively. All the equipment's list is given in the bottom left corner of (A), and their dimensions are also available on the figure's right side. W, h, l, d, t, od, id denote width, height, length, diameter, thickness, outer diameter, and inner diameter, respectively

Furthermore, microrobot, magnets, and fluidic channel dimensions are also available on this figure's right side.

The microrobot is imposed by the magnetic (F_m), diamagnetic (F_p), buoyant (F_b), gravitational (F_g), and drag forces (F_d) during its longitudinal motion. The interactions between permanent magnets generate magnetic forces on the robot. Pyrolytic graphite stabilizes microrobot levitation because of its diamagnetic properties. The buoyant force is due to the interaction between water and the untethered microrobot. Lastly, the drag force is a critical component to determine the microrobot motion and stability limit. During the longitudinal motion or to keep

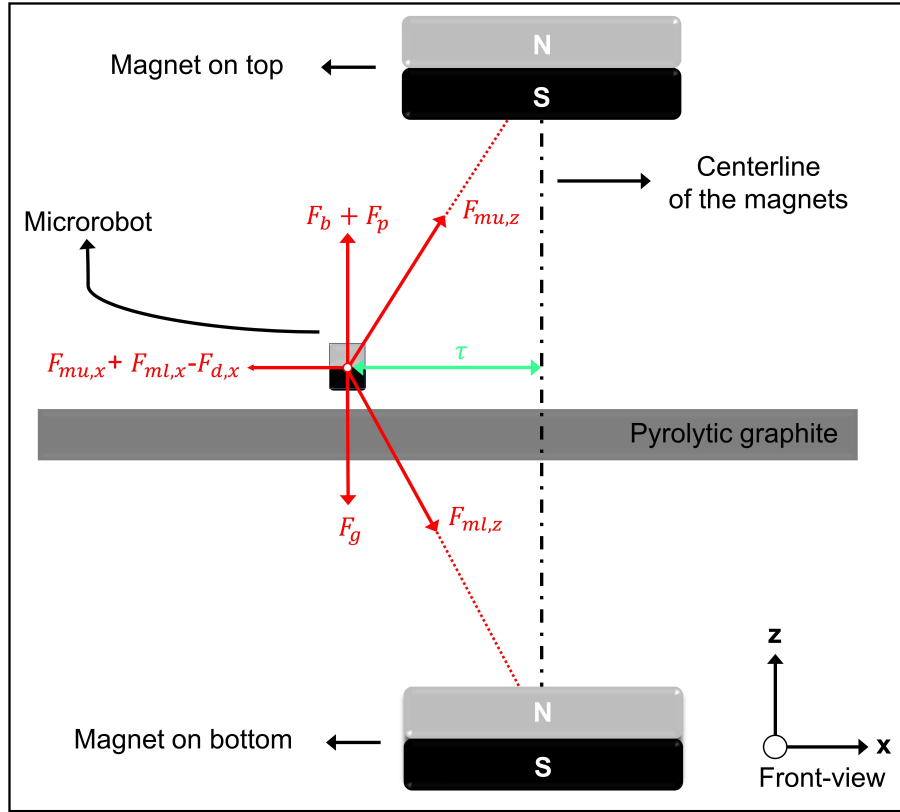


Figure 5.2 A free body diagram of the microrobot during its longitudinal motion is presented with a front view. This diagram can be used for every proposed configuration. For example, all the terms related to the bottom magnet should be removed when single configuration is applied. The magnetic force's magnitude varies for the rest of the configurations only. τ denotes the longitudinal distance from the centerline of the magnets. According to the flow rate, which generates drag force on the microrobot, τ changes exponentially

microrobot in initial position, the net magnetic force acting on the microrobot must be greater than the drag force. This condition should be satisfied in order to move the microrobot in the desired path and the speed. All of the aforementioned forces are illustrated in the Figure 5.2 as a free body diagram. In this figure, two permanent magnets are positioned on the top and the bottom. These magnets aligned with each other, and their center is named "centerline." Microrobot and centerline have a displacement, and it is denoted as τ . The microrobot and the magnets are initially aligned with each other when there is no flow applied on the fluidic channel. However, displacement occurs due to drag force resulting from the increasing amount of flow rate. Hence, the drag force effect on the microrobot can only be balanced (when $\tau = 0$, $\dot{\tau} = 0$) by a net magnetic equal force according to Eq. (5.1).

$$F_{mu,x}(\tau) + F_{ml,x}(\tau) - F_{d,x} = m_r \ddot{\tau} \quad (5.1)$$

Table 5.1 Parameters that were used in the calculation of the forces

Parameter	Value	Unit
F_g	1.588	μN
F_b	0.944	μN
F_d	0.037	μN
F_p	0.484	μN
F_m	0.160	μN
ρ_r	7400	kg/m^3
μ	0.0008891	Ns/m^2
ρ_f	997.050 (25 °C)	kg/m^3
m_r^*	0.162×10^{-6}	kg
g	9.805	m/s^2

Note: "*" Taken SOLIDWORKS (R)

The calculation of the parameters for solving this equation is explained in the following sections.

5.1.2 Analytical Calculations

It is required to calculate the longitudinal forces on the microrobot for each magnetic configuration shown in Figure 5.1 in order to calculate Eq. (5.1). The diamagnetic force which is exerted by the pyrolytic graphite on the microrobot surface can be calculated in a volumetric form as shown in Eq. (5.2).

$$F_p = \frac{\chi_d}{\mu_0} \iiint_V \left(B_x \frac{\partial B_x}{\partial z} + B_y \frac{\partial B_y}{\partial z} + B_z \frac{\partial B_z}{\partial z} \right) dv \quad (5.2)$$

To ensure the stability of the microrobot at the levitation point, Eq. (5.3) should be satisfied,

$$\nabla^2 U = -\frac{\chi V}{2\mu_0} \nabla^2 B^2 > 0 \quad (5.3)$$

where potential energy is represented by U , vacuum permeability by μ_0 , magnetic susceptibility by χ , and volume by V . Only a diamagnetic material can satisfy this stability condition [120]. The magnetic force generated on the microrobot is

calculated in a volumetric form as shown in Eq. (5.4).

$$F_m = \frac{\mu_r - 1}{2\mu_0\mu_r} \iiint_V \nabla B^2 dV \quad (5.4)$$

Gravitational, buoyant and drag forces are calculated as shown in Eq. (5.5–5.7).

$$F_g = m_r g \quad (5.5)$$

$$F_b = V_r(\rho_r - \rho_f)g \quad (5.6)$$

$$F_d = \frac{1}{2}c_d\rho_f A_r v_{fr}^2 \quad (5.7)$$

Reynolds number can be calculated based on Eq. (5.8) by considering predicted operating range 10-150 mm/s [123].

$$Re = \frac{\rho_f v_{fr} l_c}{\mu} \quad (5.8)$$

where v_{fr} is the relative operating velocity between fluid and microrobot, density of the fluid is $\rho_f = 997.05 \text{ kg/m}^3$ (at 25°C), dynamic viscosity is $\mu = 0.0008891 \text{ Ns/m}^2$, and the characteristic length is $l_c = 0.9 \text{ mm}$. Re determines flow characteristics if it is creeping flow ($Re < 1$), laminar flow ($1 < Re < 2 \times 10^5$), or turbulent flow ($2 \times 10^5 < Re$). Here, Reynolds Number is between 8.95 and 134.20 corresponding to flow rates in the range of 0.5 mL/min and 4 mL/min, so the flow is laminar. The momentum equation is given as Eq. (5.9) [124]:

$$\rho \frac{\partial \vec{v}}{\partial t} = -\vec{\nabla} P + \rho \vec{g} + \nu \nabla^2 \vec{v} + \vec{F} \quad (5.9)$$

Here, v is flow velocity, ρ is the density, and p is the pressure. Accordingly, drag coefficient can be calculated in Eq. (5.10) when $2 < Re < 500$ [125],

$$c_d = \frac{24}{Re}(1 + 0.15Re^{0.687}) \quad (5.10)$$

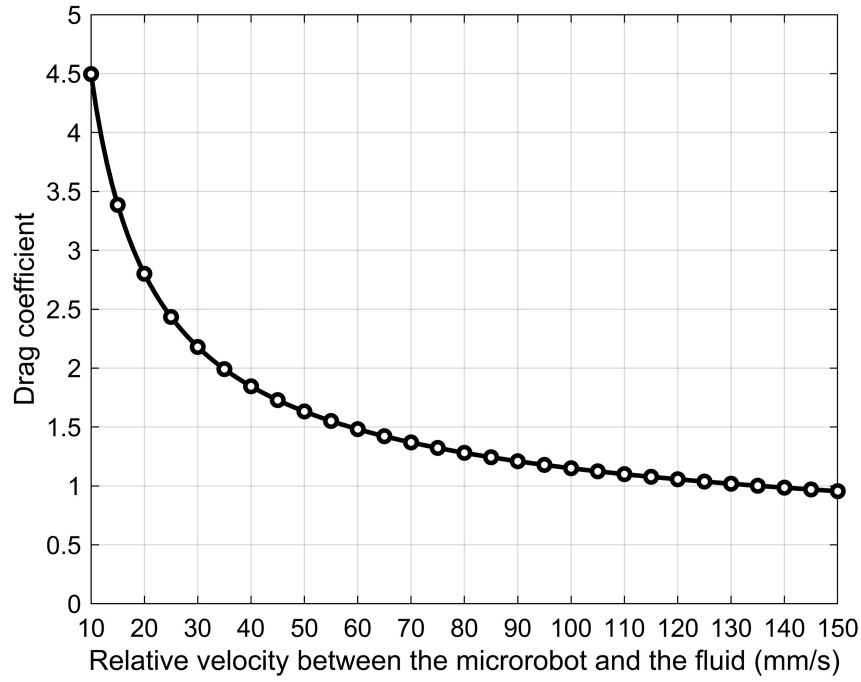


Figure 5.3 Shows the drag coefficient's variation against the relative velocity which is between fluid flow and microrobot for the laminar flow regime. It is calculated that the drag force coefficient for the predicted operating range 10-150 mm/s for microrobot and flow rate would be between $0.95 < c_d < 4.49$

According to the flow rate and boundary conditions (no slip boundary condition) Re is changed in the entire channel as velocity becomes zero near the walls and the maximum in the center. Therefore, the relationship between relative v_{fr} and c_d is given in the Figure 5.3. At the same time, numerical values of the magnetic forces for the configurations are calculated in our previous work [32, 107, 109]. The forces in the free body diagram are calculated when the $v_{fr} = 50$ mm/s and $l_c = 0.9$ mm and they are given in Table 5.1. The force values given in this table is used to calculate the longitudinal forces for all of the microrobot configurations.

5.2 Simulation Results

In this section, the longitudinal displacement of the microrobot, τ in Eq. (5.1), is calculated by using a Finite Element Method (FEM) based program, COMSOL®. The aim is to show Kerkan configuration has lower displacement according to the other configurations we proposed. In this analysis, Fluid-Multibody Interactions with assembly mode are used to observe a solid particle's relationship inside a fluidic environment. Drag force is calculated as a result of "Laminar flow" computation in the fluid module. The magnetic forces acting on the microrobot is calculated by using "Magnetic Fields, No Currents." Magnetic and drag forces are then used in "Multibody

interaction with assembly mode" in order to determine τ in Eq. (5.1). The functions of each of these modules are as follows:

- The mesh structure of the water surrounding robot inside the fluidic channel needs to be modelled using the deformable body module due to the motion of the robot. As the robot moves forward as a rigid body, the deionized water structure displaces so as to compensate for this motion.
- The robot itself is modelled using the moving mesh module since its position changes as a function of elapsed time and the flow rate. However, as the robot body is assumed to be rigid and deformable mesh module is not used in this domain.
- Since the flow regime is laminar in the working flow rates, laminar flow module is used to simulate the fluidic flow inside the channel.
- The drag force exerted on the body of the microrobot is simulated using the fluid-structure interaction module. The force calculated by this module is coupled with the moving mesh module in order to determine the displacement of microrobot meshes at each iteration.

We have performed two different simulations to confirm the levitation point and longitudinal displacement. Firstly, the total net forces acting on the microrobot is calculated when its levitation height is 100 μm . The magnets are then moved in the vertical axis in the 0.1 mm step for finding the total net force on the microrobot is equal to zero. Thus, the microrobot can be held in constant levitation height at 100 μm . Therefore, when, this becomes a levitation point. Secondly, flow rate and microrobot velocity are defined as parametrically. The aim is to observe the effects of the different magnitudes of the parameters' on the simulation results. In this way, it is easy to compare simulation data with the experimental results. Subsequently, after fixing the permanent magnets' vertical positions, the microrobot was moved across the longitudinal axis in a 0.01 mm step from the permanent magnets' center up to 20 mm. The net magnetic forces acting on the microrobot's longitudinal axis is calculated depending on the τ for all magnetic configurations in the same way.

The first step is to build the model of the magnetic field for proposed magnetic configurations. In this research, the magnetic field is induced by ring type one smaller and one larger, and one cylindrical NdFeB magnets with the configurations which is given in Figure 5.1. The magnetic flux density of the permanent magnets is used as

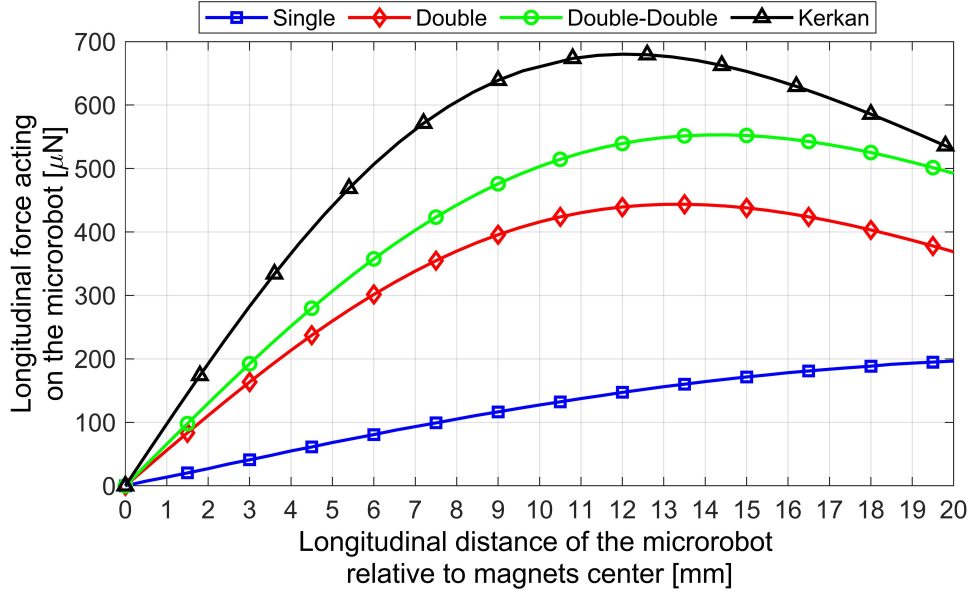


Figure 5.4 Here the longitudinal force on the microrobot is given for four different configurations. Since in the other configurations, the microrobot is subjected to magnetic fields both from above and below, the single configuration generates lower longitudinal forces in comparison. Rest of the magnetic forces' which have another magnet positioned below the channel, pull the microrobot to both sides and make its motion more stable. The magnetic force difference of a maximum of 20% was observed between double and double-double configurations. The reason for this is that there are more magnets in the double-double configuration. Thus, its magnetic field magnitude cause such a difference; however, it can be seen at higher displacement only. In the Kerkan configuration, the magnetic force increases of 43% is observed compared to the double-double configuration. Also, it can be seen that the Kerkan configuration can be effective from the initial position of the microrobot up to 20 mm

1.43T. The magnetic resistivity coefficient for the pyrolytic graphite is given in diagonal form as shown in Eq. (5.11) [120].

$$\chi_d = - \begin{bmatrix} 85 & 0 & 0 \\ 0 & 85 & 0 \\ 0 & 0 & 450 \end{bmatrix} \times 10^{-6} \quad (5.11)$$

Accordingly, the longitudinal forces are calculated and given in Figure 5.4 for the proposed configurations. In this figure, the x-axis represents the distance from the centerline of the magnets. The y-axis represents the net magnetic force that is imposed on the microrobot's longitudinal direction. Four different results can be observed due to the magnetic configuration we proposed: single, double, double-double, and Kerkan. Single configuration generates a lower magnetic force on the microrobot

Table 5.2 Simulation Results of the major parameters with respect to flow rates

		Parameters			
		Re	c_d	v_f (mm/s)	F_d (μN)
Flow Rate (mL/min)	0.5	10.384	4.404	10.288	23.947
	1	20.767	2.750	20.576	60.826
	1.5	31.150	2.143	30.864	110.636
	2	41.534	1.816	41.152	273.377
	2.5	51.917	1.607	51.440	349.050
	3	62.300	1.460	61.728	437.654
	3.5	72.684	1.349	72.017	489.190
	4	83.068	1.263	82.305	553.657

as we expected. The reason is that there is no permanent magnet that can pull the microrobot below. In this way, the magnetic field intensity can not be increased in that configuration. In the double configuration, the magnetic force changes with respect to τ are more linear than other configurations up to 9.5 mm. However, it produces 20% the lower magnetic forces than the double-double configuration. The linear region is shifted around 10.5 mm, and the produces magnetic force is higher. It is observed that Kerkan configuration produces the highest longitudinal forces and increases of 43% is observed compared to the double-double configuration. Here, it is seen that the maximum longitudinal force is achieved when the concentric offset between the magnets was between 11-13 mm. For the other configurations, no such peak values are obtained. Furthermore, the magnetic field lines' concentration is increased over the microrobot, and the result of the force characteristic is taken with a higher slope.

The relationship between the longitudinal displacement in Figure 5.4 can be determined by comparing it with the flow rate that we applied on the microfluidic chip. The flow rate generates the drag force that disrupts the equilibrium and stabilization of the microrobot. The flow rate can be converted into a flow velocity using the dimension of a square-shaped chip. Because the flow rate does not change inside the channel, it can be divided by 0.9 mm x 0.9 mm to have flow velocity. The drag forces is then calculated for the flow rate from 0.5 mL/min to 4 mL/min as shown in Table 5.2. In this table, all the parameters that we determine in our simulations are given. The Reynolds number shows an increasing characteristic with the increasing flow velocity. The drag coefficient is affected due to Re in the environment. Thus, the drag force is varying, and it causes different drag forces to occur for different microrobot speeds. By substituting the magnetic force (Figure 5.2) and drag force

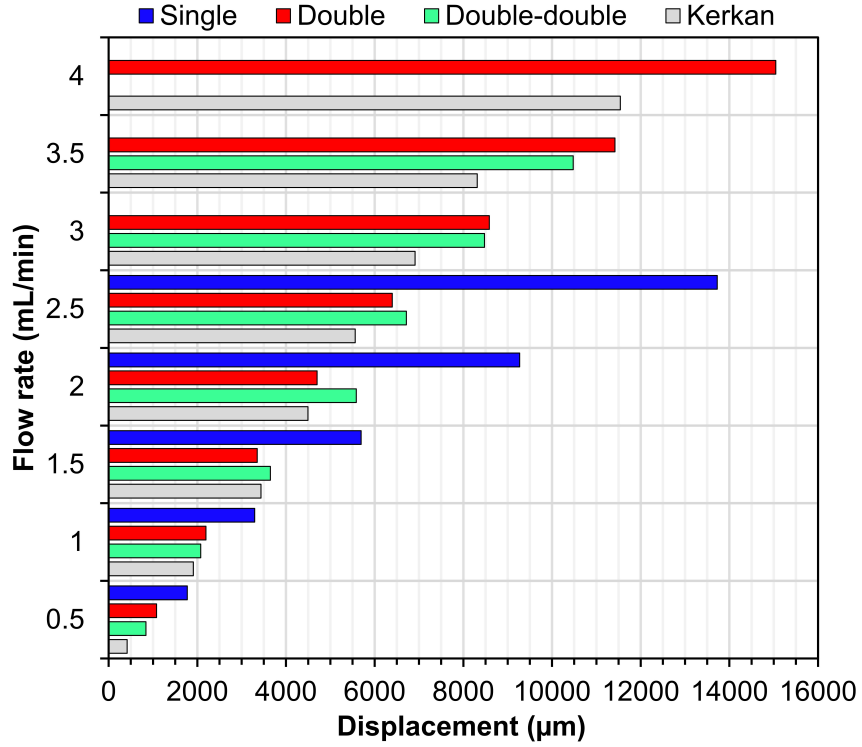


Figure 5.5 Simulation result is obtained with respect to Eq. (5.1) in the COMSOL[®]

(Table 5.2) in Eq. (5.1), the microrobot displacements are calculated as in Figure 5.5. As we expected, the microrobot shows resistance up to a certain point despite the increasing drag force values. However, when it goes out of the linear region, the displacement increases faster. This is because a certain amount of time is required for the decay of the inertial force resulting from the acceleration of the microrobot [32].

The microrobot longitudinal motion's stability is determined by observing the magnetic fields for all magnetic configurations. Kerkan configuration allows us to achieve a more stable levitation and motion of the microrobot. Here in Figure 5.6, the magnetic field lines are in the linear regime in the range of 20 mm on the horizontal axis. Microrobot levitation and longitudinal motion are more stable within this range due to a uniform magnetic field. The reason is that the magnetic field is generated from bigger to smaller magnets. Furthermore, the magnetic field is propagating to the smaller magnet; its intensity increases and can be assumed more point-wise.

5.3 Experimental Results

After analytical and simulation results are obtained, the longitudinal motion experiment is performed in the laminar flow regime with the proposed magnetic configurations. The microrobot's displacement is measured using a laser sensor

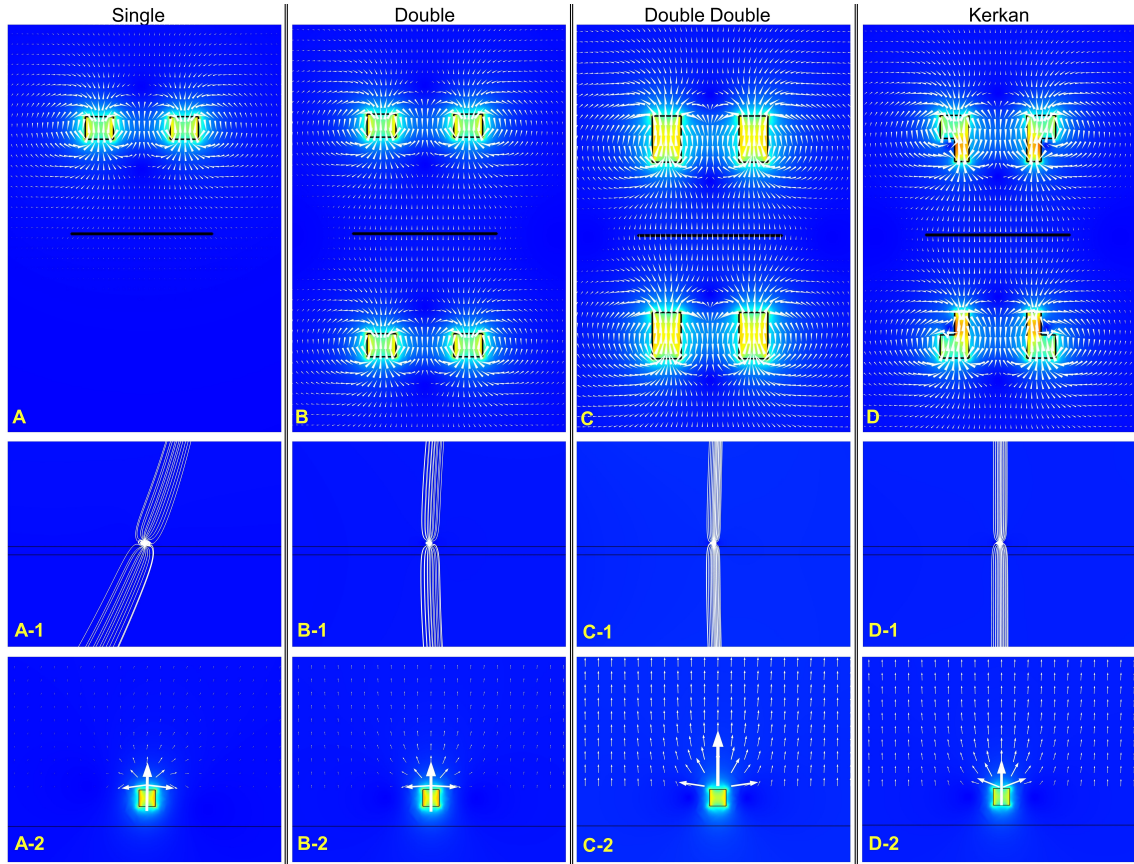


Figure 5.6 (A), (B), (C) and (D) show the general frontal-view of the magnetic field distributions for each configuration respectively. Their close-up view for the magnetic streamlines are demonstrated in (A-1), (B-1), (C-1) and (D-1) when the microrobot is displaced 10 mm from the magnet's centerline. As can be seen from the upper and bottom part of the streamlines, the magnetic field lines are more linear for the Kerkan configuration. Lastly, magnetic field force lines are presented in (A-2), (B-2), (C-2) and (D-2). As can be seen here, the magnetic field lines are given as three dominant vectors that have two horizontal components and one perpendicular. In the Kerkan configuration, horizontal components of the magnetic field force lines are slightly upwards compared to others. Thus, the levitation can be maintained with a more intense and linear magnetic field that is achieved with the Kerkan configuration

when the magnets are held in the initial position. In section 5.1, the microrobot's longitudinal motion is studied based on the τ and force equations. Here, the microrobot displacement is investigated under different flow rates. In this experiment, the microrobot longitudinal motion are evaluated at different flow rates ranging from 0.5mL/min to 4mL/min with 0.5mL/min intervals when microrobot velocity is zero. Firstly, the microrobot is levitated along the z-axis (perpendicular to the pyrolytic graphite surface). The microrobot is then positioned initially for all configurations when the levitation height of 100 μm . The microrobot the distance from the centerline of the magnets is measured in order to compare the magnetic forces generated from magnetic configurations. A lower displacement value indicates that the motion of the

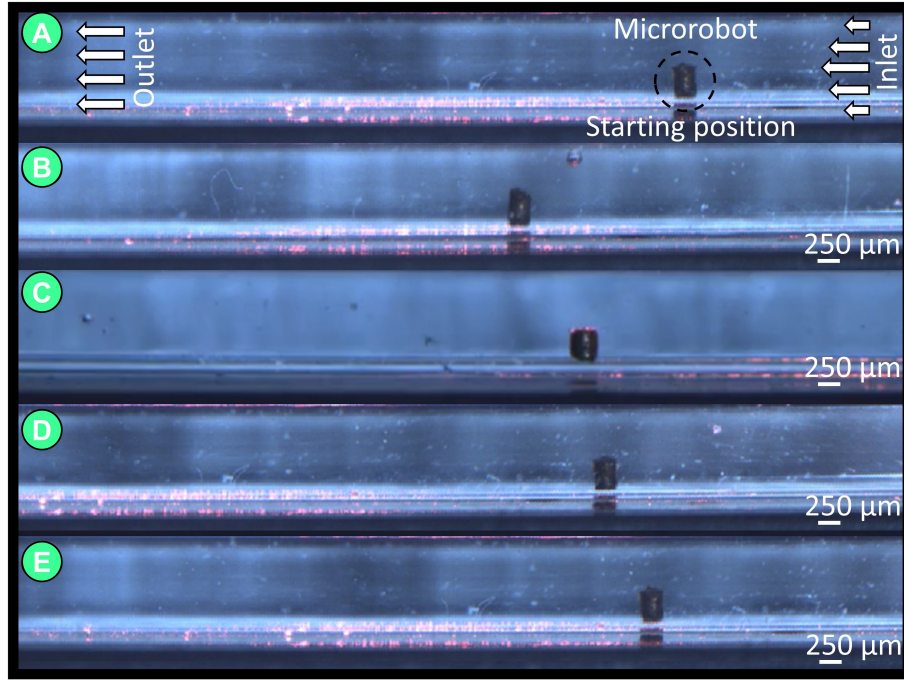


Figure 5.7 Microrobot is shown for four different configurations under 0.5 mL/min flow rate (10.3 mm/s velocity) and at a levitation height of 100 μm . In (A) the initial position of the microrobot is shown for each experiment. (B), (C), (D), and (E) represent magnetic configurations named "Single," "Double," "Double-Double," and "Kerkan" respectively. Analogous to the simulation results, it is observed that the microrobot moved backwards lesser for the Kerkan configuration. The reason for this are the magnetic field lines over the microrobot and the longitudinal forces acting on the microrobot are increased

microrobot can be modeled with a higher stiffness coefficient. As such, it is more resistant to external disturbances and exhibits a more stable behavior. Thus, this test aims to demonstrate the advantage of Kerkan configuration to the microrobot manipulation. For the comparison, the NE-1010 (Higher Pressure Variant, Wantagh, New York, US) syringe pump which has a flow rate capacity of 0-2120 mL/hr is used. During the experiments flow rates is adjusted in the of 0.5-4 mL/min and each experiment is repeated 10 times. The aim is to show the stability and repeatability of the proposed configurations. In Figure 5.7-A, the initial state of the microrobot levitated above the pyrolytic graphite is shown. (A) is the same initial condition for each experiment and configuration. The displacement under 0.5 mL/min flow velocity are shown for (B) Single, (C) Double, (D) Double-Double, and (E) Kerkan configurations. Similar to the simulation results, Kerkan has lower displacement with respect to other configurations. The maximum displacement is observed in Single configuration because of its longitudinal force is the lowest.

A more detailed and numerical comparison of each configuration is given in Figure

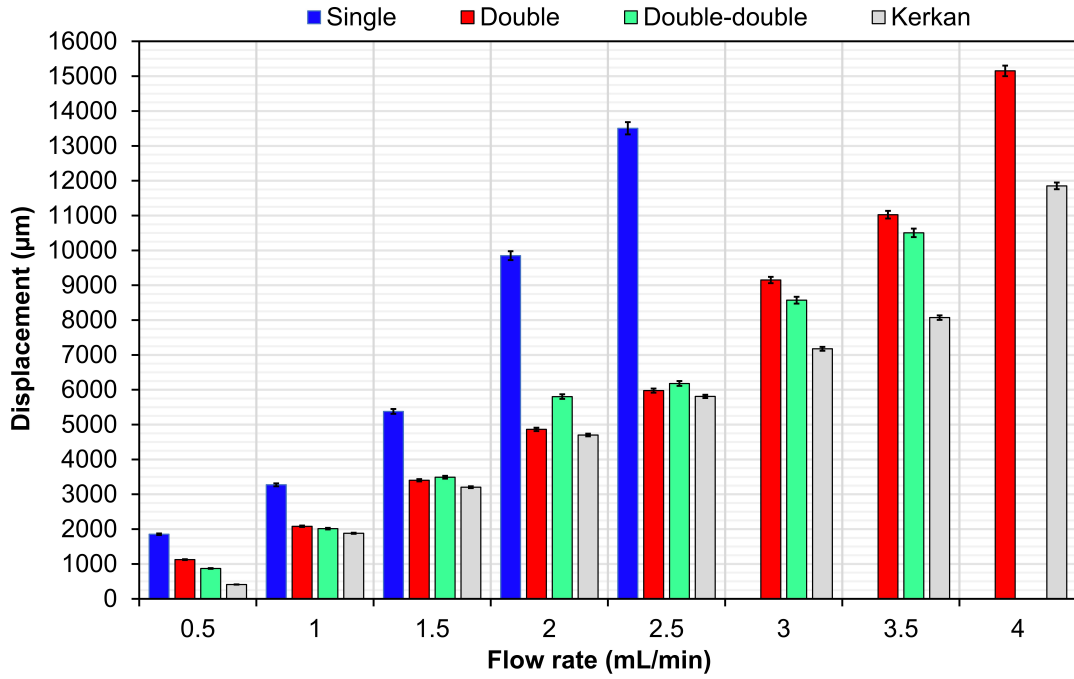


Figure 5.8 For all configurations between 0.5 mL/min and 4 mL/min the displacement values for the microrobot are given. The single configuration was able to withstand the lowest flow rate (2.5 mL/min) due to its low longitudinal force. For all flow rates, higher displacement values were observed

5.8. It is seen that the lowest displacement is observed in the Kerkan configuration. It is demonstrated that with this new configuration, the magnetic field lines in the vertical axis are concentrated on the microrobot body and with the linearized magnetic flux density. In this way, a higher longitudinal force is imposed on the microrobot body. The microrobot breakage point is observed for 2.5 mL/min flow rate for the single configuration. The displacement is increased exponentially with the increasing flow velocity. For the other configurations, the displacement has more linear characteristics than the Single configuration. However, for each flow rate, the lowest displacement value is achieved by the Kerkan configuration. Even though the Kerkan and Double-Double configurations can withstand the same maximum flow rate, the Kerkan configuration had a %21.8 lower displacement value.

The experimental results are shown in Figure 5.8 can be used to validate simulation results. Overlapping of experimental and simulation results show the validation of the proposed magnetic configuration. Comparison between experimental and simulation results are presented as error percentage in Figure 5.9-A and absolute error is demonstrated in Figure 5.9-B. The proposed configuration shows significant improvements in terms of longitudinal forces according to both simulation and experimental results. Furthermore, Figure 5.10 shows the breaking point of the

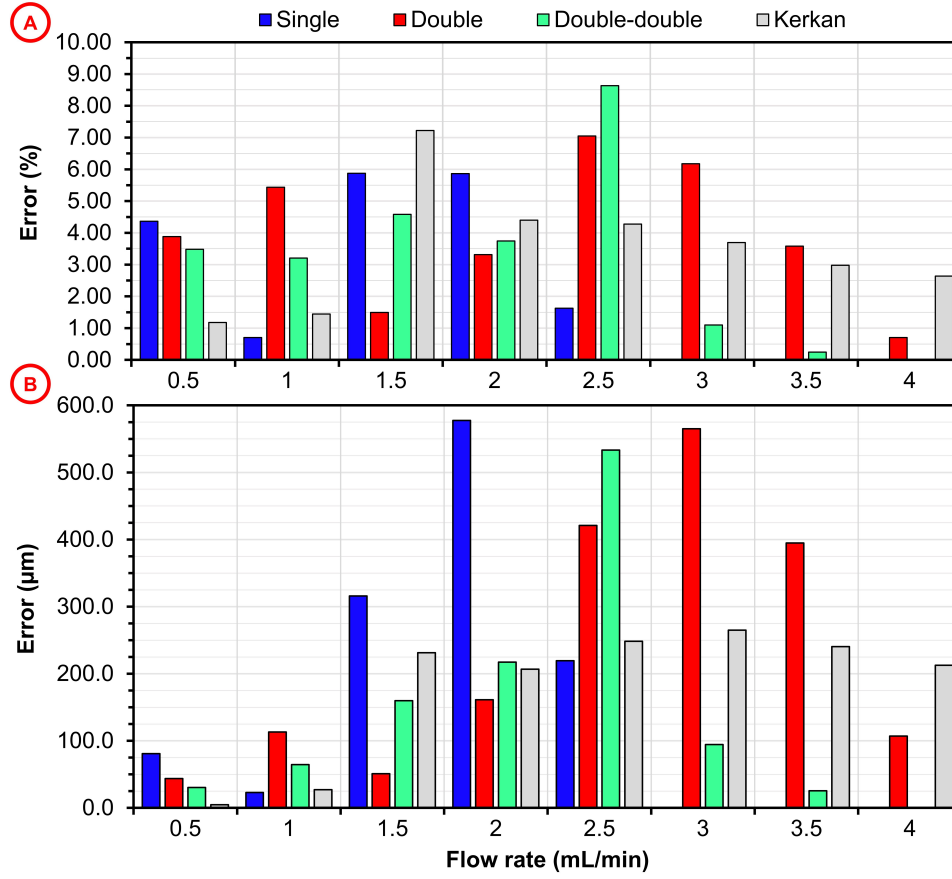


Figure 5.9 (A) shows error as percentage between experimental and simulation results. Also, the mean errors as follows: Single 3.7%, Double 3.9%, Double-Double 3.6%, and Kerkan 3.5%. (B) shows absolute error and their mean as follows: Single 152.1 μm , Double 232.1 μm , Double-Double 140.6 μm , and Kerkan 179.5 μm . As we can see, Kerkan configuration can withstand higher flow rates at almost same amount of error

magnetic configuration at maximum flow rate that they can withstand. Accordingly, the initial starting position of the microrobot for the all magnetic configuration is shown in 5.10-(A). In 5.10-(B), (C), (D), and (E) represent magnetic configurations named "Single," "Double," "Double-Double," and "Kerkan" respectively. These breaking points are and flow rates can be observed in Figure 5.9. Kerkan configuration can withstand at the highest flow rate with lower displacement rather than other configurations.

5.4 Discussion

This work presents a novel magnetic configuration that significantly improves the microrobot's longitudinal forces by generating a linear magnetic field around the microrobot. The magnetic field intensity change rate is adjustable by three axes

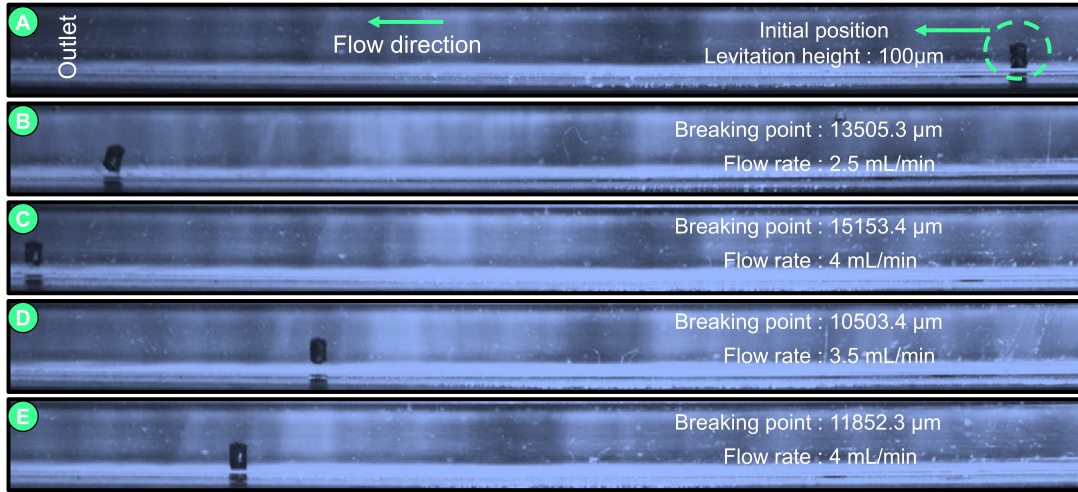


Figure 5.10 (A) shows initial starting position of the microrobot for the all magnetic configuration. (B), (C), (D), and (E) represent magnetic configurations named "Single," "Double," "Double-Double," and "Kerkan" respectively. As we can see that Kerkan configuration can withstand at higher flow rate with lower displacement rather than other configurations

motorized linear stages. This is due to relative differences between microrobot and the magnets that are used for the magnetic manipulation. Additionally, due to the sub-micron resolution of the magnetic manipulation, the proposed configurations are compared with a high accuracy.

Ring-shaped neodymium (NdFeB, N52 grade) permanent magnets are used in the proposed configurations in two different sizes. The levitation height and longitudinal displacement relative to the magnet's center are measured using a laser displacement sensor that is placed above the magnet on top. Since, the laser light should be propagated through the microrobot's upper surface to measure its height and position, the magnets have a gap in the middle of their center. That is why the ring-shaped magnet was preferred to be used. Also, the reflection angle of the sub-micron resolution laser displacement sensor (optoNCDT-ILD2300-50, Micro-Epsilon, Raleigh, NC, USA) is up to 25° . The levitation height and longitudinal displacement can only be calculated by the reflected light. Increasing the magnet layers may cause alignment problems between themselves and can block the reflected laser light from the microrobot surface. Therefore, optimum magnet thickness is selected as 8 mm according to our previous work done.

This study investigates the increasing longitudinal force of the untethered microrobot subject to high rate flow in order to move it in high precision. In microrobot studies intended to be moved in the laminar flow, the total net magnetic force's longitudinal component plays a crucial role. Vertical component of this force is used due to adjusting the levitation height. According to the analytical, simulation, and experimental results, the diamagnetic levitation stabilizes microrobot orientation. After that, the different controllers' effect on the microrobot orientation and their advantages over each other are compared. Although the open-loop (rule-based) controller is more suitable to implement than the other controllers, it requires more time to finish a reference trajectory with a more steady-state error. A less head-tilting angle is measured in the visual-feedback controller; however, detecting the microrobot with $250\text{ }\mu\text{m}$ thickness can be problematic due to optical microscope focal depth in the higher range. The magnetic field is then intensified by our new micromanipulation method named "Kerkan" rather than implementing a controller. Consequently, the microrobot can follow a linear trajectory of 4 mm and can withstand high rate laminar flow at 4.5 mL/min.

Moreover, the microrobot can be moved with a maximum speed of 50 mm/s. Therefore, the relative velocity between the microrobot and flow can be reached up to 132.6 mm/s. At a velocity of 50mm/s, the levitation of the microrobot is distorted, and the breaking point is measured as $15152.2\mu\text{m}$. These experiments show that the proposed method can be used to control microrobot motion under laminar flow conditions. Also, it can follow a linear trajectory at varying levitation heights in a microchannel. Lastly, it is also indicated that the proposed method cannot be affected by microrobot shape and size. One of the most exciting aspects of this manipulation method is that microrobots can be used for applications that require continuous-flow. On-chip diagnostic methods, liquid biopsy, hemodialysis, and cell manipulation tasks inside microfluidic channels such as cell separation and sorting can be some of the most important ones to a continuous flow to be presented. These manipulation techniques

can be used to increase the ability to perform these tasks accurately. This method can develop more robust and effective cell manipulation methods due to its intensified magnetic field with increased magnetic force.

REFERENCES

- [1] M. Medina-Sánchez, L. Schwarz, A.-K. Meyer, F. Hebenstreit, O. Schmidt, “Cellular cargo delivery: Toward assisted fertilization by sperm-carrying micromotors,” *Nano Letters*, vol. 16, Dec. 2015. DOI: 10.1021/acs.nanolett.5b04221.
- [2] Q. Jin, Y. Yang, J. Jackson, C. Yoon, D. H. Gracias, “Untethered grippers for active single cell biopsy,” *Nano Letters*, 2020.
- [3] L. Feng, A. Ichikawa, F. Arai, M. Hagiwara, “Continuous enucleation of bovine oocyte by microrobot with local flow distribution control,” in *2012 International Conference on Manipulation, Manufacturing and Measurement on the Nanoscale (3M-NANO)*, IEEE, 2012, pp. 59–64.
- [4] M. Hagiwara, T. Kawahara, Y. Yamanishi, F. Arai, “Driving method of microtool by horizontally arranged permanent magnets for single cell manipulation,” *Applied Physics Letters*, vol. 97, no. 1, p. 013 701, 2010.
- [5] G. Lucarini, V. Iacovacci, P. J. Gouveia, L. Ricotti, A. Mencias, “Design of a novel magnetic platform for cell manipulation,” *Journal of Micromechanics and Microengineering*, vol. 28, no. 2, p. 025 009, 2018.
- [6] H. Li, G. Go, S. Y. Ko, J.-O. Park, S. Park, “Magnetic actuated ph-responsive hydrogel-based soft micro-robot for targeted drug delivery,” *Smart Materials and Structures*, vol. 25, no. 2, p. 027 001, 2016.
- [7] S. Lee, S. Kim, S. Kim, J.-Y. Kim, C. Moon, B. J. Nelson, H. Choi, “A capsule-type microrobot with pick-and-drop motion for targeted drug and cell delivery,” *Advanced healthcare materials*, vol. 7, no. 9, p. 1 700 985, 2018.
- [8] H. Huang, M. Sakar, A. Petruska, S. Pané, B. Nelson, “Soft micromachines with programmable motility and morphology,” *Nature Communications*, vol. 7, p. 12 263, Jul. 2016. DOI: 10.1038/ncomms12263.
- [9] S. J. Park, S.-H. Park, S. Cho, D.-M. Kim, Y. Lee, S. Y. Ko, Y. Hong, H. E. Choy, J.-J. Min, J.-O. Park, *et al.*, “New paradigm for tumor theranostic methodology using bacteria-based microrobot,” *Scientific reports*, vol. 3, no. 1, pp. 1–8, 2013.
- [10] Q. Jin, Y. Yang, J. Jackson, C. Yoon, D. H. Gracias, “Untethered grippers for active single cell biopsy,” *Nano Letters*, 2020.
- [11] M. Turan, Y. Almalioglu, H. Araujo, E. Konukoglu, M. Sitti, “Deep endovo: A recurrent convolutional neural network (rcnn) based visual odometry approach for endoscopic capsule robots,” *Neurocomputing*, vol. 275, pp. 1861–1870, 2018.

- [12] S. Fusco, M. S. Sakar, S. Kennedy, C. Peters, R. Bottani, F. Starsich, A. Mao, G. A. Sotiriou, S. Pané, S. E. Pratsinis, *et al.*, “An integrated microrobotic platform for on-demand, targeted therapeutic interventions,” *Advanced Materials*, vol. 26, no. 6, pp. 952–957, 2014.
- [13] J. Jeong, D. Jang, S. K. Chung, “Target drug delivery technology (carrying, releasing, penetrating) using acoustic bubbles embedded in an electromagnetically driven microrobot,” in *2018 IEEE Micro Electro Mechanical Systems (MEMS)*, IEEE, 2018, pp. 59–61.
- [14] B. J. Nelson, I. K. Kaliakatsos, J. J. Abbott, “Microrobots for minimally invasive medicine,” *Annual review of biomedical engineering*, vol. 12, pp. 55–85, 2010.
- [15] D. Chang, S. Sakuma, K. Kera, N. Uozumi, F. Arai, “Measurement of the mechanical properties of single *synechocystis* sp. strain pcc6803 cells in different osmotic concentrations using a robot-integrated microfluidic chip,” *Lab on a Chip*, vol. 18, Mar. 2018. DOI: 10.1039/C7LC01245D.
- [16] T. Zhang, M. Zhang, T. Cui, “Microfluidic valves based on tio 2 coating with tunable surface wettability between super hydrophilic and super hydrophobic,” in *2011 16th International Solid-State Sensors, Actuators and Microsystems Conference*, IEEE, 2011, pp. 306–309.
- [17] A. Petrina, “Carbon nanotubes for nanomanipulation,” *Automatic Documentation and Mathematical Linguistics*, vol. 44, no. 1, pp. 44–52, 2010.
- [18] A. Vikram Singh, M. Sitti, “Targeted drug delivery and imaging using mobile milli/microrobots: A promising future towards theranostic pharmaceutical design,” *Current pharmaceutical design*, vol. 22, no. 11, pp. 1418–1428, 2016.
- [19] K. Samsami, S. A. Mirbagheri, F. Meshkati, H. C. Fu, “Stability of soft magnetic helical microrobots,” *Fluids*, vol. 5, no. 1, p. 19, 2020.
- [20] K. Kim, X. Liu, Y. Zhang, Y. Sun, “Nanonewton force-controlled manipulation of biological cells using a monolithic mems microgripper with two-axis force feedback,” *Journal of micromechanics and microengineering*, vol. 18, no. 5, p. 055 013, 2008.
- [21] S. Palagi, A. G. Mark, S. Y. Reigh, K. Melde, T. Qiu, H. Zeng, C. Parmeggiani, D. Martella, A. Sanchez-Castillo, N. Kapernaum, *et al.*, “Structured light enables biomimetic swimming and versatile locomotion of photoresponsive soft microrobots,” *Nature materials*, vol. 15, no. 6, pp. 647–653, 2016.
- [22] E. Kim, S. Jeon, H.-K. An, M. Kianpour, S.-W. Yu, J.-y. Kim, J.-C. Rah, H. Choi, “A magnetically actuated microrobot for targeted neural cell delivery and selective connection of neural networks,” *Science advances*, vol. 6, no. 39, eabb5696, 2020.
- [23] J. Li, X. Li, T. Luo, R. Wang, C. Liu, S. Chen, D. Li, J. Yue, S.-h. Cheng, D. Sun, “Development of a magnetic microrobot for carrying and delivering targeted cells,” *Science Robotics*, vol. 3, no. 19, 2018.
- [24] H. Ceylan, J. Giltinan, K. Kozielski, M. Sitti, “Mobile microrobots for bioengineering applications,” *Lab on a Chip*, vol. 17, no. 10, pp. 1705–1724, 2017.

- [25] K. E. Peyer, L. Zhang, B. J. Nelson, "Bio-inspired magnetic swimming microrobots for biomedical applications," *Nanoscale*, vol. 5, no. 4, pp. 1259–1272, 2013.
- [26] W. Hu, K. S. Ishii, Q. Fan, A. T. Ohta, "Hydrogel microrobots actuated by optically generated vapour bubbles," *Lab on a Chip*, vol. 12, no. 19, pp. 3821–3826, 2012.
- [27] S. Fusco, H.-W. Huang, K. E. Peyer, C. Peters, M. Haberli, A. Ulbers, A. Spyrogianni, E. Pellicer, J. Sort, S. E. Pratsinis, *et al.*, "Shape-switching microrobots for medical applications: The influence of shape in drug delivery and locomotion," *ACS applied materials & interfaces*, vol. 7, no. 12, pp. 6803–6811, 2015.
- [28] K. Mohamed, H. Elgamal, A. Elsharkawy, "Dynamic analysis with optimum trajectory planning of multiple degree-of-freedom surgical micro-robot," *Alexandria Engineering Journal*, vol. 57, Dec. 2018. DOI: 10.1016/j.aej.2018.10.011.
- [29] C. Hu, S. Pané, B. J. Nelson, "Soft micro-and nanorobotics," *Annual Review of Control, Robotics, and Autonomous Systems*, vol. 1, pp. 53–75, 2018.
- [30] D. Di Carlo, "Inertial microfluidics," *Lab on a Chip*, vol. 9, no. 21, pp. 3038–3046, 2009.
- [31] B. Sarkis, D. Folio, A. Ferreira, "Catalytic tubular microjet navigating in confined microfluidic channels: Modeling and optimization," *Journal of Microelectromechanical Systems*, vol. PP, Feb. 2018. DOI: 10.1109/JMEMS.2018.2803803.
- [32] A. A. Demircali, H. Uvet, "Stabilization of microrobot motion characteristics in liquid media," *Micromachines*, vol. 9, p. 363, Jul. 2018. DOI: 10.3390/mi9070363.
- [33] R. L. Urbano, A. M. Clyne, "An inverted dielectrophoretic device for analysis of attached single cell mechanics," *Lab on a Chip*, vol. 16, no. 3, pp. 561–573, 2016.
- [34] L. Xu, F. Mou, H. Gong, M. Luo, J. Guan, "Light-driven micro/nanomotors: From fundamentals to applications," *Chemical Society Reviews*, vol. 46, no. 22, pp. 6905–6926, 2017.
- [35] F. Guo, Z. Mao, Y. Chen, Z. Xie, J. P. Lata, P. Li, L. Ren, J. Liu, J. Yang, M. Dao, *et al.*, "Three-dimensional manipulation of single cells using surface acoustic waves," *Proceedings of the National Academy of Sciences*, vol. 113, no. 6, pp. 1522–1527, 2016.
- [36] X. Yan, Q. Zhou, M. Vincent, Y. Deng, J. Yu, J. Xu, T. Xu, T. Tang, L. Bian, Y.-X. J. Wang, *et al.*, "Multifunctional biohybrid magnetite microrobots for imaging-guided therapy," *Science Robotics*, vol. 2, no. 12, 2017.
- [37] A. J. Petruska, J. Edelmann, B. J. Nelson, "Model-based calibration for magnetic manipulation," *IEEE Transactions on Magnetics*, vol. 53, no. 7, pp. 1–6, 2017.
- [38] M. Xie, "Autonomous robot-aided optical tweezer system for biological cell manipulation," *The International Journal of Advanced Manufacturing Technology*, vol. 105, no. 12, pp. 4953–4966, 2019.

- [39] J. C. Breger, C. Yoon, R. Xiao, H. R. Kwag, M. O. Wang, J. P. Fisher, T. D. Nguyen, D. H. Gracias, "Self-folding thermo-magnetically responsive soft microgrippers," *ACS applied materials & interfaces*, vol. 7, no. 5, pp. 3398–3405, 2015.
- [40] I. S. Khalil, A. F. Tabak, Y. Hamed, M. E. Mitwally, M. Tawakol, A. Klingner, M. Sitti, "Swimming back and forth using planar flagellar propulsion at low reynolds numbers," *Advanced Science*, vol. 5, no. 2, p. 1700461, 2018.
- [41] I. Khalil, V. Magdanz, S. Sanchez, O. Schmidt, S. Misra, "The control of self-propelled microjets inside a microchannel with time-varying flow rates," *Robotics, IEEE Transactions on*, vol. 30, pp. 49–58, Feb. 2014. DOI: 10.1109/TR0.2013.2281557.
- [42] D. R. Frutiger, K. Vollmers, B. E. Kratochvil, B. J. Nelson, "Small, fast, and under control: Wireless resonant magnetic micro-agents," *The International Journal of Robotics Research*, vol. 29, no. 5, pp. 613–636, 2010.
- [43] C. Pawashe, S. Floyd, M. Sitti, "Modeling and experimental characterization of an untethered magnetic micro-robot," *I. J. Robotic Res.*, vol. 28, pp. 1077–1094, Jul. 2009. DOI: 10.1177/0278364909341413.
- [44] W. Hu, G. Lum, M. Mastrangeli, M. Sitti, "Small-scale soft-bodied robot with multimodal locomotion," *Nature*, vol. 554, Feb. 2018. DOI: 10.1038/nature25443.
- [45] P. Ryan, E. Diller, "Magnetic actuation for full dexterity microrobotic control using rotating permanent magnets," *IEEE Transactions on Robotics*, vol. PP, pp. 1–12, Jul. 2017. DOI: 10.1109/TR0.2017.2719687.
- [46] L. Feng, P. Di, F. Arai, "High-precision motion of magnetic microrobot with ultrasonic levitation for 3-d rotation of single oocyte," *The International Journal of Robotics Research*, vol. 35, no. 12, pp. 1445–1458, 2016.
- [47] J. H. Snoeijer, P. Brunet, J. Eggers, "Maximum size of drops levitated by an air cushion," *Physical Review E*, vol. 79, no. 3, p. 036307, 2009.
- [48] O. Sul, M. Falvo, R. Taylor, S. Washburn, R. Superfine, "Thermally actuated untethered impact-driven locomotive microdevices," *Applied Physics Letters*, vol. 89, pp. 203512–203512, Dec. 2006. DOI: 10.1063/1.2388135.
- [49] H. Maruyama, T. Fukuda, F. Arai, "Laser manipulation and optical adhesion control of functional gel-microtool for on-chip cell manipulation," in *2009 IEEE/RSJ International Conference on Intelligent Robots and Systems*, IEEE, 2009, pp. 1413–1418.
- [50] S. Bouchebout, A. Bolopion, J.-O. Abrahamians, S. Régnier, "An overview of multiple dof magnetic actuated micro-robots," *Journal of Micro-Nano Mechatronics*, vol. 7, pp. 97–113, 2012.
- [51] G.-L. Jiang, Y.-H. Guu, C.-N. Lu, P.-K. Li, H.-M. Shen, L.-S. Lee, J. A. Yeh, M. T.-K. Hou, "Development of rolling magnetic microrobots," *Journal of Micromechanics and Microengineering*, vol. 20, no. 8, p. 085042, 2010.
- [52] L. Feng, S. Zhang, Y. Jiang, D. Zhang, F. Arai, "Microrobot with passive diamagnetic levitation for microparticle manipulations," *Journal of Applied Physics*, vol. 122, no. 24, p. 243901, 2017.

- [53] K. Belharet, D. Folio, A. Ferreira, "Control of a magnetic microrobot navigating in microfluidic arterial bifurcations through pulsatile and viscous flow," in *2012 IEEE/RSJ International Conference on Intelligent Robots and Systems*, IEEE, 2012, pp. 2559–2564.
- [54] Q. Fu, S. Guo, Y. Yamauchi, H. Hirata, H. Ishihara, "A novel hybrid microrobot using rotational magnetic field for medical applications," *Biomedical microdevices*, vol. 17, no. 2, p. 31, 2015.
- [55] H.-W. Tung, D. F. Sargent, B. J. Nelson, "Protein crystal harvesting using the rodbot: A wireless mobile microrobot," *Journal of Applied Crystallography*, vol. 47, no. 2, pp. 692–700, 2014.
- [56] Y. Qiu, K. Park, "Environment-sensitive hydrogels for drug delivery," *Advanced drug delivery reviews*, vol. 53, no. 3, pp. 321–339, 2001.
- [57] R. V. Ulijn, N. Bibi, V. Jayawarna, P. D. Thornton, S. J. Todd, R. J. Mart, A. M. Smith, J. E. Gough, "Bioresponsive hydrogels," *Materials today*, vol. 10, no. 4, pp. 40–48, 2007.
- [58] G. Dogangil, O. Ergeneman, J. J. Abbott, S. Pané, H. Hall, S. Muntwyler, B. J. Nelson, "Toward targeted retinal drug delivery with wireless magnetic microrobots," in *2008 IEEE/RSJ International Conference on Intelligent Robots and Systems*, IEEE, 2008, pp. 1921–1926.
- [59] M. Sendoh, K. Ishiyama, K. I. Arai, M. Jojo, F. Sato, H. Matsuki, "Fabrication of magnetic micromachine for local hyperthermia," *IEEE transactions on magnetics*, vol. 38, no. 5, pp. 3359–3361, 2002.
- [60] F. Sato, M. Jojo, H. Matsuki, T. Sato, M. Sendoh, K. Ishiyama, K. I. Arai, "The operation of a magnetic micromachine for hyperthermia and its exothermic characteristic," *IEEE transactions on magnetics*, vol. 38, no. 5, pp. 3362–3364, 2002.
- [61] S. Byun, J.-M. Lim, S.-J. Paik, A. Lee, K.-i. Koo, S. Park, J. Park, B.-D. Choi, J. M. Seo, K.-a. Kim, *et al.*, "Barbed micro-spikes for micro-scale biopsy," *Journal of Micromechanics and Microengineering*, vol. 15, no. 6, p. 1279, 2005.
- [62] A. C. Jones, B. Milthorpe, H. Averdunk, A. Limaye, T. J. Senden, A. Sakellariou, A. P. Sheppard, R. M. Sok, M. A. Knackstedt, A. Brandwood, *et al.*, "Analysis of 3d bone ingrowth into polymer scaffolds via micro-computed tomography imaging," *Biomaterials*, vol. 25, no. 20, pp. 4947–4954, 2004.
- [63] O. Ergeneman, G. Dogangil, M. P. Kummer, J. J. Abbott, M. K. Nazeeruddin, B. J. Nelson, "A magnetically controlled wireless optical oxygen sensor for intraocular measurements," *IEEE Sensors Journal*, vol. 8, no. 1, pp. 29–37, 2008.
- [64] M. Fluckiger, B. J. Nelson, "Ultrasound emitter localization in heterogeneous media," in *2007 29th Annual International Conference of the IEEE Engineering in Medicine and Biology Society*, IEEE, 2007, pp. 2867–2870.
- [65] E. Diller, C. Pawashe, S. Floyd, M. Sitti, "Assembly and disassembly of magnetic mobile micro-robots towards deterministic 2-d reconfigurable micro-systems," *The International Journal of Robotics Research*, vol. 30, no. 14, pp. 1667–1680, 2011.

- [66] H.-W. Tung, M. Maffioli, D. R. Frutiger, K. M. Sivaraman, S. Pané, B. J. Nelson, "Polymer-based wireless resonant magnetic microrobots," *IEEE Transactions on Robotics*, vol. 30, no. 1, pp. 26–32, 2013.
- [67] M. S. Sakar, E. B. Steager, D. H. Kim, M. J. Kim, G. J. Pappas, V. Kumar, "Single cell manipulation using ferromagnetic composite microtransporters," *Applied physics letters*, vol. 96, no. 4, p. 043 705, 2010.
- [68] M. Hagiwara, T. Kawahara, L. Feng, Y. Yamanishi, F. Arai, "High performance magnetically driven microtools with ultrasonic vibration for biomedical innovations," in *2011 IEEE International Conference on Robotics and Automation*, IEEE, 2011, pp. 3453–3454.
- [69] M. Hagiwara, T. Kawahara, Y. Yamanishi, T. Masuda, L. Feng, F. Arai, "On-chip magnetically actuated robot with ultrasonic vibration for single cell manipulations," *Lab on a Chip*, vol. 11, no. 12, pp. 2049–2054, 2011.
- [70] A. Barbot, D. Decanini, G. Hwang, "On-chip microfluidic multimodal swimmer toward 3d navigation," *Scientific reports*, vol. 6, p. 19 041, 2016.
- [71] H. Xie, X. Fan, M. Sun, Z. Lin, Q. He, L. Sun, "Programmable generation and motion control of a snakelike magnetic microrobot swarm," *IEEE/ASME Transactions on Mechatronics*, vol. 24, no. 3, pp. 902–912, 2019.
- [72] S. E. Chung, X. Dong, M. Sitti, "Three-dimensional heterogeneous assembly of coded microgels using an untethered mobile microgripper," *Lab on a Chip*, vol. 15, no. 7, pp. 1667–1676, 2015.
- [73] F. Munoz, G. Alici, H. Zhou, W. Li, M. Sitti, "Analysis of magnetic interaction in remotely controlled magnetic devices and its application to a capsule robot for drug delivery," *IEEE/ASME Transactions on Mechatronics*, vol. 23, no. 1, pp. 298–310, 2017.
- [74] O. Erin, J. Giltinan, L. Tsai, M. Sitti, "Design and actuation of a magnetic millirobot under a constant unidirectional magnetic field," in *2017 IEEE International Conference on Robotics and Automation (ICRA)*, IEEE, 2017, pp. 3404–3410.
- [75] C. Pawashe, S. Floyd, M. Sitti, "Modeling and experimental characterization of an untethered magnetic micro-robot," *The International Journal of Robotics Research*, vol. 28, no. 8, pp. 1077–1094, 2009.
- [76] L. Feng, M. Hagiwara, A. Ichikawa, F. Arai, "On-chip enucleation of bovine oocytes using microrobot-assisted flow-speed control," *Micromachines*, vol. 4, no. 2, pp. 272–285, 2013.
- [77] G. Lucarini, S. Palagi, A. Levi, B. Mazzolai, P. Dario, A. Menciassi, L. Beccai, "Navigation of magnetic microrobots with different user interaction levels," *IEEE Transactions on Automation Science and Engineering*, vol. 11, no. 3, pp. 818–827, 2014.
- [78] M. Boukallel, E. Piat, J. Abadie, "Passive diamagnetic levitation: Theoretical foundations and application to the design of a micro-nano force sensor," in *Proceedings 2003 IEEE/RSJ International Conference on Intelligent Robots and Systems (IROS 2003)*(Cat. No. 03CH37453), IEEE, vol. 2, 2003, pp. 1062–1067.

- [79] R. E. Pelrine, *Magnetic field levitation*, US Patent 5,396,136, 1995.
- [80] C. Siyambalapitiya, G. De Pasquale, A. Soma, "Experimental identification of rare-earth magnetic suspensions for micro and meso scale levitating systems," *Smart Structures and Systems*, vol. 10, no. 2, pp. 181–192, 2012.
- [81] X. Wang, S. Palagummi, L. Liu, F. Yuan, "A magnetically levitated vibration energy harvester," *Smart Materials and Structures*, vol. 22, no. 5, p. 055 016, 2013.
- [82] M. Frenea-Robin, H. Chetouani, N. Haddour, H. Rostaing, J. Laforet, G. Reyne, "Contactless diamagnetic trapping of living cells onto a micromagnet array," in *2008 30th Annual International Conference of the IEEE Engineering in Medicine and Biology Society*, IEEE, 2008, pp. 3360–3363.
- [83] G. R. Souza, J. R. Molina, R. M. Raphael, M. G. Ozawa, D. J. Stark, C. S. Levin, L. F. Bronk, J. S. Ananta, J. Mandelin, M.-M. Georgescu, *et al.*, "Three-dimensional tissue culture based on magnetic cell levitation," *Nature nanotechnology*, vol. 5, no. 4, pp. 291–296, 2010.
- [84] P. Kauffmann, P. Pham, A. Masse, M. Kustov, T. Honegger, D. Peyrade, V. Haguët, G. Reyne, "Contactless dielectrophoretic handling of diamagnetic levitating water droplets in air," *IEEE transactions on magnetics*, vol. 46, no. 8, pp. 3293–3296, 2010.
- [85] H. Profijt, C. Pigot, G. Reyne, R. Grechishkin, O. Cugat, "Stable diamagnetic self-levitation of a micro-magnet by improvement of its magnetic gradients," *Journal of magnetism and magnetic materials*, vol. 321, no. 4, pp. 259–262, 2009.
- [86] C. Pigot, H. Chetouani, G. Poulin, G. Reyne, "Diamagnetic levitation of solids at microscale," *IEEE Transactions on Magnetism*, vol. 44, no. 11, pp. 4521–4524, 2008.
- [87] R. Pelrine, A. Hsu, A. Wong-Foy, B. McCoy, C. Cowan, "Optimal control of diamagnetically levitated milli robots using automated search patterns," in *2016 international conference on manipulation, automation and robotics at small scales (MARSS)*, IEEE, 2016, pp. 1–6.
- [88] L. Feng, Q. Zhou, B. Song, Y. Feng, J. Cai, Y. Jiang, D. Zhang, "Cell injection millirobot development and evaluation in microfluidic chip," *Micromachines*, vol. 9, no. 11, p. 590, 2018.
- [89] T. Yamanaka, F. Arai, "Self-propelled swimming microrobot using electroosmotic propulsion and biofuel cell," *IEEE Robotics and Automation Letters*, vol. 3, no. 3, pp. 1787–1792, 2018.
- [90] G. Bracker, X. Xiao, J. Lee, M. Reinartz, S. Burggraf, D. Herlach, M. Rettenmayr, D. Matson, R. Hyers, "Modeling of fluid flow effects on experiments using electromagnetic levitation in reduced gravity," in *Materials Processing Fundamentals 2019*, Springer, 2019, pp. 171–180.
- [91] R. Diehl, E. Hebestreit, R. Reimann, F. Tebbenjohanns, M. Frimmer, L. Novotny, "Optical levitation and feedback cooling of a nanoparticle at subwavelength distances from a membrane," *Physical Review A*, vol. 98, no. 1, p. 013 851, 2018.

- [92] A. Watanabe, K. Hasegawa, Y. Abe, "Contactless fluid manipulation in air: Droplet coalescence and active mixing by acoustic levitation," *Scientific reports*, vol. 8, no. 1, pp. 1–8, 2018.
- [93] I. S. Khalil, H. Abass, M. Shoukry, A. Klingner, R. M. El-Nashar, M. Serry, S. Misra, "Robust and optimal control of magnetic microparticles inside fluidic channels with time-varying flow rates," *International journal of advanced robotic systems*, vol. 13, no. 3, p. 123, 2016.
- [94] I. Khalil, H. Abass, M. Shoukry, A. Klingner, R. el nashar, M. Serry, S. Misra, "Robust and optimal control of magnetic microparticles inside fluidic channels with time-varying flow rates," *International Journal of Advanced Robotic Systems*, vol. 13, p. 1, Jun. 2016. DOI: 10.5772/63517.
- [95] S. Sanchez, A. Solovev, S. Harazim, O. Schmidt, "Microbots swimming in the flowing streams of microfluidic channels," *Journal of the American Chemical Society*, vol. 133, p. 701, Feb. 2011. DOI: 10.1021/ja109627w.
- [96] S. Floyd, C. Pawashe, M. Sitti, "Two-dimensional contact and noncontact micromanipulation in liquid using an untethered mobile magnetic microrobot," *IEEE Transactions on Robotics*, vol. 25, pp. 1332–1342, Jan. 2009.
- [97] K. Meng, Y. Jia, H. Yang, F. Niu, Y. Wang, D. Sun, "Motion planning and robust control for the endovascular navigation of a microrobot," *IEEE Transactions on Industrial Informatics*, 2019.
- [98] C.-L. Chang, W. Huang, S. Jalal, B.-D. Chan, A. Mahmood, S. Shahda, B. O'Neil, D. Matei, C. Savran, "Circulating tumor cell detection using a parallel flow micro-aperture chip system," *Lab Chip*, vol. 15, Feb. 2015. DOI: 10.1039/C5LC00100E.
- [99] K. Cushing, E. Undvall, Y. Ceder, H. Lilja, T. Laurell, "Reducing wbc background in cancer cell separation products by negative acoustic contrast particle immuno-acoustophoresis," *Analytica Chimica Acta*, vol. 1000, Dec. 2017. DOI: 10.1016/j.aca.2017.11.064.
- [100] P. Li, Z. Mao, Z. Peng, L. Zhou, Y. Chen, P.-H. Huang, C. Truica, J. Drabick, W. El-Deiry, M. Dao, S. Suresh, T. Huang, "Acoustic separation of circulating tumor cells," *Proceedings of the National Academy of Sciences*, vol. 112, p. 201504484, Apr. 2015. DOI: 10.1073/pnas.1504484112.
- [101] O. Yassine, C. Gooneratne, D. Abusamra, F. Li, H. Mohammed, J. Merzaban, J. Kosel, "Isolation of cells for selective treatment and analysis using a magnetic microfluidic chip," *Biomicrofluidics*, vol. 8, May 2014. DOI: 10.1063/1.4883855.
- [102] L. Mellal, K. Belharet, D. Folio, A. Ferreira, "Optimal structure of particles-based superparamagnetic microrobots: Application to mri guided targeted drug therapy," *Journal of Nanoparticle Research*, vol. 17, no. 2, p. 64, 2015.
- [103] Z. Ye, Z. Duan, Y. Su, "Theoretic and numerical analysis of diamagnetic levitation and its experimental verification," in *The International Conference on Photonics and Optical Engineering (icPOE 2014)*, International Society for Optics and Photonics, vol. 9449, 2015, p. 944907.

- [104] J.-Y. Chen, J.-B. Zhou, G. Meng, "Diamagnetic bearings for mems: Performance and stability analysis," *Mechanics Research Communications*, vol. 35, no. 8, pp. 546–552, 2008.
- [105] G. Kustler, "Diamagnetic levitation historical milestones," *Revue Roumaine Des Sciences Techniques Serie Electrotechnique Et Energetique*, vol. 52, no. 3, p. 265, 2007.
- [106] V. J. Katz, "The history of stokes' theorem," *Mathematics Magazine*, vol. 52, no. 3, pp. 146–156, 1979.
- [107] A. Demircali, K. Erkan, H. Uvet, "A study on finding optimum parameters of a diamagnetically driven untethered microrobot," *Journal of Magnetism*, vol. 22, no. 4, pp. 539–549, 2017.
- [108] N. Liao, M. Wu, F. Pan, J. Lin, Z. Li, D. Zhang, Y. Wang, Y. Zheng, J. Peng, X. Liu, *et al.*, "Poly (dopamine) coated superparamagnetic iron oxide nanocluster for noninvasive labeling, tracking, and targeted delivery of adipose tissue-derived stem cells," *Scientific reports*, vol. 6, p. 18 746, 2016.
- [109] H. Uvet, A. A. Demircali, Y. Kahraman, R. Varol, T. Kose, K. Erkan, "Micro-ufo (untethered floating object): A highly accurate microrobot manipulation technique," *Micromachines*, vol. 9, no. 3, p. 126, 2018.
- [110] E. Lauga, T. R. Powers, "The hydrodynamics of swimming microorganisms," *Reports on Progress in Physics*, vol. 72, no. 9, p. 096 601, 2009.
- [111] A. Demircali, H. Uvet, Y. Kahraman, T. Kose, S. Sisü, K. Erkan, "Precise positioning of diamagnetically levitated microrobot," in *CBU International Conference Proceedings*, vol. 5, 2017, pp. 1071–1077.
- [112] P. Varghese, S. Nain, J. S. Rathore, N. Sharma, "Experimental study on helical propulsion system of artificial nanoswimmer: Low reynolds number," in *2017 IEEE 17th International Conference on Nanotechnology (IEEE-NANO)*, IEEE, 2017, pp. 651–656.
- [113] E. M. Purcell, "Life at low reynolds number," *American journal of physics*, vol. 45, no. 1, pp. 3–11, 1977.
- [114] J. M. Camacho, V. Sosa, "Alternative method to calculate the magnetic field of permanent magnets with azimuthal symmetry," *Revista mexicana de física E*, vol. 59, pp. 8–17, Jun. 2013.
- [115] A. Demircali, R. Varol, G. Aydemir, E. N. Saruhan, K. Erkan, H. Uvet, "Longitudinal motion modeling and experimental verification of a microrobot subject to liquid laminar flow," *IEEE/ASME Transactions on Mechatronics*, 2021.
- [116] S. Tran-Cong, M. Gay, E. E. Michaelides, "Drag coefficients of irregularly shaped particles," *Powder Technology*, vol. 139, no. 1, pp. 21–32, 2004, ISSN: 0032-5910. DOI: <https://doi.org/10.1016/j.powtec.2003.10.002>. [Online]. Available: <http://www.sciencedirect.com/science/article/pii/S0032591003002973>.
- [117] G. Aydemir, A. Kosar, H. Uvet, "Design and implementation of a passive micro flow sensor based on diamagnetic levitation," *Sensors and Actuators A: Physical*, vol. 300, p. 111 621, 2019, ISSN: 0924-4247. DOI: <https://doi.org/10.1016/j.sna.2019.111621>.

- [118] M. Kim, A. Zydney, “Effect of electrostatic, hydrodynamic, and brownian forces on particle trajectories and sieving in normal flow filtration,” *Journal of colloid and interface science*, vol. 269, pp. 425–31, Feb. 2004. DOI: 10.1016/j.jcis.2003.08.004.
- [119] B. Edwards, J. Edwards, “Dynamical interactions between two uniformly magnetized spheres,” *European Journal of Physics*, vol. 38, p. 015 205, Jan. 2017. DOI: 10.1088/0143-0807/38/1/015205.
- [120] M. Simon, A. Geim, “Diamagnetic levitation: Flying frogs and floating magnets (invited),” *Journal of Applied Physics*, vol. 87, pp. 6200–6204, May 2000. DOI: 10.1063/1.372654.
- [121] J. Escalante-Martínez, J. Gómez-Aguilar, C. Calderon-Ramon, L. Morales-Mendoza, I. Cruz-Orduna, J. Laguna-Camacho, “Experimental evaluation of viscous damping coefficient in the fractional underdamped oscillator,” *Advances in Mechanical Engineering*, vol. 8, Apr. 2016. DOI: 10.1177/1687814016643068.
- [122] C. Elbuken, M. Khamesee, M. Yavuz, “Eddy current damping for magnetic levitation: Downscaling from macro- to micro-levitation,” *J. Phys. D: Appl. Phys*, vol. 39, pp. 3932–3938, Sep. 2006. DOI: 10.1088/0022-3727/39/18/002.
- [123] E. Loth, “Drag of non-spherical solid particles of regular and irregular shape,” *Powder Technology*, vol. 182, no. 3, pp. 342–353, 2008.
- [124] D. Rajagopalan, R. C. Armstrong, R. A. Brown, “Finite element methdos for calculation of steady, viscoelastic flow using constitutive equations with a newtonian viscosity,” *Journal of Non-Newtonian Fluid Mechanics*, vol. 36, pp. 159–192, 1990.
- [125] S. Tran-Cong, M. Gay, E. E. Michaelides, “Drag coefficients of irregularly shaped particles,” *Powder Technology*, vol. 139, no. 1, pp. 21–32, 2004.

A Supplementary Materials

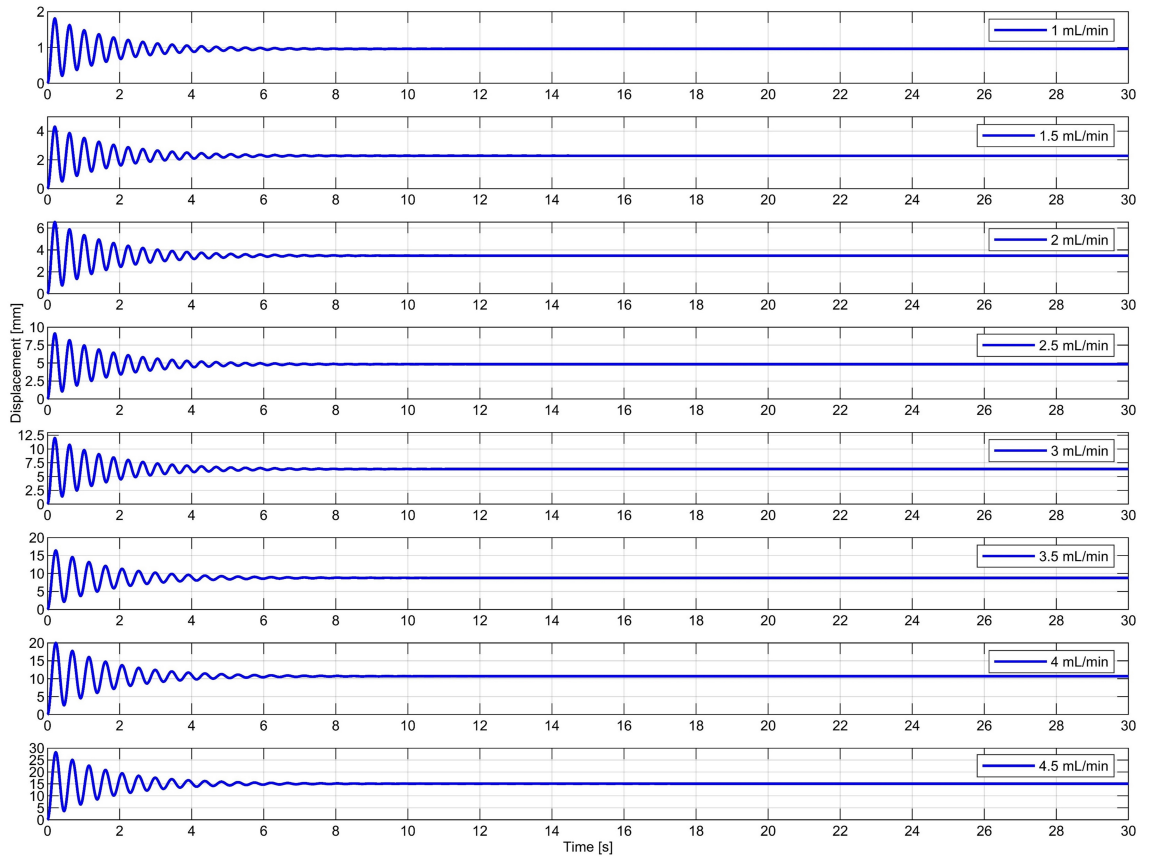


Figure A.1 Dynamic behavior of the microrobot with SU-8 body at different flow rates as predicted by the analytical model. Microrobot exhibits oscillatory behavior due to the magnetic forces' non-linear nature. After period of time when the fluidic and magnetic forces are balanced, then microrobot displacement can converge to a stable resting position.

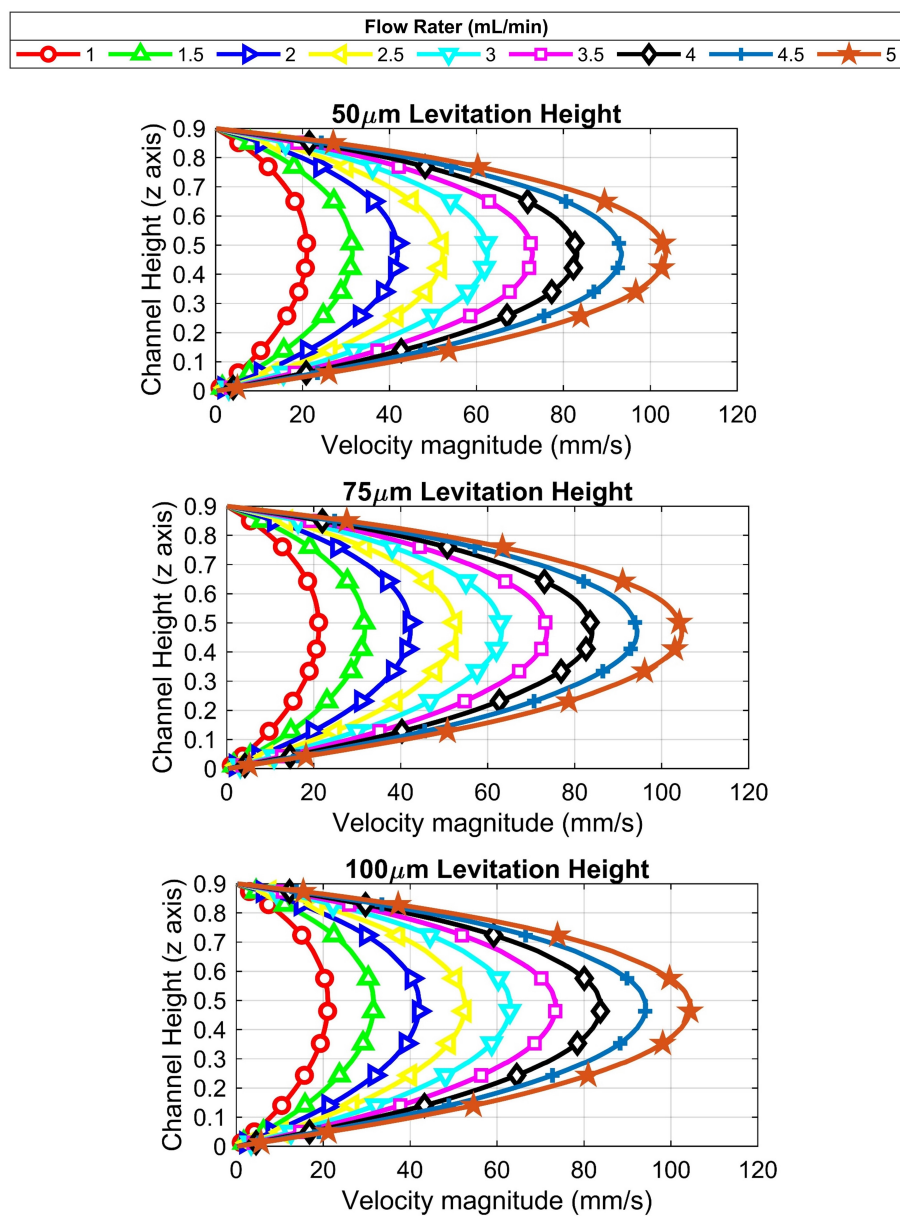


Figure A.2 This figure shows the flow profile around the microrobot for 50, 75 and 100 μm levitation heights. It was used to determine if there is a correlation between flow velocity and levitation height.

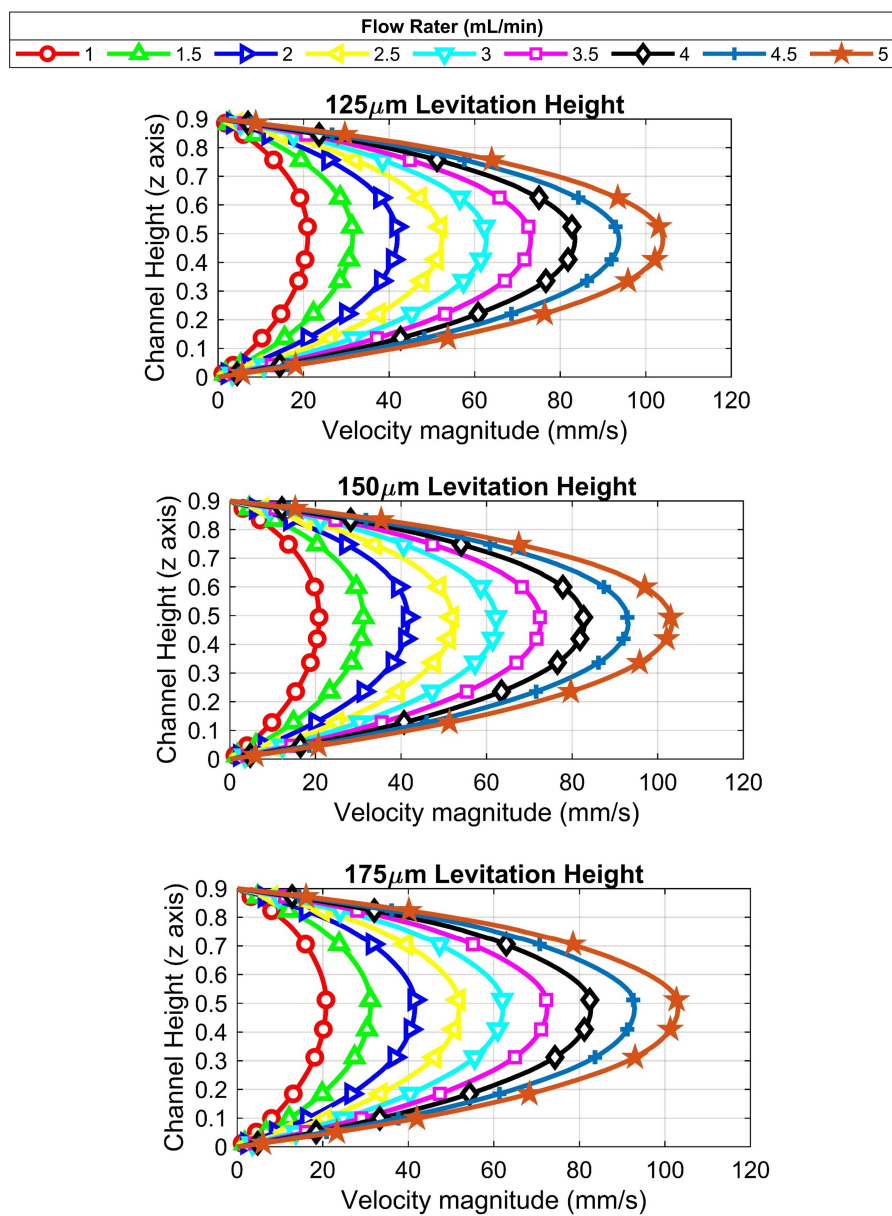


Figure A.3 This figure shows the flow profile around the microrobot for 125, 150 and 175 μm levitation heights. It was used to determine if there is a correlation between flow velocity and levitation height.

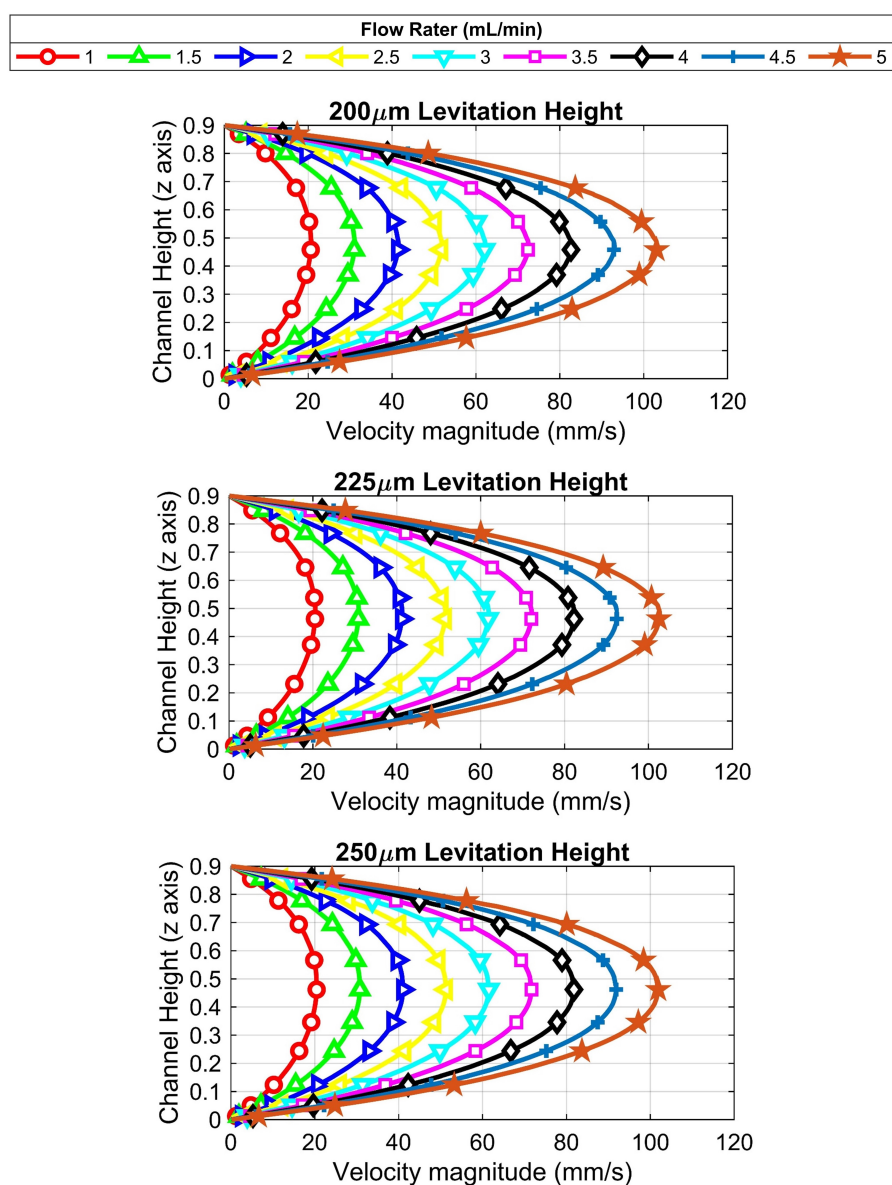


Figure A.4 This figure shows the flow profile around the microrobot for 200, 225 and 250 μm levitation heights. It was used to determine if there is a correlation between flow velocity and levitation height.

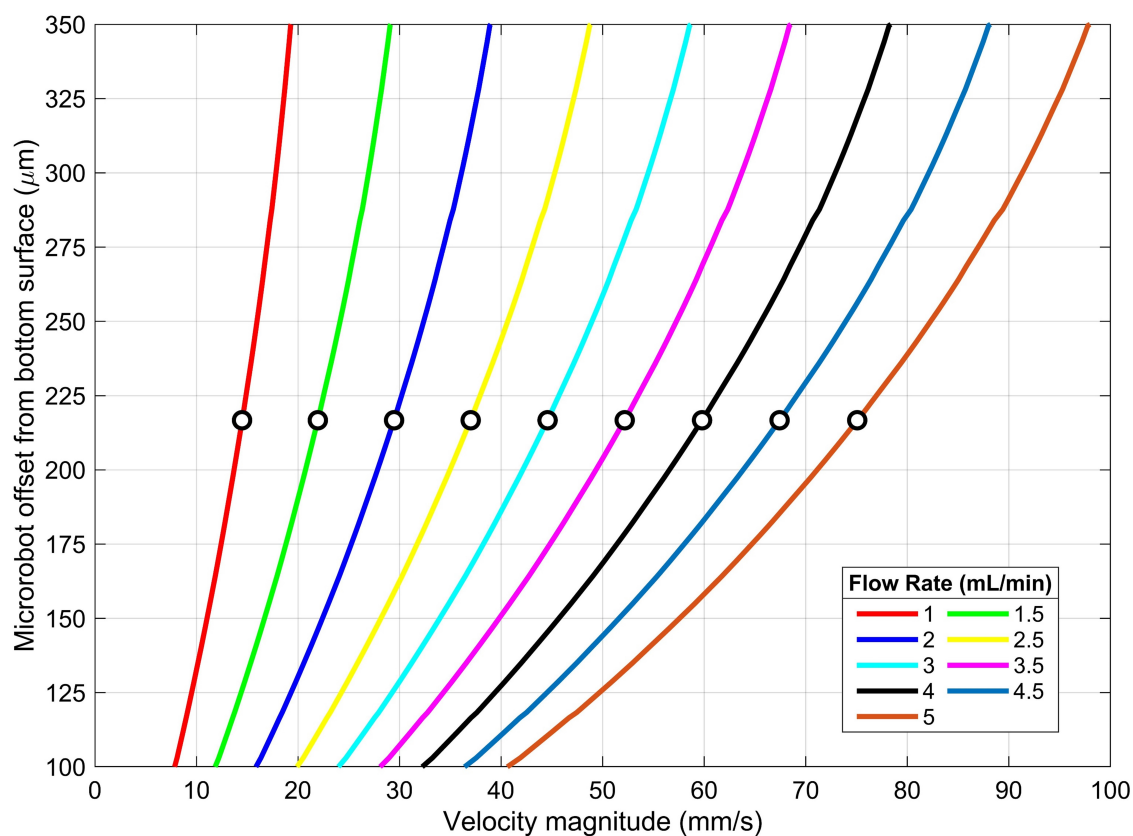


Figure A.5 This figure is used to determine the point at which the drag force is applied on the robot surface. The offset of this point from the microrobot center, which was denoted as "r" was calculated. As such, the effect of this phenomenon on the microrobot orientation was determined.

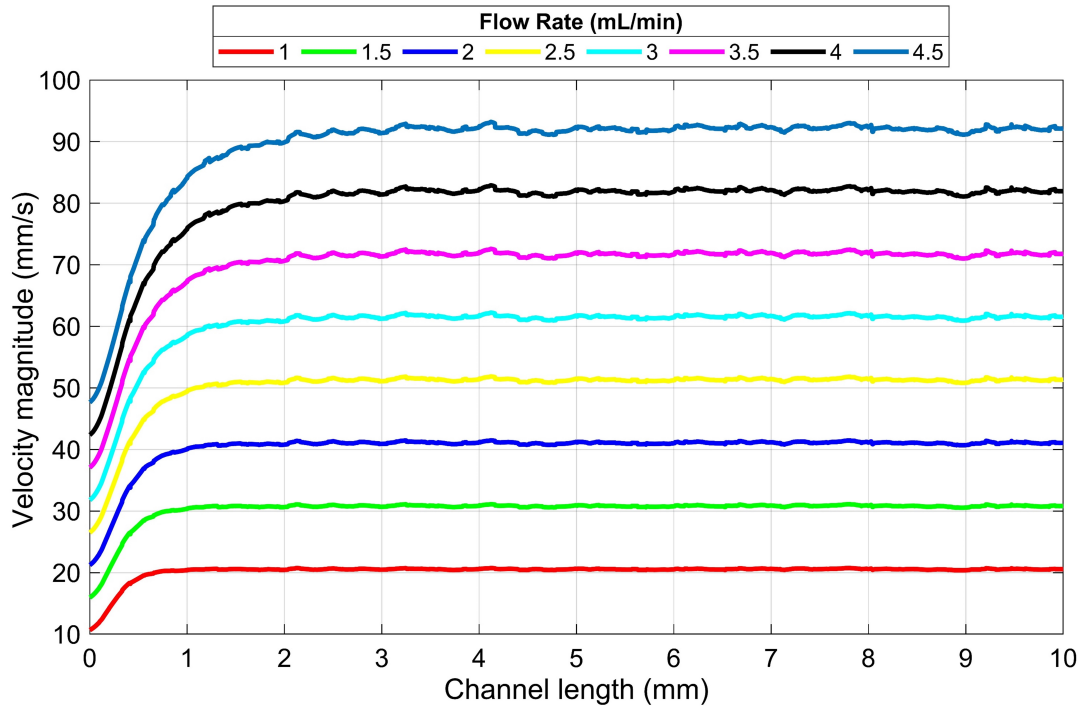


Figure A.6 This figure was used to show the impact of the hydrodynamic entrance effect on the microrobot movement. The velocity magnitude at the center of the channel gradually increases and attains a parabolic shape as it gets to the fully-developed state. This interval between the start of the channel and the point where the flow is fully developed is called the hydrodynamic entrance interval. During our calculations, the effect of this hydrodynamic entrance was taken into consideration.

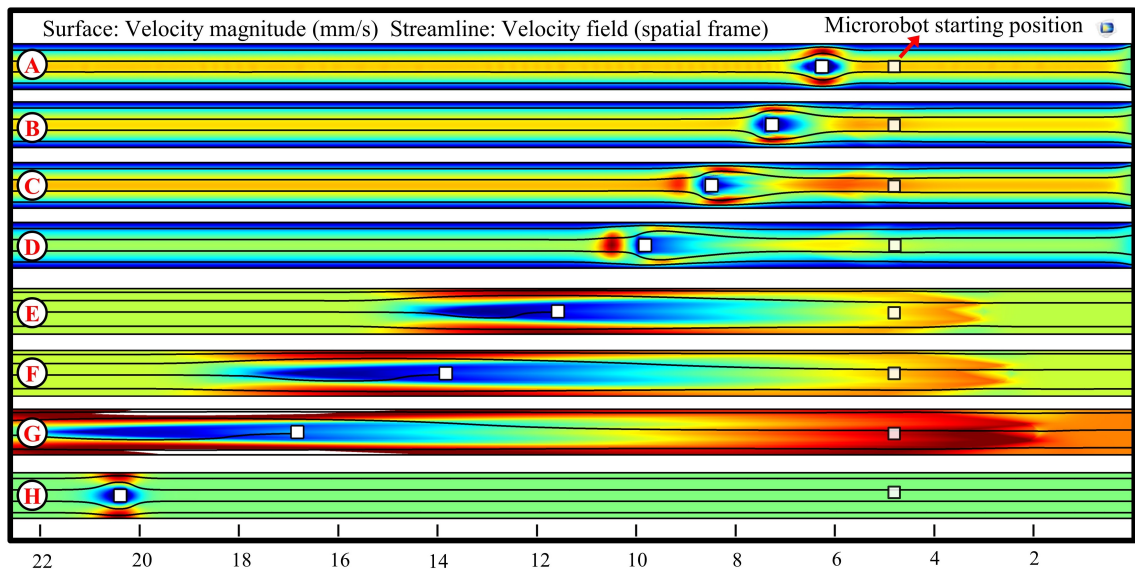


Figure A.7 This figure shows the results of the flow simulation. These results were used to determine the microrobot displacement magnitude for different flow rates.

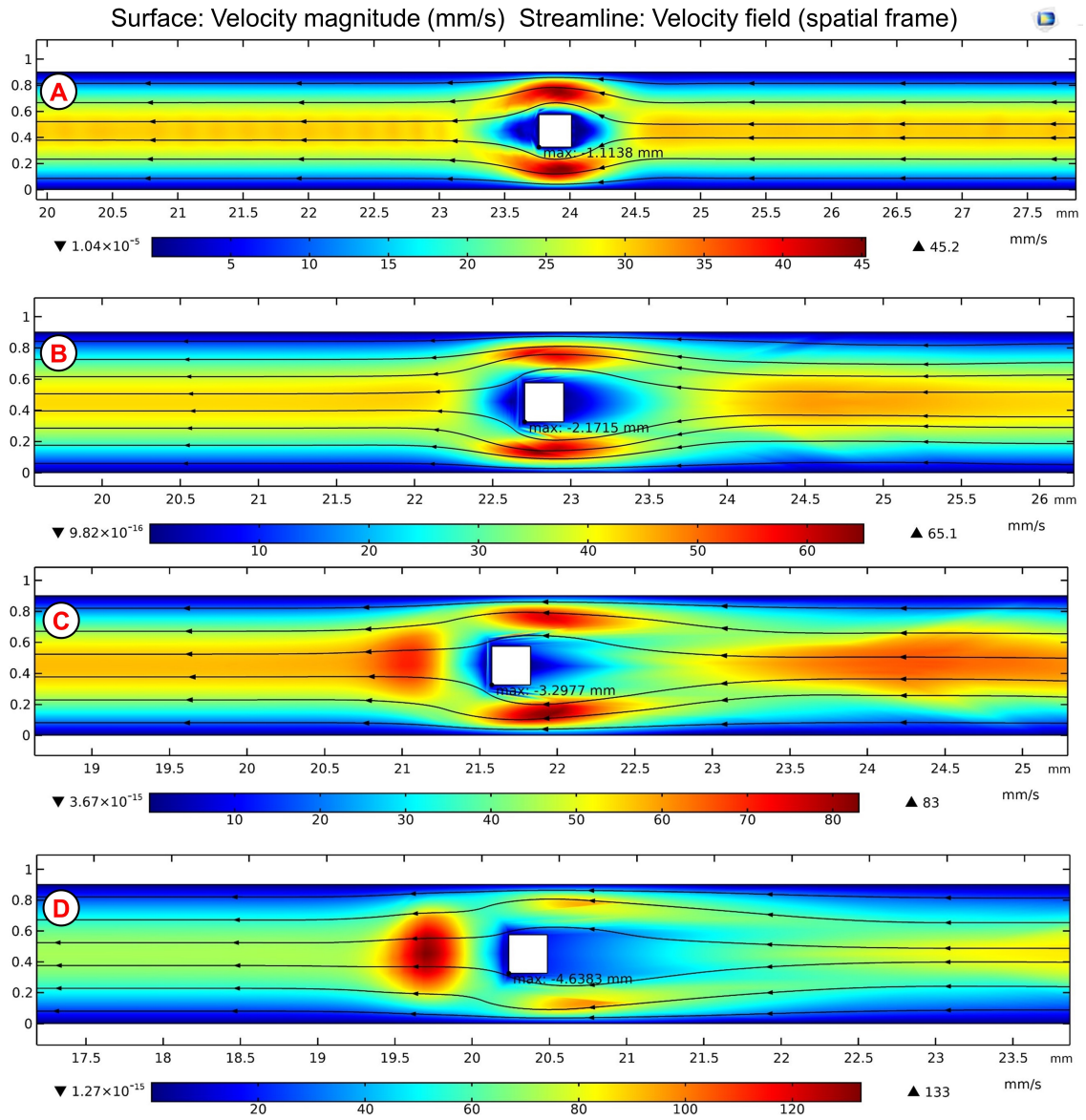


Figure A.8 This figure shows the close-up version of the flow simulation results. These results show the flow profile around the microrobot at steady-state conditions for (A) 1 (mL/min), (B) 1.5 (mL/min), (C) 2 (mL/min) and (D) 2.5 (mL/min).

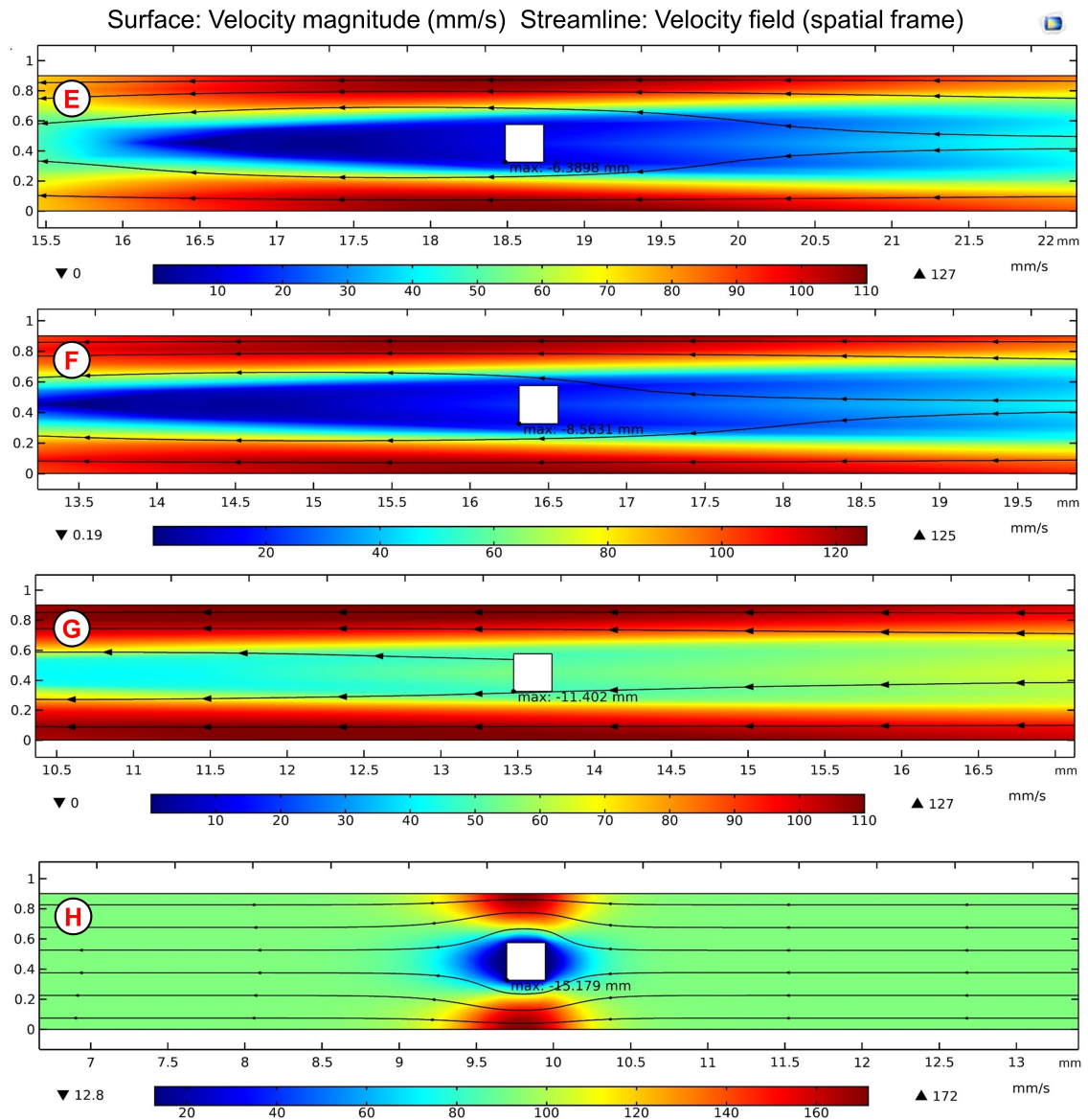


Figure A.9 This figure shows the close-up version of the flow simulation results. These results show the flow profile around the microrobot at steady-state conditions for (E) 3 (mL/min), (F) 3.5 (mL/min), (G) 4 (mL/min) and (H) 4.5 (mL/min).

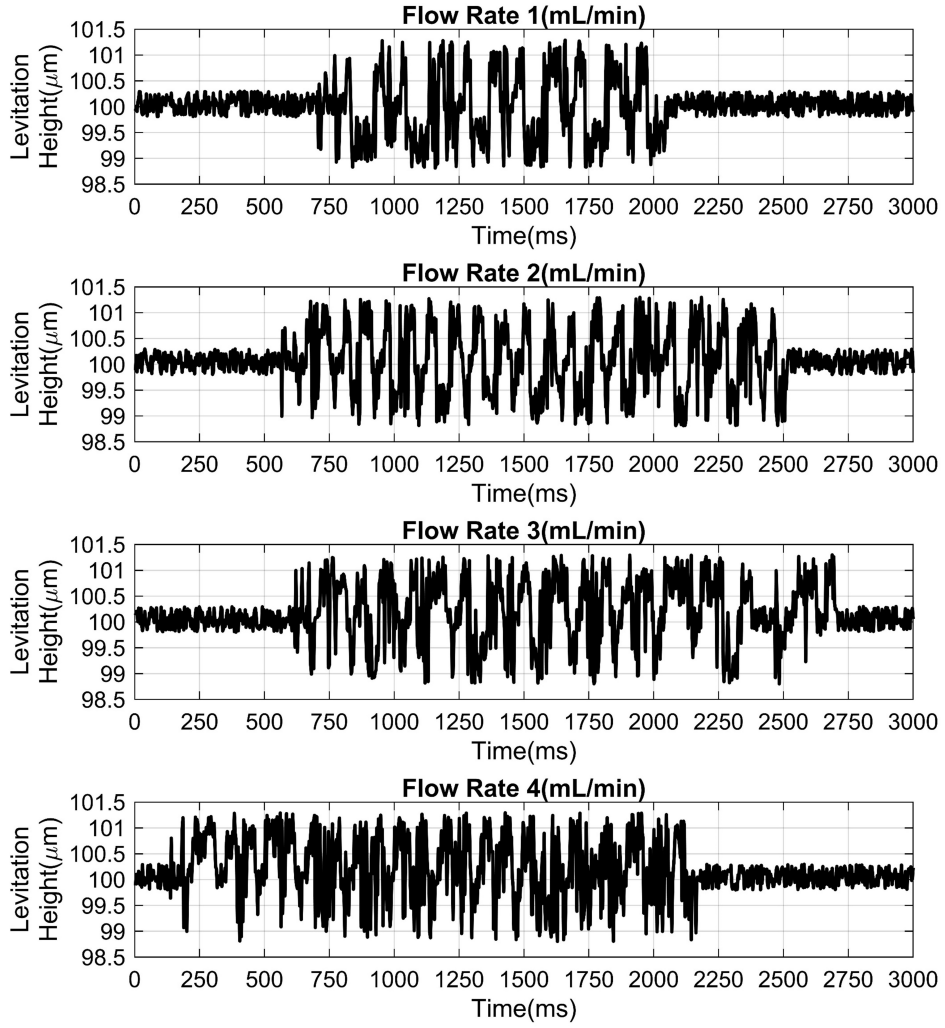


Figure A.10 This figure shows the levitation height measurements at different flow rates. The desired levitation height was $100\ \mu\text{m}$, and for the flow rates at 1 (mL/min), 2 (mL/min), 3 (mL/min) and 4 (mL/min). The deviation was less than $1.5\ \mu\text{m}$. Thus, it can be seen that the microrobot successfully operated under stable conditions when a constant flow was applied.

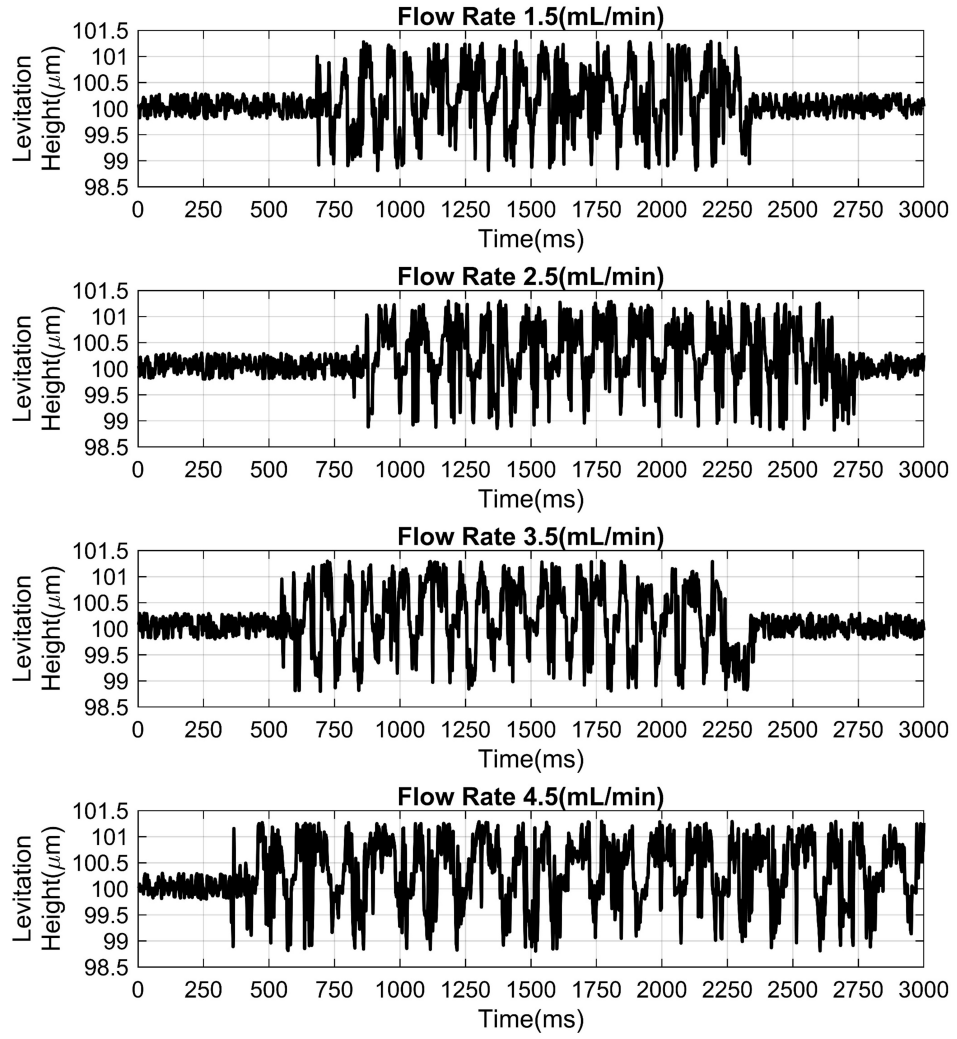


Figure A.11 This figure shows the levitation height measurements at different flow rates. The desired levitation height was 100 μm , and for flow rates at 1.5 (mL/min), 2.5 (mL/min), 3.5 (mL/min) and 4.5 (mL/min). The deviation was less than 1.5 μm . Thus, it can be seen that the microrobot successfully operated under stable conditions when a constant flow was applied.

PUBLICATIONS FROM THE THESIS

Contact Information: anildemircali1@gmail.com

Papers

1. **Demircali, A. A.**, Varol, R., Erkan, K., & Uvet, H. (2021). Untethered MicroRobot Motion Mechanism with Increased Longitudinal Force. Journal of Mechanisms and Robotics. "**Accepted**"
2. **A. Demircali**, R. Varol, G. Aydemir, E. N. Saruhan, K. Erkan and H. Uvet, "Longitudinal Motion Modeling and Experimental Verification of a Microrobot Subject to Liquid Laminar Flow," in IEEE/ASME Transactions on Mechatronics, doi: 10.1109/TMECH.2020.3049069.
3. **Demircali, A. A.**, & Uvet, H. (2018). Stabilization of Microrobot Motion Characteristics in Liquid Media. Micromachines, 9(7), 363.
4. Uvet, H., **Demircali, A. A.**, Kahraman, Y., Varol, R., Kose, T., & Erkan, K. (2018). Micro-UFO (untethered floating object): A highly accurate microrobot manipulation technique. Micromachines, 9(3), 126.
5. **Demircali, A. A.**, Erkan, K., & Uvet, H. (2017). A study on finding optimum parameters of a diamagnetically driven untethered microrobot. Journal of Magnetism, 22(4), 539-549.

Conference Papers

1. **Demircali A. A.**, Vatansever T., Saruhan E., Yilmaz A., Yilmaz B.A., Guner B., Kesen M., Erkan K., Uvet H., "A study on Increasing Longitudinal Force of Microrobot by Diamagnetic Levitation", TOK2019, Mugla, TURKEY, September 11-14
2. **Demircali A. A.**, Vatansever T., Saruhan E., Yilmaz A., Yilmaz B.A., Guner B., Kesen M., Erkan K., Uvet H., "Microrobot Control in Liquid Laminar Flow", TOK2019, Mugla, TURKEY, September 11-14
3. **Demircali A. A.**, Vatansever T., Saruhan E., Yilmaz A., Gules H., Erkan K., Uvet H., "Increasing Lateral Force of Microrobot Using Passive Diamagnetic Levitation", INSI2019, Denizli, Turkey, August 26-29

4. **Demircali A. A.**, Vatansever T., Saruhan E., Yilmaz A., Gules H., Erkan K., Uvet H., "Motion Control of Microrobot in Laminar Flow", INSI2019, Denizli, Turkey, August 26-29
5. **Demircali A. A.**, Yilmaz C.A., Üvet H., "Control of head-tilting angle of the diamagnetically levitated microrobot in liquid media", MARSS2018, NAGOYA, JAPAN, 4-8 July 2018
6. **Demircali A. A.**, Yilmaz A., Üvet H., "Orientation Control of Microrobot inside Microfluidic Chip", TORK2018, ISTANBUL, TURKEY, 12-14 April 2018
7. **Demircali A. A.**, Üvet H., "Microrobot Levitation Control in Microfluidic Chip", TOK, ISTANBUL, TURKEY, 23-27 October 2017

Awards

1. 2nd Paper Award TOK 2019 (Turkish National Committee for Automatic Control) for the paper entitled "Increasing Lateral Force of Microrobot Using Passive Diamagnetic Levitation"
2. The Scientific and Technological Research Council of Turkey(TUBITAK) 2224-A Support to Participation in International Scientific Activities Program
3. Best Paper Award TORK 2018 (Turkey Robotics Science Conference) for the paper entitled "A Microrobot Orientation Control of a Microrobot in Microfluidic Environment"
4. Best Paper Award TOK 2017 (Turkey Automatic Control Conference) for the paper entitled "A Microrobot Control in Liquid Environment"